Investigation of Sulfate Attack by Experimental and Thermodynamic Means

THÈSE N° 5263 (2012)

PAR

Wolfgang KUNTHER

EPFL

ÉCOLE POLYTECHNIQUE
FÉDÉRALE DE LAUSANNE

Suisse
2012

Abstract

This work investigates sulfate attack in complex sulfate environments by exposing different binder types to various sulfate solutions and comparing predicted phase and volume changes with experimental data. The most important aspects of this work can be grouped in three topics:

1. The **comparison of the predicted volume increase with the experimentally observed length changes**. This part of the work shows that volume increase cannot be linked directly to the observed expansions. Additionally, the volume increase model does not provide an explanation for the driving force for the space filling to overcome mechanical constraints. A more plausible explanation of expansion lies in the theory of crystallization pressure, in which crystals forming from a supersaturated solution seem to be a more applicable explanation for the deterioration differences. However, this is difficult to verify directly as it is impossible to measure the solution concentration or individual crystals exert pressure on their surroundings. It is observed that expansion occurs in systems where thermodynamic modelling predicts the co-existence of ettringite with gypsum. In such a case, if monosulfate and gypsum are both present locally, the solution can be highly supersaturated with respect to ettringite within the exposed materials. An increase of sulfate contents in the C-S-H phase has been observed for these cases, indicating increased sulfate concentrations in the pore solution while providing the necessary confinement for the crystals in intimate phase mixtures to exceed pressure.

2. The **presence of bicarbonate ions in the sulfate solution** reduces the expansion significantly for the CEM I and CEM III/B binders, and reduced the sulfate uptake in the phase assemblage. The CEM III/B mortars showed a highly leached zone at the surface in which also calcite was observed, this is attributed to the destabilisation of ettringite in the presence of

high concentrations of bicarbonate ions. The microstructural characterization combined with the information from thermodynamic modelling suggests that conditions of high supersaturation with respect to ettringite are unlikely to occur in samples exposed to solutions containing bicarbonate ions.

3. Degradation of **mortars exposed to complex magnesium containing sulfate solutions** showed that the presence of sodium, potassium and calcium in a magnesium solution reduce the deterioration symptoms significantly for the CEM I and CEM III/B mortars.

The experimental observations suggest that sulfate attack in natural environments is not only less severe, due to reduced sulfate concentrations in the field, but are likely to be affected by the presence of bicarbonate anions and the common occurrence of different cations. Both of these aspects reduce the deterioration significantly and can be assumed to occur in most natural waters.

Keywords: Sulfate attack, carbonation, thermodynamic modelling, Portland cement, blended cements, blastfurnace slag, fly ash, silica fume, sulfate (sodium, potassium, magnesium, calcium), sodium bicarbonate

Zusammenfassung

Die vorliegende Arbeit untersucht den Sulfatangriff in komplexen, sulfathaltigen Lösungen. Modellierte Mineralphasen- und Volumenänderungen werden mit experimentellen Daten verglichen. Die Ergebnisse der Arbeit lassen sich in drei Hauptaussagen zusammenfassen:

1. Der **Vergleich der berechneten Volumenzunahme mit experimentell beobachteten Dehnungen** zeigt, dass kein direkter Zusammenhang zwischen diesen Größen besteht. Die gemessenen Dehnungen der Prüfkörpern können nicht alleine auf die Volumenzunahme von Ettringit und Gips zurückführt werden. Die reine Volumenzunahme erklärt dabei nicht wie die mechanische Widerstände in den Prüfkörpern überwunden werden. Die Theorie des „Kristallisationsdrucks", welche die Druckentwicklung auf Kristalle in stark übersättigten Lösungen zurückführt, liefert eine plausible Erklärung für die beobachteten Dehnungen. Experimentell kann dies nicht direkt beobachtet werden, da die lokale Zusammensetzung der Porenlösung oder die Druckentwicklung einzelner Kristalle experimentell nicht zugänglich sind. Die größten Dehnungen wurden an Prüfkörpern gemessen in denen gleichzeitig Ettringit und Gips vorkam. Unter diesen Bedingungen enthält die Porenlösung genügend Kalzium und Sulfat so dass sie in Bezug auf Gips gesättigt ist, und mit hoher Wahrscheinlichkeit auch in Bezug auf Ettringit maximal übersättigt ist; große Drücke können generiert werden. Die erhöhten Sulfatkonzentrationen der Porenlösung lassen auch die Schwefelkonzentrationen in den C-S-H Phasen ansteigen. Die Bildung von Ettringit in direkter Umgebung der C-S-H Phasen stellt vermutlich die mechanische Beschränkung der Kristalle zur Verfügung die erlaubt, dass das chemische Potential in mechanische Energie umgewandelt werden kann.

2. Der **Einfluss von Bikarbonat Ionen in der Sulfat Lösung** reduziert die gemessenen Dehnungen für die CEM I und CEM III/B Mörtelprismen stark. Weniger Sulfat wird im Zementstein gebunden. Die CEM III/B Mörtelprismen wiesen an den Oberflächen stark ausgelaugte Zone auf welche auch Kalzit enthielten. Die Auslaugung der oberflächennahen Bereiche kann auf die Destabilisierung des Ettringits und der C-S-H Phasen durch die Bikarbonate zurückgeführt werden. Die mikrostrukturellen Untersuchungen und thermodynamischen Berechnungen legen nahe, dass eine hohe Übersättigung der Porenlösung in Bezug auf Ettringit oder Gips in Anwesenheit von Bikarbonat unwahrscheinlich ist.

3. Die **Untersuchung der verschiedenen Schädigungsmechanismen** von CEM I und CEM III/B Mörtelprismen **in komplexen magnesiumhaltigen Sulfatlösungen** haben gezeigt, dass die Präsenz anderer Kationen (Natrium, Kalium und Kalzium) die Schädigungsprozesse ebenfalls signifikant abschwächen.

Die experimentellen Beobachtungen legen nahe, dass ein Sulfatangriff unter Feldbedingungen weniger stark als in Laborversuchen ausgeprägt ist. Die Gründe dafür sind nicht nur die niedrigeren Sulfatkonzentration, sondern auch die Anwesenheit von Bikarbonat und verschiedenen Kationen.

Schlagwörter: Sulfatangriff, Karbonatisierung, thermodynamische Modellierung, Portlandzement, Portlandkompositzemente, Flugasche, Silikastaub, Hochofenzemente, Sulfate (Natrium, Kalium, Magnesium, Kalzium), Natrium Hydrogenkarbonat

Acknowledgements

Frank Bellmann	Barbara Gleich	Pietro Lura
Mohsen Ben Haha	Christophe Gosselin	Björn Marteinsson
Luigi Brunetti	Reiner Härdtl	Erika Menamkat
Köbi Burkhard	Anne-Sandra Hofer	Urs Müller
Laure Chaignat	Michelle Hughes	Beat Münch
Olga Chowaniec	Andres Idiart	Kurt Pfeiffer
Marie-Alix Dalang-Secretan	Marcel Käppeli	Claude Pilloud
Alexandre Dauzeres	Joseph Kaufmann	John Rossen
Emmanuel Denarié	Olaf Kolditz	Kurt Schmid
Florian Deschner	Georg Kosakowski	Thomas Schmidt
Belay Dilnesa	Harm-Anton Klok	Ruben Snellings
Víctor Fernàndez-Altable	Dimitri Kulik	Angela Steffen
Lucia Ferrari	Patrick Le Bescop	Walter Trindler
Robert Flatt	Gwenn Le Saout	Pavel Trtik
Patrick Fontana	Emilie L'Hopital	Ólafur Wallevik
Emmanuel Gallucci	Klaus Lipus	Frank Winnefeld
Mette Geiker	Roman Loser	Mateusz Wyrzykowski

Table of Contents

List of Tables

List of Figures

Glossary

Cement Oxide Nomenclature

A	Al_2O_3
C	CaO
c	CO_2
F	Fe_2O_3
H	H_2O
M	MgO
$	SO_3

Abbreviations

AFm	family of hydrated calcium aluminate phases, includes monosulfate, mono- and hemicarbonate, strätlingite
AFt	calcium tri sulpho aluminate phase, ettringite
BSE	backscattered electrons, method to obtain micrographs that contain phase contrast
C_3A	tricalcium aluminate, a cement clinker phase *(cement oxide nomenclature)*
C_2S	dicalcium silicate, belite, a cement clinker phase *(cement oxide nomenclature)*
C_3S	tricalcium silicate, alite, a cement clinker phase *(cement oxide nomenclature)*
C_4AF	tetracalcium aluminoferrite, a cement clinker phase *(cement oxide nomenclature)*
C-A-S-H	calcium aluminate silicate hydrate, with variable composition
C-S-H	calcium silicate hydrate, with variable composition
$C\$H_2$	calcium sulfate dihydrate, gypsum
CEM I	Portland cement, composition according to EN 197-1
CEM II	Portland fly ash cement, composition according to EN 197-1
CEM III	blastfurnace cement, composition according to EN 197-1
CEM IV	pozzolana cement, composition according to EN 197-1
EDS	energy dispersive X-ray spectroscopy
FA	fly ash, a byproduct of coal combustion

GGBFS	ground granulated blast furnace *slag*, a byproduct of steel production
HC	hemicarbonate, an AFm phase
HCO_3^-	bicarbonate ion
IA	image analysis
KOH	potassium hydroxide
wt%	mass percent
MC	monocarbonate, an AFm phase
MIP	mercury intrusion porosimetry
MS	monosulfate, an AFm phase
M-S-H	magnesium silicate hydrate
NaOH	sodium hydroxide
OPC	ordinary Portland cement (CEM I)
SCM	supplementary cementitious materials
SEM	scanning electron microscopy
SF	silica fume, a byproduct of silicon and ferrosilicon alloy production
SO_3	named as sulfate in this work; contrary to standard chemistry nomenclature (SO_4^2)
TGA	thermogravimetric analysis
TH	thaumasite
w/b	water/binder ratio; mass ratio of water to cementitious binder, including SCM's
w/c	water/cement ratio; mass ratio of water to cement
XRD	X-ray diffraction
XRF	X-ray fluorescence

1   Introduction

Sulfate attack is a complex topic as chemical, physical, and mechanical processes contribute to the deterioration. The complexity of the deterioration process has fuelled a vast amount of research without resolving the controversy about this topic (e.g. [1-6]). It is widely recognized that the sulfate containing phases ettringite and perhaps gypsum cause the damage as sulfate ions ingress into cementitious binders from their service environment.

A number of possible mechanisms have been suggested of which the "volume increase" and "crystallization pressure" are the most popular theories although no general agreement on the actual damaging mechanism has been reached. It is necessary to understand the processes in greater detail to be able to predict the interaction of binders with their aqueous environments. Especially as new binder types are developed to increase the sustainability of cement production. For these new binders only limited experience is available when it comes to durability issues, but a reliable understanding of the long term behaviour in various conditions is necessary for the fast and successful implementation of new binder types in standards and markets without relying on long term, empirical data.

The **objective** of this work is to contribute to a better understanding of sulfate attack in complex sulfate environments by investigating different binder types and comparing phase and volume changes (from thermodynamic modelling) with experimental data. The new aspects of this work can be grouped in three topics, which have been submitted as papers and are reproduced in the following chapters:

1. The comparison of the predicted volume increase with the experimentally observed length changes for different binders and sulfate solutions (Chapter 2; submitted to Cement and Concrete Research in July 2012).

2. Presence of bicarbonate ions in the sulfate solution (Chapter 3; submitted to Cement and Concrete Research in June 2012).

3. The degradation of mortars exposed to a complex, magnesium containing sulfate solution in comparison to simpler sulfate solutions (Chapter 4; submitted to Materials Structures in July 2012).

The necessary **literature overviews** are part of the individual papers/chapters as well as the **materials and methods**. The outcome of the work is summarized and commented in the **conclusions** and followed by a brief **outlook** of what could be done in the future to advance the understanding of the deterioration process further.

Additionally, a general literature survey of the relevant topics in this context, a complete description of the tested materials and methods as well as the generated data are provided in a comprehensive **appendix**, where parts of the data are also discussed and commented.

2 On the relevance of volume increase for the length changes of mortar bars in sulfate solutions

2.1 Introduction

Sulfate attack is a complex topic as chemical, physical, and mechanical processes contribute to the deterioration. The complexity of the process has fuelled a large amount of research and publications, (e.g. [1-6]) without resolving the controversy about this topic although it is widely recognized that the sulfate containing phases ettringite and perhaps gypsum cause the damage.

A number of possible mechanisms have been suggested in literature. The two most discussed in the past decades are:

- Expansion occurs due to additional volume generated by ettringite. However, a direct connection between the amount of ettringite formed and the amount of expansion has not been documented experimentally. The formation of ettringite seems to be a necessary condition for expansion, but it is not sufficient.

- The expansion is caused by crystallization pressure due to the formation of ettringite from oversaturated solution within small pores [7-11]. The crystallization pressure theory is supported by recent observations that expansion does not depend on how much ettringite is formed but strongly on where it is formed [12, 13].

Other suggested mechanisms can be dismissed:

- The topochemical formation of ettringite directly in situ from C_3A, without dissolution and precipitation reaction [14-16]: the crystal structure of C_3A and AFm are completely different to that of ettringite, so direct transformation is impossible as also discussed by [17].

- Mehta [18] suggested that ettringite could imbibe water and thereby cause expansion due to swelling. As detailed by Brown and Taylor [17], the crystal structure of ettringite makes it improbable that ettringite shows a gel-like swelling behaviour. It is unclear why ettringite

should attract water more strongly than C-S-H, ettringite is easily synthesized and in such preparations have never been noted to show swelling properties.

The volume increase explanation, and its use for modelling (e.g. [19, 20]), has persisted up to now in the literature, although in 1999, Brown and Taylor stated: "the simple view that expansion can be attributed solely to the increase in solid volume is untenable" [17]. The volume increase mechanism is based on the volume difference of one mole of a sulfate containing phase compared with the solid volume of the initial solids. For example, the volume of one mole of gypsum ($CaSO_4$ $2H_2O$; 74 cm³) is 2.25 times larger than the volume of one mole of portlandite ($Ca(OH)_2$; 33 cm³). The comparison of the volume of monosulfate (309 cm³/mol) with ettringite (707 cm³/mol) indicates a similar increase. The disadvantage of the volume increase mechanism is that it lacks an explanation for the force which is needed to cause expansion. Furthermore, the additional volume from the formation of ettringite and gypsum is generally lower than the free pore space available [21].

The crystallization pressure theory relates the chemical potential of a supersaturated solution and the pressure a crystal can develop to perform mechanical work and thereby describes the driving force for expansion caused by confined crystals according to equation 1:

$$\Delta p = \frac{RT}{V_m} \ln \frac{IAP}{K_{s0}}$$

(1)

where, Δp is the pressure; IAP the ionic activity product of the actual solution; K_{s0} the theoretical equilibrium solubility product of the crystal; so (IAP/K_{s0}) the supersaturation; T temperature; R the molar gas constant, V_m the molar volume. This mechanism has been experimentally verified [22-24].

The expansive stress in a specimen depends on the volume fraction of crytsals exerting pressure as has been discussed by Flatt and Scherer [9]. The crystallization pressure mechanism also explains

why not all ettringite formed is "expansive", as the crystals need to be confined in order to exert pressure.

This work systematically analyses the potential volume increase by thermodynamic modelling and compares it to the experimentally observed expansion. First the behaviour of the same mortar, based on a CEM I cement, exposed to different sulfate solutions and then the behaviour of mortars made with different binders in sodium sulfate solutions are discussed.

2.2 Materials and Methods

2.2.1 Materials

The CEM I (32.5 R) and CEM I HS (42.5 N HS) cement were cements from Germany, the CEM III/B (32.5 N HS LH) was from the same clinker as the CEM I cement containing 70 % slag addition. Also a CEM II/B 32.5 N (V-LL) cement containing approx. 30 % of fly ash and limestone was used. The main oxide contents and clinker phases are shown in Table 1.

Table 1: Chemical analysis of the used cements and main clinker composition according to Rietveld analysis.

cement	L.o.I	SiO_2	Al_2O_3	Fe_2O_3	CaO	MgO	SO_3	K_2O	Na_2O	TiO_2	alite	belite	aluminate	ferrite
CEM I	1.0	20.3	5.2	3.2	63.4	2.5	2.4	0.9	0.2	0.3	55.7	12.1	7.5	7.4
CEM I HS	3.7	17.9	4.3	5.9	59.8	2.4	3.1	0.8	0.6	0.4	44.2	12.9	4.6	15.4
CEM II/B	6.7	23.4	7.5	3.4	51.6	1.9	2.6	1.4	0.3	0.4	42.5	3.2	3.4	4.6
CEM III/B	0.7	29.9	9.4	1.6	47.6	4.3	4.5	0.7	0.1	0.7	17.7	3.1	1.4	1.2

Additionally, a silica fume (SF) containing mortar was produced with 12 wt% CEM I substituted by silica fume (EMSAC 500 S: L.o.I. < 2.5 %, SiO_2 > 90 %, CaO < 1.0 %, SO_3 <2.0 %, Na_2O < 1.5 %), predispersed in a slurry.

The volumes of the cement, sand and water were kept constant for all mortars. The mortars were produced with water to binder ratios of 0.55 (CEM I, CEM I HS), 0.58 (CEM I + 12% SF), 0.59 (CEM III/B) and 0.61 (CEM II/B) as the supplementary cementitious materials (SCM) have lower bulk densities than cement clinker. The sand to cement volume ratio was 3.8. Silicate aggregates were used according to DIN EN 196, part 1.

All test solutions contained 0.35 mol/ l of sulfate as sodium sulfate (50g/l), potassium sulfate (61g/l), magnesium sulfate (44.8g/l) and a sulfate mixture solution detailed in Table 2. The high sulfate concentration is comparable to that used in standard tests [25, 26]. The test solutions were prepared with deionized water. The solution volume to mortar volume ratio was 20. The solutions were exchanged after every measurement (as detailed below).

Table 2: Compositions of the tested Solutions; 0,35 mol/l correspond for Na_2SO_4 solution to 50g/l as commonly used in standard tests.

Solution	Na_2SO_4	K_2SO_4	$MgSO_4$	$CaSO_4$
Na_2SO_4	0.35 mol/l			
K_2SO_4		0.35 mol/l		
$MgSO_4$			0.35 mol/l	
Mix	0.132 mol/l	0.044 mol/l	0.088 mol/l	0.088 mol/l

2.2.2 Methods

Length changes

Length changes were determined on mortar bars (25 x 25 x 150 mm³). The bars were cut from mortar slabs to remove the surface layer of dense paste and any carbonated surface layer.

Prior to cutting, the specimens were cured for one day in a humidity chamber during setting and the first day of hardening and for an additional 27 days as slabs in saturated lime solution. Gauge alignments were glued to the ends of the cut mortar bars to improve the repeatability of the measurements. Thereafter the mortar bars were stored for 12 hours in a 95 % relative humidity chamber to harden the two component epoxy adhesive (Araldite 2014-1) before being placed into the solutions in air tight buckets.

Specimen lengths were determined in comparison to an invar bar before sulfate exposure, after 7, 14, 28, 56, 91 days of exposure and every 91 days thereafter. Lengths were measured on four specimens.

Thermodynamic Modelling

Thermodynamic calculations were carried out using the geochemical code GEMS 3 [27]. The built in PSI GEMS database was expanded with the CEMDATA07 database [28], which contains solubility products of solids relevant for cementitious systems. The dataset includes thermodynamic data of common cement minerals such as C-S-H, different AFt and AFm phases, hydrotalcite and hydrogarnets. No restrictions on the kind of hydrates calculated were imposed, with the exception of siliceous hydrogarnet ($C_3AS_{0.8}H_{4.4}$) and thaumasite whose formation was suppressed as their formation is extremely slow at ambient temperature. The degree of the CEM I and CEM I HS hydration before the exposure to the sulfate solutions was calculated to be 94 % using a kinetic model [29, 30]. It was assumed that 70 % of the slag in the CEM III/B binder had reacted (typical values for slag reaction after one year [31]). The degree of reaction of the fly ash was assumed to be 40 % [32] and 100 % for the silica fume.

The thermodynamic modelling for the sulfate mixture solution was carried out with a solution equilibrated with gypsum and free of precipitates. The calcium sulfate concentration of the calculated mixture solution was 0.007 mol/l due to gypsum precipitation.

As the presence of alkalis increases the pH of the pore solution significantly, the uptake of sodium and potassium in C-S-H phases was considered for the CEM I binder according to data provided by Hong and Glasser [33], using a distribution coefficient of 0.42 [34]. The uptake of aluminium in C-S-H was not included and thus the calculated amount of AFm phases is somewhat too high.

Sulfate attack was mimicked in the modelling by calculating the addition of increasing quantities of the sulfate solutions to the cement. This approach does not correlate with space or time and implicitly assumes that all ions in the solution penetrate into the mortar at the same rate. However, it is quickly calculated and has been shown to agree well with the phases evolution predicted with transport modelling [21] and measurements [35] for sodium sulfate solutions.

Paste samples

Paste samples were used to study the phase changes by XRD and TGA, to minimize the dilution effect occurring in mortars due to the presence of aggregate. Slabs of cement paste (40 x 140 x 160 mm^3) were cured for one day in a humidity chamber and then stored for an additional 27 days in saturated lime solution before the potentially carbonated surfaces were removed and the core sections of the slabs were cut into smaller pieces, crushed in a ceramic jaw crusher, and sieved through a 2 mm sieve.

2 g of the crushed cement pastes were added directly to the test solutions (sodium, potassium, magnesium sulfate and the sulfate mixture) in 100 ml PVC bottles and equilibrated for 1 - 1.5 years. A w/b ratio of 0.4 was applied for the CEM I binder and adjusted for the other binders to keep the

volume ratios of cement and water constant. The applied solid to solution ratio corresponds to the position of the vertical dashed line in the figures of thermodynamic modelling.

The solid phases were characterized by thermogravimetric analysis (TGA) and X-ray diffraction (XRD) after 30 minutes drying period at 40 °C, and grinding by hand. A Mettler Toldeo TGA/SDTA 851e was used, the temperature range was $30 - 980$°C with an increment of 20°C per minute in a nitrogen atmosphere. For X-ray diffraction a PANalaytical X'Pert PRO MPD diffractometer (θ-2θ) was used with an X'Celerator detector and Cu K radiation. The samples were scanned at 1.56° per minute between $5° < 2\theta < 75°$.

EDS analyses

The microstructural changes were studied on epoxy impregnated, polished and carbon coated cross sections of the mortar bars imaged with backscattered electrons in the SEM (Philips XL 30 ESEM FEG with an acceleration voltage of 15 keV). The changes of the elemental composition within the mortar bars were followed by energy dispersive X-ray spectroscopy (EDS). The EDS measurements were arranged in rectangular grids of 15 by 20 points (with14 µm between the points in both vertical and horizontal directions). Placement of the grids was chosen to represent characteristic areas at different depths. Each individual EDS measurement was assigned with a coordinate which allowed the data of the different grids to be combined in profiles expressed as distance from the surface. The actual spots measured were determined automatically by the grid and were therefore randomly distributed. Data fluctuation was high due to the heterogeneous microstructure of cement paste in mortar bars. The EDS measurements were corrected with the ZAF correction. Oxide contents (SO_3, CaO, SiO_2, Al_2O_3, MgO, Na_2O, K_2O, TiO_2, Mn_2O_3, and Fe_2O_3) were calculated from the measured elements. EDS analysis of epoxy resin in air voids or cracks, aggregates, unreacted slag or fly ash and unreacted clinker particles were removed after data acquisition based on count rate

threshold. All measurements with large amounts of portlandite, gypsum or calcite were removed in an additional data treatment step to display the changes in the C-S-H phases in the sulfate unaffected parts of the specimens. To achieve this, all EDS measurements were removed where:

$$\frac{Al}{Ca} < 0.3 - \frac{0.3}{0.5}\frac{Si}{Ca}$$

2.3   Results

2.3.1   CEM I mortars exposed to different sulfate solutions

Figure 1 shows the length changes for the CEM I mortars in the different solutions alongside the thermodynamic calculations for the four solutions. Only small length changes were observed during the first three months of sulfate exposure for all four tested solutions. Afterwards, the samples in potassium sulfate solution expanded fastest followed by the samples in sodium sulfate. These samples were discarded after one year due to the appearance of large cracks and partial loss of the gauge alignments. The samples in the magnesium sulfate and the mixture solutions showed smaller length changes.
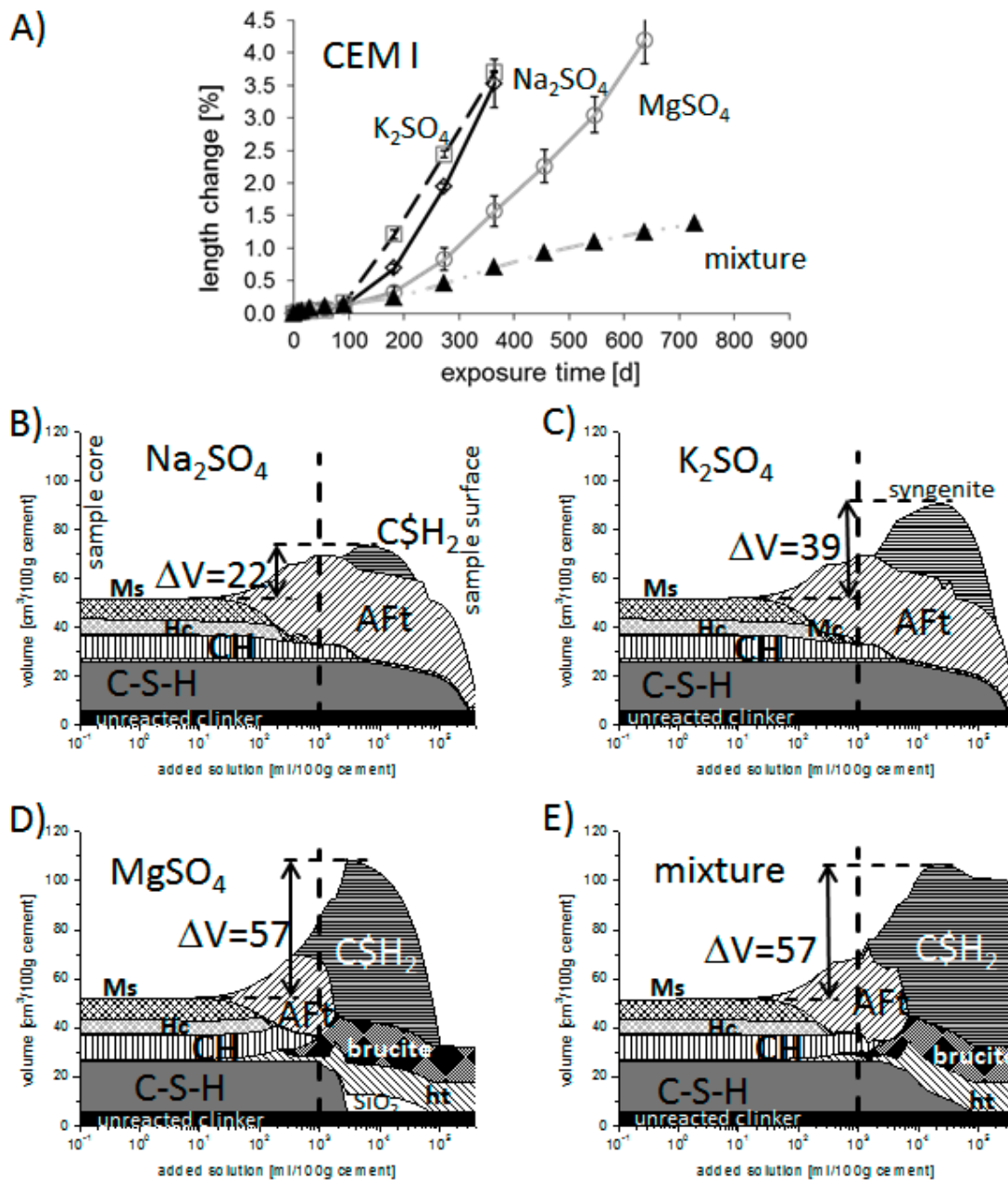
Figure 1: A) Length change over time for different sulfate solutions for mortar bars made with CEM I cement and the corresponding thermodynamic modelling for the CEM I binder exposed to B) sodium, C) potassium, D) magnesium, and E) sulfate mixture solution; AFt = ettringite, CH_2$ = gypsum, Ms = monosulfate, Hc = hemicarbonate, Mc = monocarbonate, CH = portlandite, ht = hydrotalcite; ΔV = predicted maximal volume increase.

The evolution of phases in the thermodynamic predictions is dominated first by the conversion of the AFm phases to ettringite; this is similar in all four solutions. After all available aluminate is

converted to ettringite the phases evolve differently for the different solutions. In sodium sulfate, gypsum starts to form, while in the potassium sulfate solution syngenite is formed instead. In both these cases the preformed ettringite remains stable. In the magnesium sulfate and mixture solution gypsum also forms, along with brucite and hydrotalcite. An important difference here is that the previously formed ettringite becomes unstable at higher concentrations of the solution and dissolves. The phase assemblages of the pastes equilibrated in the different solutions agreed well with the predictions of the thermodynamic modelling.

The calculated maximum volume increase is largest for the CEM I binders exposed to the magnesium sulfate and mixture solutions ($\Delta V=57$ cm³/100g cement; Figure 1D and E). Smaller volume increases are predicted for the sodium sulfate ($\Delta V=22$ cm³/100g cement) and potassium sulfate solution ($\Delta V=39$ cm³/100g cement). The calculated maximum volume increase due to ettringite formation is nearly the same for all solutions - V_{ett} ~35 cm³/100g cement – as it depends on the amount of aluminium in the AFm phases before exposure.

The predicted volume changes showed no clear relation with the observed length changes after one year (the latest time at which all the samples were measured; Figure 2). However, the samples which expanded most were predicted to have persistent ettringite alongside with gypsum.
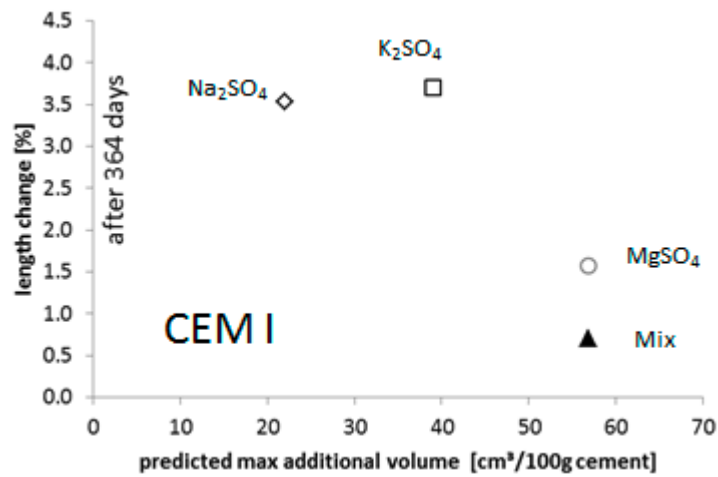
Figure 2: Comparison of the observed length changes after one year of sulfate exposure and the predicted volume increase for the CEM I mortars.

Sulfate ingress in the CEM I mortars

Figure 3 shows the profiles of sulfate content with distance from the surface, these values correspond to the amount of sulfate bound in the solid phases. At three months, before any of the samples show a take-off in expansion, these are all very similar and reflect the amount of AFm phases available to react in the pastes. These profiles indicate that the rate of ingress of the sulfate is similar for all solutions so the differences in expansion cannot be explained by difference in the sulfate ingress. Close to the surface the much higher sulfate concentrations correspond to the presence of gypsum, whose amount and distribution shows some variation between the mortars in the different solutions. Once expansion takes off, cracking occurs which facilitate sulfate ingress, which then becomes a consequence of the expansion rather than a cause.
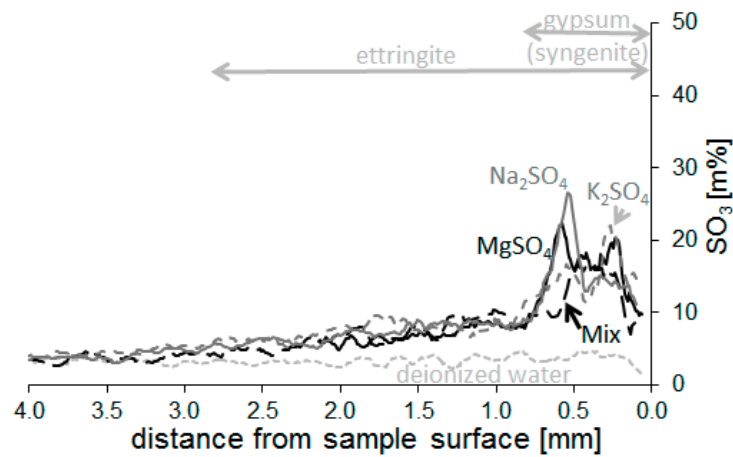
Figure 3: Median sulfate content profiles of CEM I mortar bars after 91 days exposure to the four sulfate solutions.

Generally, the experimentally observed phase changes correspond well to the predicted phase changes. However syngenite was only present for the potassium sulfate solution after longer exposure times (> 91 days) in cracks.

The formation of a brucite layer on the surfaces was observed for both magnesium sulfate and the mixture solution. This localized deposition of brucite indicates that the assumption in the thermodynamic modelling that all ions ingress at the same rate may not be strictly correct.

2.3.2 Mortars with different binders exposed to Na$_2$SO$_4$ solution

The measured length changes of the mortar bars made from five different cements exposed to sodium sulfate solution are compared with the corresponding thermodynamic predictions in Figure 4. The CEM I mortar bars expanded rapidly as previously discussed.

The length changes of the CEM II/B (V-LL) and the CEM I HS were comparable after 2.5 years of exposure but the fly ash blended cement mortars showed initially higher expansion rates which

slowed down later. The CEM I HS mortar bars expanded at later ages. The silica fume blended CEM I mortar bars expanded slowly after one year. No significant length changes were observed for the CEM III/B mortar bars.

The thermodynamic modelling of the CEM I SF and CEM I HS binder (C, D) follow the same pattern described previously that the phases of the AFm-family (monosulphate, monocarbonate and hemicarbonate) form ettringite until all aluminium is bound in this phase. Less additional ettringite is calculated to form for the silica fume blended cement (C) and the CEM I HS (D) compared to the CEM I. Gypsum is predicted to form if portlandite is present and the maximum amount of ettringite has been formed. The differences in the predicted volume increase are relatively small in contrast to the situation for the different solutions discussed above. It is also worth noting, that the predicted final volumes do not exceed the overall volume of the pastes (approximately 85 cm³/100g cement) – i.e. there is more porosity present than the volume increase. As before the paste samples showed the same phase assemblages as predicted by the thermodynamic modelling.
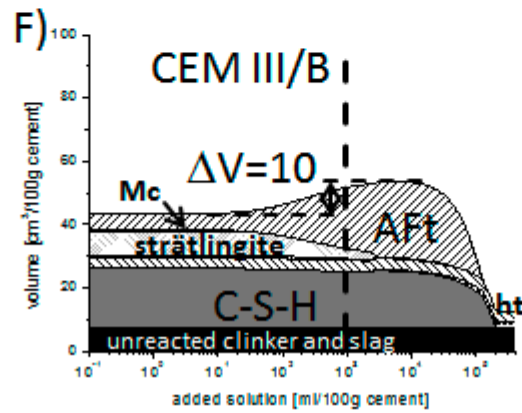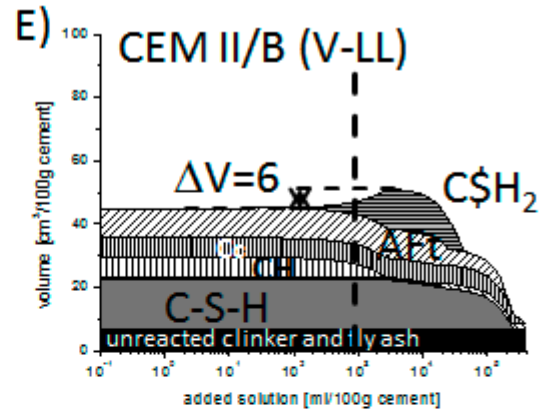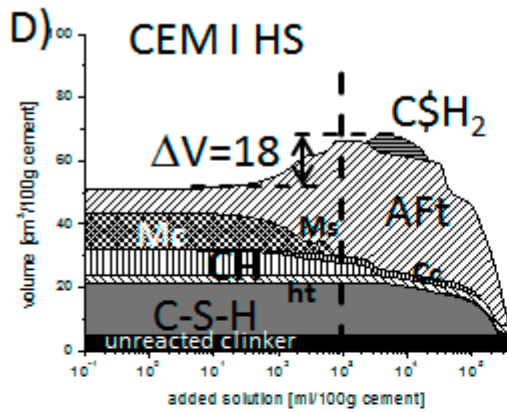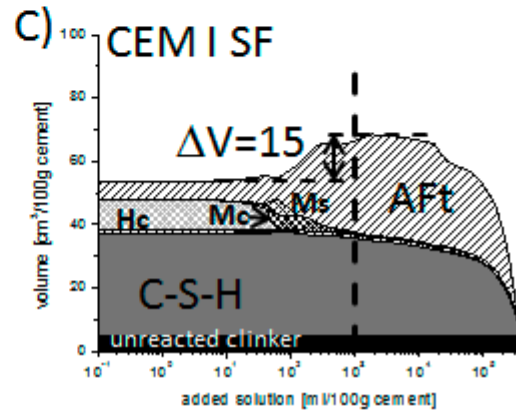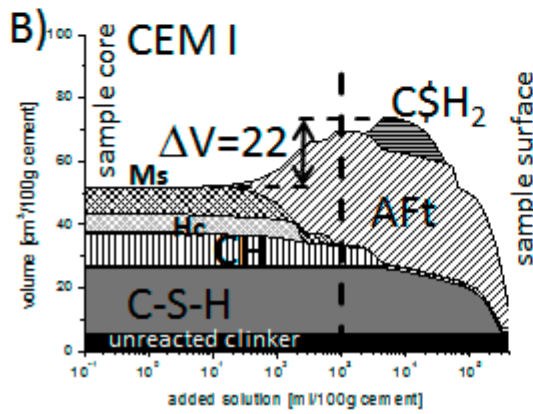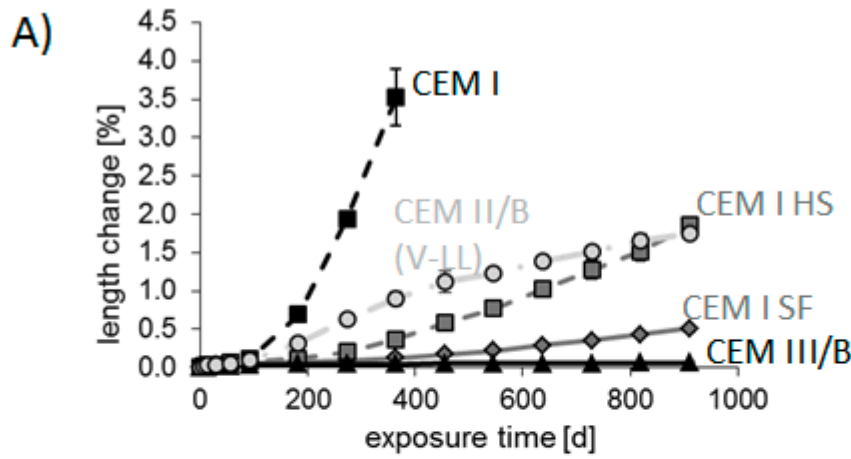
Figure 4: A) Observed length changes of different mortar bars exposed to sodium sulfate solution and the corresponding thermodynamic modelling for B) the CEM I, C) CEM I +12% SF, D) CEM I HS, E) CEM II/B and F) the CEM III/B binder exposed to sodium sulfate solution; AFt = ettringite, CH_2$ = gypsum, Ms = monosulfate, Hc = hemicarbonate, Mc = monocarbonate, Cc = calcite, CH = portlandite, ht = hydrotalcite; ΔV = predicted maximal volume increase.

Figure 5 compares the calculated volume increases to the length changes. In this case there is some trend towards higher expansion with higher volume increases, but the correlation is somewhat arbitrary. A comparison between expansion and additional ettringite gives a comparable result. Again, for the three mortars with significant length changes, the simultaneous presence of ettringite and gypsum is predicted. For the two mortars with no/little expansion, the silica fume and slag blended mortars, no gypsum is predicted.
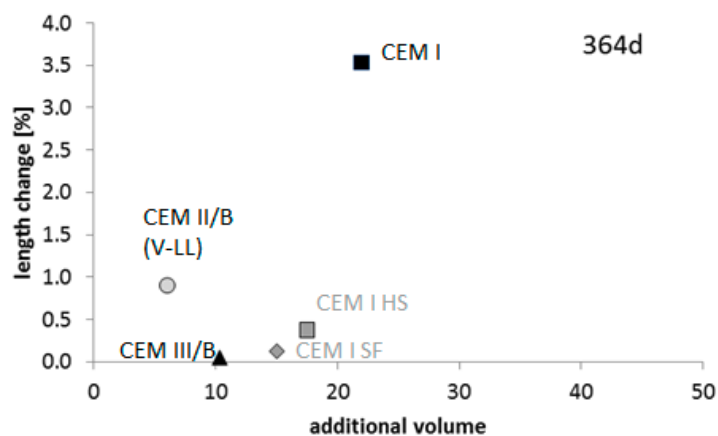
Figure 5: Comparison of the predicted volume increase and the observed length changes of different mortar bars after one year exposure to sodium sulfate solution.

Sulfate ingress in the mortars

Figure 6 shows the sulfate profiles of the five tested mortars after 91 days. There is more variation in these than for the same mortar in the different solutions (Figure 3) as expected due to the differences in the phase assemblages in the binders before exposure. Near the surface peaks correspond-

ing to gypsum formation are seen in the three cases where its formation is predicted by the thermodynamic modelling (CEM I, CEM HS and CEM II/B).

The depths of sulphate ingress were comparable for all cements, although for the CEM I slightly less penetration was observed. The higher amount of gypsum formed in the CEM I mortar and thus the binding of more sulfate near the surface may be responsible for the lower levels of sulfate at greater depths (Figure 6).
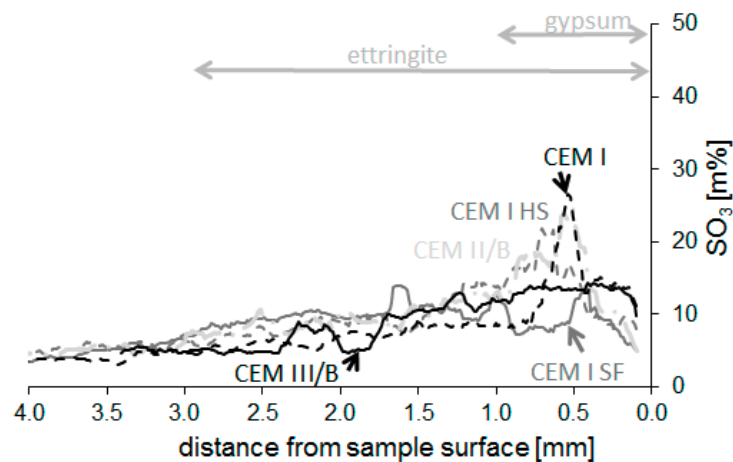
Figure 6: Median sulfate profiles of the tested mortar bars after 91 days exposure to sodium sulfate solution

2.4   Discussion

The results presented here clearly show there is no simple relation between the increase in volume of phases formed by the ingress of sulfate ions and the observed expansion. However there does seem to be a link between the coexistence of ettringite and gypsum seen in thermodynamic modelling and the tendency for expansion. As discussed in a related paper about exposure in bicarbonate solution [13], the fact that ettringite remains stable in the presence of gypsum (at higher solution concentrations) increases the probability for conditions of supersaturation with respect to ettringite to arise.

A high degree of supersaturation with respect to ettringite (AFt) is reached at high calcium and sulfate concentrations[1]. The maximum concentration of calcium and sulfate is limited by the solubility of gypsum. Thus, the maximum degree of supersaturation can be estimated by the comparison of the solubility product of ettringite with monosulfate and gypsum [9]:

$$Maximum\ Supersaturation = \frac{IAP}{K_{s0\_ettringite}} = \frac{K_{s0\_monosulfate} \cdot K_{s0\_gypsum}^{2} \cdot \{H_2O\}^{16}}{K_{s0\_ettringite}} = 10^{6.48}$$

If this value for maximum supersaturation is inserted into equation (1) (page 4), the maximum pressure generated by the growing ettringite crystals corresponds to 52 MPa. In cases where no gypsum is present, calcium and/or sulfate concentrations are lower and thus also the expected degree of supersaturation with respect to ettringite.

Considering the CEM I mortars in the different solutions, the predicted zone of common occurrence of ettringite and gypsum is larger for the sodium sulfate solution compared to the magnesium sulfate and the mixture solutions. Ettringite becomes unstable at higher concentrations where gypsum forms, considerably limiting the potential for supersaturation. However, this case is further complicated by the precipitation of magnesium as brucite at the surface, so sulfate continues to ingress without magnesium ions (hydroxide ions may be leached to maintain the charge balance). As a result, at longer ages expansion still occurs. In the potassium sulfate case, the co-existence of syngenite and ettringite is expected also to give a likelihood of supersaturation with respect to ettringite. However, it was seen that experimentally syngenite precipitated out in cracks and gypsum formed in the paste as in the sodium sulfate case. These effects seen with magnesium and potassium in the solutions could be better captured by the use of reactive transport models [4, 21, 36, 37].

In a related paper, where we present the case of exposure to a mixed sodium bicarbonate/sulfate solution, there is little expansion as the presence of bicarbonate suppresses gypsum formation [13]. To

---

[1] $K_{s0\_AFt} = \{Ca^{2+}\}^6 \cdot \{Al(OH)_4^-\}^2 \cdot \{SO_4^{2-}\}^3 \cdot \{OH^-\}^4 \cdot \{H_2O\}^{26} = 10^{-44.9}$, $K_{s0\_Ms} = \{Ca^{2+}\}^4 \cdot \{Al(OH)_4^-\}^2 \cdot \{SO_4^{2-}\} \cdot \{OH^-\}^4 \cdot \{H_2O\}^6$ $= 10^{-29.26}$ and $K_{s0\_C\$H2} = \{Ca^{2+}\} \cdot \{SO_4^{2-}\} \cdot \{H_2O\}^2 = 10^{-4.58}$; activity of water $\{H_2O\} \sim 1$; all data at 25 °

exert sufficient pressure to cause expansion, sufficient crystals need to be exposed to a supersaturated pore solution to affect the sample on the investigated scale [9, 10]. However, the micromechanics linking crystallization pressure to expansion are beyond the scope of the present paper, which focusses on the experimental observations.

Regarding the mortars with the different binders, the three systems (CEM I, CEM I/HS and CEM II/B), where gypsum is predicted (and seen experimentally) to form, expand much more than the two systems where gypsum is not predicted (CEM III/B and CEM I/SF). A small amount of gypsum was observed to precipitate locally in the CEM I/SF mortar, which may explain why it expands slightly after long exposure times. The difference in the rate of expansion between the CEM I and the CEM I/HS mortars is more interesting. The EDS microanalyses in the core of the samples (Figure 7) clearly indicate that the C-S-H contains more ettringite than AFm phase in the CEM I/HS case than in the CEM I. As there is less AFm confined within the C-S-H so there is less possibility for expansive ettringite to form.
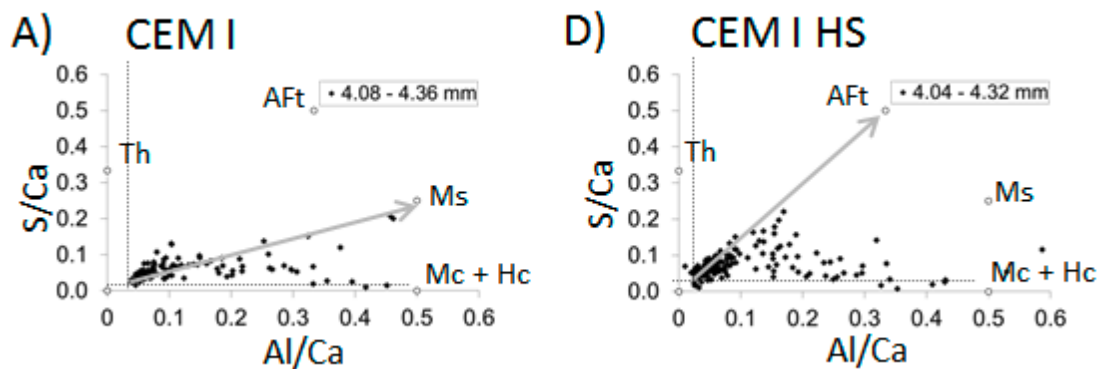
Figure 7: Atomic ratio plots (Al/Ca to S/Ca) of the cement pastes in the sulfate unaffected parts of A) CEM I and B) CEM I HS mortar bars exposed to sodium sulfate solution for 91 days.

2.5   Conclusions

The amount of volume increase due to the formation of ettringite, gypsum and/or syngenite during the interaction with sulfate solutions has no direct link to the amount of expansion observed in different solution or the expansion of different binders. While the formation of sulfate containing solids is a prerequisite for expansion, the supersaturation in solution and thus the force exerted by the forming mineral seems to be decisive.

All investigated binders, for which large zones of coexistence of ettringite and gypsum (or syngenite) were predicted, displayed more rapid expansions than mortars in which no gypsum was predicted and only small, localized amounts of gypsum were observed. The development of crystallization pressure due to crystals in supersaturated pore solution is more probable when gypsum and ettringite can co-exist thermodynamically. In this situation, any remaining unconverted AFm phases (such as those confined in C-S-H) experience a solution which is supersaturated with respect to ettringite and consequently the formation of ettringite generates expansive crystallisation pressure.

3   Influence of bicarbonate ions on the deterioration of mortar bars in sulfate solutions

3.1   Introduction

The mechanisms causing expansion and deterioration in cements due to the interaction with sulfate are not well understood [17]. Most commonly the expansion is linked to the formation of ettringite and thus the creation of additional volume. However, only if the pore solution is highly supersaturated, the growth of crystals can generate pressure [7, 9-11]. The expansive stress developed is related to the volume fraction of the crystalline phase that grows in confined pores, to the size and shape of the pores and to the degree of oversaturation. The fraction of phases which grows unrestrained in a pore space exert no expansive stress. In a recent paper, Yu and Scrivener [12] presented evidence that expansion in sodium sulfate solutions can be attributed to the formation of ettringite within the confines of C-S-H gel. As sulfate ions ingress into the material, they react with AFm phases in large deposits, to give ettringite without expansion. During this stage the concentration of sulfate ions in solution remains low due to reaction with the AFm. Once this "readily available" source of alumina has been consumed, the sulfate concentration in solution increases (reflected in the change in S/Ca ratio of the C-S-H). This provides the level of supersaturation needed for ettringite to form from AFm phases embedded in the C-S-H gel. Some authors [2, 38-40] presented data indicating that also gypsum formation can lead to expansion. However, the preponderance of gypsum in cracks (where neither supersaturation nor constraint are probable), strongly suggests that the cracks form first and then gypsum forms in them.

In sulfate containing ground waters carbonates are also often present. In areas with carbonate containing soils and rocks, high dissolved bicarbonates concentrations of up to 1 g/l can be present [41]. Bicarbonate (HCO_3^-) is the dominant carbonate species in aqueous solutions at pH values between 7 and 10. However, despite the widespread presence of bicarbonate ions in natural waters,

their role in the deterioration of concrete due to sulfate ions (so called "sulfate attack") is not well established.

There are indications that carbonation of concrete prior to the interaction with sulfates enhances its sulfate resistance [42-44]. Laboratory studies [38, 45] suggested that the precipitation of $CaCO_3$ and thus the reduction of the available $Ca(OH)_2$ content led to the formation of less expansive products.

This work investigates the changes in deterioration of two mortars, based on a CEM I and on a CEM III/B cement, during exposure to sodium sulfate solution and to solutions containing simultaneously sodium sulfate and sodium bicarbonate. The experimental observations are compared to thermodynamic modelling and phase characterization to understand the differences in deterioration.

3.2 Materials and methods

3.2.1 Materials

The CEM I cement was commercial cement from Germany, the CEM III/B was a commercial cement, from the same clinker containing 70% slag addition. The main oxide contents and main clinker phase contents of the cements used, a CEM I and a CEM III/B, are shown in Table 3 and Table 4.

Table 3: Chemical Composition of the cements used (CEM I 32.5 R, CEM III/B 32.5 N HS LH).

Cement type	SiO_2	Al_2O_3	Fe_2O_3	CaO	MgO	SO_3	K_2O	Na_2O	CO_2	L.o.I.
				[m%]						
CEM I	20.3	5.2	3.1	63.4	2.5	2.4	0.9	0.2	0.4	1.0
CEM III/B	29.9	9.4	1.6	47.6	4.3	4.5	0.7	0.1	1.1	0.7
slag	37.0	12.6	0.5	40.5	5.4	2.4	0.6	0.4	0.3	0.0

Table 4: The main cement clinker phases according to Rietveld analysis (typical error +/- 1-2%).

cement	alite	belite	aluminate	ferrite
CEM I	55.7	12.1	7.5	7.4
CEM III/B	17.7	3.1	1.4	1.2

The volumes of the cement, sand and water were kept constant for both mortars. The mortars were produced with water to binder ratios of 0.55 (CEM I) and 0.59 (CEM III/B) as the slag cement has a lower bulk density. The sand to cement volume ratio was 3.8. A silica sand was used according to DIN EN 196, part 1.

The test solutions contained sodium sulfate, 0.35 mol/ liter (50g/l sodium sulfate), and sodium sulfate and sodium bicarbonate, both 0.35 mol/ liter (50g/l sodium sulfate and 30g/l sodium bicarbonate; referred to as "bicarbonate solution"). The high sulfate concentration is comparable to standard tests [25, 26]. The test solutions were prepared with deionized water using a solution volume to mortar volume ratio of 20. The solutions were exchanged after every measurement (as detailed below).

3.2.2 Methods

Length changes

Length changes were determined on mortar bars (25 x 25 x 150 mm³). The bars were cut from mortar slabs to remove the surface layer of dense paste and any carbonated surface layer.

Prior to cutting, the specimens were cured for one day in a humidity chamber during setting and the first day of hardening and for an additional 27 days as slabs in saturated lime solution. Gauge alignments were glued to the ends of the cut mortar bars to improve the repeatability of the measurements. Thereafter, the mortar bars were stored for 12 hours in a 95 % relative humidity chamber to harden the two component epoxy adhesive (Araldite 2014-1) before being placed into the solutions in air tight buckets.

Specimen lengths were determined in comparison to an invar bar before sulfate exposure and after 7, 14, 28, 56, 91 days of exposure and every 91 days after. Lengths were measured on four specimens.

Thermodynamic modelling

Thermodynamic calculations were carried out using the geochemical code GEMS 3 [27]. The built in PSI GEMS database was expanded with the CEMDATA07 database [28], which contains solubility products of solids relevant for cementitious systems. The dataset includes thermodynamic data of common cement minerals such as C-S-H, different AFt and AFm phases, hydrotalcite and hydrogarnets. No restrictions on the kind of hydrates calculated were imposed, with the exception of siliceous hydrogarnet ($C_3AS_{0.8}H_{4.4}$) and thaumasite whose formation was suppressed as its formation is kinetically hindered at ambient temperature. The degree of the CEM I hydration before the exposure to the sulfate solutions was calculated to be 94 % using a kinetic model [29, 30]. It was assumed that 70 % of the slag in the CEM III/B binder had reacted (typical values for slag reaction are around 40% at one month and 70% after one year).

The uptake of sodium and potassium in C-S-H phases was considered for the CEM I binder according to data provided by Hong and Glasser [25] using a distribution coefficient of 0.42 [34], as the

presence of alkalis increase the pH of the pore solution significantly. The uptake of aluminum in C-S-H was not included in the model.

Sulfate attack was mimicked in the modelling by calculating the addition of increasing quantities of sulfate solutions to the cement. This approach does not correlate with space or time and implicitly assumes that all ions in the solution penetrate into the mortar at the same rate: However, it is quickly calculated and has been shown to agree well with the phases evolution predicted with transport modelling [21] and measurements [35] for sodium sulfate solutions.

Paste experiments

Paste samples were used to study the phase changes by XRD and TGA, to minimize the dilution effect occurring in mortars, due to the presence of aggregate. The two test solutions (sodium sulfate with and without sodium bicarbonate) were added directly to 1.5 g of the cements in 100 ml PVC bottles and equilibrated for 5 months. This ratio corresponds to the position of the vertical dashed line in the figures of thermodynamic modelling.

The pH of the solutions equilibrated with the paste samples were measured to compare with the modeled effect of the bicarbonates on the pore solutions. A Knick pH-meter 766 and a Knick SE pH/Pt1000 electrode were used. The electrode was calibrated with buffer solutions (pH 7 and 12).

The solid phases were characterized by thermogravimetric analysis (TGA) and X-ray diffraction (XRD) after 30 minutes drying period at 40 °C, and grinding by hand. A Mettler Toldeo TGA/SDTA 851e was used, the temperature range was 30 – 980°C with an increment of 20°C per minute in a nitrogen atmosphere. For X-ray diffraction a PANalaytical X'Pert PRO MPD diffractometer (θ-2θ) was used with an X'Celerator detector and Cu K radiation. The samples were scanned at 1.56° per minute between $5° < 2\theta < 75°$.

EDS measurements and data treatment

The microstructural changes were studied on epoxy impregnated, polished and carbon coated cross sections of the mortar bars imaged with backscattered electrons in the SEM (Philips XL 30 ESEM FEG with an acceleration voltage of 15 keV). The changes of the elemental composition within the mortar bars were followed by energy dispersive X-ray spectroscopy (EDS). The EDS measurements were arranged in rectangular grids of 15 times 20 points (vertical and horizontal distances between the measurements were equal to 14 μm). The placement of the grids was chosen to represent characteristic areas at the investigated depths. Each individual EDS measurement was assigned with a coordinate which allowed the data of the different grids to be combined to give profiles expressed as distance from the surface.

The actual spots measured were determined automatically by the grid and were therefore randomly distributed. Data fluctuation was high due to the heterogeneous microstructure of cement paste. Analyses corresponding to epoxy resin in air voids or cracks, aggregates, unreacted slag and clinker particles were removed after data acquisition based on count rate threshold. The EDS measurements were corrected with the ZAF correction. Oxide contents (SO_3, CaO, SiO_2, Al_2O_3, MgO, Na_2O, K_2O, TiO_2, Mn_2O_3, and Fe_2O_3) were calculated from the measured elements.

All measurements with large amounts of portlandite, calcite and gypsum were removed in an additional data treatment to display the changes in the C-S-H phases in different penetration depths. To achieve this, all EDS measurements were removed where:

$$\frac{Al}{Ca} < 0.3 - \frac{0.3}{0.5}\frac{Si}{Ca}$$

Mercury intrusion porosimetry

Mercury intrusion porosimetry (MIP) was carried out on millimeter size pieces cut from a slice of the mortar bar, which were placed in isopropanol for two hours and subsequently dried at 40 °C for one week. Thermo Fisher Pascal 140/440 equipment was used. The samples were pre-intruded to 395 kPa in the Pascal 140 and then placed in the Pascal 440 were intrusion was from atmospheric pressure to a maximum pressure of p_{max} = 200 MPa was measured [46]. For the exposed samples, slices were taken from the surface and the core of the samples.

3.3   Results

3.3.1   Length changes

Figure 8 shows the length changes for both mortars in both solutions. In the sodium sulfate solution the CEM I mortar bars start to expand dramatically after about one month, with the first signs of cracking and spalling on edges and corners after two months of exposure. The samples displayed large cracks at the end of the tests (364 days). In the mixed sodium sulfate, sodium bicarbonate solution there is little sign of expansion for about one year, after which expansion is seen in two of the four samples. For this reason three expansion curves are plotted from this point. These samples only showed deterioration at the ends. The other two specimens expanded after more than 700 days of exposure and showed similar cracking patterns. This variability is largely an artifact of the measurement. The ends are not sealed and sulfates ingress here in several directions; the glued on studs mean that deformation at the ends has a large impact on the overall measurement. The microstructure and other details of the deteriorated regions are examined further below. However, overall it is clear that the deterioration is much reduced in the presence of the bicarbonate ions.

The CEM III/B mortar shows little sign of expansion (<0.1%) in either solution (Figure 8B). This agrees with previous work, indicating that cements containing high quantities of slag show good resistance to sulfate attack.
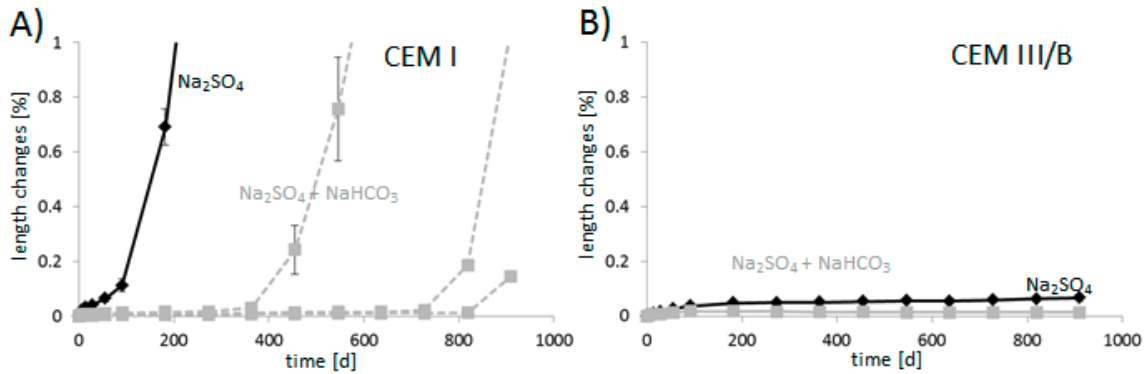
Figure 8: Length changes of A) CEM I and B) CEM III/B mortar bars exposed to sodium sulfate (black) and bicarbonate solution (grey).

3.3.2 Thermodynamic modelling

As already published for CEM I binders [36, 47], thermodynamic modelling of the changes caused by the interaction with sodium sulfate predicts for the CEM I the destabilization of portlandite and the AFm phases (monosulfate and hemicarbonate) and the precipitation of ettringite and gypsum (Figure 9A). Only after all the AFm phases have been converted to ettringite does portlandite dissolve and gypsum precipitate. Ettringite remains stable in the range of gypsum formation. Calcium silicate hydrates (C-S-H) are predicted to dissolve at the highest addition of sodium sulfate (close to the surface).
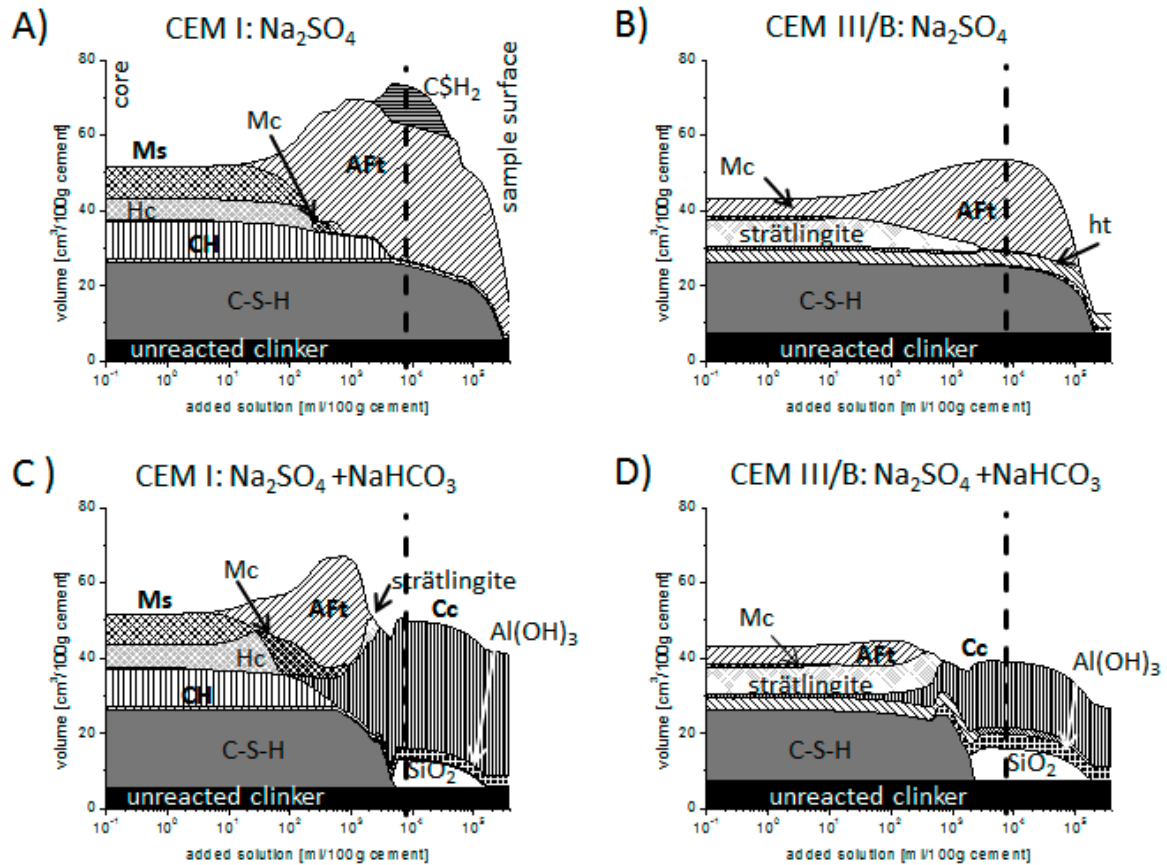
Figure 9: Schematic representation of the phase changes of the main cement hydrates of the CEM I (left) and CEM III/B (right) binder exposed to sodium sulfate (A and B) and sodium bicarbonate solution (C and D), AFt = ettringite, CH = portlandite, Cc = calcite, C$H₂ = gypsum, Hc = hemicarbonate, Mc = Monocarbonate, Ms = Monosulfate, ht = hydrotalcite; the vertical dashed lines indicate the predicted composition of the paste experiments.

The calculated phase assemblage of the unaffected CEM III/B (corresponding to the left hand side (small solution concentrations) of Figure 9B and D) consists of C-S-H, ettringite, strätlingite (an AFm phase, $Ca_2Al_2SiO_2(OH)_{10}\ 3H_2O$) and small amounts of monocarbonate and calcite. Portlandite was not predicted for the CEM III/B phase assemblage.

The addition of the sodium sulfate solution was calculated to increase the amount of ettringite at the expense of strätlingite and monocarbonate (Figure 9B). The precipitation of gypsum was not predicted. Less additional ettringite was calculated to form in the CEM III/B, although this cement has

a higher total Al_2O_3 content than the CEM I (Table 3). A significant part of the Al_2O_3 remained in unreacted slag particles – approximately 26 wt% of the total Al_2O_3 are present in unreacted slag at a degree of slag reaction of 70 %. Another 16 wt% of Al_2O_3 are predicted to be bound in hydrotalcite ($Mg_4Al_2(OH)_{14}$ $3H_2O$). Furthermore aluminum taken up by the C-S-H is not available to form ettringite [48]. The aluminum uptake in C-S-H phases can be estimated as Al/Si = 0.18, (from EDS analyses below). This corresponds to an uptake of approximately 37 wt% of the total Al_2O_3. Thus it is estimated that only 20 wt% of the Al_2O_3 is available to form ettringite in the CEM III/B binder.

The phase changes predicted for both binders exposed to the bicarbonate solution are shown in Figure 9C for CEM I and Figure 9D for the CEM III/B. In the CEM I case, first ettringite forms at the expense of AFm phases as before, the maximum amount of ettringite formed is only slightly less than in the sodium sulfate case. The dramatic difference is that once all the available alumina has formed ettringite, calcite starts to form consuming calcium and suppressing the formation of gypsum. From this point ettringite becomes unstable. This instability of ettringite can be expected to reduce the likelihood of supersaturation of the pore solution with respect to ettringite. At the highest concentrations (representing the near surface of the samples) calcite and small amounts of amorphous silica and aluminum hydroxide are predicted as stable phases.

Similar phase changes are predicted for the CEM III/B binder (Figure 9D), except that the predicted amount of ettringite is much smaller than for the sodium sulfate exposure.

The interaction of $NaHCO_3$ with cement hydrates precipitates calcite and consumes Ca^{2+} from $Ca(OH)_2$, ettringite and C-S-H:

$$Ca^{2+} + Na^+ + HCO_3^- + 2OH^- \leftrightarrow CaCO_3 + Na^+ + OH^- + H_2O$$
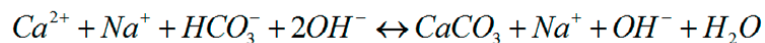
The pH of the pore solution is predicted to decrease considerably. The predicted pH for the corresponding paste experiments, represented as dashed, vertical lines in Figure 9, are summarized in Table 5 along with the real values measured as discussed below.

Table 5: Predicted pH of the test solutions corresponding to the paste experiments.

	Na_2SO_4 solution	Bicarbonate solution
CEM I, modeled	13.1	10.0
CEM I, measured	12.7	9.7
CEM III/B modeled	12.3	8.9
CEM III/B measured	12.5	9.0

3.3.3 Paste samples

TGA and XRD analyses of the paste samples exposed to sodium sulfate solution for 5 months show the presence of C-S-H, gypsum and ettringite for the CEM I and the complete dissolution of portlandite and AFm phases. In the CEM III/B samples mainly ettringite and C-S-H and traces of calcite were observed while no portlandite or gypsum was detected.

In the samples exposed to bicarbonate solution, calcium carbonates (calcite and aragonite) were observed as the only crystalline phase. Neither portlandite, ettringite nor gypsum was detected in the paste samples.

The observed phases compare well with the thermodynamic predictions as shown in Figure 9.

The pH values were around 12.6 for the samples immersed in Na_2SO_4 solution and much lower (<10) for the samples in the bicarbonate solution (Table 5). Both, the observed phase assemblage and the pronounced changes in the pH value of the pore solution confirm the changes predicted by thermodynamic modelling.

3.3.4 Sulfate profiles

Figure 10 shows the sulfate profiles obtained in mortar bars exposed to sodium sulfate and bicarbonate solution for three months. The sulfate content is higher towards the surface for the mortars

with both binders exposed to sodium sulfate solution, as previously reported by other researchers for plain Portland cements [35, 36]. Differences between the CEM I and CEM III/B samples were the larger amount of gypsum precipitated and the greater depth to which ettringite had formed in the CEM I sample. Lower sulfate concentrations at the surface were observed for the CEM III/B; gypsum precipitation occurred only occasionally in cracks and air voids, as also described by Gollop and Taylor [48]. At later ages, when the samples were expanding and cracked the differences between the mortars with the different binders became more pronounced.
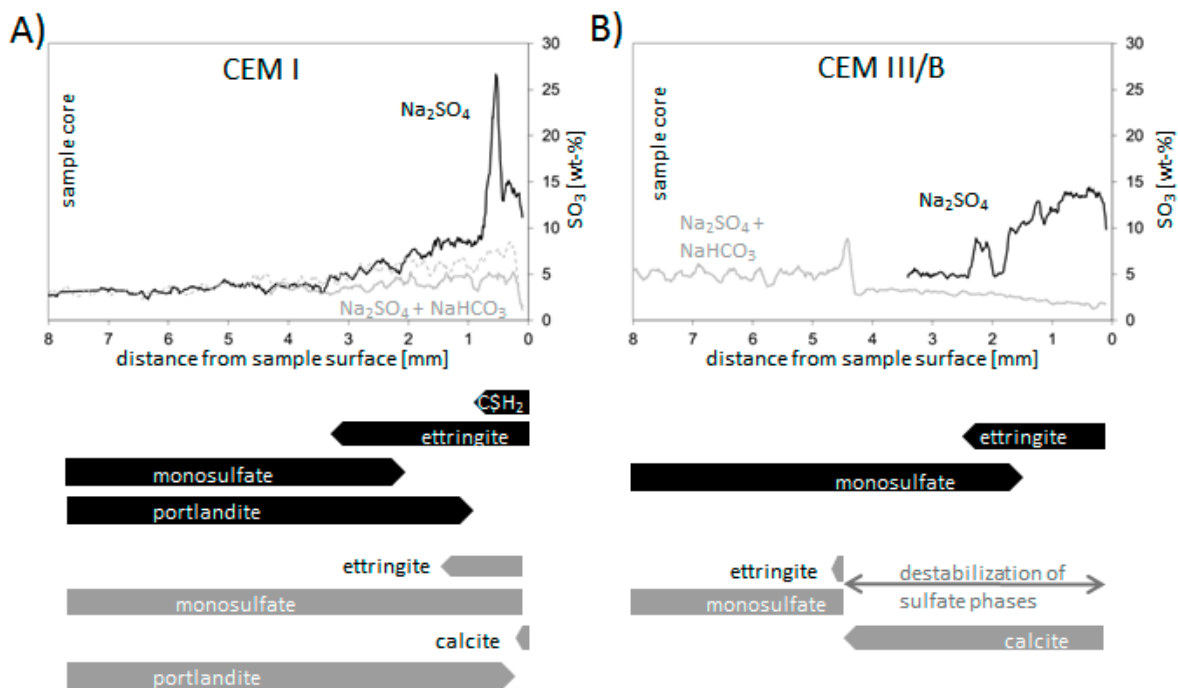
Figure 10: Sulfate profiles for A) CEM I and B) CEM III/B mortar bars exposed for 91 days to sodium sulfate (black) and sodium bicarbonate solution (grey, the dashed line is the profile after 546 days of exposure); below the profiles the regions of the most important, observed phases are indicated.

When bicarbonate ions were present in the test solution a much lower amount of sulfate was incorporated in the phase assemblage (grey lines, Figure 10). The CEM III/B binder showed distinct leaching up to 4.3 mm from the surface (grey line, Figure 10B) after 91 days that progressed almost through the whole sample during the 2.5 years testing period.

3.3.5 Microstructures

Figure 11A shows the microstructure of the samples exposed to sodium sulfate solution, here gypsum veins have formed in surface parallel cracks. In the bicarbonate solution after 91 days of exposure (Figure 11B) there are dispersed clusters of calcite in the proximity of the surface. The formation of a calcite "layer", as might be implied from the thermodynamic modelling is not seen. At very late ages (500 days) the deposits of calcite become more extensive and might be interpreted as a "layer" similar to that reported previously for samples exposed to seawater [49].

Close to the surface, away from the areas of calcite precipitation, some ettringite can be detected and its amount increases slowly with time. The increase in formation of ettringite accounts for the increase in sulfate profile between 91 and 546 days (dotted grey line in Figure 10A).
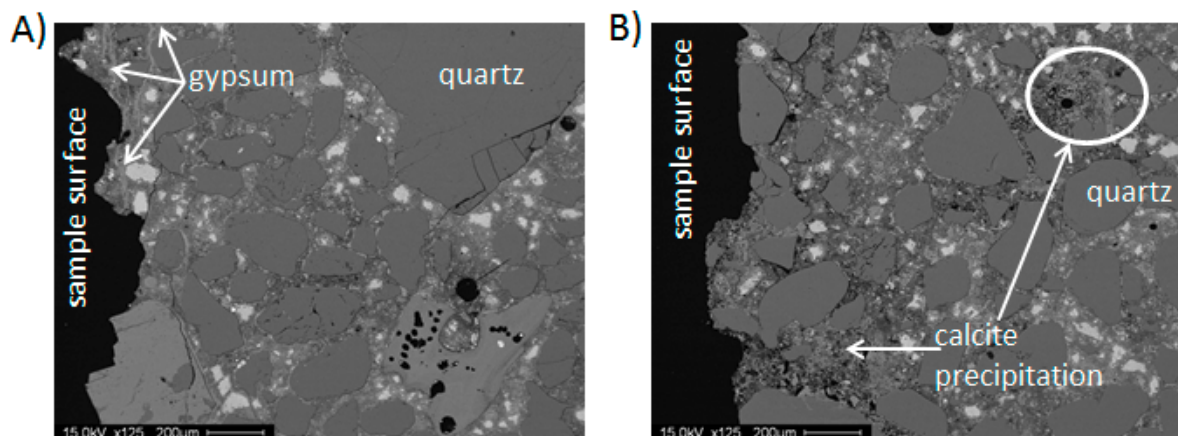
Figure 11: BSE micrographs of the leached zone in the CEM I mortar bar exposed to A) sodium sulfate solution and B) the bicarbonate solution for 91 days.

Figure 12 shows the microstructure of the CEM III/B mortar exposed to sodium sulfate solution. Only a thin leached layer at the surface is observable and gypsum was only found as occasional precipitates in air voids. Signs of expanding pastes such as cracks around aggregates were not observed (although some aggregates were removed during samples preparation and conditioning, giving large black gaps at the surface).
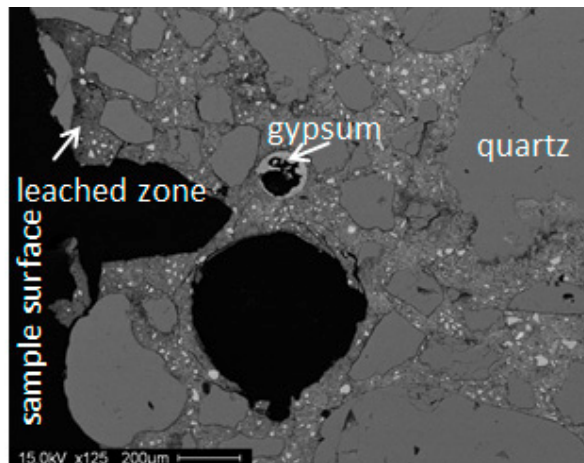
Figure 12: BSE micrographs of the surface region of a CEM III/B mortar bar exposed to sodium sulfate solution for 91 days.

The microstructural changes in the CEM III/B mortar exposed to the bicarbonate solution (Figure 13) were quite different to the CEM I binder. There were dispersed precipitates of calcite and sulfate phases were absent in the surface zone, consistent with the sulfate profile in Figure 10B. In between the leached and unaffected part of the sample was a small zone with slightly higher sulfate concentrations. These zones are illustrated in Figure 13B.
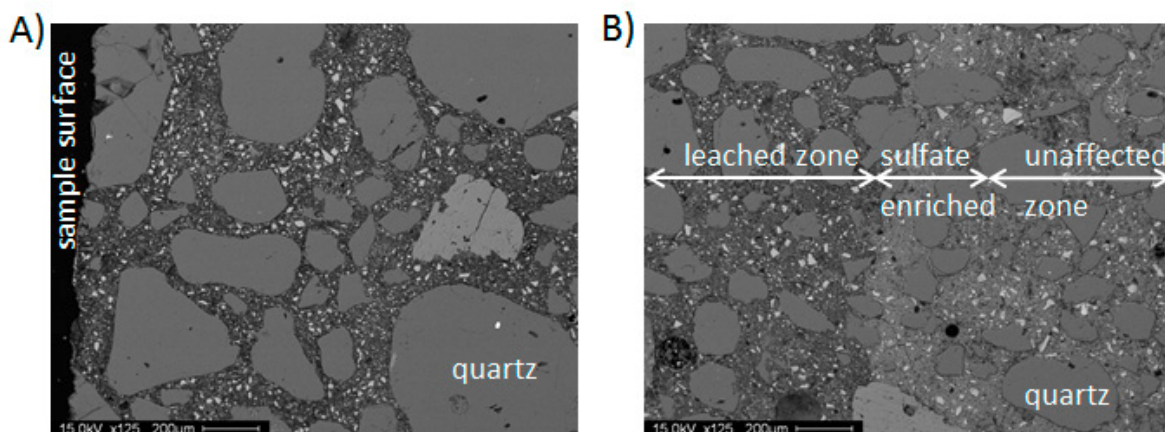
Figure 13: BSE micrographs of A) the leached zone in the CEM III/B mortar bar exposed to the bicarbonate solution for 91 days and B) the transition zone of the leached and unaffected zone at a depth of approximately 4.3 mm.

3.3.6 EDS analyses

In cement pastes C-S-H, AFm phases and ettringite are usually finely intermixed. EDS analyses can be used to study the phases present and estimate the C-S-H composition. Figure 14 shows the evolution of the EDS analyses in the undifferentiated product (avoiding areas of anhydrous grains, calcium hydroxide and gypsum) with distance from the surface for the CEM I mortar exposed in the two solutions for 91 days.
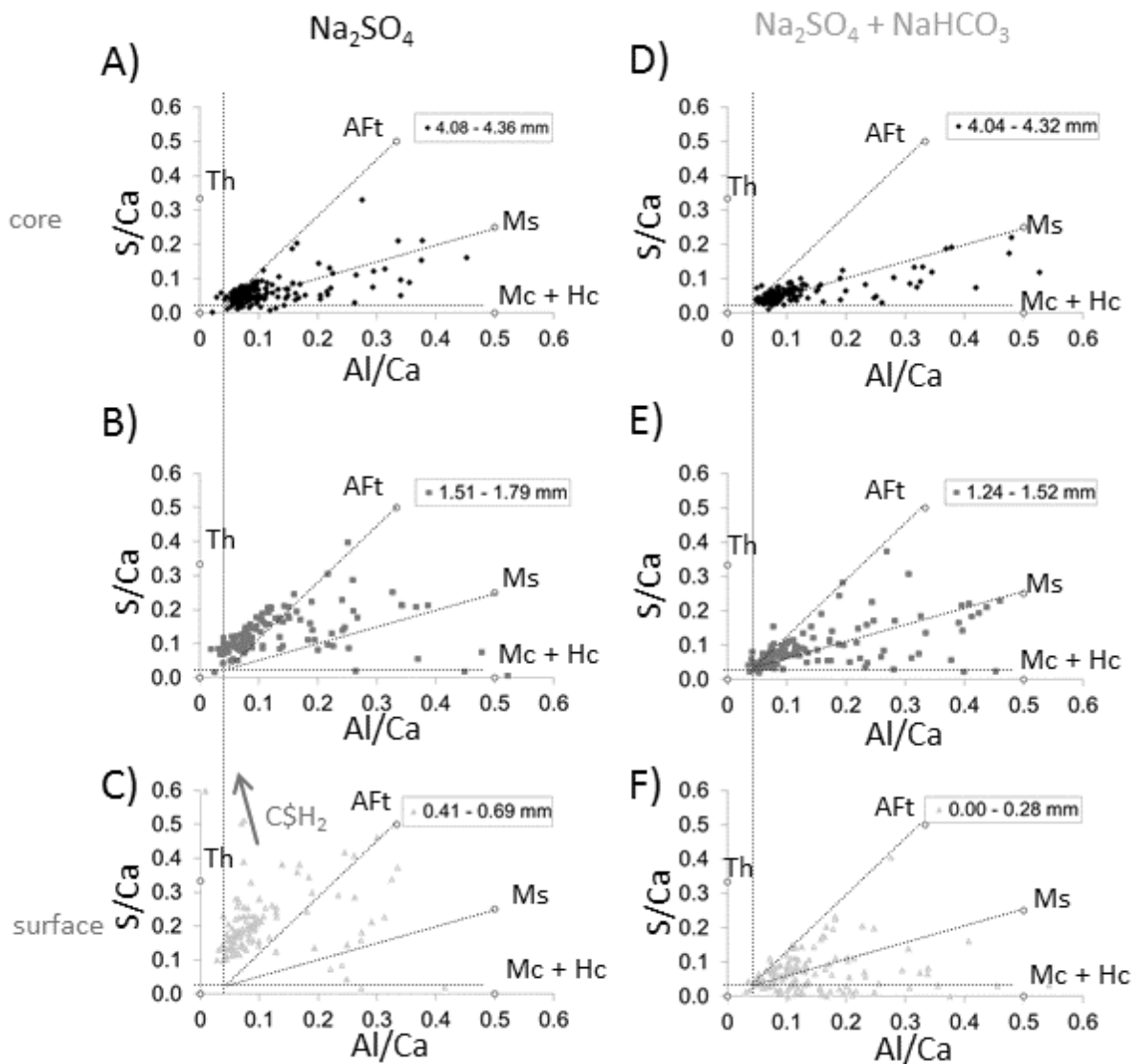
Figure 14: Atomic ratio plots (Al/Ca to S/Ca), modified by the removal of EDS measurements that were dominated by portlandite, calcite or gypsum, at selected depths for CEM I exposed for 91 days to sodium sulfate (top; A to C) and bicarbonate solution (bottom; D to F).

The core of the samples (Figure 14A and D), more than 4mm from the surface, corresponds to the unaffected region and shows C-S-H intermixed with AFm phases and small amounts of ettringite. In the sodium sulfate solution more ettringite and less AFm is found nearer to the surface (Figure 14B) at the same time there is a shift in the cloud of points corresponding to the C-S-H towards higher sulfur to calcium ratios. Close to the surface (Figure 14C) the analyses correspond to mixtures of C-S-H and ettringite, there is a further increase in the S/Ca of the C-S-H and some points corresponding to mixtures of C-S-H with gypsum. The Al/Ca ratios (indicated by the vertical dotted lines) do not change significantly indicating the aluminum in C-S-H does not participate in the reactions with sulfate (as previously reported [48]).

The increase in S/Ca ratio is important as this is considered to reflect the higher sulfate concentration of the solutions as studied by Barbarulo et al. [50, 51] and discussed by Yu and Scrivener [12]. The sulfate concentration of the solution is critical in affecting the supersaturation with respect to ettringite. High supersaturation is needed for ettringite to form from AFm phases in the CS-H and to develop crystallization pressures giving expansion. In fact the increase in S/Ca ratios was also reported by Gollop and Taylor [52] although they did not make the link with solution concentration.

In the bicarbonate solution (Figure 14D-F) there is some shift from C-S-H/AFm mixtures in the core to C-S-H/ettringite mixtures towards the surface. However, most importantly, there is no significant shift in the composition of the C-S-H cloud. Unfortunately we do not have data for the absorption of sulfate ions on C-S-H in the presence of bicarbonate ions, so we cannot infer what is happening to the sulfate concentration in solution. Nevertheless, this difference between the two solutions is quite striking and does suggest that the solution affects the development of crystallization pressure by ettringite formation avoiding expansive forces.
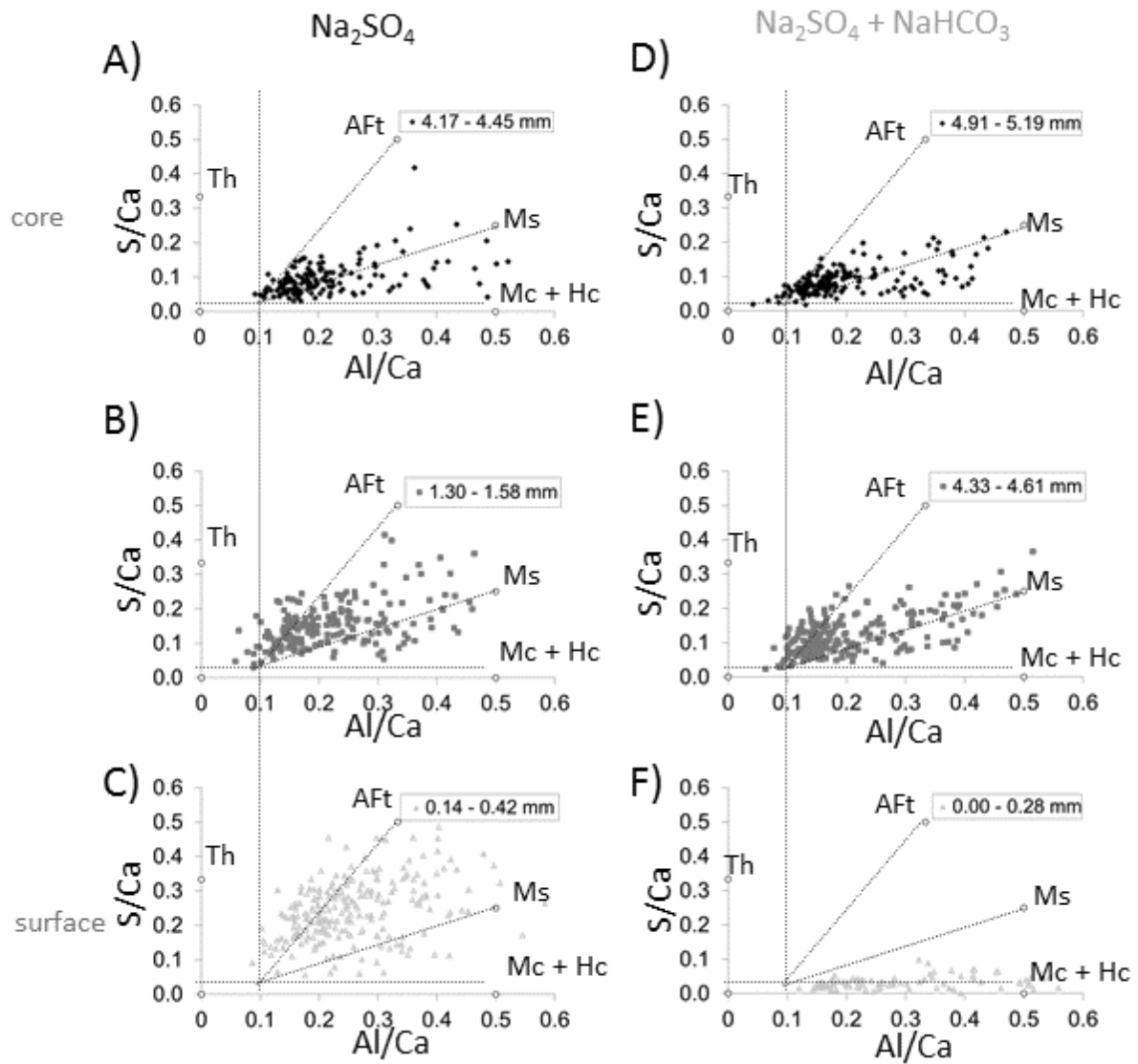
Figure 15: Atomic ratio plots (Al/Ca to S/Ca), modified by the removal of EDS measurements that were dominated by portlandite, calcite or gypsum, at selected depths for CEM III/B exposed for 91 days to sodium sulfate (top; A to C) and bicarbonate solution (bottom; D to F).

For the CEM III systems the EDS analyses are shown in Figure 15. In the unaffected core there is a clear shift in the C-S-H compositions to higher Al/Ca as expected for slag blends. As the surface is approached, the S/Ca ratios increase as before. So it would be expected that the changes in the sulfate concentration in solutions are similar. However, in the slag blends, there is much less available AFm phase (as discussed in section 3.3.2). The wider scatter of points, with less points close the C-

S-H indicates less ettringite within the C-S-H (as opposed to in large pores). Furthermore, there may also be differences in the concentration of other ions in solutions. All these aspects can explain why expansion does not occur – due to different supersaturation, less AFm present and a tendency for ettringite not to form in C-S-H.

In the bicarbonate solution there is no increase in the S/Ca ratio as for the CEM I case. Furthermore, the analyses close to the surface show the disappearance of sulfate containing phases.

3.3.7 Observations on expanded CEM I specimens in bicarbonate solution

As discussed in section 3.1 there was some degradation at the extremities of the CEM I samples at long ages in the bicarbonate solution. Cracks formed on the ends of the specimens where the solution penetrated the samples from three directions (Figure 16). Potentially, this is due to the long intervals between solution exchanges. The bicarbonate ions are bound in calcite and the solution may locally tend toward sodium sulfate solution. Under these conditions the formation of ettringite or gypsum would be possible.

Figure 16: Visual signs of deterioration of the expanding mortar bars were cracking on the specimens ends after 637 days of exposure to sodium bicarbonate solution.

The surface zones are heavily leached due to the high amount of free surface. If a crack forms in this weakened region, bicarbonate ions will be strongly bound on the exposed surface of the crack and not penetrate further into the specimen. Figure 17 shows microstructures of deteriorated bars. In the surface zone (Figure 17A) a network of calcite veins is observable along with heavily leached areas. At greater depths (Figure 17B) classic signs of expansion as seen in sodium sulfate solution are visible.
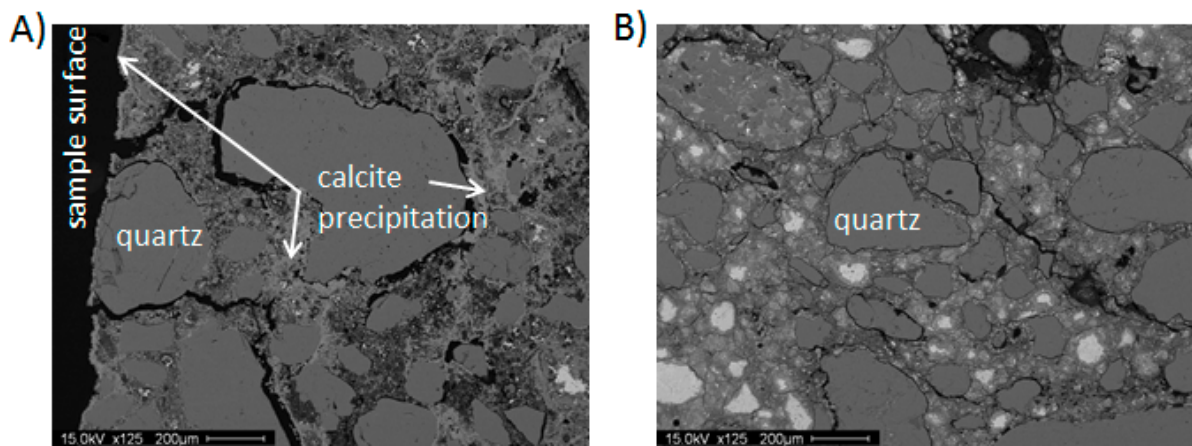
Figure 17: BSE micrographs of A) the leached zone in the CEM I mortar bar exposed to the bicarbonate solution for 546 days and B) the microstructure of an area at greater depth.

3.3.8 Porosity

Deposits of calcite were seen in the surface region. At very long ages these deposits were dense, but still discontinuous (Section 3.3.5). Other researchers have suggested that a calcite surface *layer* is formed which is "protective" [49, 53]. Changes in the porosity of the surface region were looked at to see if this was affected by calcite deposition.

Figure 18 compares the pore volume of the surface and core region of the CEM I mortar after 18 months of exposure to sodium bicarbonate solution. It can be seen that the overall pore volume was

slightly less for the carbonated surface zone (Figure 18) and the pore entries moved to smaller sizes, but this effect is fairly minor and unlikely to significantly impact the ingress of ions.
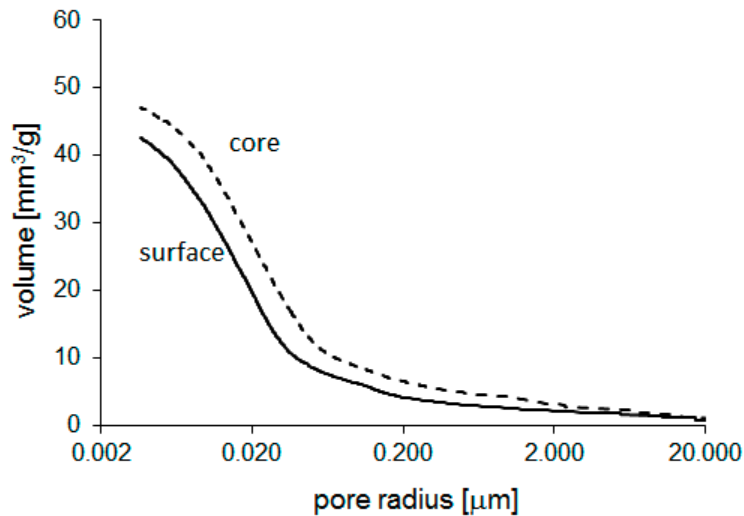
Figure 18: Cumulative pore size distribution of the surface (full line) and core (dashed line) regions of the CEM I mortar bars after 1.5 years of exposure to sodium bicarbonate solution

3.4   Discussion

Qualitatively, the experimental observations agree with the predictions of thermodynamic modelling. The formation of calcite in the surface zone is observed for CEM I mortars exposed to the bicarbonate solution, but there is no substantial evidence that this significantly inhibits the transport of ions – the level of sulfate beyond the calcite layer continues to increase (Figure 10A).

Thermodynamic modelling of the CEM I binder, predicts the formation of similar maximum amounts of ettringite in the systems without and with bicarbonate. The important difference is that ettringite becomes unstable at solution concentrations beyond that needed to form this maximum amount. At this point gypsum would precipitate in sodium sulfate solution, but calcite forms in the bicarbonate case. Furthermore, the EDS analyses also show that there is no increase in the S/Ca ratio of the C-S-H phase (Figure 14). Together these observations suggest that it is more difficult to get conditions of supersaturation with respect to ettringite to give crystallization pressure over suffi-

ciently large regions to generate expansion in the presence of bicarbonate ions. A high degree of supersaturation with respect to ettringite is reached at high calcium and sulphate concentrations; the maximum calcium and sulphate concentrations are limited by gypsum precipitation. Thus, the highest degree of oversaturation is reached under conditions where gypsum can precipitate, while monosulphate is still present. This phase combination has also been used to by Flatt and Scherer [9] to estimate the maximum supersaturation of ettringite.

If gypsum is absent, the calcium and sulphate concentrations and thus the degree of supersaturation with respect to ettringite will be lower. The absence of gypsum together with the destabilization of ettringite, in the presence of calcite, explain the reduced expansions observed in the presence of bicarbonate.

The CEM III/B samples did not expand in either solution. Thermodynamic modelling showed that the CEM III/B had less potential for ettringite formation due to the limited availability of Al_2O_3, thus reducing the amount ettringite that could exert pressure. Gypsum was observed only occasionally, such that a high supersaturation with respect to ettringite is not probable. However, it is noted that, for slags with higher alumina content, deterioration, loss of surface and cracking have been observed over longer exposure times [54]. In this study, in the bicarbonate solution, extensive leaching occurred close to the surface and progressed through the specimen during the tests. This extensive leaching might itself pose a problem over the very long term as after 2.5 years of exposure almost 10 mm were affected by leaching.

Thaumasite formation was not observed experimentally as expected due to its slow formation at ambient temperature [47]. In the long term, however, the formation of thaumasite could be possible.

3.5   Conclusions

Bicarbonates have a significant effect on the deterioration of the two investigated binders in the presence of sulfate ions. The expansions for the CEM I mortar were significantly delayed and then only occurred at the ends of the specimen. Thermodynamics modelling shows that ettringite becomes unstable in the presence of bicarbonate ions and gypsum does not form. This implies that conditions where ettringite can form from a highly supersaturated solution, so exerting crystallization pressure are less likely to occur. The absence of strongly supersaturated conditions with respect to ettringite are suported by the EDS analyses of the C-S-H.

Calcite is formed at the surface in these systems in bicarbonate solution, but the lack of continuity to give a "layer" and the continued ingress of sulfate suggest that it does not provide a physical barrier. Any effect on ion transport is less relevant than the changed phase stabilities.

The slag mortar bars did not expand significantly in either solution. However in the solution containing bicarbonate, calcium containing phases (other than calcite) such as calcium hydroxide, C-S-H and ettringite were destabilized progressively throughout the whole specimens. It seems likely that the newly formed phase assemblage is stable. However, the reduced density and increased permeability might cause other deterioration issues under field conditions.

The present work shows that the overall composition of the aqueous solution is an important parameter that determines the deterioration of the specimens by the ingress of sulfate ions, especially when bicarbonates are present. The presence of carbonate species in the aqueous environment (such as ground waters) has the potential to reduce sulfate related degradation, which may partially explain why the number of reported cases under field conditions is relatively small. This has strong implications for the relevance of most laboratory test which study only sodium sulfate solutions.

4 Deterioration of mortar bars immersed in magnesium containing sulfate solutions

4.1 Introduction

Magnesium is a common cation in natural waters and thus often in contact with concrete structures. The attack is labelled as sulfate attack when the magnesium is combined with sulfate ions, such solutions have been extensively investigated in laboratory studies. The combined occurrence of sulfate and magnesium ions is known to be a severe form of sulfate attack as the both the sulfate and magnesium ions interact with cement hydrates [55]. Gollop and Taylor [52, 56] reported that the deterioration is more severe at the edges and corners than at the plane surfaces.

The solubility of magnesium sulfate in water is high. However, magnesium hydroxide (brucite) precipitates in high pH environments due to a very limited solubility of this mineral. The hydroxide ions are supplied by destabilization of cement hydrates like portlandite and C-S-H. The result of this process is decalcification of the binder with precipitation of gypsum as the released calcium reacts with the sulfate ions in solution.

Testing with magnesium sulfate is reported as being more deleterious for blended cements, like slag blended CEM III/B cement with high levels of cement substitution [57, 58]. Slag blended cements have been reported to show surface deterioration rather than expansion compared to CEM I binders [59]. The formation of M-S-H and brucite have been reported for different cements exposed to magnesium sulfate solutions [58, 60, 61]. M-S-H phases are the last stage of deterioration after decalcification of the C-S-H phases [62, 63].

The formation of a dense composite layer of brucite and gypsum on the surface has been assumed to reduce the ionic transport [64]. Smaller length changes were reported along with a brucite layer for samples exposed to seawater compared to groundwater, it was suggested that the brucite layer

could have slowed down the ingress of ions [64]. However, recent work, by the authors, on the influence of bicarbonates on sulfate attack [13] suggests an alternative explanation for the reduction of length changes due to the destabilization of ettringite, which lowers the likelihood of supersaturation with respect to ettringite and hence expansive crystallisation pressure.

National standards, such as ASTM C 1012 [26], were developed for plain Portland cement based binders and these typically use sodium sulfate solutions and focus on length changes. The possibility of testing complex sulfate solutions, containing other or combinations of sulfate salts, is suggested in the ASTM standard for special exposure conditions. However, studies of the deterioration of sulfate salts other than magnesium or sodium are uncommon and mixture solutions are only reported to simulate seawater, with the focus on chloride ingress rather than sulfate attack.

The objective of this work is to understand the differences in deterioration for mortars made from a Portland cement and slag blended cement exposed to different sulfate solutions based on sodium and magnesium sulfates.

4.2   Materials and methods

4.2.1   Materials

The CEM I cement was commercial cement from Germany, the CEM III/B was also a commercial cement, from the same clinker containing 70% slag addition. The main oxide contents and main clinker phases of the cements used, a CEM I and a CEM III/B, and are shown in Table 6 and 7.

Table 6: Chemical composition of the cements used (CEM I 32.5 R, CEM III/B 32.5 N HS LH)

Cement type	SiO$_2$	Al$_2$O$_3$	Fe$_2$O$_3$	CaO	MgO	SO$_3$	K$_2$O	Na$_2$O	CO$_2$	L.o.I.
				[m%]						
CEM I	20.3	5.2	3.1	63.4	2.5	2.4	0.9	0.2	0.4	1.0
CEM III/B	29.9	9.4	1.6	47.6	4.3	4.5	0.7	0.1	1.1	0.7
slag	37	12.6	0.5	40.5	5.4	2.4	0.6	0.4	0.3	0.0

Table 7: The main cement clinker phases according to Rietveld analysis (typical error +/- 1-2%).

cement	alite	belite	aluminate	ferrite
CEM I	55.7	12.1	7.5	7.4
CEM III/B	17.7	3.1	1.4	1.2

The volumes of the cement, sand and water were kept constant for both mortars. The mortars were produced with water to binder ratios of 0.55 (CEM I) and 0.59 (CEM III/B) as the slag cement has a lower bulk density. The sand to cement volume ratio was 3.8. Sand was used according to DIN EN 196, part 1.

The exposure solutions contained 0.35 mol/ liter sulfate of sodium (50 g/l); magnesium (44.8 g/l) or a mixture of sodium, magnesium, calcium, and potassium (for detailed composition see Table 8). Some of the calcium sulfate precipitated from the mixture solution; approx. 10% of the added calcium sulfates were calculated to be dissolved, the rest buffers the solution and might dissolve at later times. The high sulfate concentration is comparable to standard tests [25, 26]. Another magnesium sulfate solution was used with 10% of this concentration (0,035 mol/l).

Table 8: Molar composition of the sulfate mixture solution.

Sulfate salt	[mol/l]
Na_2SO_4	0,132
K_2SO_4	0,044
$MgSO_4$	0,088
$CaSO_4$	0,088

All test solutions were prepared with deionized water using a solution volume to mortar volume ratio of 20. The solutions were exchanged after every measurement (as detailed below).

4.2.2 Methods

Length changes

Length changes were determined on mortar bars (25 x 25 x 150 mm³). The bars were cut from mortar slabs to remove the surface layer of dense paste and any carbonated surface layer.

Prior to cutting, the specimens were cured for one day in a humidity chamber during setting and the first day of hardening and for additional 27 days as slabs in saturated lime solution. Gauge alignments were glued to the ends of the cut mortar bars to improve the repeatability of the measurements. Thereafter the mortar bars were stored for 12 hours in a 95 % relative humidity chamber to harden the two component epoxy adhesive (Araldite 2014-1) before being placed into solution in air tight buckets.

Specimen lengths were determined in comparison to an invar bar before sulfate exposure and after 7, 14, 28, 56, 91 days of exposure and every 91 days after. Lengths were measured on four specimens.

EDS measurements and data treatment

The microstructural changes were studied on epoxy impregnated, polished and carbon coated cross sections of the mortar bars imaged with backscattered electrons in the SEM (Philips XL 30 ESEM FEG with an acceleration voltage of 15 keV). The changes of the elemental composition within the mortar bars were followed by energy dispersive X-ray spectroscopy (EDS). The EDS measurements were arranged in rectangular grids of 15×20 points (vertical and horizontal distances points = 14 μm). The placement of the grids was chosen to represent characteristic areas at the depths investigated. Data fluctuation was high due to the heterogeneous microstructure. The EDS measurements were corrected with the ZAF correction. Oxide contents (SO_3, CaO, SiO_2, Al_2O_3, MgO, Na_2O, K_2O, TiO_2, Mn_2O_3, and Fe_2O_3) were calculated from the measured elements. Each individual EDS measurement was assigned with a coordinate which allowed the data of the different grids to be combine as profiles expressed as distance from the surface. EDS analysis of epoxy resin in air voids or cracks, aggregates, unreacted slack and clinker particles were removed after data acquisition based on count rate threshold.

The used maximum oxide profiles display only the maximum oxide content from a group of measurements at the same depth instead of the average of this group. Maximum profiles indicate the phase changes more clearly than average profiles by minimising the effects of intermixing of phases and averaging of data.

4.3 Results

4.3.1 CEM I

Only small length changes were observed during the first three months of sulfate exposure (Figure 19). The subsequent expansion differed significantly for the different sulfate solutions. The fastest expansion was observed for the sodium sulfate solution. The expansions observed for the magnesium sulfate solution were smaller and the expansion of the mixture solution, which contained mainly sodium sulfate plus lower quantities of magnesium, calcium and potassium, was even lower. The samples exposed to the magnesium sulfate solution of lower concentration expanded less than the samples exposed to magnesium sulfate solution of higher concentration, but similar to the samples exposed to the sulfate mixture solution, although the sulfate ion content is ten times higher in the mixture solution.
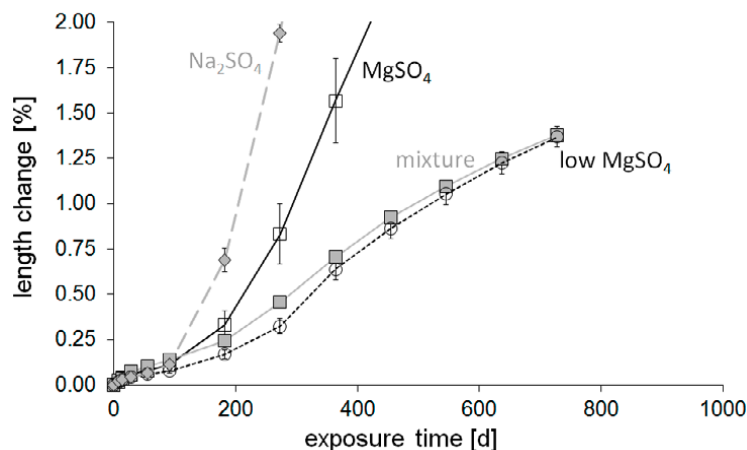
Figure 19: Length changes of CEM I Mortar bars exposed to different sulfate solutions.

In addition to the expansion, deterioration of the edges and corners of the specimens occurred as early as after four weeks for exposure to magnesium sulfate solutions (0.35 mol/l). At the higher magnesium concentration (0.35 mol/l) brucite precipitated as white deposits on the surface of prisms (Figure 20A). For the lower magnesium concentration (0.035 mol/l; Figure 20B) and the

sulfate mixture solution (Figure 20C) there was much less deposition of brucite. The detailed microstructural investigations focussed on the surfaces away from the ends where one-dimensional transport can be expected.
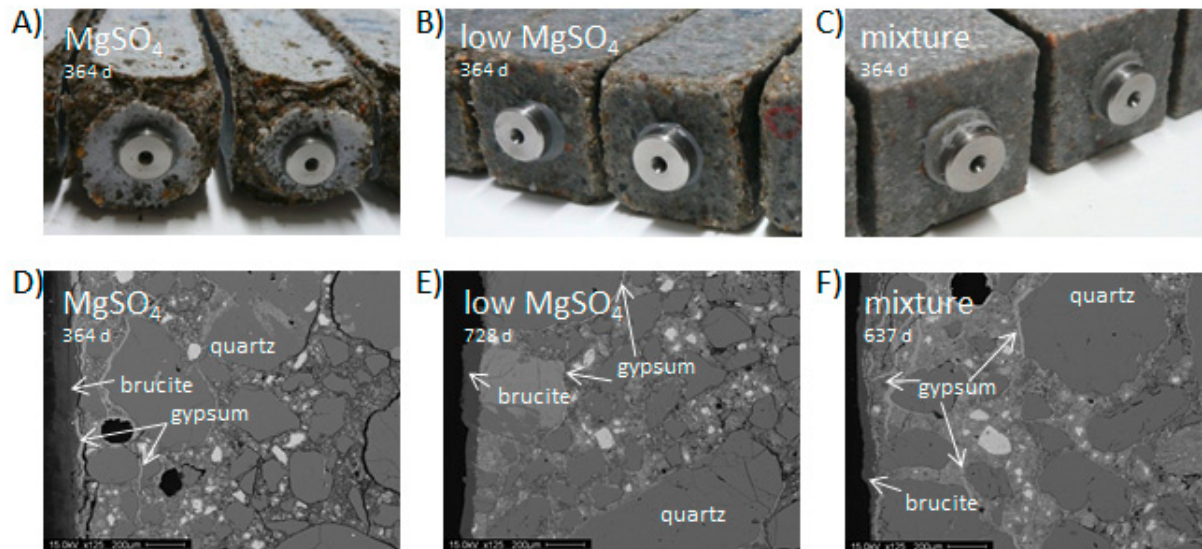
Figure 20: Visual appearance after one year of exposure and later. BSE micrographs of CEM I mortar bars exposed to A) and C) $MgSO_4$, B) an D) low $MgSO_4$, C) and F) sulfate mixture solution.

Figure 20 shows the visual appearance of the ends of the mortar bars at one year along with micrographs perpendicular to the main surfaces taken at one year for the $MgSO_4$ solution; and around 2 years for the low magnesium and sulfate mixture solutions. The samples exposed in sodium sulfate solution are not shown as these have been discussed elsewhere [13]. The micrographs show samples exposed in solution containing magnesium ions form a brucite layer on the surface. Veins of gypsum can be clearly identified in the high $MgSO_4$ and mixture solutions, whereas there are only a few deposits of this phase around aggregate particles in the low $MgSO_4$ case. There is much more cracking evident in the sample exposed to the high magnesium sulfate solution than the other two test solutions.

The sulfate profiles are very similar for the three magnesium containing solutions (Figure 21) after 91 days of exposure (before larger expansions are observed). It has been shown [65] that the binding before cracking is very similar for sulfate solutions containing different cations (Na_2SO_4, K_2SO_4, $MgSO_4$ and the sulfate mixture; all with 0.35 mol/l sulfates) as it is determined by the phase assemblage of the mortar before exposure (amount of AFm phases which can transform to ettringite). Even at a ten times lower sulfate ion concentration "low $MgSO_4$" a similar sulfate uptake in the cement paste is observed after 3 months (Figure 21, black dashed line). This confirms that during the first months, the speed of sulfate ion ingress and the amount of sulfate binding depends on the binder only.
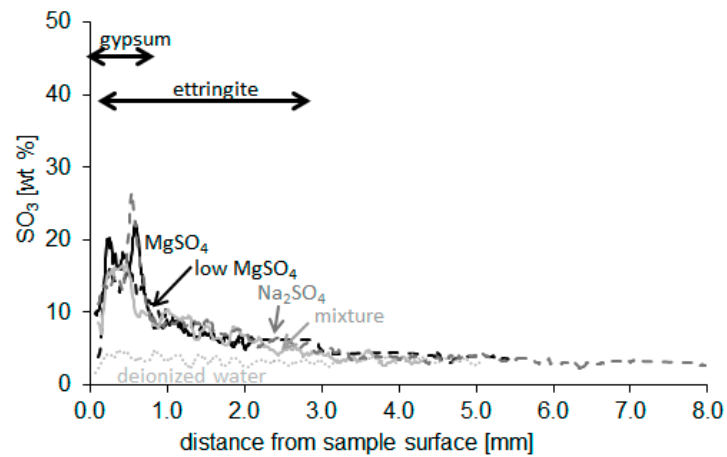
Figure 21: Median sulfate content profiles of CEM I mortar bars after 91 days exposure to the different test solutions.

Figure 22 shows maximum oxide profiles for magnesium, sulfate and calcium, which are more sensitive indicators for phase changes than average profiles. The profiles illustrate that magnesium reacts very rapidly on the surface of the specimens, where brucite precipitates, and the depth of penetration changes little with time (Figure 22A). Nevertheless, the zone inside of the brucite layer continues to change with the formation of ettringite and gypsum (Figure 22B) and disappearance of

portlandite (Figure 22B and C). After one year, ettringite has formed to a depth of 6 mm, but this sample has cracked by this stage facilitating sulfate ingress.
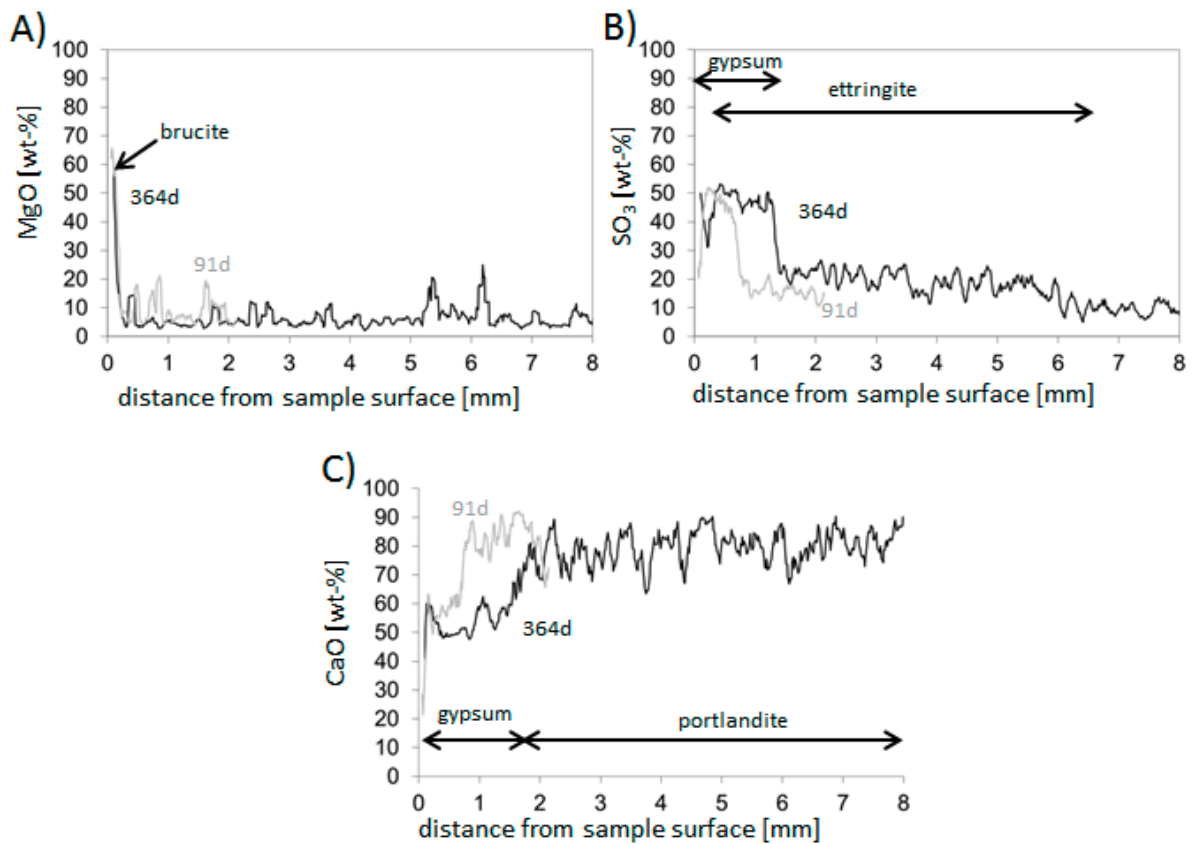
Figure 22: Maximum oxide content profiles for A) MgO , B) SO_3 and C) CaO in CEM I mortar bars exposed to magnesium sulfate solution (0.35 mol/l) for different times; arrows indicate phases present after 1 year.

4.3.2 CEM III/B

The observed length changes of the CEM III/B mortar bars (Figure 23) are much smaller than for the previously discussed CEM I mortars. Only the exposure to magnesium sulfate solution (0.35 mol/l) leads to some expansion and even here a large part of the observed length changes may be due to the severe degradation seen at the ends in proximity of the glued on gauge alignments. The first signs of surface degradation on edges and corners were seen after only four weeks of magnesium sulfate exposure; after 1 year the ends were degraded significantly (Figure 24A). The amount

of surface degradation seems visually comparable to that of the CEM I mortars in the same solution, but during handling of the samples the surface of the CEM III samples was clearly weaker and more easily removed.
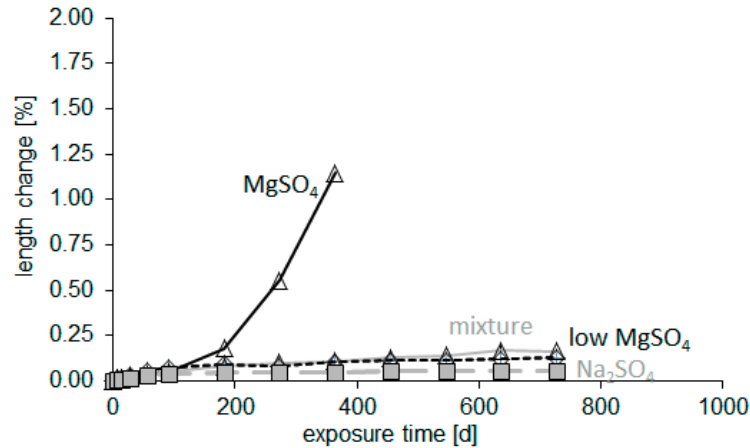
Figure 23: Length changes and visual appearance of CEM III/B Mortar bars exposed to different sulfate solutions.

The samples exposed to the lower concentrated magnesium sulfate solution (0.035 mol/l) showed somewhat less spalling at the edges and corners (Figure 24B), which only progressed slowly during the second year of testing. In this solution the degradation of the surface of the CEM III mortars is clearly more severe than in the CEM I case.

No spalling at edges and corners occurred for the samples exposed to the sulfate mixture solution during the first year (Figure 24C). This last observation is remarkable as the sulfate concentration is ten times higher and the magnesium concentration 2.5 times higher in the mixture solution compared to the low magnesium sulfate concentration (Figure 24B). Nevertheless some spalling started on edges and corners for the samples exposed to the sulfate mixture solution during the second year of exposure, which was not the case for the CEM I mortars.
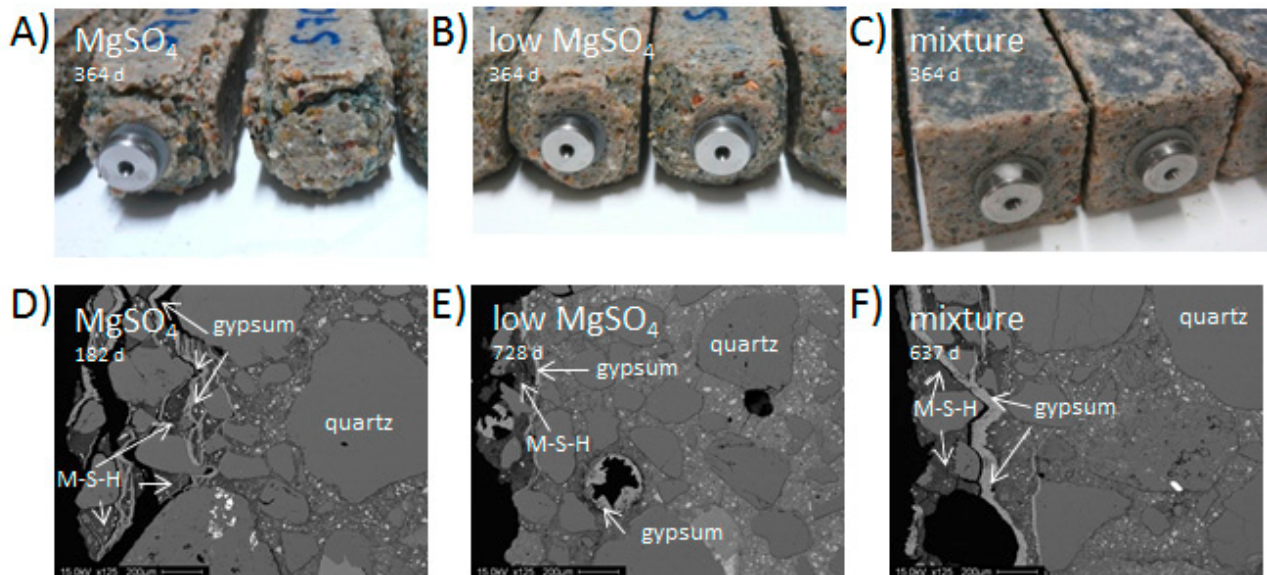
Figure 24: Visual appearance after one year of exposure and BSE micrographs of CEM III/B mortar bars exposed to A) and D) $MgSO_4$, B) an E) low $MgSO_4$, C) and F) sulfate mixture solution.

In all three samples gypsum veins have formed and the material between the veins is dominated by M-S-H phase (Figure 24D - F). The Mg/Si ratios of EDS measurements were mostly between 0.6 - 1 in the M-S-H domains as described in the literature [56, 63]. The lower calcium content of the slag blended mortars means that gypsum formation leads to a stronger decalcification of C-S-H, so that M-S-H forms instead of leached C-S-H and brucite as in the case of CEM I. As mentioned, the surfaces of the samples in the both pure magnesium sulfate solutions were easily lost during sample handling. So the original surfaces cannot be identified. Surface erosion for slag blended cements appears to be an iterative process as further phase changes are facilitated by the removal of the previous surface. The irregular surfaces in Figure 24D and E and particularly the partial lack of an M-S-H region at the surface in Figure 24E clearly illustrate this phenomenon of surface loss.

Figure 25 shows the sulfate profiles, although there is some uncertainty about the exact depths due to surface loss. Again, the sulfate binding appears to be very similar for the all the mortars with the same binder exposed to the magnesium containing solutions (Figure 25). However, the sulfate pen-

etration is less than that observed for the CEM I binder. (The profile for the mixture solution is that at one year as measurements were not made for this sample at 91 days).
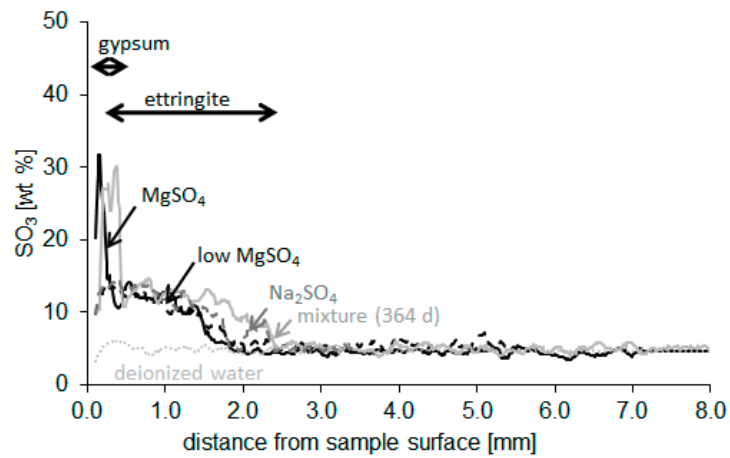
Figure 25: Median sulfate content profiles of CEM III/B mortar bars after 91 days (and one year for the sulfate mixture) exposure to the different test solutions.

Figure 26 shows the maximum oxide profiles of MgO, SO_3, and CaO. Again, the magnesium penetration is very limited (approx. < 0.6 mm). The MgO content in surface proximity is smaller than for CEM I due to the precipitation of M-S-H instead of brucite.

In contrast to the CEM I mortars, the changes in SO_3 and CaO are also confined to the surface zone (within 1 – 2 mm) and seem to not progress during the test duration, even when expansion of the high $MgSO_4$ sample is observed (Figure 23). However, as discussed above, the repeated falling off of the surface layers results in the formation of new surfaces which may explain the apparent low penetration depth.
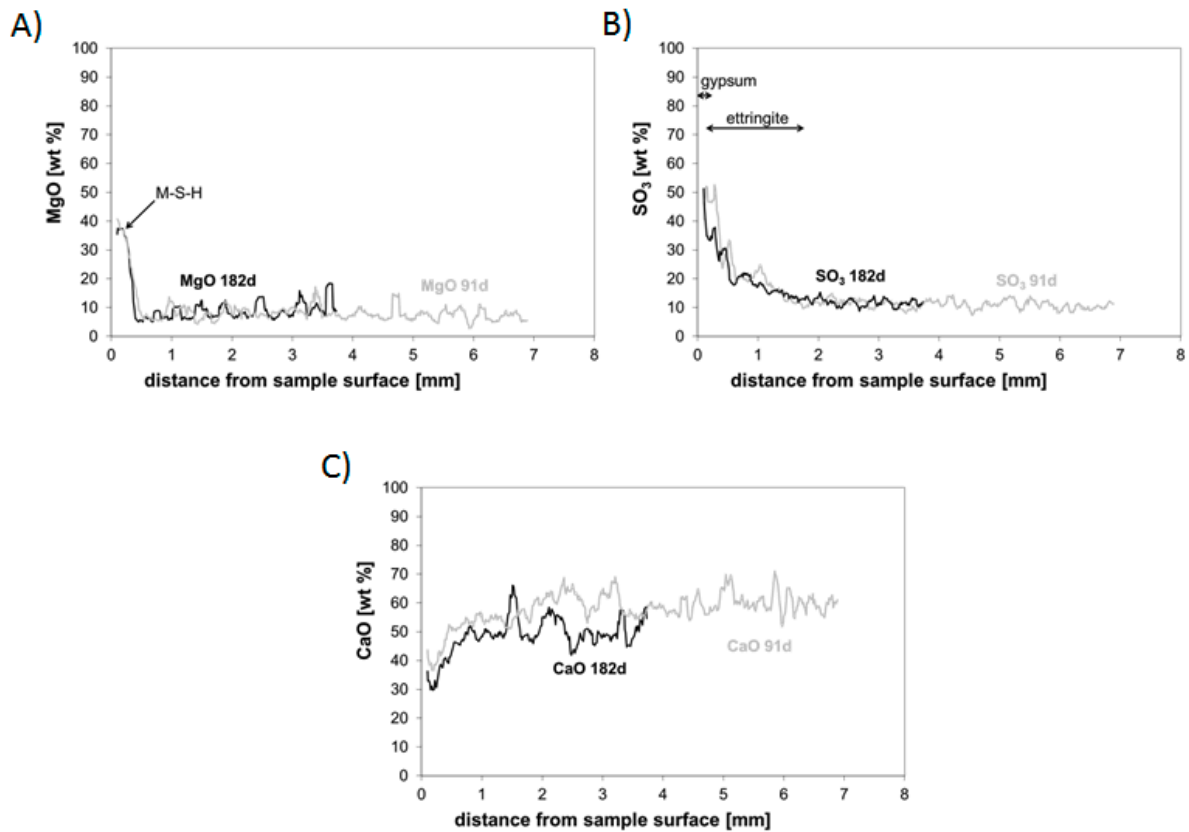
Figure 26: Maximum oxide content profiles for A) MgO , B) SO$_3$ and C) CaO in CEM III/B mortar bars exposed to magnesium sulfate solution (0.35 mol/l) for different times; indicated arrows indicate present phases after 182 days.

4.4 Discussion

The CEM I mortar expanded in all the solutions. The expansions seem to "take-off" at similar times, but expand at different rates thereafter. Apart from the low MgSO$_4$ solution, all the solutions have similar concentrations of sulfate ions, so the type of counter-ion present has an important effect on expansion. In particular the mixture solution which contains both sodium and magnesium ions shows much less expansion than either of the "pure" solutions. The reasons for these differences are not clear, we can speculate that the different ions affect the degree of supersaturation with respect to ettringite in the pore solution, but this cannot be measured directly.

As noted previously a layer of brucite was seen to form on the surface of the CEM I mortars in solutions containing magnesium. However there was no evidence that this prevented the ingress of sulfate ions (as seen in the profiles, Figure 21 and Figure 22) or prevented expansion (Figure 19). Surface erosion is a less significant form of deterioration for the CEM I mortars as it occurs only on the edges and corners. On the main faces of the prisms the original surfaces persist over long exposure time.

For the CEM III/B binder, surface erosion is the dominant deterioration mechanism. Weak zones, of predominantly M-S-H, form and fall off; exposing fresh surface to degradation. Consequently the sulfate ions do not penetrate to any significant depth and macroscopic expansion does not occur. Any length changes observed are due to surface degradation in proximity of the gauge alignments, and would probably not be seen if the alignment pins were more deeply embedded.

As for the expansion of the CEM I mortars, the surface degradation in the mixture solution was much less for both binders than either of the single salt solutions. And even more remarkably the surface degradation in the mixture solution was much less than the low $MgSO_4$ solution which contained 2.5 times less magnesium and ten times less sulfate. The same general phase changes occur in all three magnesium containing solutions, so it is unclear which factors contribute to the improved performance of the mixture solution, or if these factors differ for the two binders.

4.5   Conclusions

This paper confirms previous observations that the magnesium sulfate solutions cause more surface damage than sodium sulfate solutions. However, the relative importance of expansion and surface deterioration are very different for CEM I and CEM III/B binders. In the CEM I binders expansion dominate deterioration, even when surface deterioration is also present. For the CEM III/B binder, severe surface degradation can occur without any macroscopic expansion being measured. This underlines the unsuitability of expansion related tests for such binders.

The second main conclusion is that samples immersed in solutions containing different cations showed less expansion and also much less surface deterioration than samples containing only $MgSO_4$ or Na_2SO_4. The combination of different sulfate salts did not correspond to a superposition of the individual effects. Interestingly, both the surface erosion and the expansion were reduced, although the mechanisms remain unclear at the moment. The fact that a complex sulfate solution leads to slower deterioration process highlights the need to understand the interaction of ions in the test and pore solution better to be able to predict the performance of new binders in general.

Mixed solutions are likely to be present under real exposure situations to natural waters, which might help explain why relatively few cases of sulfate attack are described in the field. In addition, other anions such as bicarbonates (frequently present in natural water) may also strongly reduce the expansion caused by sulfate ions [13].

5 Conclusions and Outlook

5.1 Conclusions

The comparison of the predicted and observed phase changes provides valuable insights into the degradation phenomena. The phase changes predicted agreed very well with the paste samples and in most cases also with the mortar samples. Deviations from the thermodynamic predictions could be related to the kinetics of phase formations or are due to the simplified assumptions that all ions penetrate with the same rate as differences in the binding of different ions allows different penetration depths.

However, it was shown that the observed length changes are not directly linked to the predicted volume increase from the applied thermodynamic modelling. Explanations for expansion based purely on the volume increase can be dismissed, especially as this concept does not provide a driving force for the mechanical work to overcome mechanical constraints.

This leaves "crystallization pressure" as the most plausible explanation for expansion, which provides a proven mechanism for the conversion of chemical potential into mechanical work. However it is difficult to confirm this mechanism experimentally as we cannot directly measure the solution concentration at different depths from the exposed surface. The different deterioration symptoms of the binders in different sulfate solutions provide a good indicator that the on-going processes are strongly affected by the aqueous environment and the consequent changes in the pore solution. Indirectly, the changes of the pore solution can be also deduced by monitoring the phase changes in specimens and the sulfate distribution in C-S-H.

Systems in which the predicted and experimentally observed phase assemblages showed the simultaneous presence of ettringite and gypsum consistently showed larger expansions than phase assemblages for which no gypsum precipitation was predicted. This agrees with the expectations that higher supersaturations with respect to ettringite can be generated under these conditions. The in-

crease of sulfate contents in the C-S-H phase has been observed for these cases, indicating the increased sulfate concentration in the pore solution while providing the necessary confinement for the crystals in intimate phase mixtures to exceed pressures.

In the presence of bicarbonate ions ettringite is destabilized and no gypsum precipitates. Consequently there is a low probability of large supersaturations with respect to ettringite. This reduces the degradation significantly. The uptake of sulfate in C-S-H is not observed. The CEM I binder deteriorates much later and only on the corners of the specimens. The sulfate containing phases in the CEM III/B binder are destabilized, which may prevent sulfate uptake in general as severe leaching has been observed. Bicarbonate ions are common carbon species in natural waters and may also reduce or delay deterioration in the field cases.

Even at high concentration of sulfate ions, solutions with a mixture of cations, similar to those commonly found in ground waters, produce much less deterioration than solution of either magnesium sulfate or sodium sulfate alone. The cause for the reduced deterioration is unclear but these effects can also be expected to reduce the symptoms of sulfate attack in the field.

With regard to the rate of ingress of sulfate ions it appears that this is little affected by the porosity or permeability of the binders. The thermodynamic modelling shows that sulfates react with the phases present to give fist ettringite and then in some cases gypsum. This binding of sulfates seems to dominate the rate of ingress in the first stage of exposure before cracking occurs. The dominant role of sulfate binding by the phases present means that different sulfate solutions also provide the same sulfate profiles before significant cracking and expansions were observed.

A comparison of the deterioration of CEM I and CEM III showed that CEM I mortars, which deteriorate by expansion, had much deeper sulfate penetration due to the conversion of AFm-phases to ettringite. The pressure development in deeper parts of the specimens seems to allow the specimens to display significant length changes before they crack and disintegrate. This is in contrast to the CEM III/B mortars, which show almost no expansion, but deteriorate by removal of the surfaces.

These samples bind sulfates almost only in proximity of the surfaces. It can be expected that the development of tensile stresses in proximity of the surfaces leads to the removal of the surface layer of the affected material.

5.2 Outlook

This work shows that the nature of the sulfate containing aqueous environment is of high importance for deterioration. It can be expected that the pore solution composition in the binders and thus the supersaturation with respect to ettringite is influenced by the aqueous environment. Unfortunately the extent of supersturation under different conditions is unclear. The ability to measure the composition of the pore solution or individual crystals within the microstructure would provide new opportunities to investigate sulfate attack from a more fundamental level but are unlikely due to the limitations of the analytical techniques.

Consequently, it could be helpful to experiment with the pressure generation of ettringite crystals in different exposure conditions under more controlled conditions than mortar bars can provide. Simple test set-ups could be designed to experimentally determine the excess pressure generated by an ettringite sample (paste), while minimizing transport aspects (and thus look at relatively homogenous pressure generation), while controlling the porosity/density of the samples to improve the understanding of the conditions of pressure generation.

From these aspects the necessary information for the mechanical implementation might be obtained. Other important aspects such as the kinetics of the pressure generation and pore solution information could also be estimated if the tests provide homogeneous conditions. These aspects could then be implemented into complex modelling tools which combine reactive transport with mechanical aspects to model the deterioration in greater detail and less unknown parameters.

References

[1] M.D. Cohen, B. Mather, Sulfate attack on concrete - research needs, ACI Materials Journal, 88 (1991) 62-69.

[2] B. Tian, M.D. Cohen, Does gypsum formation during sulfate attack on concrete lead to expansion?, Cement and Concrete Research, 30 (2000) 117-123.

[3] A. Neville, The confused world of sulfate attack on concrete, Cement and Concrete Research, 34 (2004) 1275-1296.

[4] F.P. Glasser, J. Marchand, E. Samson, Durability of concrete -- Degradation phenomena involving detrimental chemical reactions, Cement and Concrete Research, 38 (2008) 226-246.

[5] J. Marchand, J. Skalny, Materials science of concrete: sulfate attack mechanisms, American Ceramic Society, 1999.

[6] J. Skalny, J. Marchand, I. Odler, Sulfate attack on concrete, Spon Press, 2002.

[7] X. Ping, J.J. Beaudoin, Mechanism of sulphate expansion I. Thermodynamic principle of crystallization pressure, Cement and Concrete Research, 22 (1992) 631-640.

[8] D. Min, T. Mingshu, Formation and expansion of ettringite crystals, Cement and Concrete Research, 24 (1994) 119-126.

[9] R.J. Flatt, G.W. Scherer, Thermodynamics of crystallization stresses in DEF, Cement and Concrete Research, 38 (2008) 325-336.

[10] G.W. Scherer, Crystallization in pores, Cement and Concrete Research, 29 (1999) 1347-1358.

[11] M. Steiger, Crystal growth in porous materials--II: Influence of crystal size on the crystallization pressure, Journal of Crystal Growth, 282 (2005) 470-481.

[12] C. Yu, K. Scrivener, Mechanism of expansion of mortars immersed in sodium sulphate solution, Cement and Concrete Research, submitted (2012).

[13] W. Kunther, B. Lothenbach, K. Scrivener, Influence of bicarbonate ions on the deterioration of mortar bars under sulfate attack, Cement and Concrete Research, submitted (2012).

[14] H. Lafuma, Théorie de l'expansion des ligants hydrauliques, La Revue des Matériaux de Construction et de Travaux Publics, 243 (1929) 441-444.

[15] I. Odler, J. Colán-Subauste, Investigations on cement expansion associated with ettringite formation, Cement and Concrete Research, 29 (1999) 731-735.

[16] M.D. Cohen, C.W. Richards, Effects of the particle sizes of expansive clinker on strength-expansion characteristics of type K expansive cements, Cement and Concrete Research, 12 (1982) 717-725.

[17] P.W. Brown, H.F.W. Taylor, The role of ettringite in external sulfate attack, Materials Science of Concrete: Sulfate Attack Mechanisms, The American Ceramic Society, (1999) 73-98.

[18] P.K. Mehta, Mechanism of expansion associated with ettringite formation, Cement and Concrete Research, 3 (1973) 1-6.

[19] X. Zuo, W. Sun, Simulations on expansive strain of concrete caused by ettringite growth under sulfate attack, Advanced Materials Research, 250-253 (2011) 1906-1911.

[20] S. Sarkar, S. Mahadevan, J.C.L. Meeussen, H. van der Sloot, D.S. Kosson, Numerical simulation of cementitious materials degradation under external sulfate attack, Cement and Concrete Composites, 32 (2010) 241-252.

[21] B. Lothenbach, B. Bary, P. Le Bescop, T. Schmidt, N. Leterrier, Sulfate ingress in Portland cement, Cement and Concrete Research, 40 (2010) 1211-1225.

[22] S. Taber, The growth of crystals under external pressure, American Journal of Science, 41 (1916) 532-556.

[23] C.W. Correns, Growth and dissolution of crystals under linear pressure, Discussions of the Faraday Society, 5 (1949) 267-271.

[24] R. Flatt, M. Steiger, G. Scherer, A commented translation of the paper by C.W. Correns and W. Steinborn on crystallization pressure, Environmental Geology, 52 (2007) 187-203.

[25] SIA, SN EN 197-1, Cement Part 1: Composition, specifications and conformity criteria for common cements (2000).

[26] ASTM International, ASTM C 1012 Standard test method for length change of hydraulic-cement mortars exposed to a sulphate solution (2004).

[27] D. Kulik, T. Wagner, S.V. Dmytrieva, G. Kosakowski, K.V. Chudnenko, U. Berner, GEM-selektor geochemical modelling package: numerical kernel GEMS3K for coupled simulation codes, Computational Geochemistry, submitted, (2012).

[28] B. Lothenbach, T. Matschei, G. Möschner, F.P. Glasser, Thermodynamic modelling of the effect of temperature on the hydration and porosity of Portland cement, Cement and Concrete Research, 38 (2008) 1-18.

[29] L.J. Parrott, D.C. Killoh, Prediction of cement hydration, British Ceramic Proceedings, (1984) 41-53.

[30] B. Lothenbach, G. Le Saout, E. Gallucci, K. Scrivener, Influence of limestone on the hydration of Portland cements, Cement and Concrete Research, 38 (2008) 848-860.

[31] V. Kocaba, E. Gallucci, K.L. Scrivener, Methods for determination of degree of reaction of slag in blended cement pastes, Cement and Concrete Research, 42 (2012) 511-525.

[32] M. Ben Haha, K. De Weerdt, B. Lothenbach, Quantification of the degree of reaction of fly ash, Cement and Concrete Research, 40 (2010) 1620-1629.

[33] S.-Y. Hong, F.P. Glasser, Alkali binding in cement pastes: Part I. The C-S-H phase, Cement and Concrete Research, 29 (1999) 1893-1903.

[34] B. Lothenbach, F. Winnefeld, Thermodynamic modelling of the hydration of Portland cement, Cement and Concrete Research, 36 (2006) 209-226.

[35] T. Schmidt, B. Lothenbach, M. Romer, J. Neuenschwander, K. Scrivener, Physical and microstructural aspects of sulfate attack on ordinary and limestone blended Portland cements, Cement and Concrete Research, Volume 39 (2009) 1111-1121.

[36] Y. Maltais, E. Samson, J. Marchand, Predicting the durability of Portland cement systems in aggressive environments--Laboratory validation, Cement and Concrete Research, 34 (2004) 1579-1589.

[37] E. Samson, J. Marchand, J.J. Beaudoin, Modeling the influence of chemical reactions on the mechanisms of ionic transport in porous materials: An overview, Cement and Concrete Research, 30 (2000) 1895-1902.

[38] F.M. Lea, The mechanism of sulphate attack on Portland cement, Canadian journal of research, Section B, Chemical Sciences, 27 (1949) 297-302.

[39] T. Thorvaldson, Chemical aspects of the durability of cement products, Proceedings of the third international symposium on the chemistry of cement, Cement and Concrete Association, London (1954) 436-466.

[40] P.J.M. Monteiro, K.E. Kurtis, Time to failure for concrete exposed to severe sulfate attack, Cement and Concrete Research, 33 (2003) 987-993.

[41] J.J. Thomas, S.A. FitzGerald, D.A. Neumann, R.A. Livingston, State of water in hydrating tricalcium silicate and Portland cement pastes as measured by quasi-elastic neutron scattering, Journal of the American Ceramic Society, 84 (2001) 1811-1816.

[42] J. Figg, Field studies of sulfate attack on concrete, Materials Science of Concrete, The American Ceramic Society, Westerville, Ohio (1999) 315-324.

[43] W.H. Harrison, D.C. Teychenné, Sulphate resistance of buried concrete; second interim report on long-term investigation at Northwick Park, Department of the Environment, 1981.

[44] M.D.A. Thomas, R.F. Bleszynski, C.E. Scott, Sulfate attack in a marine environment, Materials Science of Concrete, The American Ceramic Society, Westerville, Ohio (1999) 301-313.

[45] P.S. Mangat, J.M. El-Khatib, Influence of initial curing on sulphate resistance of blended cement concrete, Cement and Concrete Research, 22 (1992) 1089-1100.

[46] G.J. Witkamp, J.P. Van der Eerden, G.M. Van Rosmalen, Growth of gypsum : I. Kinetics, Journal of Crystal Growth, 102 (1990) 281-289.

[47] T. Schmidt, B. Lothenbach, M. Romer, K. Scrivener, D. Rentsch, R. Figi, A thermodynamic and experimental study of the conditions of thaumasite formation, Cement and Concrete Research, 38 (2008) 337-349.

[48] R.S. Gollop, H.F.W. Taylor, Microstructural and microanalytical studies of sulfate attack. IV. Reactions of a slag cement paste with sodium and magnesium sulfate solutions, Cement and Concrete Research, 26 (1996) 1013-1028.

[49] N.R. Buenfeld, J.B. Newman, The development and stability of surface layers on concrete exposed to sea-water, Cement and Concrete Research, 16 (1986) 721-732.

[50] R. Barbarulo, H. Peycelon, S. Prene, Experimental study and modelling of sulfate sorption on calcium silicate hydrates, Annales de Chimie - Science des Matériaux, (2003) S5-S10.

[51] A. Packter, The precipitation of calcium sulphate dihydrate from aqueous solution : Induction periods, crystal numbers and final size, Journal of Crystal Growth, 21 (1974) 191-194.

[52] R.S. Gollop, H.F.W. Taylor, Microstructural and microanalytical studies of sulfate attack III. Sulfate-resisting portland cement: Reactions with sodium and magnesium sulfate solutions, Cement and Concrete Research, 25 (1995) 1581-1590.

[53] M. Schwotzer, T. Scherer, A. Gerdes, Protective or damage promoting effect of calcium carbonate layers on the surface of cement based materials in aqueous environments, Cement and Concrete Research, 40 (2010) 1410-1418.

[54] V. Fernàndez-Altable, G. Le Saoût, K. Scrivener, Evidence of a two-step mechanism of sulphate attack in OPC-slag blended mortars, Cement and Concrete Research, in preparation (2012).

[55] F.P. Glasser, The thermodynamics of attack on cement with special reference to sulfate, Concrete in aggressive aqueous environments - performance, testing and modeling, RILEM Publications S.A.R.L., Toulouse, France (2009) 3-17.

[56] R.S. Gollop, H.F.W. Taylor, Microstructural and microanalytical studies of sulfate attack. I. Ordinary portland cement paste, Cement and Concrete Research, 22 (1992) 1027-1038.

[57] C.D. Lawrence, The influence of binder type on sulfate resistance, Cement and Concrete Research, 22 (1992) 1047-1058.

[58] R.S. Gollop, H.F.W. Taylor, Microstructural and microanalytical studies of sulfate attack. IV. Reactions of a slag cement paste with sodium and magnesium sulfate solutions, Cement and Concrete Research, 26 (1996) 1747-1747.

[59] Rasheeduzzafar, O.S.B. Al-Amoudi, S.N. Abduljanwad, M. Maslehuddin, Magnesium-sodium sulfate attack in plain and blended cements, Journal of Materials of Civil Engeneering, 6 (1994) 201-.

[60] D.R.M. Brew, F.P. Glasser, Reactions of sulphate-resistant Portland cement and its blends with silica fume and aqueous magnesium sulphate, Advances in Cement Research, 14 (2002) 101-111.

[61] D. Bonen, M.D. Cohen, Magnesium sulfate attack on portland cement paste-I. Microstructural analysis, Cement and Concrete Research, 22 (1992) 169-180.

[62] D. Bonen, Composition and appearance of magnesium silicate hydrate and its relation to deterioration of cement-based materials, Journal of the American Ceramic Society, 75 (1992) 2904-2906.

[63] D.R.M. Brew, F.P. Glasser, Synthesis and characterisation of magnesium silicate hydrate gels, Cement and Concrete Research, 35 (2005) 85-98.

[64] M. Santhanam, M. Cohen, J. Olek, Differentiating seawater and groundwater sulfate attack in Portland cement mortars, Cement and Concrete Research, 36 (2006) 2132-2137.

[65] W. Kunther, B. Lothenbach, K. Scrivener, On the relevance of volume increase for the length changes of mortar bars in sulfate solutions, Cement and Concrete Research, submitted (2012).

[66] E.D. Hill Jr., A note on the history of type V cement development, Materials Science of Concrete: Sulfate Attack Mechanisms, American Ceramic Society, Westerville, Ohio (1999) 207-210.

[67] M.G. Alexander, Concrete durability: aspects of degradation in aggressive environments, 13th International Congress on the Chemistry of Cement, Madrid, Spain (2011) supplement.

[68] F.P. Glasser, The thermodynamics of attack on Portland cement with special reference to sulfate, Concrete in Aggressive Aqueous Environments, Performance, Testing and Modeling, Rilem Publications S.A.R.L., Toulouse, France (2009) 3-17.

[69] K. Van Tittelboom, N. De Belie, A critical review on the test methods for evaluating the resistance of concrete against sulfate attack, Concrete in Aggressive Aqueous Environments - Performance, Testing and Modeling, RILEM Publications S.A.R.L., Toulouse, France (2009) 298-306.

[70] Sulfate Resistance - State of the Art, Institute Belge de Normalisation, Bruxelles, Belgium, 2006.

[71] C.F. Ferraris, P.E. Stutzman, K.A. Snyder, Sulfate resistance of concrete: a new approach, Portland Cement Association, Skokie, Illinois, 2006.

[72] A.E. Idiart, C.M. López, I. Carol, Chemo-mechanical analysis of concrete cracking and degradation due to external sulfate attack: a meso-scale model, Cement and Concrete Composites, 33 (2011) 411-423.

[73] R.J. Flatt, Salt damage in porous materials: how high supersaturations are generated, Journal of Crystal Growth, 242 (2002) 435-454.

[74] G.W. Scherer, Factors affecting crystallization pressure International RILEM Workshop on Internal Sulfate Attack and Delayed Ettringite Formation RILEM Publications SARL, (2004) 139 - 154.

[75] P. Goltermann, Mechanical predictions of concrete deterioration - part 1: Eigenstresses in concrete, ACI Materials Journal, 91 (1994) 543 - 550.

[76] P. Goltermann, Mechanical predictions of concrete deterioration - part 2: classification of crack patterns, ACI Materials Journal, 92 (1995) 58-63.

[77] E.J. Garboczi, Stress, displacement, and expansive cracking around a single spherical aggregate under different expansive conditions, Cement and Concrete Research, 27 (1997) 495-500.

[78] F. Goetz-Neunhoeffer, J. Neubauer, Refined ettringite (Ca_6 Al_2 $(SO_4)_3$ $(OH)_{12}$ 26 H_2O) structure for quantitative X-ray diffraction analysis, Powder Diffraction, 21 (2006) 4-11.

[79] W.R. Wilcox, The relation between classical nucleation theory and the solubility of small particles, Journal of Crystal Growth, 26 (1974) 153-154.

[80] A. Chabrelie, Mechanisms of degradation of concrete by external sulfate ions under laboratory and field conditions, PhD Thesis, EPFL, Lausanne, 2010.

[81] C. Famy, K.L. Scrivener, A. Atkinson, A.R. Brough, Influence of the storage conditions on the dimensional changes of heat-cured mortars, Cement and Concrete Research, 31 (2001) 795-803.

[82] H.F.W. Taylor, C. Famy, K.L. Scrivener, Delayed ettringite formation, Cement and Concrete Research, 31 (2001) 683-693.

[83] V. Alunno Rossetti, G. Chiocchio, A.E. Paolini, Expansive properties of the mixture C_4ASH_{12} - 2CS I. An hypothesis on the expansion mechanism, Cement and Concrete Research, 12 (1982) 577-585.

[84] B. Bary, Simplified coupled chemo-mechanical modeling of cement pastes behavior subjected to combined leaching and external sulfate attack, International Journal for Numerical and Analytical Methods in Geomechanics, 32 (2008) 1791-1816.

[85] B. Tian, M.D. Cohen, Expansion of alite paste caused by gypsum formation during sulfate attack, Journal of Materials in Civil Engineering, 12 (2000) 24-25.

[86] R.B. Perkins, C.D. Palmer, Solubility of ettringite ($Ca_6[Al(OH)_6]_2(SO4)_3$ $26H_2O$) at 5-75°C, Geochimica et Cosmochimica Acta, 63 (1999) 1969-1980.

[87] A. Gabrisová, J. Havlica, S. Sahu, Stability of calcium sulphoaluminate hydrates in water solutions with various pH values, Cement and Concrete Research, 21 (1991) 1023-1027.

[88] F. Bellmann, B. Möser, J. Stark, Influence of the sulfate concentration on the results of laboratory investigations of sulfate resistance, 12th International Congress on the Chemistry of Cement, Montreal, Canada (2007) 9.

[89] R.S. Gollop, H.F.W. Taylor, Microstructural and microanalytical studies of sulfate attack. V. Comparison of different slag blends, Cement and Concrete Research, 26 (1996) 1029-1044.

[90] G. Li, P. Le Bescop, M. Moranville-Regourd, Synthesis of the U phase (4CaO 0.9Al_2O_3 1.1SO_3 0.5Na_2O 16H_2O), Cement and Concrete Research, 27 (1997) 7-13.

[91] B.A. Clark, P.W. Brown, The formation of calcium sulfoaluminate hydrate compounds: Part II, Cement and Concrete Research, 30 (2000) 233-240.

[92] X. Pardal, I. Pochard, A. Nonat, Experimental study of Si-Al substitution in calcium-silicate-hydrate (C-S-H) prepared under equilibrium conditions, Cement and Concrete Research, 39 (2009) 637-643.

[93] T. Matschei, R. Skapa, B. Lothenbach, F.P. Glasser, The distribution of sulfate in hydrated Portland cement paste, 12th International Congress on the Chemistry of Cement, Montreal, Canada (2007) 13.

[94] R. Skapa, Optimum Sulfate Content of Portland Cement, PhD Thesis, University of Aberdeen, Aberdeen, Scotland, UK, 2009.

[95] N. Hearn, F. Young, W/C ratio, porosity and sulfate attack - a review, Materials Science of Concrete: Sulfate Attack Mechanisms, American Ceramic Society, (1999) 189-205.

[96] J.M. Galíndez, J. Molinero, On the relevance of electrochemical diffusion for the modeling of degradation of cementitious materials, Cement and Concrete Composites, 32 (2010) 351-359.

[97] E. Samson, J. Marchand, Modeling the effect of temperature on ionic transport in cementitious materials, Cement and Concrete Research, 37 (2007) 455-468.

[98] R. Barbarulo, J. Marchand, K.A. Snyder, S. Prené, Dimensional analysis of ionic transport problems in hydrated cement systems: Part 1. Theoretical considerations, Cement and Concrete Research, 30 (2000) 1955-1960.

[99] I. Biczók, Concrete corrosion; concrete protection, Akadémiai Kiadó, Budapest, Hungary, 1972.

[100] M.E. Gaze, N.J. Crammond, The formation of thaumasite in a cement:lime:sand mortar exposed to cold magnesium and potassium sulfate solutions, Cement and Concrete Composites, 22 (2000) 209-222.

[101] F. Bellmann, B. Möser, J. Stark, Influence of sulfate solution concentration on the formation of gypsum in sulfate resistance test specimen, Cement and Concrete Research, 36 (2006) 358-363.

[102] P.C. Hewlett, Lea's chemistry of cement and concrete, Elsevier Butterworth-Heinemann, Oxford, United Kingdom, 2004.

[103] W. Kurdowski, The protective layer and decalcification of C-S-H in the mechanism of chloride corrosion of cement paste, Cement and Concrete Research, 34 (2004) 1555-1559.

[104] M. Santhanam, M.D. Cohen, J. Olek, Mechanism of sulfate attack: A fresh look: Part 1: Summary of experimental results, Cement and Concrete Research, 32 (2002) 915-921.

[105] D. Bonen, M.D. Cohen, Magnesium sulfate attack on portland cement paste -- II. Chemical and mineralogical analyses, Cement and Concrete Research, 22 (1992) 707-718.

[106] A. Leemann, R. Loser, Analysis of concrete in a vertical ventilation shaft exposed to sulfate-containing groundwater for 45 years, Cement and Concrete Composites, 33 (2011) 74-83.

[107] H.T. Cao, L. Bucea, A. Ray, S. Yozghatlian, The effect of cement composition and pH of environment on sulfate resistance of Portland cements and blended cements, Cement and Concrete Composites, 19 (1997) 161-171.

[108] P.S. Mangat, J.M. Khatib, Influence of fly ash, silica fume, and slag on sulfate resistance of concrete, ACI Materials Journal, 92 (1995) 542-553.

[109] B. Lothenbach, K. Scrivener, R.D. Hooton, Supplementary cementitious materials, Cement and Concrete Research, 41 (2011) 1244-1256.

[110] D. Damidot, F.P. Glasser, Thermodynamic investigation of the CaO-Al$_2$O$_3$-CaSO$_4$-K$_2$O-H$_2$O system at 25°C, Cement and Concrete Research, 23 (1993) 1195-1204.

[111] K. Lipus, J. Rickert, Impact of low magnesium concentrations on sulphate resistance of cement fly ash blends at practical relevant sulphate attack conditions, 13th International Congress on the Chemistry of Cement, Madrid Spain (2011) 391-397.

[112] B. Lothenbach, T. Schmidt, Influence of limestone on sulphate ingression, in: M. Alexander, A. Bertron (Eds.) Concrete in Aggressive Environments; Performance, Testing and Modeling, RILEM, Toulouse, France, 2009, 212-219.

[113] F.W. Locher, Zur Frage des Sulfatwiderstands von Hüttenzementen, Zement Kalk Gips, Cement lime gypsum ZKG international, (1966) 395-401.

[114] R.S. Gollop, H.F.W. Taylor, Microstructural and microanalytical studies of sulfate attack. IV. Reactions of a slag cement paste with sodium and magnesium sulfate solutions V. Comparison of different slag blends, Cement and Concrete Research, 26 (1996) 1747-1747.

[115] V. Fernandez-Altable, C. Yu, G. Le Saout, K. Scrivener, Characterisation of slag blends and correlation with their sulphate resistance in static and semi-dynamic conditions, 13th International Congress on the Chemistry of Cement, Madrid Spain (2011) 434-440.

[116] E.F. Irassar, A. Di Maio, O.R. Batic, Sulfate attack on concrete with mineral admixtures, Cement and Concrete Research, 26 (1996) 113-123.

[117] E.F. Irassar, O.R. Batic, Effects of low calcium fly ash on sulfate resistance of OPC cement, Cement and Concrete Research, 19 (1989) 194-202.

[118] K. Torii, M. Kawamura, Effects of fly ash and silica fume on the resistance of mortar to sulfuric acid and sulfate attack, Cement and Concrete Research, 24 (1994) 361-370.

[119] K. Torii, K. Taniguchi, M. Kawamura, Sulfate resistance of high fly ash content concrete, Cement and Concrete Research, 25 (1995) 759-768.

[120] South African Council for Scientific and Industrial Research, Corrosion of concrete sewers, South African Council for Scientific and Industrial Research, 1959.

[121] A.M. Neville, Properties of concrete, Pearson Education Limited, Harlow, England, 2002.

[122] A. Leemann, B. Lothenbach, H. Siegrist, C. Hoffmann, Influence of water hardness on concrete surface deterioration caused by nitrifying biofilms in wastewater treatment plants, International Biodeterioration & Biodegradation, 64 (2010) 489-498.

[123] L.J. Parrott, Variations of water absorption rate and porosity with depth from an exposed concrete surface: effects of exposure conditions and cement type, Cement and Concrete Research, 22 (1992) 1077-1088.

[124] F. Bellmann, W. Erfurt, J. Stark, Gefährdungspotential der betonschädigenden Thaumasitbildung, Bauhaus-Universität Weimar Weimar, Germany, 2010.

[125] R. Sersale, R. Cioffi, B. De Vito, G. Frigione, F. Zenone, Sulphate attack of carbonated and uncarbonated Portland and blended cement mortars, 10th International Congress on the Chemistry of Cement, Göteborg Sweden (1997) 4 iv017.

[126] P.J. Tumidajski, G.W. Chan, K.E. Philipose, An effective diffusivity for sulfate transport into concrete, Cement and Concrete Research, 25 (1995) 1159-1163.

[127] D. Kulik, U. Berner, E. Curti, Modelling geochemical equilibrium partitioning with the GEMS-PSI Code, Paul Scherrer Institute (PSI), Villigen, Switzerland, 2004.

[128] W. Hummel, U. Berner, E. Curti, F.J. Pearson, T. Thoenen, Nagra/PSI chemical thermodynamic data base 01/01, in, Universal Publishers/uPUBLISH.com. 565, USA; also published as Nagra Technical Report NTB 02-16, Wettingen, Switzerland, 2002.

[129] T. Thoenen, D. Kulik, Nagra/PSI chemical thermodynamic database 01/01 for the GEM-Selektor (V.2-PSI) geochemical modeling code. PSI TM-44-02-09, in, Paul-Scherer-Institute (PSI) Villingen, Switzerland, 2003.

[130] K. De Weerdt, M. Ben Haha, G. Le Saout, K.O. Kjellsen, H. Justnes, B. Lothenbach, Hydration mechanisms of ternary Portland cements containing limestone powder and fly ash, Cement and Concrete Research, 41 (2011) 279-291.

[131] U. Müller, Personal communication, in, BAM Bundesanstalt für Materialforschung und -Prüfung, Berlin, Germany, 2010.

[132] N. Hearn, R.D. Hooton, M.R. Nokken, Pore structure, permeability, and penetration resistance characteristics of concrete, ASTM Special Technical Publication, (2006) 238-252.

[133] K.K. Aligizaki, Pore structure of cement-based materials, Taylor & Francis, London and New York, 2005.

[134] S. Diamond, Mercury porosimetry: An inappropriate method for the measurement of pore size distributions in cement-based materials, Cement and Concrete Research, 30 (2000) 1517-1525.

[135] J. Kaufmann, R. Loser, A. Leemann, Analysis of cement-bonded materials by multi-cycle mercury intrusion and nitrogen-sorption, Journal of Colloid and Interface Science, (2009) 730-737.

[136] C. Salmas, G. Androutsopoulos, Mercury porosimetry: contact angle hysteresis of materials with controlled pore structure, Journal of Colloid and Interface Science, 239 (2001) 178-189.

[137] M. Ben Haha, E. Gallucci, A. Guidoum, K.L. Scrivener, Relation of expansion due to alkali silica reaction to the degree of reaction measured by SEM image analysis, Cement and Concrete Research, 37 (2007) 1206-1214.

[138] K.L. Scrivener, Backscattered electron imaging of cementitious microstructures: understanding and quantification, Cement and Concrete Composites, 26 (2004) 935-945.

[139] F.P. Glasser, D. Damidot, M. Atkins, Phase development in cement in relation to the secondary ettringite problem, Advances in Cement Research, 7 (1995) 57-68.

[140] B. Lothenbach, E. Wieland, A thermodynamic approach to the hydration of sulphate-resisting Portland cement, Waste Management, 26 (2006) 706-719.

[141] J.J. Thomas, D. Rothstein, H.M. Jennings, B.J. Christensen, Effect of hydration temperature on the solubility behavior of Ca-, S-, Al-, and Si-bearing solid phases in Portland cement pastes, Cement and Concrete Research, 33 (2003) 2037-2047.

[142] C.J. Warren, E.J. Reardon, The solubility of ettringite at 25°C, Cement and Concrete Research, 24 (1994) 1515-1524.

[143] D. Damidot, M. Atkins, A. Kindness, F.P. Glasser, Sulphate attack on concrete: limits of the AFt stability domain, Cement and Concrete Research, 22 (1992) 229-234.

[144] K.O. Kjellsen, R.J. Detwiler, O.E. Gjørv, Pore structure of plain cement pastes hydrated at different temperatures, Cement and Concrete Research, 20 (1990) 927-933.

[145] S. Goto, D.M. Roy, The effect of w/c ratio and curing temperature on the permeability of hardened cement paste, Cement and Concrete Research, 11 (1981) 575-579.

[146] T. Matschei, F.P. Glasser, Temperature dependence, 0 to 40 °C, of the mineralogy of Portland cement paste in the presence of calcium carbonate, Cement and Concrete Research, 40 (2010) 763-777.

[147] T. Matschei, B. Lothenbach, F.P. Glasser, The role of calcium carbonate in cement hydration, Cement and Concrete Research, 37 (2007) 551-558.

[148] T. Matschei, B. Lothenbach, F.P. Glasser, The AFm phase in Portland cement, Cement and Concrete Research, 37 (2007) 118-130.

[149] D. Damidot, S. Stronach, A. Kindness, M. Atkins, F.P. Glasser, Thermodynamic investigation of the $CaO-Al_2O_3-CaCO_3-H_2O$ closed system at 25°C and the influence of Na_2O, Cement and Concrete Research, 24 (1994) 563-572.

[150] M. Buil, E. Revertegat, J. Olivier, A model of the attack of the pure water or undersaturated lime solutions on cement, Stabilization and Solidification of Hazardous, Radioactive, and Mixed Wastes, ASTM Philadelpia (1992) 227-241.

[151] J. Marchand, D. Bentz, E. Samson, Y. Maltais, Influence of calcium hydroxide dissolution on the transport properties of hydrated cement systems, Workshop on the Role of Calcium Hydroxide in concrete, The American Ceramic Society, Holmes Beach, Anna Maria Island, Florida, USA (2000) 113-129.

6 Appendix

6.1 Sulfate Attack – A Literature Survey

6.1.1 Sulfate Attack

Hardened cement paste is chemically reactive. The mineralogical composition changes depending on the service conditions. Sulfate attack is the technical term for the deleterious interaction of hardened cement paste with sulfate ions that migrate from the service environment into the cementitious binder. Such alterations are influenced by various factors including temperature, relative humidity (wetting/drying) and the chemical composition of the solution that exchanges ions with the cement paste. The physical and chemical properties of the cements play an essential role as well. All of the mentioned factors vary with time and space due to the involved transport mechanism and can lead to various degradation types like softening, loss of cohesion, cracking, delamination or expansion.

Sulfate attack is a very complex degradation mechanism for cementitious binder. Generally, it is believed that the expansion is driven by late ettringite and/or gypsum formation but other phases like thaumasite can form under specific conditions and affect the deterioration process.

6.1.2 A Brief History and Overview

In Germany and Italy cements were developed in the beginning of the twentieth century, which followed a concept from Le Chatelier, by substitution of alumina with iron oxide [6, 66]. The identification of aluminates in cement as a critical compound for sulfate attack was an important step and the limitation of aluminate phases in cement clinker is still represented in today's prescriptive standards.

Many reviews, state of the art reports, conference proceedings and comprehensive books are available on the topic of sulfate attack [3, 5, 6, 67-70]. While the general processes are clear, many aspects are still under debate.

One of the key aspects, besides the presence of sulfates, is the presence of water. Water serves as transport medium and allows the sulfate ions to enter the cementitious binder; the degradation itself requires some water but no saturated conditions. The presence of water as a transport media links sulfate attack to other transport related topics like leaching and decalcification.

6.1.3 Sulfate Attack in Research and Concrete Technology

Until approximately 1990 the investigation on sulfate attack focussed on the changes of length or compressive strength for samples exposed to sulfate environments in the laboratory or under field exposure, with only few studies using also analytical techniques. Gradually, more analytical techniques were employed and combined to investigate cementitious binder exposed to sulfates, typically at the end of the exposure period. Most laboratory experiments focused on sodium sulfate solutions with magnesium sulfate being the second most investigated sulfate solution.

Several approaches were used to reduce the testing times for the laboratory tests, often in combination. The main approaches to accelerate the deterioration were the increase of sulfate concentration, the reduction of curing time, and the use of binders with high w/b ratios to increase the permeability of the samples.

Today, no European standard test is in effect and older national standard tests are under debate as they produce artefacts and are subjected to size effects; partially these artefacts are described by Ferraris et al. [71]. Standard tests are nevertheless of interest for the construction industry as they provide guidance for engineers in cases where prescriptive standards are not applied directly.

One of the main flaws of the observation of length changes is that the mechanical interactions, which lead ultimately to the observed expansion, between different mineralogical zones are unclear [72], and that it is impossible to obtain from the sum parameter "length change" information about the underlying mechanisms. In research projects advanced analytical techniques are employed to investigate the systems typically at the end of the exposure period. The reduced costs of computer calculation time increased also the use and development of computer based models in the last two decades drastically, including the development of powerful thermodynamic and reactive transport models.

6.1.4   Limitations of the Investigation

In this thesis, the experimental results are compared to modelling with equilibrium thermodynamics, which limits the arguments that can be followed, as (i) thermodynamic modelling cannot be applied to investigate systems if thermodynamic properties are unknown and (ii) thermodynamic calculations can only predict the total volume generated but provides no microstructural information. Equilibrium thermodynamics was used in this work to calculate volume and phase changes. Volume increase is in a porous material a necessary condition for pressure development but not a sufficient one [17].

Also the expansion mechanism of sulfate attack is still under debate. Brown and Taylor [17] reviewed the expansion mechanisms for sulfate attack that were discussed in the last decades like different ettringite morphologies and growth locations. They concluded that a combination of mechanisms seems likely as no single mechanism seems capable of explaining the observed degradations.

One of the most promising mechanisms is the concept of crystallization pressures developed by growing crystals under supersaturated and confined conditions, which will be discussed in the next section.

6.1.5   Crystallization Pressure as a Cause for Length Changes

Crystals growing in supersaturated solutions are able to do work, like lifting a weight or pushing particles, under defined conditions by converting chemical energy into mechanical work [10, 22]. The concept is based on the presence of a solution oversaturated with respect to a crystal. The pressure that is required to prevent a crystal to grow (Δp) can be calculated according to the following equation and represents the maximal pressure generated by a crystal for a given supersaturation:

$$\Delta p = \frac{RT}{V_m} \ln \frac{IAP}{K_{s0}}$$

where R is the molar gas constant, T the temperature, V_m the molar volume and IAP is the ionic activity product and K_{s0} the theoretical equilibrium solubility product of a crystal under ambient pressure. The IAP is determined by the actual concentrations in the solution. The degree of supersaturation is defined by the ratio of IAP/K_{s0}. Supersaturation is influenced by changes in temperature, relative humidity (evaporation), or pressure. In specimen affected by sulfate attack under isothermal, isobaric, saturated conditions, as it is typically

the case for laboratory tests, the diffusion of sulfate ions and slow precipitation kinetics are the causes for a possible supersaturation of the pore solution with respect to sulfate bearing crystals.

The requirements to generate pressure in porous materials due to supersaturation include crystal growth in a confined space under maintenance of a supersaturated liquid film between the crystal and the pore wall [7, 9-11]. The geometrical requirement for the confinement is that the entrances of a pore are smaller than the pore, which allows the crystals to form a surface with more curvature at the pore entrance (Figure 27). Curved surfaces have more surface energy, i.e. a surface that is in equilibrium with a higher concentrated solution.
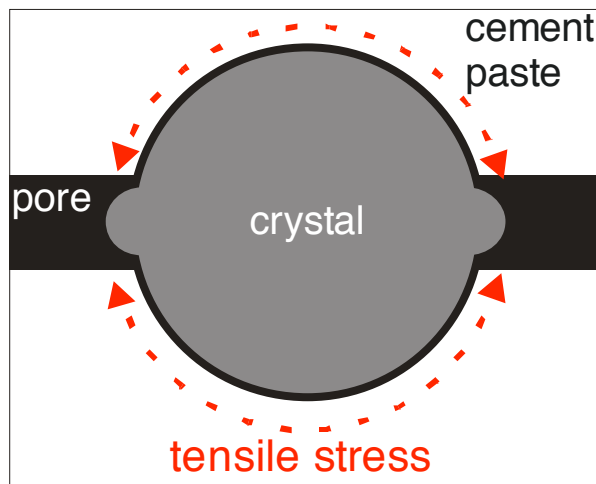
Figure 27: Large crystal growing in a spherical pore with cylindrical pore entrances (modified after [11, 73])

The main part of the crystal, which has less surface curvature and thus less surface energy, remains under these conditions in a supersaturated solution without growing through the smaller pore entrances. Otherwise the crystal would dissolve and contribute to the growth of a larger crystal in unconfined space. The formation of larger crystals and growing in unconfined spaces is thermodynamically preferred (Ostwald ripening).

A higher surface curvature of the crystal, than present at the pore entrance, would be required to fill the pore completely if a pore has an irregular outline, like a small pit [74]. Such a pit would not be filled with the crystal as such a surface would require higher supersaturation to be stable. No pressure from a growing crystal could be exerted, which complicates the analysis as the pore wall could be exposed to different pressures. Generally, simplified geometries are discussed as the pore structure of a cementitious material is very complex.

Classical mechanics can be used to understand the stress development in materials assuming material parameters and geometries, which are both unknown on the scale of interest but these models help understand observed crack patterns, like ring cracks around aggregates, typical for expanding pastes, or radial cracks for expanding domains in a non-expanding matrix [75-77]. The material around an expanding domain fails due to tensile stresses [75-77]. For growing crystals in a pore this corresponds to tensile stresses in the cement paste induced by the pressure generated by a growing crystal (Figure 27). The developed tensile stress is can be expressed in relation to the pore dimensions and strain to avoid making assumption about unknown material parameters. The maximal tensile stresses occur at the "interface" between the expansive domain and pore wall [75-77].

For a more uniform expansion mechanism, like delayed ettringite formation, another expression based on volume fractions of crystals exerting pressure in the sample has been described [9, 10]. Minimal pore radii are calculated for spherical (> 20 nm) and cylindrical (> 2 nm) pores for delayed ettringite formation [9]. The calculated pore radius for cylindrical pores is in the range of the maximal distance in the unit cell of ettringite (1.94 nm), which corresponds to the larger width of a single ettringite needle [78]. The nucleation of crystals in a constrained system has a limit that depends on the particle size of the formed crystal and might be larger than one unit cell of a crystal [79].

External sulfate attack is more complex than delayed ettringite formation, because it cannot be assumed that the expansion of the cement paste occurs uniformly throughout the sample as the sulfate ingress advances in a front. The expanding parts of a specimen have to overcome the restrain from sulfate unaffected parts before significant length changes are observed, which complicates the mechanical investigation. Additionally, to make an assumption about the maximal supersaturation is difficult as the pore solution is often oversaturated with respect to gypsum, which potentially increases the supersaturation beyond values which are assumed for delayed ettringite formation.

That crystallization pressure is only exerted after a confined pore is fully filled with an crystal explains to some extent why no linear relation was found between ettringite formation and observed expansion for sulfate attack [8, 80], delayed ettringite formation [81, 82], and model systems [15, 83]. This could be due to small differences in crystal contents between a pore almost filled, i.e. without pressure development, and a crystal that exerts pressure. The filling of pores could also explain the delay in observed expansion, as only small length changes are observed during the unconfined growth of crystals in pores.

Thermodynamic modelling techniques, based on an equilibrium approach, are not able to calculate supersaturation without imposing kinetics for phase precipitation and dissolution [84].

6.1.6   Relevant Phases for Sulfate Attack

Monosulfate ($Ca_4 Al_2 (SO_4) (OH)_{12} 6H_2O$), monocarbonate ($Ca_4 Al_2 (CO_3) (OH)_{12} 5H_2O$) or other AFm phases are present if the sulfate concentrations are too low to stabilize ettringite. Cements with high C_3A contents or generally hydrated cements with a high AFm content are susceptible to sulfate attack. Ettringite crystals ($Ca_6 Al_2 (SO_4)_3 (OH)_{12} 26H_2O$) are therefore the principal suspects for the pressure generation. Ettringite crystals form from aluminate phases in the presence of sufficient calcium, sulfates and water.

Cements with high C_3S and low C_3A contents are also susceptible to sulfate attack [39, 40], even binders that lack aluminate bearing phases altogether expand due to gypsum formation ($CaSO_4 2 H_2O$ or $C\$H_2$; [2, 38, 85]). As a consequence, the formation of both crystalline phases, ettringite and gypsum, can be considered to be responsible for expansion. Ettringite is normally present in hydrating cements and in most cases not deleterious unless the formation occurs after setting. Gypsum is typically part of unhydrated cements and reacts during normal hydration within hours.

Ettringite is stable at pH values above 10.5 [86, 87], gypsum is stable throughout a large range of pH values and of the possible sulfate containing phases the only one stable at pH values below 10. However, gypsum is less likely to form at very high pH values [88].

Gollop and Taylor [48, 52, 56, 89] investigated several cements under sodium and magnesium sulfate exposure. Generally, a leached and decalcified zone was found on the surface with gypsum bands running below

the surface. Deeper within the samples, ettringite was found that had formed on the expense of monosulfate. Monosulfate was found in the unaffected core of the mortar specimen. It was concluded that ettringite initiated the damage while gypsum was formed later.

Additionally, syngenite ($K_2Ca(SO_4)_2 H_2O$) can precipitate in the presence of high sulfate and potassium concentrations. The U-phase ($Ca_4 Al_{0.9} (SO_4)_{1.1} (Na_2O)_{0.5} 16H_2O$ [90]), a phase of the AFm family and therefore with variable composition, is stable under very high sodium concentrations and at higher temperatures [91].

The thaumasite form of sulfate attack is not within the scope of this work. Thaumasite ($Ca_3Si(OH)_6(CO_3)(SO_4)12H_2O$) formation is relatively fast at low temperatures but very slow around 20 °C [47] and is thus not relevant for the time frame and temperatures examined in this work.

Sulfate can be adsorption or absorption by C-S-H or C-A-S-H phases. This is not considered in the thermodynamic calculations due to a lack of thermodynamic data. The sulfate uptake depends on the calcium to silicon ratio of C-S-H and the presence of aluminium in C-A-S-H phases [92-94]. A reduction of available sulfate due to binding in C-S-H/C-A-S-H affects the formation of monosulfate, ettringite, and gypsum.

6.1.7 Transport and Permeability

The permeability/diffusivity of the cement paste is of importance as a well-connected pore network facilitates ionic transport and thereby allows the fast deterioration of cementitious materials in aggressive environments. The pore space of cementitious materials depends on the kind and amount of hydrates formed and on the mix design as the initially used mixing water provides the initial pore space. The complete filling of the pores during hydration is not expected for conventional cementitious materials as typically more water is used than chemically needed for complete hydration.

It has also been found that the chemical composition of the cement has a large influence on the performance of cementitious binders if the water/cement (w/c) ratio is higher than 0.45 while binders with a w/c ratio lower than 0.45 are not susceptible to sulfate attack [40, 95].

The relation between diffusion and microstructures of hydrated cement is often investigated by modelling techniques due to the complex and multi-scale pore structure in hydrated cements. The permeability of the cements determines the transport and interaction with ions in solution. The ions interact with each other and with the solids present in chemical reactions and physical interactions [21, 37, 96, 97]. The concentrations of the ions in solution depend on the local equilibrium of pore solution and solid phases, provided that the transport is slower than the phase formation kinetics [98].

6.1.8 Different Sulfate Solutions

6.1.9 Alkali Sulfates

Generally, sodium and potassium sulfate are assumed to interact similarly with cementitious materials and are therefore often discussed together using the term alkali sulfates [6, 67]. However, differences are expected in highly concentrated solutions as syngenite might precipitate in the presence of very high potassium sulfate and the U-phase in the presence of very high sodium concentrations.

Sodium Sulfate

Sodium sulfate solution is the most commonly used sulfate solution in sulfate tests as only little interaction of sodium with the cement hydrates is expected. Typically, monosulfate and other AFm phases react with the sulfate, calcium, and water to form ettringite. Gypsum precipitates at high sulfate concentrations or where no aluminates are present [47]. At very high sodium sulfate concentrations the U-phase may precipitate [90].

Potassium Sulfate

Very little data is published on the interaction of potassium sulfate with cementitious binders. Biczók [99] mentions that potassium sulfate is less harmful to Portland cements than sodium, magnesium or calcium sulfate solutions. However, Biczók [99] does not name the criterion on which he bases this statement. Additionally to ettringite and gypsum, syngenite ($K_2Ca(SO_4)_2$ H_2O) can precipitate when potassium sulfate is used in high concentrations [100, 101].

Magnesium Sulfate

Magnesium sulfate solution is the second most commonly used laboratory test solution. Magnesium hydroxide (brucite, $Mg(OH)_2$) precipitates close to the surface in hydrated cements additionally to the formation of ettringite and gypsum. The formation of dense double layer consisting of a brucite and a gypsum layer is observed for Portland cements and is claimed to be responsible for the reduced sulfate penetration and expansion [49, 102-104]. The binding of hydroxide in the very insoluble brucite reduces the pH value of the pore solution and is compensated by hydroxide release from portlandite and C-S-H. A strong decalcification, which is observed to reduce the cohesion of the binder, and gypsum precipitation are the main features of this process. In the leached zones also other amorphous or poorly crystalline phases like silica (SiO_2) and magnesium-silicate-hydrates (M-S-H) are observed [56, 105].

Calcium Sulfate

Tests employing calcium sulfate solution cannot be carried out at higher concentrations, as the solubility of gypsum in water is low (0.016 mol/l equalling 1.2 g SO_3/l) compared to the other sulfate salts (sodium, potassium and magnesium sulfate). However, gypsum or anhydrite present in the host rock of the concrete structures can be a continuous source of sulfates and therefore damages are observed [106].

It is expected that the presence of calcium in the sulfate solution reduces calcium leaching [1, 6] as no calcium needs to be leached to form ettringite and the diffusion gradient is reduced due to the presence of calcium in solution.

6.1.10 Influence of Mineral Admixtures on the Sulfate Resistance of Cements

The literature survey focuses only on cementitious binders similar to those used by the author, which are Portland cement dominated blends with silica fume, fly ash and limestone, and slag blended cements with high degrees of substitution. Alternative binders, like slag based supersulfated cements or geopolymer based binders, might display superior sulfate resistance in similar tests but are not discussed in this work.

The use of SCM's is generally regarded to be beneficial for the sulfate resistance of cements [107, 108].

The addition of SCM's has several effects [109]:

- Portland cement, which is susceptible for sulfate attack, is diluted by silica rich SCM's.

- The pozzolanic reaction of SCM's with portlandite reduces the amount of portlandite that can be affected by aggressive solutions.

- At the same time the microstructure is refined, which reduces the permeability /diffusivity.

- Due to the so-called filler effect the cement hydration is promoted, which also refines the microstructure.

- The reactivity of fly ash and slag particles is typically lower than the reactivity of Portland cement phases, which allows fixing significant amounts of the aluminium in unreacted particles. In addition, the low Ca/Si C-S-H formed in the presence of silica rich SCM's can immobilise additional aluminium [92] thus lowering the potential for ettringite formation.

It has been suggested that the concentrations of aluminium in the pore solution are reduced in the presence of high calcium concentrations [110]. Cements, which are relatively poor in calcium like blended cements, might allow aluminium to travel further away from dissolution sites, which increases the possibility to precipitate aluminium bearing crystals like ettringite in unconfined spaces. However, such cements generally also have pore solutions with lower pH values, an effect that decreases dissolved aluminium concentrations. On the other hand, binders low in calcium suffer more from decalcification than Portland cements, which makes blended cements more prone to magnesium sulfate attack [89, 105, 111]. Surface deterioration of blended cements does not necessarily contribute to expansions [58, 89, 111].

The amount of calcium sulfates originally present in a Portland cement, which is often adjusted when cements are blended, influences the susceptibility of the cement to sulfate attack as more ettringite and less AFm phases are present in the hydrated Portland cement and thus a lower potential for additional ettringite formation [112].

However, the performance of SCM blended cements also depends on the material properties, chemical composition and the sulfate environment [89, 113, 114]. The substitution levels vary for the different SCM's to be effective. The substitution is lowest for silica fume (5-15 percent, [107, 108]), higher for fly ash blended cements ([107, 108]) and highest for slag blended cements (above 65%, [113]).

Influence of Silica Fume

Silica fume has the highest reactivity of the used SCM's due to the small particle size [109]. It consists of silica and thereby dilutes the aluminium from the cement and lowers the calcium to silica ratio of the cement paste, which makes silica fume blended cements more susceptible to magnesium sulfate attack [105]. The permeability of silica fume blended cements is typically low and contributes to the improved performance.

Influence of Granulated Blast Furnace Slag

Ground granulated blast furnace slags (GGBFS) have typically slower reaction kinetics than silica fume and contain more calcium and aluminium [109]. Slag blended cements, incorporating high amounts of slag, are considered to be sulfate resistant while Portland cements are regarded as not appropriate for the use in sulfate environments [25]. Cements with substitution of Portland cement with slag contents larger than 65 % show a good sulfate resistance [113]. The same study showed that portlandite and AFm phases are much reduced in the binders with high slag contents although the total Al_2O_3 content can be much higher than in Portland ce-

ments. However, a large fraction of Al_2O_3 can be present in the unreacted slag particles. In principal, the AFm content of hydrated slag blended cements could be higher than for Portland cements. Recent work on this topic suggests that monosulfate can form from previously unreacted slag particles [115]. The late formation of monosulfate increases the potential to from late ettringite and thus the potential for late expansion. The microstructure of slag blended cements is refined and has less capillary pores which are mostly responsible for the transport properties of the material.

Influence of Fly Ash

Fly ash has typically slower reaction kinetics than silica fume and slag [109] and contains most calcium and least silica of the used SCM's. The sulfate resistance of fly ash blended cements depends on the substitution degree and composition of the fly ash as calcium rich fly ashes can be susceptible to aggressive environments but more cases of improved performance are reported [108, 116-119].

6.1.11 Effect of Carbonation on the Sulfate Resistance

The expression carbonation is used when H_2CO_3 forms in solution from CO_2 from the air and reacts with hydrated cement paste. H_2CO_3 dissociates at high pH values:

$$H_2CO_3 \Leftrightarrow CO_3^{2-} + 2H^+$$
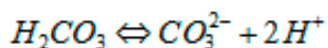
Carbonation thus reduces the pH value by the release of protons into the pore solution and the reduction of portlandite, which forms calcite in the presence of carbonate ions. Ettringite and other cement hydrates are destabilized and the reinforcement depassivates due to the reduction of pH in the pore solution. Extensive carbonation is therefore deleterious for reinforced concrete.

In addition to carbonation due to CO_2 from the air, ground waters in calcite and dolomite containing environments can contain high concentrations of bicarbonates (HCO_3^-, up to 1 g/l). The transport of bicarbonate ions with water into cementitious materials can thus also cause carbonation. The reduction in pH from bicarbonate is less severe as only one H^+ per bicarbonate ion is liberated. However, the high bicarbonate concentrations in ground water and continuous supply can result in considerable carbonation. Under field conditions sulfate attack and carbonation due to the presence of dissolved bicarbonate can occur simultaneously and influence each other.

The combination of sulfate attack and carbonation is not well documented. Field studies suggest that carbonation is beneficial for the resistance of hardened cementitious materials against sulfate attack [42, 120]. Two arguments are used to explain the improved performance of carbonated samples, (i) the formation of a dense, protective calcite layer and (ii) the unavailability of calcium to form expansive phases. The two arguments are briefly discussed, a separation of the effects by experiments has not been attempted in the literature, however both mechanisms are likely to contribute at the same time to the improved performance of the materials.

The link between sulfate attack and carbonation has been investigated on samples carbonated in air before sulfate containing solutions were applied. The presented work focuses on the simultaneous occurrence of both sulfates and bicarbonates as this is the relevant condition for underground structures.

Protective Layer Formation

Biczók [99] mentioned that "normal Portland cement, sensitive to sulfate attack can be made sulfate-resistant by carbonation" without providing details on the mechanism. A positive, retarding effect of potentially protective carbonate films on the expansion is acknowledged [99]. Neville [121] also identified the beneficial influence of carbonation on all transport induced deterioration mechanisms, which he explained with lower permeability and sorptivity. A densification of carbonated concrete surfaces has been observed experimentally for Portland cements [122, 123]. Carbonate layers are often found in field samples exposed to sulfate environments [124]. Aragonite, a metastable form of calcium carbonate ($CaCO_3$), is often found in seawater; its persistence is influenced by the presence of magnesium ions [49].

Coarsening of the pore structures of blended cements is reported for carbonated samples [45, 125].

Chemical Effects of Carbonation

Lea [38] published experiments on mortars made from lime and silica gel only. The amount of reactive free lime in the hardened samples was experimentally reduced by carbonation, resulting in lower expansions of the carbonated samples. The observed lower expansion was attributed to a ecreased gypsum formation due to the carbonation of the free lime. Lea [38] showed that the fixing of calcium in thermodynamically stable calcium carbonate prevents the formation of sulfate bearing phases, although he investigated a system relatively far from common cementitious materials. For mortars made from Portland cement, Lea concluded that "the removal of free calcium hydroxide by carbonation only retards expansion in sodium sulfate solutions" due to the interaction of sulfates with calcium aluminate phases [38].

Mangat and El-Khatib [45] investigated the influence of initial curing conditions of concretes and pastes produced with OPC, fly ash, blastfurnace slag, and silica fume. The increased sulfate resistance of the carbonated samples was also explained with the reduction of available portlandite to form additional sulfate bearing phases.

Sersale et al. [125] studied CEM I, CEM III/B, and CEM IV mortar bars exposed to sodium and magnesium sulfate solutions. The results showed that carbonation before sulfate exposure increased the sulfate resistant. This was attributed to the consumption of portlandite in the carbonated regions.

6.2   Materials and Methods

Concept of the Measurement Campaign

The aim of this work is to compare the performance of various cements in different sulfate solutions. Some sulfate solutions are commonly used for laboratory tests, like sodium and magnesium sulfate solutions, and others are less common like potassium sulfate, sulfate mixtures, or bicarbonate containing solutions. Several different cements were part of the measurement campaign. The experimental data were compared to thermodynamic modelling. To facilitate the comparison of the different systems the same structure was used for each investigated solution, reflecting the concept of the measurement campaign, which is described in the following:

Macroscopic Changes

The sections for each investigated system start with the introduction and discussion of the observed length and mass changes. The measurement of length changes is the most used indicator for volume stability of samples under sulfate attack. However, no standard test was used to measure the expansion of the mortar bars but the same sulfate concentration was used (50 g Na_2SO_4/l) as in the Swiss SIA standard [25] for sulfate resistance of concrete samples. The use of mortar bars of similar dimensions to the SIA standard increases the paste content and reduces the amounts of aggregates of the specimen and accelerates the expansion. In plain cement paste samples the transport would be slower, due to the absence of sand or larger aggregates [126].

The drying cycles, which are prescribed in the SIA standard [25], were not applied in order to have diffusion as the only transport mechanism. The use of drying and wetting cycles accelerates the sulfate uptake but complicates the deterioration mechanism as salt crystallisation might occur and extensive drying might alter hydrated cement phases and the microstructure.

The observed macroscopic length changes were used to identify the different stages of deterioration. At different times mortar samples were investigated for their phase composition and the change thereof with penetration depth, especially before and after the samples showed an increase of the expansion rate.

Phase Changes

The composition of the phase assemblages and the changes due to the interaction with the sulfate solutions were predicted by thermodynamic modelling. Also the volume changes and the amount of sulfates bound was calculated and discussed. The predicted phase changes were compared to experimental data gained from paste and mortar samples.

Paste experiments were carried out at different water to liquid ratios to verify the thermodynamic calculations. The paste samples consisted either of small particles of ground, hydrated cement pastes or in some cases the unhydrated cement was mixed directly with the sulfate solution and equilibrated for several months. Thus the sulfate transport was minimized, mechanical aspects were reduced and most importantly

no loss of material during equilibration of the cement paste and test solution occurred as the sulfate solutions were not exchanged. The samples were characterized by **TGA** and **XRD**.

The investigation of the **mortar experiments** was more complex as transport, mechanical aspects and the exchange of the testing solution increased the complexity of the tests. The samples were characterized by **EDS** measurements as a compromise between qualitative characterizations on a small scale and the characterization of the sulfate fronts that moved inwards and required several millimetre of depth to be investigated. The measured data provides several ways of analysis, as phase characterization by atomic ratio plots and oxide profiles (median, maximal values).

The experimental data were compared to the thermodynamic investigations to identify agreement and deviations between the different information to gain a better understanding how the phases interact and might contribute to the observed macroscopic changes.

6.3 Materials

Nine cements were used to prepare a variety of cement pastes (w/b: "cem", "0.40", "0.70") and mortar bars (w/b: "0.55"), and exposed to a variety of test solutions. Tests were conducted with up to eleven solutions, including reference samples stored in deionized water and saturated lime solution. However, only for the CEM I and CEM III/B cements all sulfate and reference solutions were investigated, as they represent the most extreme positions of the used commercial cements.

6.3.1 Cements

The oxide contents, loss on ignition, Blaine surface area and density of the used cements are shown in Table 1. The cements blended in the laboratory (CEM I +2% gypsum, CEM II/B, and CEM III/C) were mixed and homogenized over a period of 12 – 14 hours. The silica fume blended binders were prepared upon mixing as a silica fume slurry was used (EMSAC 500S). The water content of the slurry was taken into account for the mixing water.

Table 9: Chemical composition of the investigated cements; calculated (*)

		CEM I				CEM II/A		CEM II/B*	CEM III/B	CEM III/C*
			+2% gypsum*	+6% SF*	+12% SF*	HS	V-LL	V-LL		
SiO$_2$	[%]	20.3	20.1	27.8	34.0	17.9	23.4	24.0	29.9	30.6
Al$_2$O$_3$	[%]	5.2	5.1	4.6	4.2	4.3	7.5	8.9	9.4	9.8
Fe$_2$O$_3$	[%]	3.1	3.0	2.8	2.5	5.9	3.4	3.3	1.6	1.4
CaO	[%]	63.4	62.7	56.7	51.1	59.8	51.6	45.8	47.6	46.2
MgO	[%]	2.5	2.6	2.3	2.0	2.4	1.9	2.2	4.3	4.4
SO$_3$	[%]	2.4	3.0	2.4	2.3	3.1	2.6	3.0	4.5	4.6
K$_2$O	[%]	0.9	0.9	0.8	0.7	0.8	1.4	1.5	0.7	0.7
Na$_2$O	[%]	0.2	0.2	0.3	0.5	0.6	0.3	0.4	0.1	0.2
TiO$_2$	[%]	0.3	0.3	0.3	0.3	0.4	0.4	0.2	0.7	0.7
Mn$_2$O$_3$	[%]	0.1	0.1	0.1	0.0	0.1	0.1	0.0	0.1	0.1
P$_2$O$_5$	[%]	0.3	0.2	0.2	0.2	0.4	0.2	0.1	0.1	0.1
SrO	[%]	0.0	0.0	0.0	0.0	0.1	0.0	0.0	0.0	0.0
BaO	[%]	0.0	0.0	0.0	0.0	0.0	0.0	0.0	0.0	0.0
CO$_2$	[%]	0.4	0.2	0.3	0.5	0.7	2.0	2.4	0.3	0.3
LOI (950°C) [%]		1.01	n.m.	n.m.	n.m.	3.66	6.73	n.m.	0.74	n.m.

6.3.2   Sulfate Solutions

The concentrations of sulfate salts per litre of solution are listed in gram per litre for the investigated sulfate solutions in Table 10. The used concentrations are generally identified by their mol quantities to facilitate the comparison of the different concentrations, as the mass of 0.35 mol of the different sulfate salts differs (sodium sulfate: 50.0 g; potassium sulfate: 61.7 g; magnesium sulfate 42.2 g). The concentration of 0.35 mol/l is a common sulfate solution concentration for accelerated laboratory tests [25, 26]. All solutions were prepared with deionized water.

Table 10: Salt composition of the test solutions, *lower concentrations (0.035 mol/l) in italics*

	single salt	sulfate mixture	sodium bicarbonate	*magnesium bicarbonate*	bicarbonate mixture
	(0.35 mol/l)	(0.35 mol/l)	(0.35 mol/l)	*(0.035 mol/l)*	(0.35 mol/l)
			[g/l]		
Na_2SO_4	50.0	18.8	50	---	18.8
K_2SO_4	61.7	7.7	---	---	7.7
$MgSO_4\,7H_2O$	86.3	21.6	---	*8.6*	21.6
$CaSO_4\,2H_2O$	---	15.2	---	---	15.2
$NaHCO_3$	---	---	29.6	*3.0*	29.6

Additional tests were conducted with saturated lime solution, deionised water, and a lower concentrated bicarbonate mixture solution (0.035 mol/l). The obtained results can be found in the Appendices.

6.4 Sample Preparation

6.4.1 Mortar Samples

Mortar bars were used to observe length and mass changes during sulfate exposure. Additionally, the development of the dynamic E-modulus was monitored during sulfate exposure for selected test series.

For investigations using scanning electron microscopy (SEM), cross sections were cut, vacuum impregnated with epoxy resin, polished, and coated with carbon for BSE and EDS investigations.

The mortar bars were produced with constant water, aggregate and cement volumes to ensure a similar initial pore volume of the mortar bars, which requires the adjustment of the water to binder ratios as the cements have different densities. The reference water to binder ratio of the CEM I cement was "0.55", and is used as indicator to simplify the identification of mortar samples. The water to binder ratios for the different mortars are listed in Table 11. The sand to cement volume ratio was 3.8.

The mortar bars, which were cast as slabs (4 x 16 x 28 cm^3), were cut to prisms of the dimensions 2.5 x 2.5 x 15 cm^3 for the length and mass changes; the surfaces were cut to facilitate sulfate ingress and to remove a potential carbonation layer from curing. Curing consisted of one day in a humidity chamber with 100 percent relative humidity and 27 days storage in saturated lime solution. Gauge alignments were glued to the ends of the mortar bars to improve the repeatability of the measurements. The samples were stored in a 95 percent relative humidity environment during hardening of the two component epoxy adhesive (Araldite 2014-1) for 12 hours.

Table 11: Mix designs of mortar slabs; 2.7 kg CEN normsand (DIN EN 196 - Part 1) were used as aggregates

	w/b = "0.55"	
	cement	w/b
	[g]	[---]
CEM I	848.0	0.55
+ 2% gypsum	842.7	0.55
+ 6% SF	827.2	0.56
+ 12% SF	809.1	0.58
CEM I HS	842.7	0.55
CEM II/A	770.4	0.61
CEM II/B	743.8	0.63
CEM III/B	786.5	0.59
CEM III/C	781.7	0.60

Stopping of Hydration/Sulfate Exposure

The hydration was stopped by placing the specimens in isopropyl alcohol for 2 hours, before being dried at 40°C if mortar bars were removed from the testing schedule and required storage or further sample preparation.

6.4.2   Paste Samples

Paste samples were used to verify the thermodynamic calculations. The samples were investigated with TGA and XRD, few samples were also impregnated with epoxy resin, polished and carbon coated before being investigated in the SEM.

Cement Paste "cem"

The "cem" paste samples were prepared from CEM I and CEM III/B cements only. The cements were mixed directly with sulfate solutions in 100 ml PVC bottles, curing was not necessary as the water to cement (w/c) ratio was high (66.7). This solid to liquid ratio corresponds to $10^{3.8}$ ml/100 g cement in the thermodynamic calculations, as displayed in most graphs in this work on the "added solution"-axis. The sulfate solutions were not exchanged to avoid the loss of fine particles.

Cement Paste "0.40" and "0.70"

Crushed cement pastes were prepared with different water to binder ratios, which are labelled according to the CEM I equivalent water to binder (w/b) ratio to simplify the naming ("0.40" and "0.70"). The w/b ratios for the different cement pastes are listed in Table 12. Constant water and cement volumes were used, in analogy to the mortar mix design, to ensure a similar initial pore volume of the paste samples.

The cement paste slabs (4 x 16 x 14 cm^3) were cured for one day in a humidity chamber with 100 percent relative humidity and storage for 27 days in saturated lime solution before the potentially carbonated surfaces were removed and the core sections of the slabs were cut into smaller pieces, crushed in a ceramic jaw crusher, and sieved through a 2 millimetre sieve for the "0.4" cement paste. The "0.7" cement paste could not be sieved as the paste contained too much water and clogged the sieve.

The solid to liquid ratio for the thermodynamic calculations varies around 10^3 ml/100 g cement depending on the binder and is indicated in the graphs as a vertical line across the "added solution"-axis. The small deviations are not relevant as the axis itself has a logarithmic scale. The sulfate solutions were not exchanged to avoid the loss of fine particles.

Table 12: Mix designs of the cement pastes

	w/b = "0.40"		w/b = "0.70"	
	cement	w/b	cement	w/b
	[g]	[---]	[g]	[---]
CEM I	1224.9	0.40	902.6	0.70
+ 2% gypsum	1217.3	0.40	897.0	0.70
+ 6% SF	1109.0	0.44	862.2	0.73
+ 12% SF	1028.5	0.48	831.5	0.76
CEM I HS	1217.2	0.40	896.9	0.70
CEM II/A	1112.9	0.44	820.0	0.77
CEM II/B	1074.4	0.46	---	---

CEM III/B	1136.1	0.43	837.1	0.75
CEM III/C	1129.1	0.43	832.0	0.76

Stopping of Hydration after Sulfate Exposure

The samples were investigated after 5 month of sulfate exposure for the "cem" pastes and longer exposure times for the crushed cement pastes. The crushed cement paste samples required longer exposure times as the larger cement paste particles provided more "microstructure" than the "cem" pastes. The samples were vacuum filtered through a Whatman 40 filter, and rinsed with isopropyl alcohol and diethyl ether. The remaining solids were examined by XRD and TGA on the same day to minimize carbonation after a short drying period at 40 °C and soft grinding by hand.

6.5 Measurement Methods

6.5.1 Length and Mass Changes

Lengths changes were measured in comparison to an invar bar at 7, 14, 28, 56, 91, and every 91 days after that until the specimens were considered to be destroyed due to severe cracking or surface deterioration. Lengths were measured on four specimens and averaged. The test solution volume was 20 times larger than the volume of the mortar samples and exchanged after every measurement. The sample mass was determined after the length was measured.

6.5.2 Thermodynamic Modelling

Thermodynamic calculations were carried out using the geochemical code GEMS 3 [127]. The built in PSI GEMS database [128, 129] was expanded with the CEMDATA07 database [28], which contains solubility products of solids relevant for cementitious systems. The degree of the CEM I hydration before the exposition to the sulfate solutions was calculated using the approach of Parrott and Killoh [29, 30]. It was assumed that 20% of the fly ash [32, 130], 40 % of the slag, and 80% of the silica fume had reacted until the end of the curing period of 28 days. A full reaction of the SCM's, especially for silica fume, was not assumed because portlandite was found in samples cured for 28 days (see Appendix A3), which shows that not all silica fume has reacted during the initial curing period. Image analysis was used to estimate the degree of reaction of the SCM's, but the error of the data was large and the values not used for the modelling (see Appendix A5).

Sulfate attack was mimicked by adding increasing quantities of sulfate solutions to the cement. The cement equilibrated with no or little of the sulfate solution relates to the unaffected part of the specimen in the centre of the mortar bar, while the cement equilibrated with a large quantity of sulfate solution describes the phase assemblage near the surface of the mortar bar. The predictions were quickly calculated and showed a good qualitative agreement with measurements [47] and transport modelling [21], but they do not correlate with time and space. The local equilibrium of pore solution and solid phases can be assumed if the transport is slower than the phase formation kinetics [98].

6.5.3 Phase Characterization

Thermogravimetric (TGA) and X-ray diffraction (XRD) were performed on paste samples, while energy dispersive X-ray spectroscopy (EDS) was used on mortar samples to characterize the phase assemblages.

X-ray Diffraction

X-ray diffraction was performed in a PANalaytical X'Pert PRO MPD diffractometer (θ-2θ) with an X'Celerator detector and copper Kα radiation.

Thermogravimetric Measurements

Thermogravimetric measurements were performed with a Mettler Toldeo TGA/SDTA 851e on 10 to 15 mg samples. The temperature range was 30 – 980°C with an increment of 20°C per minute in a nitrogen atmosphere.

Energy Dispersive X-ray Spectroscopy

The changes of the elemental composition within the mortar bars were followed by energy dispersive X-ray spectroscopy (EDS). The measurements were performed with a Philips XL 30 ESEM FEG with an acceleration voltage of 15 keV, as a compromise between interaction volume and excitation of the iron Kα emission, on epoxy impregnated, polished, and carbon coated mortar specimens.

Oxide Profiles

The EDS measurements were arranged in rectangular grids of 15 times 20 points (vertical and horizontal distance equals 14 μm). Placement of the grids was chosen to represent characteristic areas at the investigated depths while minimizing the amount of clinker and aggregates to be measured. The actual measurement spots were determined automatically within the grid and were therefore randomly distributed. Data fluctuation was high due to the heterogeneous microstructure of cement paste in mortar bars. EDS analysis of air voids, cracks, aggregates, unreacted SCM's, and clinker grains were removed after data acquisition based on the count rate, which had a higher accuracy than a selection based on chemical information. The removal of data was visually checked for approximately 30 - 40 % of the measurements and it was concluded that the accuracy was above 99 percent.

The performed EDS measurements were corrected for atomic number differences, absorption, and fluorescence (ZAF correction). The obtained data were expressed relative to the measured elements (Na, Mg, Al, Si, S, K, Ca, Ti, Mn, Fe). Oxide profiles (Na_2O, MgO, Al_2O_3, SiO_2, SO_3, K_2O, CaO) were calculated for the cement paste to facilitate the comparison with already published data. An example of such a dataset is shown in Figure 28A) for a sulfate profile of a CEM I mortar bar.
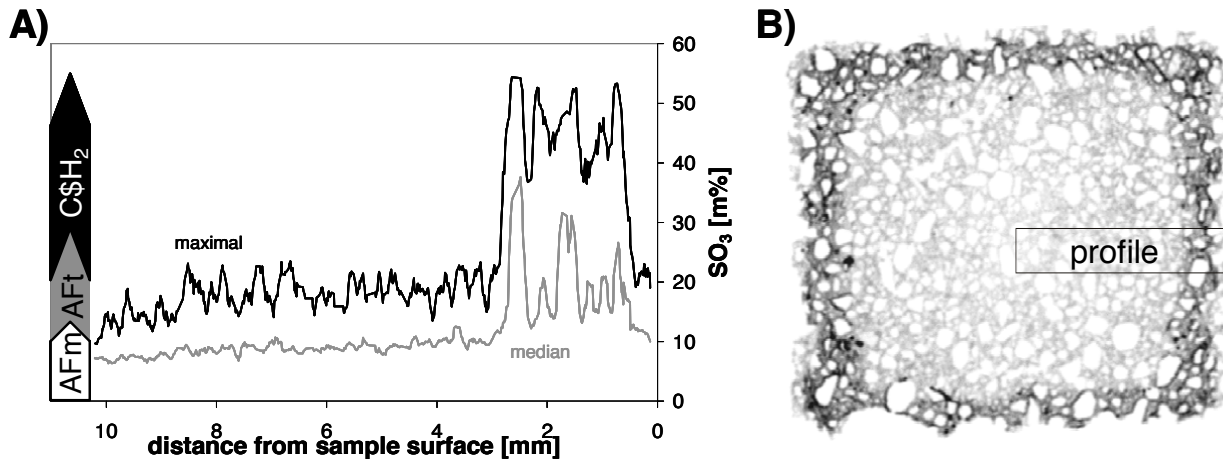
Figure 28: A) maximal and median sulfate profiles and B) sulphur micro X-ray fluorescence map [131] of the cross section of a CEM I mortar bar exposed to sodium sulfate solution for one year; the area where the profiles were obtained is indicated with the box in B

Each data point in the profile was determined from a minimum of five, in average ten, EDS measurements. The displayed profiles in this work are shown as a moving average of 8 depths to smoothen the data without losing the main features (e.g. Figure 28A). The displayed concentrations are lower than the theoretical values, and the highest observed values, because mixed analysis were common and the use of moving averages to smooth the data reduced the determined values additionally.

All profiles start at zero, i.e. at the outermost surface, usually where a cut sand grain indicated the original mortar bar surface. The displayed moving averages start after the first eight depth values. Profiles were obtained starting close to the middle of one of the side faces because some top faces displayed precipitates and bottom faces were losing particles earliest (see also Figure 28B).

The differences of penetration depth on the four faces were studied exemplary. It was concluded that the variation of the penetration depth varies in a range of up to four hundred microns also depending on the arrangement of sand grains. Lateral expansions were neglected for the assignment of coordinates but they might increase the variability.

Figure 28B shows the micro X-ray fluorescence map of the mortar investigated mortar bar, which has been converted to grey levels and colour inverted to increase the visibility on paper. The reduction of the sulfate concentration is captured better by the EDS measurements, while the sulphur map provides a better overview. The sulfate concentration in the cement is 2.4 wt% SO_3, but heterogeneously distributed between ettringite, monosulfate and sorbed to C-S-H/C-A-S-H. The sulfate contents of different phases in cementitious materials are very different (gypsum: 46.5%, ettringite: 19.1%, monosulfate: 12.9%, C-S-H: $\leq 0.1\%$, portlandite/calcite: 0%, these values are even higher for EDS analysis as water and hydroxyl molecules are not measured).The important feature of Figure 28A is that the sulfate concentration of the peaks are similar in zones dominated of gypsum (> 50 percent) and ettringite (22 - 25 percent). Sulfate ions are transported through solution into the specimen along a diffusion gradient. Surface near regions contain therefore more sulfate than the core of a specimen and allow a separation between unaffected and affected areas. The maximal values are more sensitive to changes than average or median values and provide penetration depths closer to the actual sulfate penetration.

Phase Characterization by Maximal Oxide Profiles

Exemplary, the sulfate and calcium oxide profiles are displayed in Figure 29 for the CEM I mortar exposed for one year. The maximal calcium oxide profile connects the maximally observed value of at least five, in average ten, EDS measurements for each distance of the profile and the maximal sulfate profile connects the

same type of data for sulfate. EDS measurements are not reliable for light elements like hydrogen, carbon and oxygen due to the low signal intensity and are not part of the measured elements.
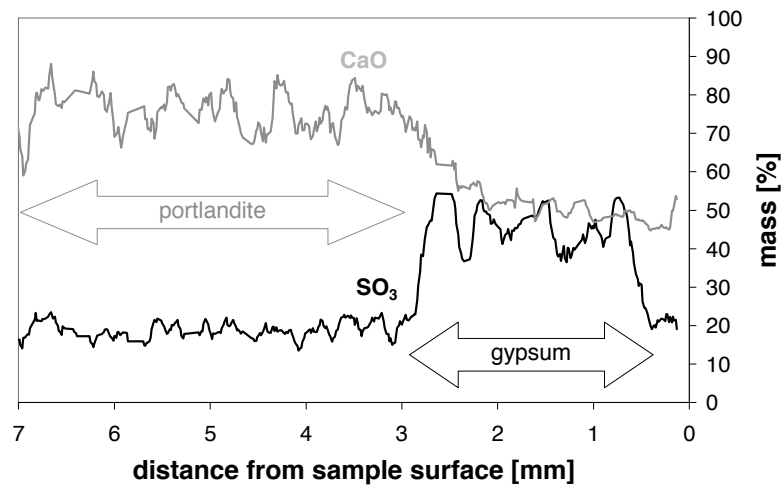
Figure 29: Profiles of measured maximal sulfate and calcium oxide contents in an CEM I mortar bar exposed to sodium sulfate solution for 364 days; the arrows indicate the presence of gypsum and portlandite, which control the maximal concentration values under the given test conditions

To determine oxide contents recalculation was necessary. Oxides were chosen to be displayed to facilitate the comparison with data from the literature.

The maximal CaO value at each depth shows that between the surface of the specimen and approximately two millimetre portlandite and calcite are essentially absent (CaO content of portlandite and calcite: 100 percent, Figure 29), which is also supported by atomic ratio plots. The maximally observed CaO concentration suggests the presence of C-S-H (jennite, 61 percent CaO), gypsum (41 percent CaO) or mixtures of those phases as the present phases with the highest calcium oxide content instead of portlandite or calcite. The EDS measurement that provided the maximal calcium oxide content did usually not provide the highest sulfate concentration. Both values have typically no relation and must not add up to 100 percent. The maximal sulfate concentration corresponds in analogy to the presence of gypsum and the lower plateau to ettringite as has been explained before.

Phase Characterization by Atomic Ratio Plots

The same EDS data points from the profiles were used for the atomic ratio plots to characterize the phase assemblage. The chemical composition determined by EDS measurements was normalized to the overall content of the measured elements. Thus the external addition of sulfates reduces the relative amount of other elements measured while the leaching of calcium has the opposite effect. The normalization during EDS data treatment requires a careful interpretation of the data as the data becomes relative to the changes, which might amplify the changes.

6.5.4   Dynamic E-Modulus

A Labek Elastometer ELM 324 was employed to observe the changes in acoustic/ultrasonic resonance frequency and response time for mortar bars during sulfate exposure. The measurements were performed in direction of the length measurement directly after length and mass changes were performed.

The dynamic E-modulus was calculated according to the following equation:

$$E_{dyn} = 40.01 \cdot 10^{-5} \cdot C_a \cdot f_D^2 \cdot m \frac{l}{b^2}$$

where C_a is a geometry dependent correction factor, f_D is the measured resonance frequency and m is the mass, l the length and b the width of the specimen.

6.6   Porosimetry

The pore structures of the different mortars were characterized with different techniques before sulfate exposure to aid the understanding of the different microstructures that developed during curing and to improve the understanding of the on-going transport related porosity aspects. The investigations were not continued during sulfate exposure. Information about the pore structure was gathered by mercury intrusion porosimetry (MIP), water conductivity, and image analysis (IA) on mortar samples. Generally no technique used to characterize porosities or pore structures is undisputed [132, 133]. The discussions about the different techniques and their applicability to cementitious materials suggest that the sample preparation is a crucial, but not the only factor that influences the measurements. It is difficult to compare the different techniques also because the techniques describe different pore size ranges of the pore volume. Image analysis only captures the larger or "coarse" pores, mercury intrusion porosimetry covers a wide range. Diamond [134] suggested that only the breakthrough pore size and total intrudable pore space should be used as comparative indices, as the pore structure is not ordered by size which does not allow to characterize the pore size distribution of the first intrusion. The water conductivity method describes the changes in water content and transport in the microstructure during samples conditioning, which is used to estimate the so-called water conductivity of a building unit with a thickness of 0.2 m.

Mortar Sample Preparation

The samples were prepared together with the mortar bars for length and mass changes. Hydration was stopped by solution exchange with isopropanol alcohol followed by drying at 40°C for seven days.

Water Conductivity

Water absorption was performed on mortar samples according to Suisse SIA standard [25]. This technique describes water transport properties of the tested mortar by using different saturation states during and after water uptake of previously dried samples. The different degrees of water saturation are used to determine so called capillary pore content (50°C), gel pore content (110°C) and air void content (vacuum saturated). Additional water saturation under vacuum/pressure is performed if the overall density is calculated to be lower than 2.65 kg/m^3 or higher than 2.75 kg/m^3 as it is assumed that not all air voids were filled during the normal sample conditioning. The water conductivity is calculated for a building unit with a thickness of 0.2 m according to the following equation:

$$q_w = \frac{M_{24}}{t_{24}} \frac{U_E/2}{U_E - U_B} \frac{h_{24}}{400}$$

The water conductivity q_w has the unit g/(m^{2}h) and is calculated from the water uptake during 24 hours (M_{24}) normalized by the testing time (t_{24}), h_{24} is the water front height at t_{24}, U_B is the initial water content of the sample, and U_E is the percentage of hydration pores of the total porosity. Comparable standard deviations are given in the SIA standard with 1.5 percent for the water conductivity. An overview of the main porosity data is given in Table 13.

Table 13: Water conductivity obtained on mortars <u>before</u> sulfate exposure; according to SN EN 206-1

cement	initial water content		hydration pores		total porosity		air content		water conductivity	
	U_B	std dev	U_E	std dev	n	std dev	LP	std dev	q_w	std dev
CEM I	4.1	0.3	17	0.1	18.7	0.1	1.6	0	31	2.4
CEM I + 2% gypsum	4.6	0	18.1	0.1	19.7	0.1	1.7	0.1	29	0.3
CEM I + 6% SF	6.6	0.2	19.6	0.2	24.4	0.2	4.7	0.4	4	0.1
CEM I + 12% SF	8.2	0.1	20.7	0.1	24.8	0.4	4.1	0.5	5	0.2
CEM I HS	4.2	0.2	18.8	0	19.9	0.3	1.1	0.3	27	2.4
CEM II/A V-LL	3.5	0.1	19.4	0.1	20.0	0.1	0.6	0	35	0.5
CEM III/B	10	0.1	20.8	0.1	22.4	0.2	1.6	0.1	5	0.1
CEM III/C	10.1	0.1	20.8	0.1	22.4	0.1	1.6	0.1	4	0.2

The advantage of this technique is that it determines quantities that are directly related to water transport in the samples, which is one of the key aspects for transport related durability mechanisms. However, the samples are dried at up to 110°C, which is likely to affect the microstructure severely. Pore sizes are not determines, only volume contents are determined.

Mercury Intrusion Porosimetry

Mercury intrusion porosimetry was performed on Thermo Fisher Pascal 140/440 equipment. First, the samples were pre-intruded to 395 kPa (release to atmospheric pressure) in the Pascal 140 and then moved to the Pascal 440 were intrusion was from atmospheric pressure to a maximum pressure of $p_{max} = 200$ MPa and then released (extruded) to atmospheric pressure again. Without sample removing a second cycle to p_{max} and release to atmospheric pressure was added [135]. The benefit of this technique is that it covers the broadest range of pore sizes of the techniques used, but it applies large pressures which are likely to introduce artefacts. The mercury volume at a given pressure does not indicate a certain pore size during the first intrusion as the microstructure is complex and not ordered according to the pore sizes from large to smaller pores. Some pores, so called ink bottle pores might not be investigated because they are only filled ones, if at all. The content of ink bottle pores can be estimated by the difference of the total porosity minus the remaining mercury in the samples after the first intrusion cycle. The porosities of the mortars before sulfate exposure are summarized in Table 14.

Table 14: Volume and porosity values from MIP measurements, 28 days of curing

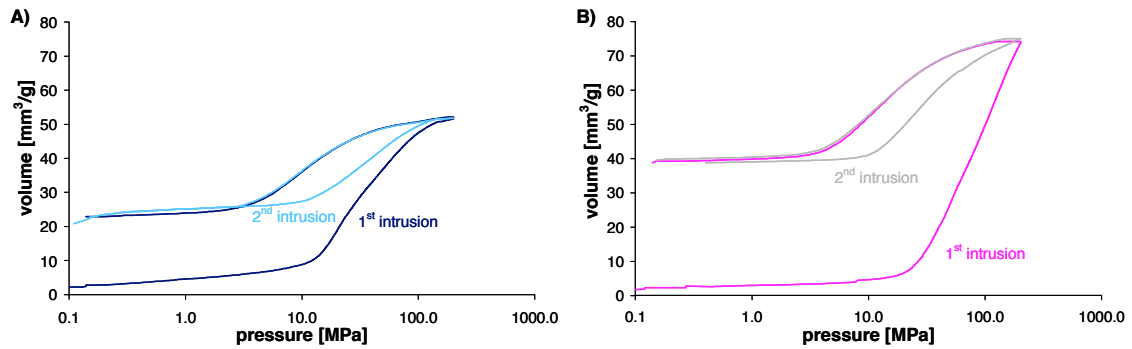| cement	1. Intrusion		2. Intrusion	
	Tot. Cum. Vol. [mm^3/g]	Total porosity [%]	Tot. Cum. Vol. [mm^3/g]	Total porosity [%]
CEM I	63.40	13.7	33.72	7.3
CEM I + 2% gypsum	64.68	13.4	31.94	6.6
CEM I + 6% SF	63.69	13.3	28.03	5.9
CEM I + 12% SF	50.12	10.6	21.28	4.5
CEM I HS	63.66	13.6	32.62	7.0
CEM II/A V-LL	66.95	14.2	35.08	7.4
CEM II/B V-LL	68.37	14.8	33.77	7.3
CEM III/B	73.98	15.8	36.25	7.7
CEM III/C	78.44	16.6	38.02	8.0

Figure 30: Relationship between the mercury volume and the applied pressure for A) CEM I and B) CEM III/B mortar, before sulfate exposure

The pressure that needed to be applied to increase the used mercury volume significantly was higher for CEM III/B mortar than for the CEM I mortar, indicating a refined pore structure for the slag blended mortar. Figure 30 shows that the same total pore volume is assessed for the two intrusion cycles and indicates that no severe changes in the microstructure occurred. The hysteresis of the second intrusion cycle can be explained by the different contact angles of advancing and retracting mercury during testing [136].

Image Analysis

The samples for IA were prepared exactly like for the SEM/EDS analysis (section 3.4.3.4). Cross sections were cut, vacuum impregnated with epoxy resin, polished, and coated with carbon to obtain BSE micrographs.

The set-up of the micrograph acquisition was exactly as described for SEM and BSE analysis (section 3.4.3.4). BSE image analysis was used to determine the amount of unreacted slag, fly ash as well as the amount of coarse porosity. The technique uses grey level histograms and morphological segmentation to determine the different phases observed in a BSE image [32, 137]. The grey level in the backscattered electron images depends on the average atomic number of the examined area [138]. Unreacted slag or clinker particles appear in bright, hydrates appear grey and the pores appear black. The degree of reaction of the anhydrous slag or fly ash was determined by comparing the anhydrous SCM content in the hydrated pastes with the known, initial volume in the unhydrated paste. The uncertainty is high for fly ash blended cements (certainly in the range of $\pm$ 5 -10 percent (Table 15), which is why these values were not used for the thermodynamic modelling). Fly ash blended samples are generally difficult to segment because the fly ash particles display similar grey values as cement hydrates. The use of morphological filter is therefore required. Most investigated binders did not require the use of morphological filters, the mortars based on CEM I and CEM III cement. The process of image analysis for fly ash blended cements was described by Ben Haha et al. [32] in detail.

Table 15: Results of image analysis on mortars <u>before</u> sulfate exposure; standard deviation approx. ± 2%

cement	coarse porosity	C-S-H	portlandite	anhydrous	degree of hydration
	[%; normalized to cement paste]				
CEM I	14	62	18	6	83
CEM I + 2% gypsum	12	61	19	8	77
CEM I + 6% SF	9	85	1	5	85
CEM I + 12% SF	5	91	1	4	89
CEM I HS	16	65	8	11	70
CEM II/A	22	49	1	5 / *23 (FA)**	72 / *1 (FA)**
CEM II/B	28	58	4	4 / *6 (FA)**	75 / 53 (FA)*
CEM III/B	11	65	1	1 / *22 (slag)**	100 / *10 (slag)**

* second number applies to the supplementary cementitious material

Discussion of the Results of the Different Techniques

General Remarks

In this section, the porosity data obtained by MIP, IA and water conductivity measurements are compared with the progress of the ettringite front, and some observed length changes. However, porosity data were obtained for the initial conditions after 28 days curing, before sulfate exposure. It was not the objective of this work to characterize the on-going changes in the pore size distribution or total pore volume during sulfate exposure, although this type of information would be very useful. The presented data is therefore rather a base for discussion than a comprehensive study of the pore structure and the related transport aspects.

The permeability/diffusivity and the distribution of pore space in the microstructure are crucial for the progress of deterioration because the sulfates penetrate the samples slower than the mineralogical changes occur. Especially since the theories of developing crystallization pressures include always the confinement as a necessary condition [7, 9-11, 73]. Generally it is assumed that a low permeability is beneficial for the sulfate resistance of cementitious binders [40].

Comparison of the different porosity data sets

Selected results of MIP, water conductivity and IA are summarized in Table 16. The data shows that the total porosities as obtained by water conductivity measurements and MIP show little variation, with the values of the water conductivity are larger. The values for the coarse porosity as obtained by IA provide more variability, in a similar range as the water conductivity measurements. All samples were cured for 28 days, which is a relatively short curing time for slag and fly ash blended cements as these SCM's react slowly.

The values for the water conductivity allow the separation of the different mortar samples according to their water transport properties during sample conditioning providing that sufficient water penetrated the samples. The data suggests that the mortars made from silica fume and slag blended cements have much lower water conductivity than the CEM I based mortars, which corresponds to empirical knowledge. However, the values are so close for the two silica fume and the two slag blended cements that the water permeability is so low that it does not really allow to separate the different mortars. Therefore it is difficult to compare the data between the different techniques:

- The capillary porosity as determined by water conductivity does not compare with the different water conductivity values (permeability). The very small variability of the capillary porosity does not relate to a similar permeability. For example the CEM I mortar has almost the same capillary porosity as the CEM I blended with 6 percent silica fume but the measured water conductivity is reduced significantly for image analysis if silica fume was used.

- The water conductivity porosities do not relate to the total porosities obtained by MIP. This is especially evident for the slag blended mortars for which low water conductivities were observed, but the total porosity, as determined by MIP, is much larger for the CEM III/B mortar than for the CEM I mortar (Table 16), which corresponds well with the lower bulk density of the mortars.

- The capillary pore content obtained from the water conductivity measurement corresponds relatively well to the coarse porosity from IA.

Table 16: Overview of the porosity and transport related data from water conductivity, MIP, and IA of samples cured for 28 days; before sulfate exposure, (*n.m.*) not measured;

(*) ink pores are equivalent to the trapped mercury in the samples and include potentially air voids

Method	Water Conductivity (WC)			ink pores (*combined*)	MIP		Image Analysis
	Conduct.	*total p. – air voids*	capillary p.	*ink p. (**MIP**) – air voids (**WC**)*	total p.	*ink pores**	coarse porosity
	[g/(m²h)]	**[vol%]**	**[vol%]**	**[vol%]**	**[vol%]**	**[vol%]**	**[vol%]**
CEM I	31	*17.1*	12.9	*4.8*	13.7	*6.4*	14
CEM I+CH_2	29	*18.0*	13.5	*5.1*	13.4	*6.8*	12
CEM I+6% SF	4	*19.7*	13.0	*2.8*	13.3	*7.5*	9
CEM I+12% SF	5	*20.7*	12.5	*2.0*	10.6	*6.1*	5
CEM I HS	27	*18.8*	14.6	*5.5*	13.6	*6.6*	16
CEM II/A	35	*19.4*	15.9	*6.2*	14.2	*6.8*	22
CEM II/B	n.m.	*n.m.*	n.m.	*n.m.*	14.8	*7.5*	28
CEM III/B	5	*20.8*	10.8	*6.4*	15.8	*8.0*	11
CEM III/C	4	*20.8*	10.7	*6.9*	16.6	*8.5*	n.m.

Comparison of the Porosity Data and Progressing Ettringite Fronts

The water conductivity values provide a similar assessment of sulfate transport in the different mortars as the observed ettringite formation depths (Table 16). The water conductivity is high for the CEM I based mortars (CEM I, CEM I +2 percent gypsum, CEM I HS) and the CEM II/A mortar. The water conductivity was not investigated on CEM II/B mortar because of bleeding during samples production and the slow reaction of the fly ash, which also explains the high initial sulfate penetration in for this mortar. High sulfate penetration depths were observed for all mortars with high water conductivity values, especially after larger expansions were observed.
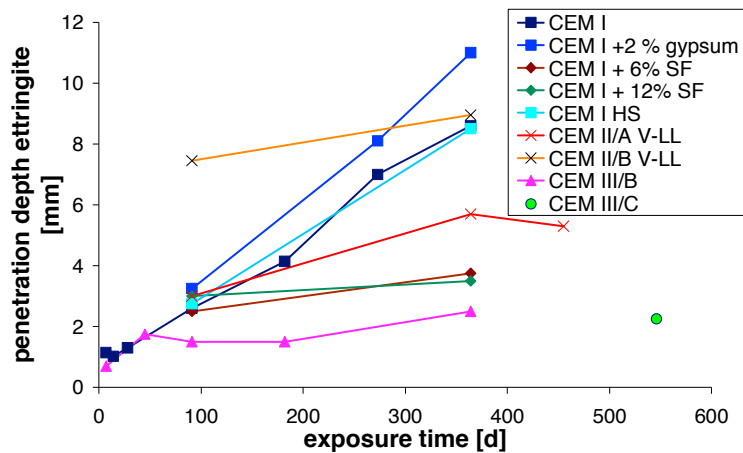
Figure 31: Development of the maximal ettringite formation depth with time for the different cement mortars; penetration depth approx. ± 0.2 mm

The mortar bars with low water conductivity, made with CEM I with silica fume addition and slag blended cements, display small ettringite penetration depths. The actual value of the water conductivity cannot directly be used to separate the different binders directly as water conductivity is identical for the two silica fume mortars and the two slag blended mortars. Altogether, the water conductivity provides a good first approximation of the permeability of the samples.

The total porosities provided by MIP measurements do not provide a good insight as the largest total porosities were observed for the slag blended mortars, which rather shows that the total porosities are not the relevant quantity and that the actual pore structure and connectivity are the important parameters.

Changes in Pore Size Distribution during Curing

Figure 32 shows that the mortar prepared with CEM II/A cement showed almost no expansion during the first year of sodium sulfate exposure after additional curing (19 months in total). That additional curing is beneficial for CEM II/A mortar is expected as the fly ash reaction is slow.
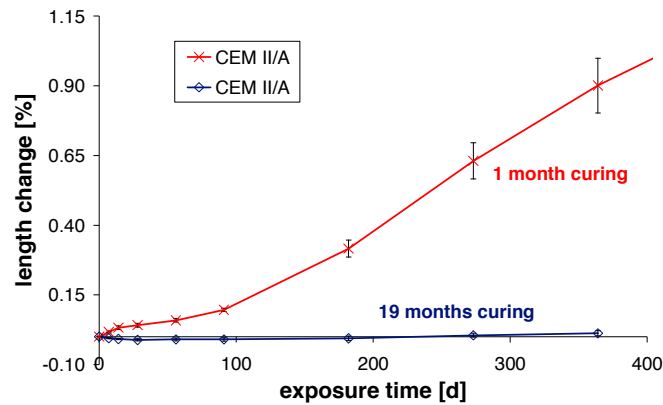
Figure 32: Linear expansion of CEM II/A mortars tested with sodium sulfate solution at 20°C after curing for one and nineteen months in saturated lime solution

The permeability after one month curing was initially high. MIP results indicate that the total porosity did not change much during the additional curing time of 19 months (Figure 33A). The pore structure was refined during the additional curing (Figure 33B). More small pores, smaller than 10-20 nm and less large pores, of up to few hundred nanometre pore radius, were calculated based on the MIP measurements.

The pore radii were calculated from the data obtained by the second intrusion cycle to describe the connected porosity, excluding the ink pores and air voids which trap mercury (see Figure 33A).
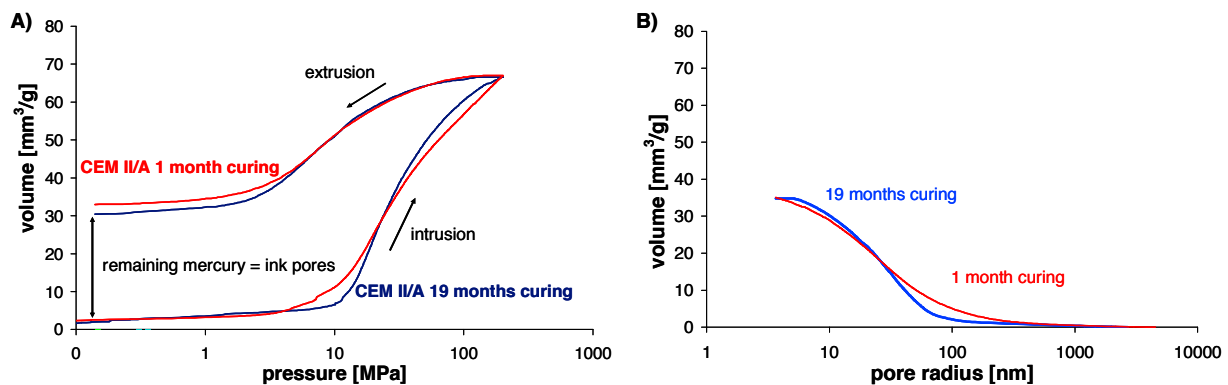
Figure 33: A) comparison of the first mercury intrusion for the CEM II/A mortar after different curing times and B) the corresponding cumulative volume to pore radius as obtained from the second intrusion to obtain the pore size distribution of the connected pores by excluding ink pores

Which Pore Size Controls the Connected Pore Network?

The distribution changes of the calculated pore radii of the connected pores as determined from the second intrusion are shown in the following graphs. The volume for the CEM II/A and the CEM I mortar are displayed in Figure 34. The CEM II/A microstructure of the connected pore network was refined for pore radii larger than 50 nm, and an increased amount of pores between 20 and 50 nm was observed (Figure 34A). During the same time only small changes were observed for the CEM I mortar (Figure 34B).
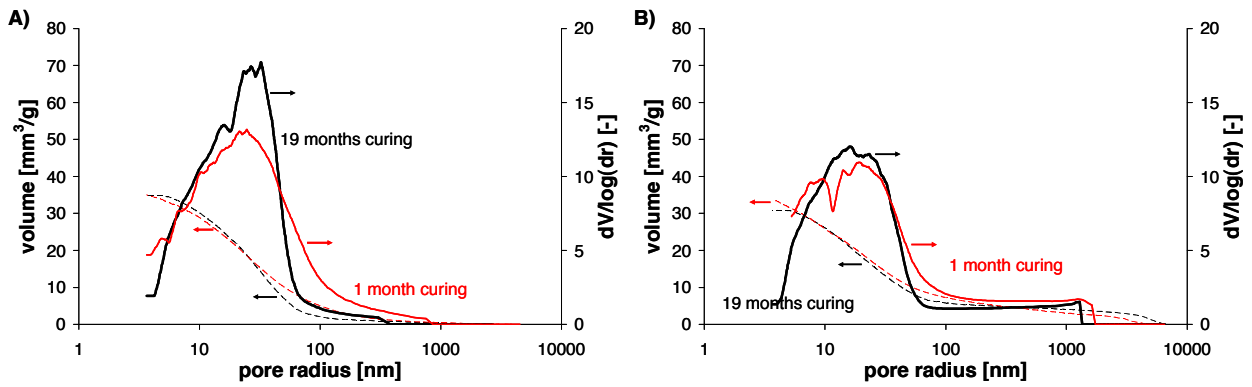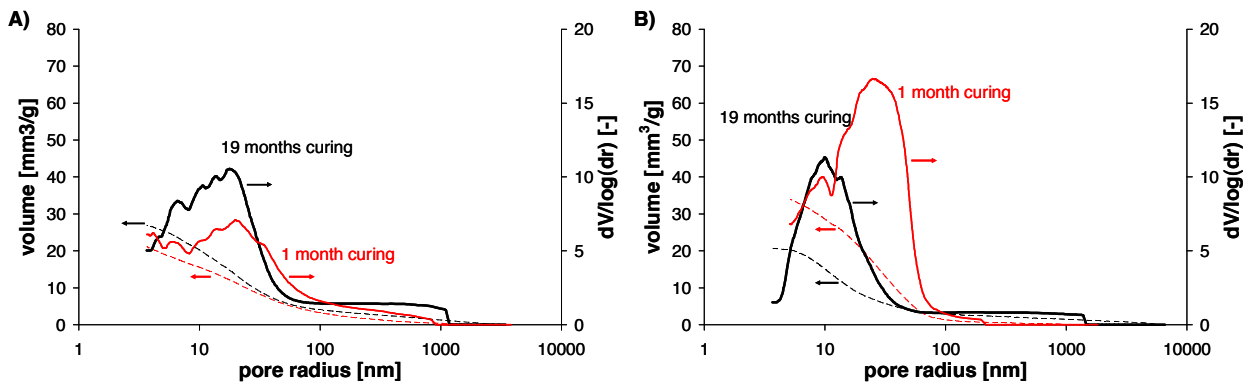
Figure 34: Changes in the pore radius distribution displayed as cumulative and derivative curve of A) CEM II/A and B) CEM I mortar with time

The changes in pore size distribution of the calculated pore radii and the volume for the CEM I +12 percent silica fume and the CEM III/B mortar with curing are displayed in Figure 35. Both binders display a clear refinement of the connected pore network during additional curing, with the most volume being contributed by pores with calculated radii below 20 nm. This suggests that the pore network is very fine and slow transport should be expected for the CEM III/B and CEM I + 12 percent of silica fume. This corresponds well with the low water conductivity for these mortars.

Figure 35: Changes in the pore radius distribution displayed as cumulative and derivative curve of A) CEM I + 12 percent silica fume and B) CEM III/B mortar with time

The pore entrances of pores in which stressed crystals grow needs to be smaller than the pore itself to maintain a sufficiently high degree of supersaturation [11, 73]. These pores could be thought of as ink bottle pores. The volume of mercury in MIP tests, which remains in the sample after the first intrusion, could indicate the total amount of these ink bottle pores, but this volume could also contain mercury trapped in air voids, an approximation of the ink pores (by MIP) without air voids (by water conductivity) has been included. However, the combination of data seems to relate not so well with the observed expansions or ettringite penetration as the lowest amount of "corrected" ink pores would be assigned to the silica fume blended mortars while the highest amount is assigned to the slag blended mortars, which displayed even less length changes than the silica fume blended mortars.

Potentially not all of pores allow the nucleation and growth of crystals due to space or thermodynamic constrains. Locher [113] suggested that the microstructure of slag blended cements could be too fine to allow the formation of ettringite, unfortunately without providing data. Wilcox [79] stated that the particle size of a crystal could be a barrier for nucleation depending on the surface energy of the particle small particles. The

minimal pore diameter cannot be smaller than the width of an ettringite needle (unit cell) plus space to maintain a solution layer that fills the distance towards the surface of the pore. The maximal distance of an ettringite unit cell is determined as 1.94 nm based on data from Rietveld refinement of synthesized ettringite crystals [78].

Additionally, the influence of present sulfates and the availability of calcium and aluminium in solution as well as the on-going hydration are not considered and the following aspects could additionally affect the distribution of potential sites to generate crystallization pressure base on the porosity measurements:

- A part of the trapped mercury is located in bigger pores, which do not contribute to the expansion, while potentially consuming supersaturation in unconstrained crystal growth, which is difficult to assess.

- The connectivity/percolation in the pore structure are important to maintain the supersaturation during growth and pressure development. An open pore structure can help consuming supersaturation of small crystals due to the growth of larger, thermodynamically more stable, crystals in large pores and air voids.

Additional MIP Data
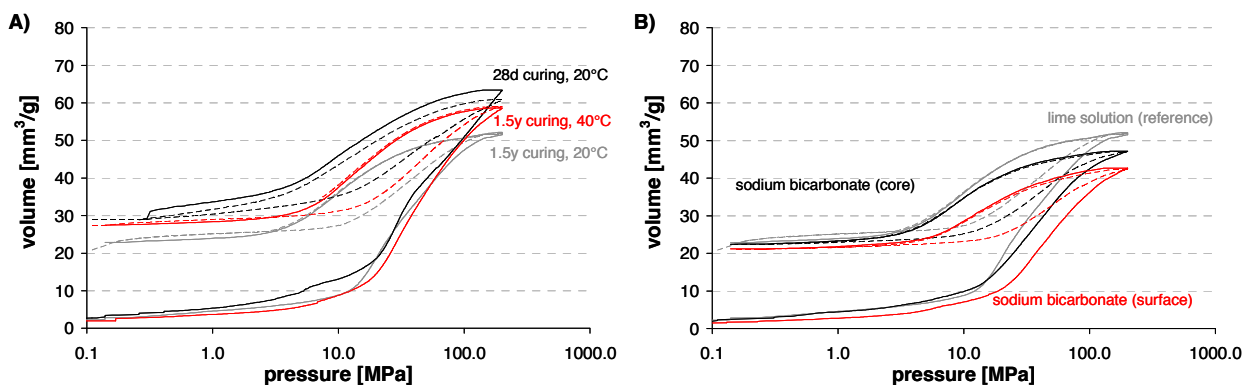
Figure 36: Intrusion and extrusion branches of the first and second MIP cycle of CEM I mortar bars A) cured in lime solution at 20°C and 40°C and B) surface and core parts of a sample exposed to sodium bicarbonate solution
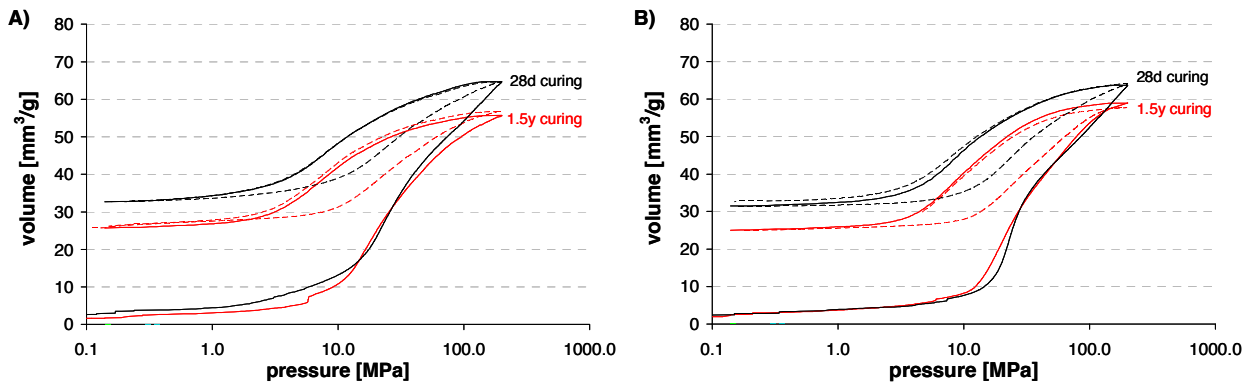
Figure 37: Intrusion and extrusion branches of the first and second MIP cycle of A) CEM I +2% gypsum mortar bars and B) CEM I HS mortar bars cured in lime solution
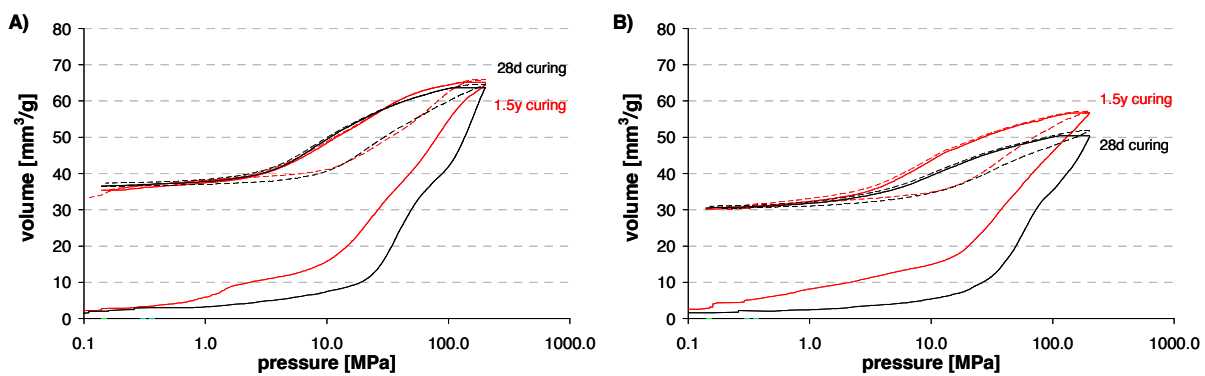

Figure 38: Intrusion and extrusion branches of the first and second MIP cycle of A) CEM I +6% silica fume mortar bars and B) CEM I +12% silica fume mortar bars cured in lime solution
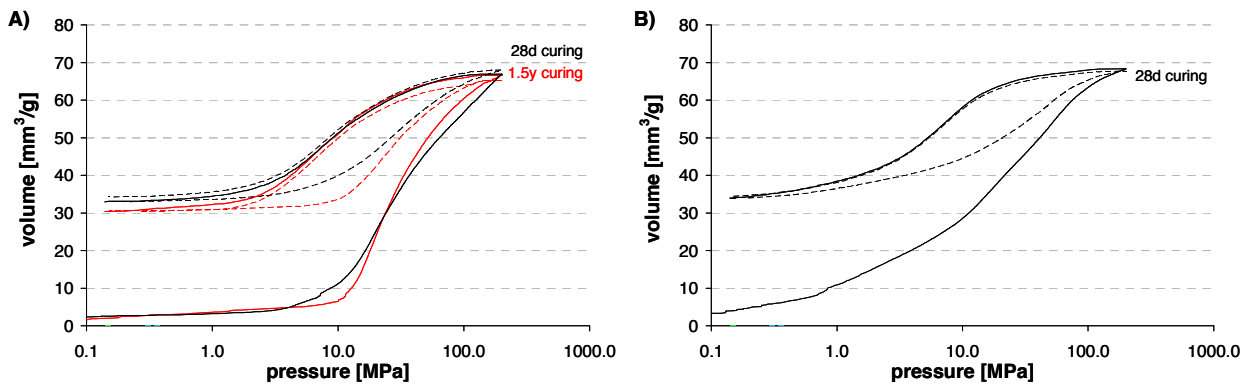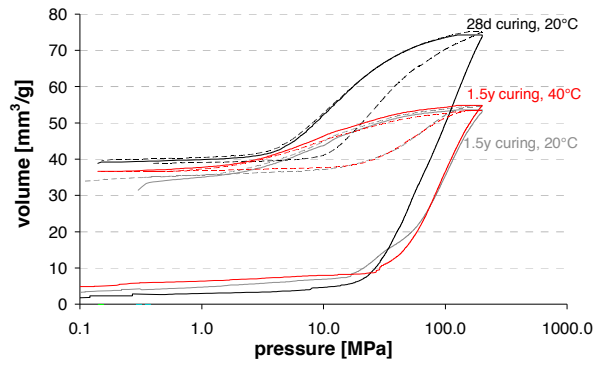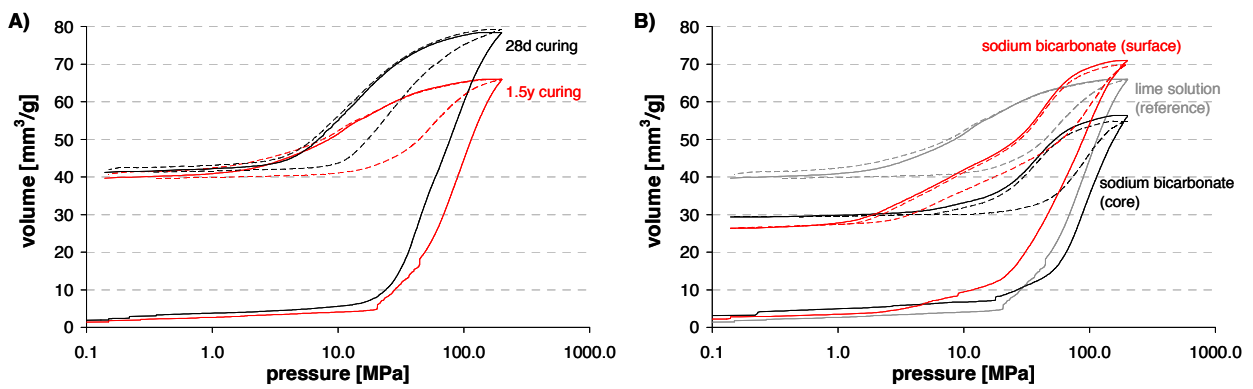

Figure 39: Intrusion and extrusion branches of the first and second MIP cycle of A) CEM II/A mortar bars and B) CEM II/B mortar bars cured in lime solution

Figure 40: Intrusion and extrusion branches of the first and second MIP cycle of CEM III/B mortar bars cured in lime solution at 20°C and 40°C

Figure 41: Intrusion and extrusion branches of the first and second MIP cycle of CEM III/C mortar bars A) cured in lime solution and B) surface and core parts of a sample exposed to sodium bicarbonate solution

6.7 Sodium Sulfate Solutions - Additional Aspects

6.7.1 Ionic Transport and the Influence of the pH Value of the Test Solution

During ionic exchange between the test solution and the sample, sodium and sulfate are expected to penetrate the cementitious matrix, and ions with a high solubility, like potassium, might leave the sample.

Figure 42 illustrates the loss of potassium, expressed in K_2O profiles, for the CEM I and CEM III/B mortar bars exposed to sodium sulfate. The initial K_2O content of the unhydrated cements was similar; 0.9 for the CEM I and 0.7 for the CEM III/B. The distribution of the potassium oxide was heterogeneous during the first few weeks in the CEM I mortar bars. The comparison of the profiles at different times shows that of the potassium oxide was leached almost completely from the CEM I mortar between 91 and 182 days of exposure (Figure 42A). The expansion rate was also increased during the same period. It cannot be concluded from the presented data whether there is a direct link between the leaching of potassium and the observed expansion. However, the depletion of potassium in the profiles illustrates that the potassium transport in the pore solution is faster than the sulfate binding. The transport varies considerably between different ions.

The potassium oxide is more equally distributed in the mortar bars made with CEM III/B and changes little with time (Figure 42B), CEM III/B mortars have refined microstructures and C-S-H phases with lower Ca/Si ratios. C-S-H with a reduced Ca/Si ratio binds more alkali than calcium rich C-S-H [33]. This effect might contribute to a better distribution and binding of potassium.
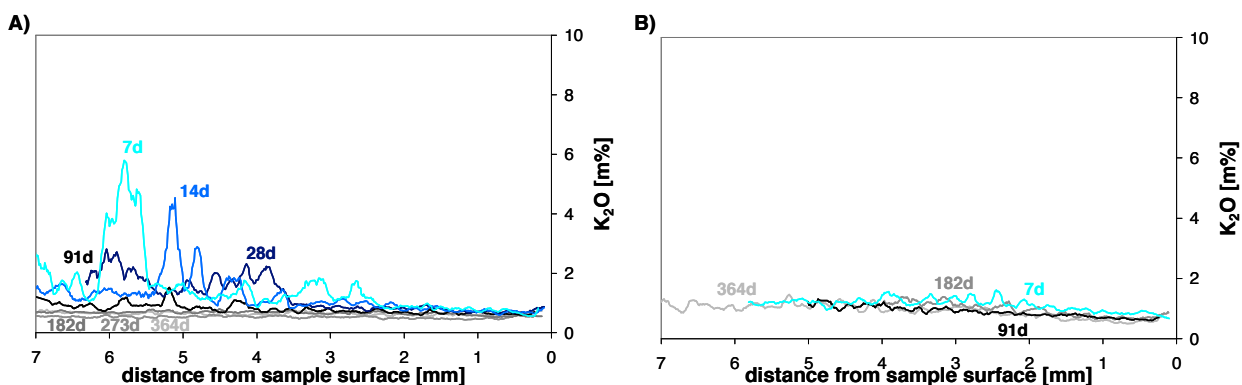

Figure 42: K_2O profiles of A) CEM I and B) CEM III/B mortar bars exposed to sodium sulfate solution for exposure times between 7 days and one year

High alkali concentrations increase the pH, sulfate and aluminium concentration of the pore solution but reduce the calcium concentration, which could affect the supersaturation of the pore solution with respect to ettringite [139]. The reduction of expansion at higher pH values could also be due to the increase of aluminium concentrations [140], which can affect the location where ettringite could nucleate and grow. A higher aluminium concentration in the pore solution could also increase the oversaturation with aluminate phases, depending on the other phases present in solution.

Bellmann et al. [88] increased the pH of the testing solution by NaOH addition and observed a reduction of expansion. A similar observation has been observed for delayed ettringite formation. Famy et al. [81] showed for cases of delayed ettringite formation that the expansion of mortar bars increased when leaching of alkali occurred during storage time. Expansion was greatly reduced in KOH solution [81].

Flatt and Scherer [9] used an expression to investigate the influence of hydroxide on the supersaturation of the pore solution with respect to ettringite for delayed ettringite formation. The equation employs also the solubility products (K_{s0}) of monosulfate and portlandite:

$$IAP_{AFt(AFm,CH)} = K_{s0\_AFm}K_{s0\_CH}^2 \frac{\{SO_4^{2-}\}^2\{H_2O\}^{20}}{\{OH^-\}^4}$$

The equation shows that an increase in pH will reduce the supersaturation of the pore solution with respect to ettringite for a solution in equilibrium with monosulfate and portlandite. The interpretation is consistent with the reported experimental data.

Fernàndez-Altable et al. [115] suggested that the deterioration of slag blended mortar bars is reduced by frequent solution exchange compared to tests in which the solution were not exchanged and higher pH values were maintained throughout the experiments. The difference in deterioration was assigned to a higher hydroxide activity in the general ionic activity product for ettringite:

$$IAP_{AFt} = \{Ca^{2+}\}^6\{Al(OH)_4^-\}^2\{SO_4^{2-}\}^3\{OH^-\}^4$$

Slag blended cements do not contain much portlandite at high substitution levels, which does not allow to use the previously used ionic activity product for ettringite ($IAP_{Aft(AFm,CH)}$) that has been used for CEM I binders in equilibrium with monosulfate and portlandite but limits also the pH of the test solution as less hydroxide can be released by the binder. Cao et al. [107] reported that slag blended cements were more severely affected by changes in pH value than CEM I based binders.

6.7.2 Influence of Specimen Size

Curing, Temperature and Size Effects

Figure 43 shows the different maximum ettringite and gypsum penetration depths compared with the observed length change of the time of observation. Several sizes of the CEM I mortar bars included, which requires the change to relative penetration depths.

The data shows that small relative penetration depths, < 20 percent penetration for ettringite and < 10 percent for gypsum, result in small length changes. This confirms the general understanding that a very dense and impermeable binder performs better in a sulfate environment [40].

The relation between the length changes and penetration depth are different for ettringite and gypsum for larger penetration depths. The relation between ettringite penetration depth and observed length changes is complex (Figure 43A). The observed values for mid-size mortar bars (2.5 x 2.5 cm^2) are connected with a line and show that a consistent trend is observable. This trend is affected by the different exposure and curing conditions and by size effects.

The gypsum development seems to follow one trend, contrary to the ettringite, for the different sizes, curing times and temperature (Figure 43B).
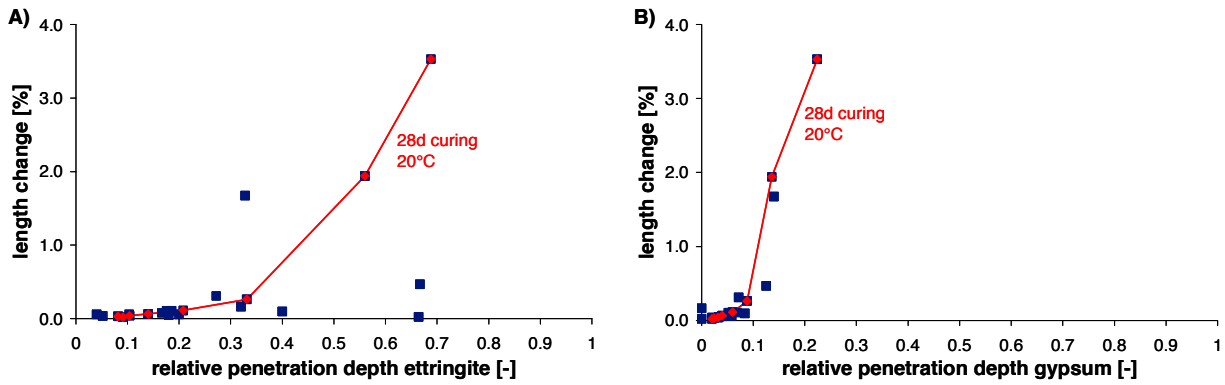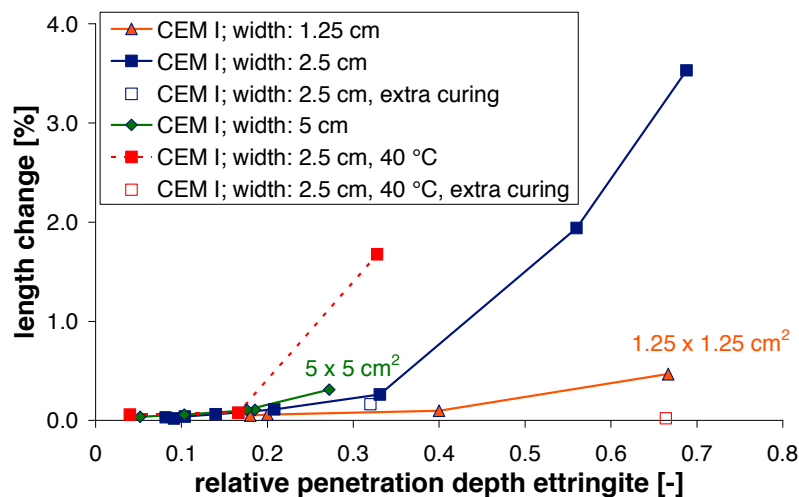
Figure 43: Comparison between measured length changes and relative A) ettringite and B) gypsum penetration depths for CEM I mortar bars exposed to sodium sulfate after different curing times and different temperatures; red line connects the observed properties for samples cured for 28 days and exposure at 20°C (2.5 x 2.5 x15 cm^3)

Figure 44 provides more details for the effects of the different curing and exposure condition on specimen of different sizes with respect to ettringite. The observed length changes are lower with decreased sample width. Exposure at 40 °C increases the observed expansions while curing at 40°C before sulphur exposure reduces the observed expansion. This shows that the observed macroscopic changes, using the same cement and sulfate solution, depend on the sample size, curing history and test conditions and might only be compared if most of these parameters are identical.

Figure 44: Comparison between measured length changes and relative ettringite penetration depths for CEM I mortar bars exposed to sodium sulfate after different curing times and conditions; triangles indicate samples with cross sections of 1.25 x 1.25 cm^2, squares indicate samples with cross sections of 2.5 x 2.5 cm^2, diamonds indicate samples with cross sections of 5 x 5 cm^2; full samples represent samples cured for 28 days and empty symbols represent samples cured for 25 months

Sulfate Binding

Figure 45A displays the penetration depth of ettringite over time for CEM I mortar bars of different sizes and at different temperatures. The ettringite penetration depth is similar for the two larger sample sizes at 20°C (green and blue data). The observed penetration seems to be somewhat higher for the early exposure to sodium sulfate solution at 40°C. The ettringite penetration is higher for the smallest prisms at 20°C most likely due to the sample preparation procedure, as the prisms stayed for several hours in a 95 percent relative humidity chamber before sulfate exposure while the glue for the measurement pins hardened. During this time the samples dried slightly, which could have accelerated the sulfate penetration once the samples were immersed into sulfate solution.

Figure 45B shows the development of the gypsum penetration depth with time. The graphs show that the gypsum precipitation was similar for all specimen stored at 20°C while the gypsum precipitation was slightly accelerated for the 40°C samples. The increase of gypsum precipitation of gypsum might be due to increased diffusion rates, chemical reactions rates or both.
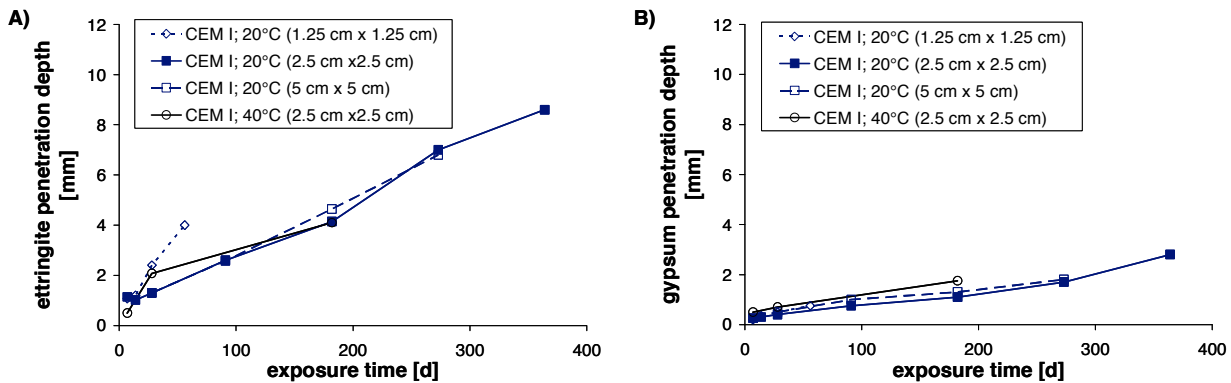

Figure 45: Development of the maximal A) ettringite and B) gypsum penetration depth with time for CEM I mortar prisms of different sizes and temperatures (20°C and 40°C); penetration depth approx. ± 0.2 mm

Length Changes and Dynamic E-Modulus

Figure 46A shows that mortar specimen of different sizes made with the same cement display different expansion behaviours. The smaller the samples are, the faster they expand. The width of the specimen doubles between the different specimen dimensions (1.25 cm, 2.5 cm, and 5 cm), the volume increases with a factor of four and the surface to volume ratio decreases with increased width. The volume ratio of the samples and the sulfate solution is constant at 20.

The geometrical aspect should favour the resistance of bigger samples due to a reduced surface to volume ratio, which could limit the interaction of the sample and the solution. Figure 46 shows that the penetration rate is similar for the different sample sizes. More time is therefore required to penetrate similar volume fractions of the larger specimen. The different expansions times and rates depend on transport and mechanical processes.

Measuring the dynamic E-modulus is a destruction free method to obtain data about the structural integrity of the specimen by determining a stress strain relation from measurements of resonance frequencies of propagating sound/ultrasound waves. The dynamic E-modulus increased at the beginning of the test for samples that are cured for one month (Figure 46B). In section 0 it is shown that the increase of dynamic E-modulus is not observed in mature samples that are exposed to sodium sulfate solution. This suggests that the on-going hydration in relatively young samples is responsible for the increase in dynamic E-modulus and not the late ettringite formation due to sulfate ingress.
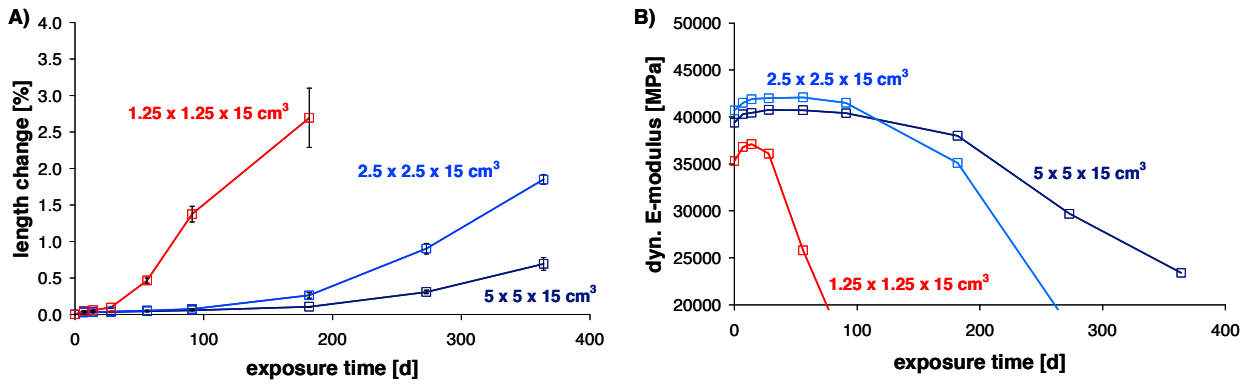
Figure 46: Development of the A) length changes and B) dynamic E-modulus over time for three different sizes of CEM I mortar bars at 20°C

A comparison of Figure 46A and B shows that the reduction of the dynamic E-modulus is inverse proportional to the observed length changes. An increase in length change is accompanied by a reduction of dynamic E-modulus, which illustrates that the expansion is a useful indicator for internal damage.

6.7.3   Influence of Exposure Temperature

CEM I

The observed length changes are larger for the samples cured at 40°C (Figure 47). The thermodynamically predicted phase assemblages and volume changes are very similar.

The temperature increase could have effects that reduce the expansion, like the increase of ettringite solubility [86, 141] and potential reorganization of the pore structure towards larger pores. The reason for the increased expansion should therefore be found in increased reaction rates of chemical processes, as can be approximated by the Arrhenius equation:

$$k = Ae^{-\frac{E_a}{RT}}$$

where k is the rate constant of the chemical process, A is an empirical factor, E_a is the activation energy of the chemical process, R is the molar gas constant, and T the temperature,

The diffusion related transport should not be affected significantly. For illustrational purposes Fick's first law can be used. Fick's first law states that the diffusion flux (J_i) of each species i is inversely proportional to the temperature:

$$J_i = -\frac{Dc_i}{RT}\frac{\partial\mu_i}{\partial x}$$

where D is the diffusion coefficient, c the concentration,   the chemical potential and x is the diffusion length. The temperature dependence of this expression is offset by the temperature dependence of the diffusion coefficient of charged particles (Einstein relation):

$$D = \frac{\mu_q k_B T}{q}$$

where $_q$ the electrical mobility of the charged particle, k_B is the Boltzmann constant, and q is the electrical charge of the particle. Using the relation of the molar gas constant and the Bolzman constant,

$$R = N_A k_B$$

where N_A represents the Avogadro constant. Fick's first law can then be written as expression that does not directly depend on the temperature:

$$J_i = -\frac{\mu_q c_i}{N_A}\frac{\partial \mu_i}{\partial x}$$
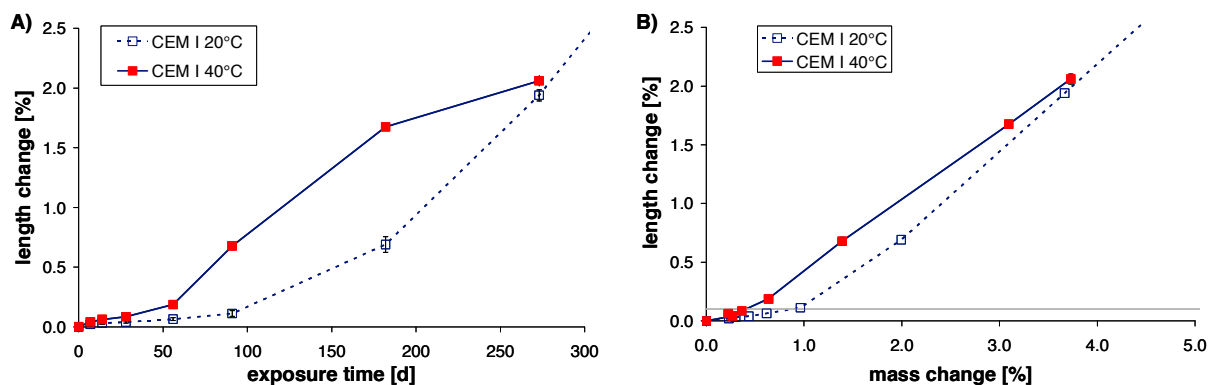
Figure 47: A) Linear expansion and B) relation between mass and length changes of CEM I mortar bars during exposure to sodium sulfate solution at 20°C and 40°C

Figure 47B shows the relationship between the mass uptake and length changes for the CEM I mortar bars for the exposure temperature of 40°C. The CEM I mortar bars expand at 40°C almost with a constant relation between length and mass changes. Less mass was taken up during the first few weeks of exposure compared to the samples stored at 20°C.

CEM III/B

The CEM III/B mortar bars display at 40°C storage also almost no length changes and lose mass continuously due to calcium leaching (Figure 48A). The mass loss is due to calcium leaching (Figure 48B). The leaching is not observed
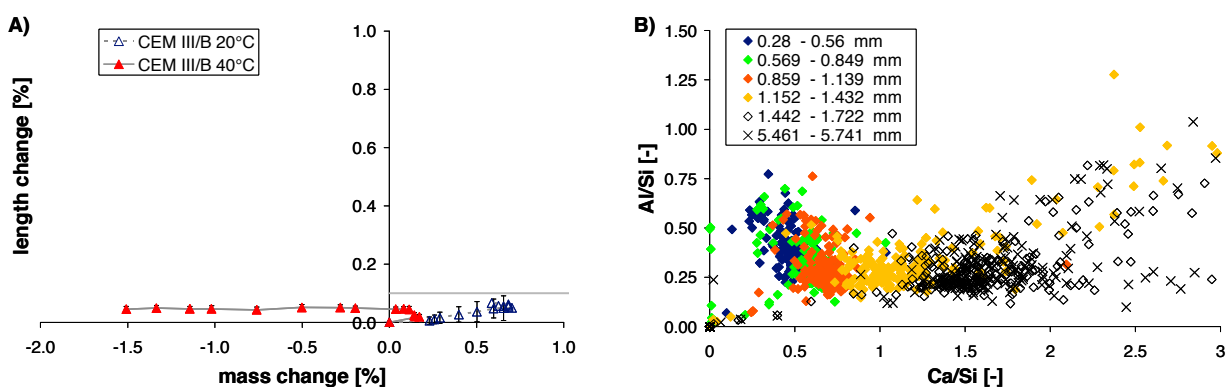
Figure 48: A) Mass uptake to length change relation changes for the CEM III/B mortars when the sulfate exposure temperature is changed from 20°C to 40°C and B) changes in the Al/Si to Ca/Si ratios with depth for the CEM III/B mortar exposed to sodium sulfate solution for 637 days at 40°C

6.7.4   Effect of Prolonged Curing

Length Changes

Mortar bars made from all CEM I cements and the CEM II/A cement were exposed to sodium sulfate after 25 months of curing of the mortar bars in saturated lime solution. The recorded length changes are displayed in Figure 49. The additional curing led to faster expansions. Similar results have been obtained by Ferraris et al. [71]. Taylor et al. [82] discussed a similar phenomenon for delayed ettringite formation.

The CEM II/A mortar showed only small expansion compared to the samples cured for 28 days,. For the CEM II/A mortar additional curing was beneficial, several mechanisms seemed to overlap. Additional curing time should refine the pore structure, which appeared to accelerate the expansion for the other mortars. The fly ash mortar bars were bleeding during sample preparation, which provides a better connected pore structure which might help to consume supersaturation by facilitating recrystallization of crystals in unconfined spaces.
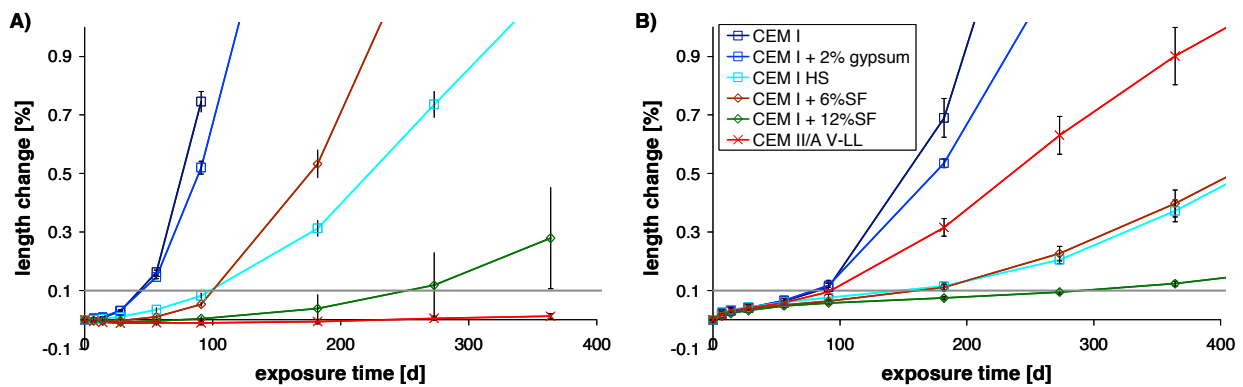
Figure 49: Length changes of mortar bars made from different cements tested with sodium sulfate solution at 20°C after A) curing for additional two years and B) the length changes of the reference mortars cured for 28 days in saturated lime solution

Initial Swelling

The initial swelling at the beginning of the exposure period was reduced. After 28 days curing all mortar prisms were exposed to a 95% relative humidity environment in which the specimen could dry slightly for a few hours, while the glue for the measurement pins hardened, before the measurements started. The loss of pore solution due to slight drying facilitated the ingress of sulfate solution and swelling occurred during exposure to sulfate solution. The longer cured samples had already pins and needed no additional preparation time in which drying could occur.

Figure 50 shows exemplary the length changes in the first 50 days of CEM I mortars cured for 28 days and 25 months at 20°C and then exposed to sodium sulfate solution at 20°C in blue and the mortar cured for 28d at 20°C, additional 24 month curing at 40°C in saturated lime solution with consecutive immersion into sodium sulfate solution at 40°C. The swelling during the first weeks was reduced to a minimum for the additionally cured samples. The quick transition between curing and sulfate exposure allowed no drying of the samples.
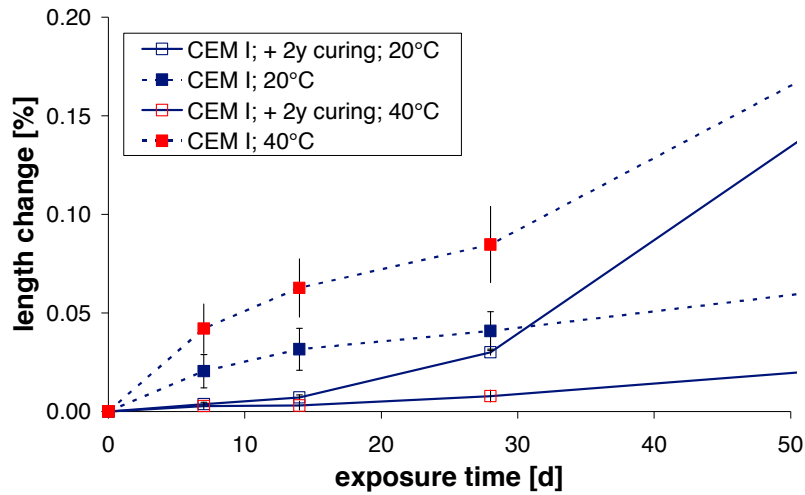
Figure 50: Early age linear expansion of the CEM I tested with sodium sulfate solution at 20°C and 40 °C with curing times of 1 month (solid lines) and 25 months (dashed lines)

Effect of Prolonged Curing at 40°C

Length Changes

The temperature of curing and sulfate exposure has a strong influence on the linear expansion of the mortar bars. Samples cured at 20°C for 28 days but exposed at 20°C and 40°C expand differently (Figure 51). The faster expansions of the samples cured for 28 days and, exposed to 40°C sulfate solution should be influenced by faster chemical reactions. The ettringite solubility is increased at higher temperatures [86, 142, 143], the increased solubility and accelerated reaction rates should reduce a possible supersaturation.
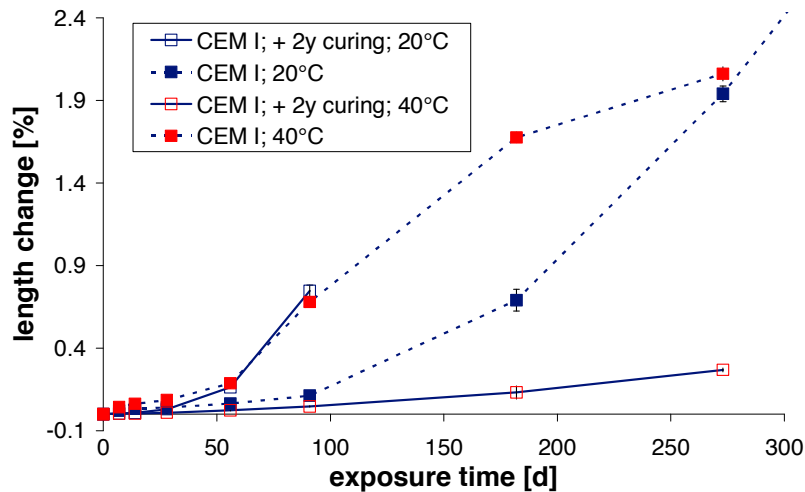
Figure 51: Linear expansion of the CEM I tested with sodium sulfate solution at 20°C and 40 °C with curing times of 1 month (dashed lines) and 25 months (solid lines)

However, if the samples are cured for two additional years at 40°C in saturated lime solution little expansion is observed after exposure to sodium sulfate solution. This is due to interaction of several aspects:

- Change in transport properties due to changes in the pore structure; coarsening of pore structure and higher permeability [144, 145] which might also affect the pores which could otherwise contribute to the expansion.

- Increase in ettringite solubility.

- Change in mineralogy.

Together, these aspects allow the ettringite to precipitate in spaces where the stress generation does not occur during testing. The thermodynamically predicted phase assemblages and volume changes are very similar for 28 days cured samples. The reason for the different expansion behaviours are therefore more likely to be found in the microstructural changes than in changes in thermodynamic properties; an increased solubility enhances the relocation of crystals into larger pores.

Mineralogical Changes

Figure 52 shows the changes in the phase assemblage during additional curing in saturated lime solution by comparing the phase assemblage before sulfate exposure, which consists of portlandite, C-S-H and AFm phases, with the phase assemblages after two additional years. The phase assemblage changed during curing in saturated lime solution. Monosulfate is destabilized and monocarbonate and ettringite are observed instead. This is unexpected because thermodynamic calculations predict monosulfate. Three potential mechanisms can be involved, i) the recrystallization of small ettringite crystals, which developed during hydration (Appendix A3), ii) the carbonation of sulfate AFm which also stabilizes ettringite [30, 130, 146-149], or iii) calcium leaching could affect the distribution of sulfates in the phase assemblage.
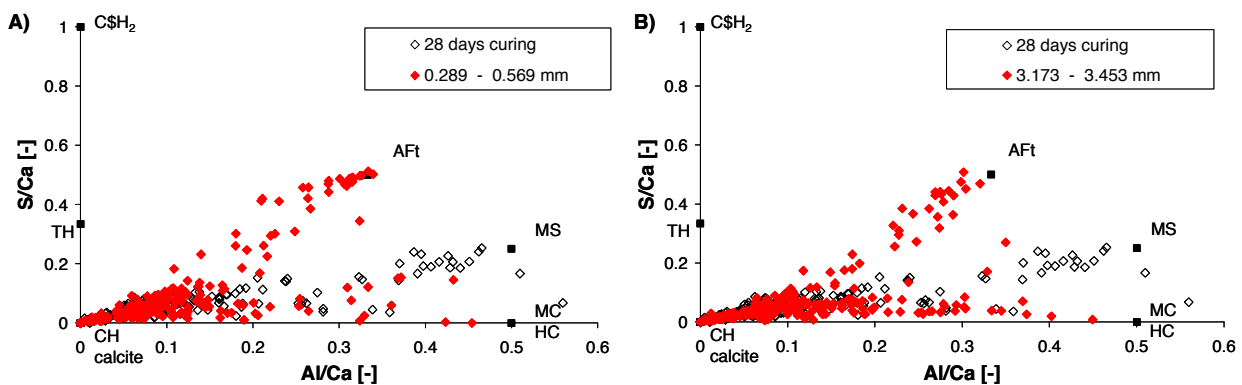
Figure 52: Comparison of the S/Ca to Al/Ca ratios of the bulk phase assemblage of the CEM I mortar bars after 24 additional months of curing in saturated lime solution at A) 20°C (full symbols) and B) 40°C (full symbols) and the reference phase assemblage before additional curing (empty symbols)

Additionally, to the described phase changes are large portlandite crystals leached in surface proximity. This aspect is important because the drop in CaO allows the observation of calcite, which cannot be distinguished otherwise as portlandite and calcite have the same CaO concentrations in EDS analysis (100 percent). Figure 53A shows that the sulfate concentrations are increased in surface proximity due to the stabilization of ettringite in surface proximity, while Figure 53B shows that the portlandite is leached at the surface, visible in the drop of maximally observed calcium concentration.
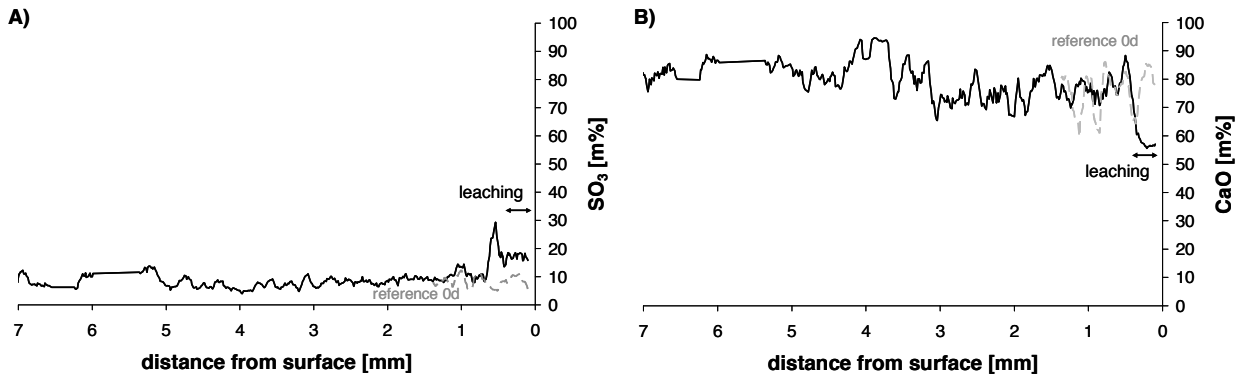
Figure 53: A) sulfate profile and B) CaO profile of CEM I cured for 25 months at 20°C before sulfate exposure

In the next section it will be shown that at longer curing times the mass of the mortar bars reduces after an initial mass gain for the 20°C samples. Portlandite is a very soluble cement hydrate and it has been shown for undersaturated lime solutions that portlandite can be leached over longer curing times [150]. The most likely explanation for the observed leaching is that the used calcium hydroxide used to prepare the lime solution carbonated during the two years of storage or that calcite was formed in the solution during curing. In addition, the pH of a saturated lime solution (approx. 12.5), even without carbonation, is much lower than the pH of the pore solution of mortar (approx. 13.5). Such a reduction in pH in surface proximity increases the calcium solubility and facilitates calcium leaching.

Similar changes are also observed for the samples cured at 40°C for two years (Figure 54). The extent of ettringite stabilization and portlandite leaching is much larger and affects almost the first 3.5 millimetres from the surface (Figure 54A). In surface proximity calcite is observed where the CaO contents increase again significantly (Figure 54B).
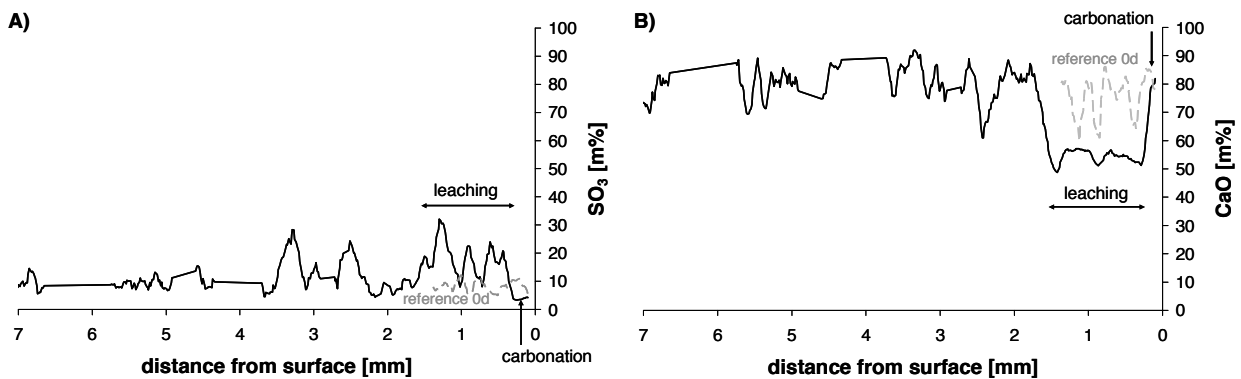
Figure 54: A) sulfate profile and B) CaO profile of CEM I cured for 25 months at 40°C before sulfate exposure

The difference between the curing at 20 and 40°C is the depth to which these changes occur, up to 0.5 mm at 20°C and up to 3.5 mm at 40°C. The increased portlandite leaching is due to increased reaction rates, at higher temperatures. The leaching of portlandite is expected to increase the porosity of the samples [151], which would additionally enhance the progress of portlandite dissolution. As a consequence, the potential to form late ettringite under the elevated temperature is greatly reduced for the samples cured at 40°C, but not completely prevented.

The difference between the two affected zones (0 - 0.6 mm for 20°C; 0 – 3.5 mm for 40°C) suggests that more than 40 percent of the specimen volume was affected additionally by curing at 40°C compared to the 20°C. This reduces the potential to form late ettringite significantly and explains why almost no expansions were observed.

Relation between Mass and Length Changes

Comparing the mass to length changes for the differently cured mortar bars indicates that part of the early mass uptake can be attributed to the on-going hydration. Figure 55 shows a comparison between the mortars made from CEM I and its blends with gypsum and silica fume. It seems that the initial relation between length changes and mass gain due to hydration and sulfate attack follow the same initial behaviour (Figure 55A and B).
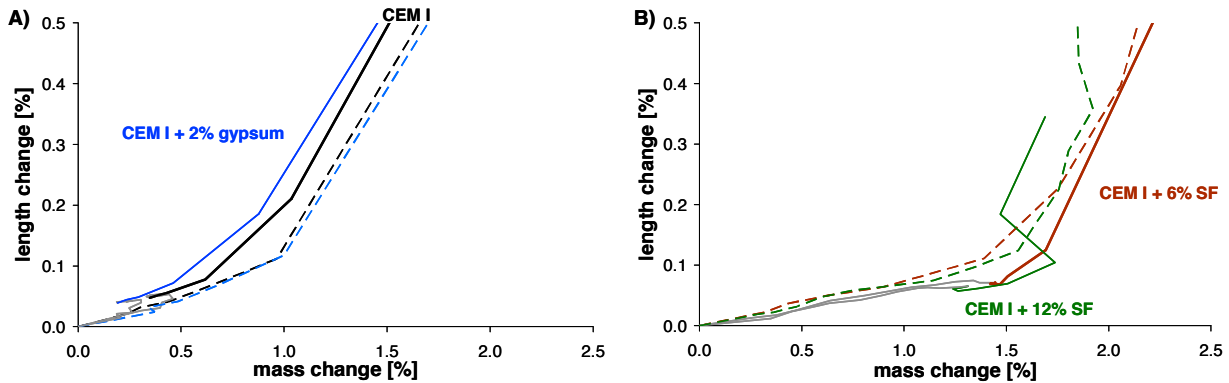
Figure 55: A) Relationship between the mass changes and length changes for the CEM I and its blend with gypsum and B) for the CEM I blends with silica fume during exposure to sodium sulfate solution; cured for 1 month (dashed lines), and 25 months (in bold lines); the development during curing in saturated lime solution is displayed by grey lines

CEM I Based Mortars

The CEM I and CEM I +2percent gypsum mortar bars start to lose mass due to leaching after long curing times compared to the 28 days cured samples (Figure 55A). Mass uptake restarts and expansion follows once the samples are exposed to sodium sulfate solution. The following mass uptake and expansion behaviour shows the same characteristic as the reference (28 days curing), but the lines are parallel. A similar behaviour is observed for the mortar bars made with CEM I HS cement (Figure 56).

Silica Fume and Fly Ash Blended Mortars

The silica fume blended mortars gain more mass than the two CEM I mortars, which could indicate the consumption of lime from solution in pozzolanic reactions. Mass uptake continues and expansion follows once the samples are exposed to sodium sulfate solution. The following mass uptake and expansion behaviour shows a similar characteristic as the reference (28 days curing).

A similar behaviour is observed for the mortar bars made with CEM II/A cements (Figure 56).
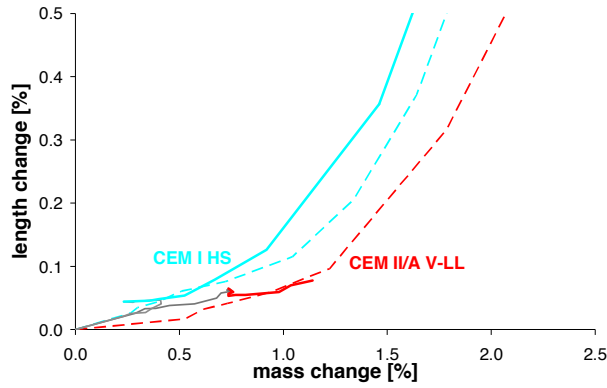
Figure 56: Relationship between the mass changes and length changes for the CEM I HS and CEM II/A during exposure to sodium sulfate solution; cured for 1 month (dashed lines), and 25 months (in bold lines; the development during curing in saturated lime solution is displayed by grey lines

This shows that the expansion of sulfate exposed mortar bars does not only depend on the chemical potential of the cements to form "expansive" phases, but also on the degree of space filling by cement hydrates in general. This highlights that the pore structure is an important factor for the observed length changes. The pore structure of the different binders provides something like a physical potential for the expansion as the time and location of formation of potentially "expansive" phases also determines the observed changes. The on-going hydration contributes to the space filling in the samples and contributes thereby to the expansion due to late ettringite formation.

Dynamic E-modulus

Figure 57A shows the development of the dynamic E-modulus for the CEM I mortar bars, which were cured for 25 months before sulfate exposure. A comparison with the length changes in Figure 57B shows that the dynamic E-modulus drops when expansions are observed. The same observation was obtained for samples cured for 28 days. For the extensively cured samples at 40°C no decrease in dynamic E-modulus and only small length changes were observed.
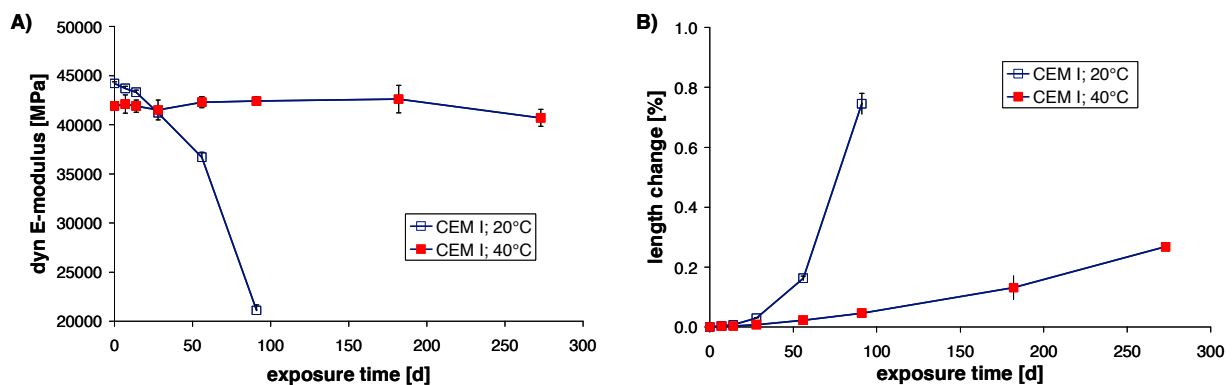
Figure 57: A) Development of the dynamic E-modulus and B) length changes over time for CEM I mortar bars cured for 25 months at 20°C and 40°C before exposure to sodium sulfate solution

Figure 58 shows that none of the extra cured mortars increased the dynamic E-modulus during subsequent exposure to sodium sulfate solution. This suggests that the impact of the on-going hydration is still observable after 28 days.
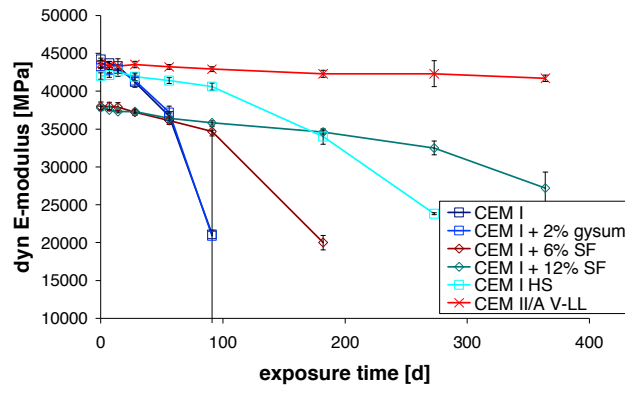
Figure 58: Development of the dynamic E-modulus over time for extra-long cured samples at 20°C

Phase Characterization by XRD, TGA and EDS

Table 17: XRD characterization of pastes made from all tested cements before sulfate exposure, 28 days curing

cement	reference w/b	testing age	main phases			
CEM I	0.4		portlandite	ettringite	monosulphate	calcite
	0.7		portlandite	ettringite	monosulphate	
CEM I +2% gypsum	0.4		portlandite	ettringite		
	0.7		portlandite	ettringite	calcite	
CEM I +6% SF	0.4	before SO₃ exposure	portlandite	ettringite	monosulphate	
	0.7		portlandite	ettringite	monosulphate	
CEM I +12% SF	0.4		portlandite	ettringite	monosulphate	
	0.7		portlandite	ettringite	monosulphate	
CEM I HS	0.4		portlandite	ettringite	calcite	
	0.7		portlandite	ettringite	monocarbonate	calcite
CEM II/A	0.4		portlandite	ettringite	monocarbonate	calcite
	0.7		portlandite	ettringite	monocarbonate	calcite
CEM II/B	0.4		portlandite	ettringite	calcite	
CEM III/B	0.4		portlandite	ettringite	monosulphate	calcite
	0.7		portlandite	ettringite	monosulphate	monocarbonate
CEM III/C	0.4		portlandite	ettringite		
	0.7		portlandite	ettringite	monosulphate	monocarbonate

Table 18: TGA characterization of pastes made from all tested cements before sulfate exposure, 28 days curing

cement	reference w/b	testing age	portlandite	g/100g	calcite	g/100g	CSH / ettringite	bound water (30 - 455 °C) g/100g
CEM I	0.4		-3.5	14.4	-2.1	4.8	-7.3	15.2
	0.7		-4.5	18.5	-2.4	5.5	-6.9	14.5
CEM I +2% gypsum	0.4		-3.5	14.4	-2.1	4.8	-7.6	14.8
	0.7		-4.5	18.5	-2.5	5.7	-8.2	15.7
CEM I +6% SF	0.4	before SO₃ exposure	-1.6	6.6	-1.6	3.6	-9.0	17.2
	0.7		-3.4	14.0	-2.0	4.5	-8.9	18.7
CEM I +12% SF	0.4		-2.5	10.3	-1.8	4.1	-8.2	17.0
	0.7		-1.7	7.0	-1.9	4.3	-10.0	18.9
CEM I HS	0.4		-3.5	14.4	-3.9	8.9	-8.1	15.6
	0.7		-4.0	16.5	-3.6	8.2	-7.7	15.7
CEM II/A	0.4		-3.2	13.2	-6.5	14.8	-8.1	14.7
	0.7		-4.0	16.5	-6.2	14.1	-7.6	14.9
CEM II/B	0.4		-2.2	9.0	-5.5	12.5	-9.7	15.9
CEM III/B	0.4		-1.4	5.8	-2.5	5.7	-11.2	15.6
	0.7		-1.5	6.2	-2.4	5.5	-9.3	16.4
CEM III/C	0.4		-1.1	4.5	-2.6	5.9	-9.0	13.9
	0.7		-1.2	4.9	-2.4	5.5	-9.5	15.6

6.8 Phase Characterization by XRD, TGA and EDS

XRD

Table 19: XRD characterization of CEM I pastes

cement	solution	reference w/b	testing age			main phases	
CEM I	0.35 mol/l sodium sulphate solution	0.4	1.5y	portlandite	ettringite	gypsum	thenardite
	0.35 mol/l sodium sulphate solution; 40°C	0.4	1.5y	ettringite			
	0.35 mol/l sodium bicarbonate solution	0.4	1.5y	calcite			
	0.027 mol/l calcium hydroxide	0.4	1.5y	portlandite	calcite	ettringite	gypsum
	0.027 mol/l calcium hydroxide; 40°C	0.4	1.5y	portlandite	calcite	ettringite	monocarbonate
	0.35 mol/l potassium sulphate solution	0.4	1y	arcanite	syngenite	portlandite	ettringite
	0.35 mol/l magnesium sulphate solution	0.4	1.5y	gypsum	brucite	ettringite	
	0.035 mol/l magnesium sulphate solution	0.4	1y	ettringite	ettringite	ettringite	
	0.035 mol/l magnesium sulphate bicarbonate solution	0.4	1y	calcite	ettringite	ettringite	calcite
	0.35 mol/l sulphate mixture solution	0.4	1y	gypsum	brucite	ettringite	
	0.35 mol/l bicarbonate mixture solution	0.4	1y	calcite	ettringite	ettringite	
	0.035 mol/l bicarbonate mixture solution	0.4	1.5y	calcite	portlandite	portlandite	
	deionized water	0.4	1y	portlandite	ettringite	monocarbonate	monocarbonate
CEM I	0.35 mol/l sodium sulphate solution	0.7	1.5y	ettringite	portlandite	gypsum	
	0.35 mol/l sodium sulphate solution; 40°C	0.7	1.5y	portlandite	ettringite	ettringite	
	0.35 mol/l sodium bicarbonate solution	0.7	1.5y	calcite			
	0.027 mol/l calcium hydroxide	0.7	1.5y	portlandite	ettringite	monocarbonate	calcite
	0.027 mol/l calcium hydroxide; 40°C	0.7	1.5y	portlandite	calcite	ettringite	gypsum
	0.35 mol/l potassium sulphate solution	0.7	1y	portlandite	ettringite	syngenite	
	0.35 mol/l magnesium sulphate solution	0.7	1.5y	gypsum	brucite		
	0.035 mol/l bicarbonate mixture solution	0.7	1.5y	calcite	aragonite	ettringite	
	0.035 mol/l bicarbonate mixture solution	0.7	1.5y	calcite	ettringite	portlandite	
CEM I	0.35 mol/l sodium sulphate solution	cem	5m	gypsum	ettringite	ettringite	
	0.35 mol/l sodium bicarbonate solution	cem	5m	aragonite	calcite		
	0.035 mol/l magnesium sulphate solution	cem	5m	calcite	ettringite	brucite	
	0.035 mol/l magnesium bicarbonate solution	cem	5m	calcite	ettringite		
	0.35 mol/l sulphate mixture solution	cem	5m	gypsum	brucite	calcite	ettringite
	0.35 mol/l bicarbonate mixture solution	cem	5m	aragonite	calcite		

Table 20: XRD characterization of CEM I + 2% gypsum pastes

cement	solution	reference w/b	testing age	main phases			
CEM I + 2% gypsum	0.35 mol/l sodium sulphate solution	0.4	1.5y	ettringite	portlandite	gypsum	
	0.027 mol/l calcium hydroxide	0.4	1.5y	portlandite	calcite	monosulphate	monocarbonate
	0.35 mol/l bicarbonate mixture solution	0.4	1.5y	calcite	ettringite	gypsum	
CEM I + 2% gypsum	0.35 mol/l sodium sulphate solution	0.7	1.5y	ettringite	portlandite	gypsum	
	0.027 mol/l calcium hydroxide	0.7	1.5y	portlandite	ettringite	calcite	monocarbonate
	0.35 mol/l bicarbonate mixture solution	0.7	1.5y	calcite	ettringite	aragonite	gypsum

Table 21: XRD characterization of CEM I + 6% silica fume pastes

cement	solution	reference w/b	testing age	main phases			
CEM I + 6% SF	0.35 mol/l sodium sulphate solution	0.4	1.5y	ettringite	calcite		
	0.027 mol/l calcium hydroxide	0.4	1.5y	C-S-H			
	0.35 mol/l bicarbonate mixture solution	0.4	1.5y	calcite	aragonite	gypsum	ettringite
CEM I + 6% SF	0.35 mol/l sodium sulphate solution	0.7	1.5y	ettringite	monocarbonate	calcite	monocarbonate
	0.027 mol/l calcium hydroxide	0.7	1.5y	portlandite	ettringite	gypsum	ettringite
	0.35 mol/l bicarbonate mixture solution	0.7	1.5y	calcite	aragonite		

Table 22: XRD characterization of CEM I + 12% silica fume pastes

cement	solution	reference w/b	testing age	main phases			
CEM I + 12% SF	0.35 mol/l sodium sulphate solution	0.4	1.5y	ettringite	monocarbonate	calcite	ettringite
	0.027 mol/l calcium hydroxide	0.4	1.5y	portlandite	calcite	monocarbonate	ettringite
	0.35 mol/l bicarbonate mixture solution	0.4	1.5y	calcite	gypsum	aragonite	
CEM I + 12% SF	0.35 mol/l sodium sulphate solution	0.7	1.5y	ettringite	calcite		
	0.027 mol/l calcium hydroxide	0.7	1.5y	CSH	ettringite		
	0.35 mol/l bicarbonate mixture solution	0.7	1.5y	calcite	aragonite	gypsum	

Table 23: XRD characterization of CEM I HS pastes

cement	solution	reference w/b	testing age	main phases			
CEM I HS	0.35 mol/l sodium sulphate solution	0.4	1.5y	ettringite	gypsum	portlandite	
	0.027 mol/l calcium hydroxide	0.4	1.5y	portlandite	calcite	ettringite	
	0.35 mol/l bicarbonate mixture solution	0.4	1.5y	calcite			
CEM I HS	0.35 mol/l sodium sulphate solution	0.7	1.5y	ettringite	portlandite	gypsum	
	0.027 mol/l calcium hydroxide	0.7	1.5y	portlandite	calcite	ettringite	monocarbonate
	0.35 mol/l bicarbonate mixture solution	0.7	1.5y	calcite	aragonite	ettringite	gypsum

Table 24: XRD characterization of CEM II/A pastes

cement	solution	reference w/b	testing age	main phases			
CEM II/A	0.35 mol/l sodium sulphate solution	0.4	1.5y	ettringite	calcite		
	0.027 mol/l calcium hydroxide	0.4	1.5y	calcite	monocarbonate	ettringite	
	0.35 mol/l bicarbonate mixture solution	0.4	1.5y	calcite			
CEM II/A	0.35 mol/l sodium sulphate solution	0.7	1.5y	ettringite	calcite	monocarbonate	
	0.027 mol/l calcium hydroxide	0.7	1.5y	calcite	portlandite	ettringite	
	0.35 mol/l bicarbonate mixture solution	0.7	1.5y	calcite	aragonite		

Table 25: XRD characterization of CEM II/B pastes

cement	solution	reference w/b	testing age	main phases		
CEM II/B	0.35 mol/l sodium sulphate solution	0.4	1y	calcite	ettringite	
	0.027 mol/l calcium hydroxide	0.4	1y	portlandite	calcite	ettringite
	0.35 mol/l bicarbonate mixture solution	0.4	1y	aragonite	calcite	monocarbonate

Table 26: XRD characterization of CEM III/B pastes

cement	solution	reference w/b	testing age	main phases
CEM III/B	0.35 mol/l sodium sulphate solution	0.4	1.5y	calcite, ettringite
	0.35 mol/l sodium sulphate solution; 40°C	0.4	1.5y	ettringite, calcite
	0.35 mol/l sodium bicarbonate solution	0.4	1.5y	calcite
	0.027 mol/l calcium hydroxide	0.4	1.5y	calcite, portlandite, ettringite, monocarbonate
	0.027 mol/l calcium hydroxide; 40°C	0.4	1.5y	calcite, ettringite, monocarbonate
	0.35 mol/l potassium sulphate solution	0.4	1.5y	arcanite, ettringite
	0.35 mol/l magnesium sulphate solution	0.4	1.5y	gypsum
	0.035 mol/l magnesium sulphate solution	0.4	1y	ettringite, calcite, brucite
	0.035 mol/l magnesium bicarbonate solution	0.4	1y	calcite, ettringite, aragonite
	0.35 mol/l sulphate mixture solution	0.4	1y	gypsum, ettringite
	0.35 mol/l bicarbonate mixture solution	0.4	1.5y	calcite, aragonite
	0.035 mol/l bicarbonate mixture solution	0.4	1.5y	calcite, ettringite
	deionized water	0.4	1y	calcite, ettringite
CEM III/B	0.35 mol/l sodium sulphate solution	0.7	1.5y	ettringite, calcite
	0.35 mol/l sodium sulphate solution; 40°C	0.7	1.5y	ettringite, calcite
	0.35 mol/l sodium bicarbonate solution	0.7	1.5y	calcite
	0.027 mol/l calcium hydroxide	0.7	1.5y	calcite, ettringite
	0.027 mol/l calcium hydroxide; 40°C	0.7	1.5y	monosulphate, calcite, monocarbonate
	0.35 mol/l potassium sulphate solution	0.7	1.5y	arcanite, ettringite, monocarbonate
	0.35 mol/l magnesium sulphate solution	0.7	1.5y	gypsum
	0.35 mol/l bicarbonate mixture solution	0.7	1.5y	aragonite, calcite, arcanite, monocarbonate
	0.035 mol/l bicarbonate mixture solution	0.7	1.5y	calcite, ettringite, monocarbonate
CEM III/B	0.35 mol/l sodium sulphate solution	cem	5m	ettringite, calcite
	0.35 mol/l sodium bicarbonate solution	cem	5m	aragonite, calcite
	0.035 mol/l magnesium sulphate solution	cem	5m	ettringite, calcite
	0.035 mol/l magnesium bicarbonate solution	cem	5m	calcite, ettringite
	0.35 mol/l sulphate mixture solution	cem	5m	gypsum, brucite
	0.35 mol/l bicarbonate mixture solution	cem	5m	aragonite, calcite, sodium sulphate

Table 27: XRD characterization of CEM III/C pastes

cement	solution	reference w/b	testing age	main phases			
CEM III/C	0.35 mol/l sodium sulphate solution	0.4	1.5y	ettringite	calcite		
	0.35 mol/l sodium bicarbonate solution	0.4	1.5y	calcite	calcite		
	0.027 mol/l calcium hydroxide	0.4	1.5y	calcite	ettringite	monosulphate	monocarbonate
	0.35 mol/l potassium sulphate solution	0.4	1.5y	ettringite	calcite	arcanite	
	0.35 mol/l magnesium sulphate solution	0.4	1.5y	gypsum			
	0.35 mol/l bicarbonate mixture solution	0.4	1.5y	calcite	aragonite		
	0.035 mol/l bicarbonate mixture solution	0.4	1.5y	calcite	ettringite		
CEM III/C	0.35 mol/l sodium sulphate solution	0.7	1.5y	ettringite	calcite		
	0.35 mol/l sodium bicarbonate solution	0.7	1.5y	calcite	calcite	monocarbonate	
	0.027 mol/l calcium hydroxide	0.7	1.5y	calcite	ettringite		
	0.35 mol/l potassium sulphate solution	0.7	1.5y	ettringite	calcite		
	0.35 mol/l magnesium sulphate solution	0.7	1.5y	gypsum			
	0.35 mol/l bicarbonate mixture solution	0.7	1.5y	aragonite	calcite		
	0.035 mol/l bicarbonate mixture solution	0.7	1.5y	calcite	ettringite		

TGA

Table 28: TGA characterization of CEM I pastes and measured pH values

cement	reference w/b	solution	testing age	pH	gypsum	gypsum g/100g	portlandite	portlandite g/100g	calcite	calcite g/100g	CSH / ettringite	brucite	brucite g/100g	syngenite	syngenite g/100g	bound water (30 - 455 °C) g/100g
CEM I	0.4	0.35 mol/l sodium sulphate solution	1.5y	13	-2.8	13.2	-2.1	8.5	-1.7	4.0	-11.6					22.3
	0.4	0.35 mol/l sodium sulphate solution; 40°C	1.5y	12.46			-2.0	8.1	-1.9	4.4	-18.0					23.3
	0.4	0.35 mol/l sodium bicarbonate solution	1.5y	13.04					-19.6	44.5	-6.1					10.2
	0.4	0.027 mol/l calcium hydroxide	1.5y	12.62			-5.8	23.6	-2.1	4.7	-10.6					17.9
	0.4	0.027 mol/l calcium hydroxide; 40°C	1.5y	11.91			-4.0	16.4	-3.9	8.8	-11.6					19.7
	0.4	0.35 mol/l potassium sulphate solution	1y/3y	*13.08*			-1.1	4.5	-1.1	2.4	-10.9			-1.7	2.4	15.9
	0.4	0.35 mol/l magnesium sulphate solution	1.5y	11.7	-12.3	58.6					-6.3	-4.0	13.0			25.4
	0.4	0.035 mol/l magnesium sulphate solution	1y	12.67			-1.1	4.4	-2.0	4.6	-15.9	-2.6	8.5			24.6
	0.4	0.035 mol/l magnesium bicarbonate solution	1y	12.57					-8.6	19.5	-15.0	-1.9	6.0			22.2
	0.4	0.35 mol/l sulphate mixture solution	1y/3y	12.44	-11.7	56.0					-6.0	-2.3	7.3			23.7
	0.4	0.35 mol/l bicarbonate mixture solution	1.5y	*12.11*			-2.1	8.8	-8.3	18.9	-12.6	-1.2	4.0			17.1
	0.4	0.035 mol/l bicarbonate mixture solution	1y	12.84					-3.0	6.8	-15.2					21.4
	0.4	deionized water	1y	12.64			-3.5	14.4	-1.5	3.4	-9.9					19.5
CEM I	0.7	0.35 mol/l sodium sulphate solution	1.5y	12.77	-5.2	24.8	-1.3	5.5	-1.4	3.2	-12.5					24.1
	0.7	0.35 mol/l sodium sulphate solution; 40°C	1.5y	12.52			-2.4	9.8	-1.9	4.3	-18.5					24.2
	0.7	0.35 mol/l sodium bicarbonate solution	1.5y	12.75												
	0.7	0.027 mol/l calcium hydroxide	1.5y	12.42			-4.9	20.2	-2.4	5.4	-10.4					20.4
	0.7	0.027 mol/l calcium hydroxide; 40°C	1.5y	11.95			-5.0	20.7	-2.9	6.7	-10.8					17.4
	0.7	0.35 mol/l potassium sulphate solution	1y/3y	*13.08*			-1.7	6.9	-1.7	3.9	-12.7			-1.9	2.7	18.4
	0.7	0.35 mol/l magnesium sulphate solution	1.5y	9.91	-13.2	63.1					-2.8	-2.8	9.1			22.9
	0.7	0.35 mol/l bicarbonate mixture solution	1.5y	12.47					-14.9	33.8	-10.7	-1.9	6.3			17.1
	0.7	0.035 mol/l bicarbonate mixture solution	1.5y	12.66			-2.4	9.9	-4.1	9.2	-15.6	-1.0	3.4			23.0
CEM I	cement	0.35 mol/l sodium sulphate solution	5m	12.7	-6.1	29.3			-23.7	53.9	-7.0					17.1
	cement	0.35 mol/l sodium bicarbonate solution	5m	9.79							-2.6					5.9
	cement	0.035 mol/l magnesium sulphate solution	5m	12.42	-12.4	59.4			-0.7	1.6	-5.0	-1.9	6.1			22.0
	cement	0.035 mol/l magnesium bicarbonate solution	5m	8.63					-26.3	59.8	-3.2					6.7
	cement	0.35 mol/l sulphate mixture solution	5m	12.56					-1.5	3.3	-16.5	-2.1	6.9			23.8
	cement	0.35 mol/l bicarbonate mixture solution	5m	12.51					-12.1	27.6	-9.5	-1.9	6.3			15.4

Table 29: TGA characterization of CEM I + 2% gypsum pastes and measured pH values

cement	reference w/b	solution	testing age	pH	gypsum	g/100g	portlandite	g/100g	calcite	g/100g	CSH / ettringite	brucite	g/100g	syngenite g/100g	bound water (30 - 455 °C) g/100g
CEM I + 2%	0.4	0.35 mol/l sodium sulphate solution	1.5y	12.8	-3.6	17.3	-1.8	7.4	-1.3	2.9	-13.5				24.6
gypsum	0.4	0.027 mol/l calcium hydroxide	1.5y	12.32			-3.0	12.4	-6.6	14.9	-13.9				20.4
	0.4	0.35 mol/l bicarbonate mixture solution	1.5y	12.4	-1.5	7.0			-15.8	36.0	-8.0	-1.9	6.3		16.4
CEM I + 2%	0.7	0.35 mol/l sodium sulphate solution	1.5y	12.79	-4.9	23.4	-1.3	5.4	-1.7	3.8	-13.6				25.0
gypsum	0.7	0.027 mol/l calcium hydroxide	1.5y	12.33			-5.0	20.5	-2.4	5.4	-10.9				20.7
	0.7	0.35 mol/l bicarbonate mixture solution	1.5y	12.15	-2.1	10.1			-15.9	36.2	-8.0	-1.7	5.5		16.5

Table 30: TGA characterization of CEM I + 6% silica fume pastes and measured pH values

cement	reference w/b	solution	testing age	pH	gypsum	g/100g	portlandite	g/100g	calcite	g/100g	CSH / ettringite	brucite	g/100g	syngenite g/100g	bound water (30 - 455 °C) g/100g
CEM I + 6% SF	0.4	0.35 mol/l sodium sulphate solution	1.5y	12.35					-0.9	2.1	-16.4				20.7
	0.4	0.027 mol/l calcium hydroxide	1.5y	12.21					-1.6	3.6	-13.8				18.6
	0.4	0.35 mol/l bicarbonate mixture solution	1.5y	10.24					-13.9	31.6	-8.7				14.3
CEM I + 6% SF	0.7	0.35 mol/l sodium sulphate solution	1.5y	12.7					-3.0	6.7	-18.3				26.3
	0.7	0.027 mol/l calcium hydroxide	1.5y	12.35			-2.3	9.4			-12.8				21.7
	0.7	0.35 mol/l bicarbonate mixture solution	1.5y	10.87	-3.0	14.3			-14.2	32.4	-7.1				16.3

Table 31: TGA characterization of CEM I + 12% silica fume pastes and measured pH values

cement	reference w/b	solution	testing age	pH	gypsum	g/100g	portlandite	g/100g	calcite	g/100g	CSH / ettringite	brucite	g/100g	syngenite g/100g	bound water (30 - 455 °C) g/100g
CEM I + 12% SF	0.4	0.35 mol/l sodium sulphate solution	1.5y	12.61					-0.9	2.0	-16.8				21.8
	0.4	0.027 mol/l calcium hydroxide	1.5y	12.33			-2.7	11.0	-1.8	4.2	-12.8				19.0
	0.4	0.35 mol/l bicarbonate mixture solution	1.5y	11.45					-8.9	20.2	-11.9	-1.5	4.9		17.7
CEM I + 12% SF	0.7	0.35 mol/l sodium sulphate solution	1.5y	12.41					-1.7	3.8	-12.5				23.3
	0.7	0.027 mol/l calcium hydroxide	1.5y	12.32					-0.8	1.8	-16.0				20.1
	0.7	0.35 mol/l bicarbonate mixture solution	1.5y	10.29					-18.5	42.0	-6.9				11.3

Table 32: TGA characterization of CEM I HS pastes and measured pH values

cement	reference w/b	solution	testing age	pH	gypsum	g/100g	portlandite	g/100g	calcite	g/100g	CSH / ettringite	g/100g	brucite	g/100g	syngenite	g/100g	bound water (30 - 455 °C) g/100g
CEM I HS	0.4	0.35 mol/l sodium sulphate solution	1.5y	12.77	-3.7	17.7	-1.5	6.0	-2.6	5.9	-9.9						21.3
	0.4	0.027 mol/l calcium hydroxide	1.5y	12.36			-3.8	15.7	-3.9	8.8	-9.0						18.4
	0.4	0.35 mol/l bicarbonate mixture solution	1.5y	12.41					-18.3	41.6	-7.1		-1.8	5.9			12.0
CEM I HS	0.7	0.35 mol/l sodium sulphate solution	1.5y	12.78	-5.0	24.0	-1.5	6.2	-2.7	6.2	-11.8						23.1
	0.7	0.027 mol/l calcium hydroxide	1.5y	12.37			-4.0	16.6	-4.3	9.8	-11.0						19.0
	0.7	0.35 mol/l bicarbonate mixture solution	1.5y	11.91					-20.2	45.9	-5.9		-2.0	6.6			12.1

Table 33: TGA characterization of CEM II/A-pastes and measured pH values

cement	reference w/b	solution	testing age	pH	gypsum	g/100g	portlandite	g/100g	calcite	g/100g	CSH / ettringite	g/100g	brucite	g/100g	syngenite	g/100g	bound water (30 - 455 °C) g/100g
CEM II/A	0.4	0.35 mol/l sodium sulphate solution	1.5y	12.72					-2.7	6.2	-20.4						25.0
	0.4	0.027 mol/l calcium hydroxide	1.5y	12.3			-1.7	7.1	-5.9	13.4	-9.4						19.0
	0.4	0.35 mol/l bicarbonate mixture solution	1.5y	11.52					-20.6	46.8	-4.5						8.1
CEM II/A	0.7	0.35 mol/l sodium sulphate solution	1.5y	12.7					-3.7	8.3	-21.2						27.3
	0.7	0.027 mol/l calcium hydroxide	1.5y	12.38			-1.8	7.5	-6.3	14.3	-12.5						20.7
	0.7	0.35 mol/l bicarbonate mixture solution	1.5y	10.63					-19.6	44.7	-7.4						11.8

Table 34: TGA characterization of CEM II/B-pastes and measured pH values

cement	reference w/b	solution	testing age	pH	gypsum	g/100g	portlandite	g/100g	calcite	g/100g	CSH / ettringite	g/100g	brucite	g/100g	syngenite	g/100g	bound water (30 - 455 °C) g/100g
CEM II/B	0.4	0.35 mol/l sodium sulphate solution	1y	12.59					-3.5	7.9	-19.4						24.4
	0.4	0.027 mol/l calcium hydroxide	1y	12.53			-2.4	10.0	-6.1	13.8	-16.7						20.5
	0.4	0.35 mol/l bicarbonate mixture solution	1y	8.31					-26.0	59.1	-2.8						6.2

Table 35: TGA characterization of CEM III/B pastes and measured pH values

cement	reference w/b	solution	testing age	pH	gypsum	gypsum g/100g	portlandite	portlandite g/100g	calcite	calcite g/100g	CSH/ettringite	brucite	brucite g/100g	bound water (30-455°C) g/100g
CEM III/B	0.4	0.35 mol/l sodium sulphate solution	1.5y	12.73					-1.2	2.6	-18.8			22.2
	0.4	0.35 mol/l sodium sulphate solution; 40°C	1.5y	11.88					-1.2	2.8	-19.6			25.0
	0.4	0.35 mol/l sodium bicarbonate solution	1.5y	10.86					-12.3	28.0	-4.7			7.0
	0.4	0.027 mol/l calcium hydroxide	1.5y	--					-3.3	7.6	-14.1			19.8
	0.4	0.027 mol/l calcium hydroxide; 40°C	1.5y	12.42					-3.3	7.5	-15.1			20.7
	0.4	0.35 mol/l potassium sulphate solution	1.5y	12.88					-0.8	1.8	-13.8			17.3
	0.4	0.35 mol/l magnesium sulphate solution	1.5y	9.16	-14.7	70.2					-2.6	-2.6		22.6
	0.4	0.035 mol/l magnesium sulphate solution	1y	12.14					-1.8	4.2	-18.6	-1.3	4.3	27.3
	0.4	0.035 mol/l magnesium bicarbonate solution	1y	11.9					-8.3	18.9	-13.7	-0.9	3.0	20.1
	0.4	0.35 mol/l sulphate mixture solution	1.5y	11.71	-14.0	66.9			-3.1	7.0	-0.8			21.9
	0.4	0.35 mol/l bicarbonate mixture solution	1y	9.24			-1.5	6.2	-13.4	30.4	-4.4			8.4
	0.4	0.035 mol/l bicarbonate mixture solution	1.5y	12.53					-4.7	10.7	-15.5			21.0
	0.4	deionized water	1y	12.29					-3.2	7.4	-14.3			21.1
CEM III/B	0.7	0.35 mol/l sodium sulphate solution	1.5y	12.62					-0.8	1.9	-21.6			29.2
	0.7	0.35 mol/l sodium sulphate solution; 40°C	1.5y	11.93							-20.9			26.5
	0.7	0.35 mol/l sodium bicarbonate solution	1.5y	10.25					-14.5	32.9	-3.9			7.4
	0.7	0.027 mol/l calcium hydroxide	1.5y	12.28					-2.4	5.4	-12.9			22.4
	0.7	0.027 mol/l calcium hydroxide; 40°C	1.5y	12.42					-2.7	6.1	-15.1			21.6
	0.7	0.35 mol/l potassium sulphate solution	1.5y	12.75							-19.1			26.6
	0.7	0.35 mol/l magnesium sulphate solution	1.5y	8.73	-12.7	60.5					-4.8	-2.0		23.4
	0.7	0.35 mol/l bicarbonate mixture solution	1.5y	9.15					-18.5	42.0	-4.4	-1.3	4.1	9.5
	0.7	0.035 mol/l bicarbonate mixture solution	1.5y	12.5					-4.2	9.6	-16.8	-1.2	3.9	25.0
CEM III/B	cement	0.35 mol/l sodium sulphate solution	5m	12.5					-1.0	2.3	-14.4			19.0
	cement	0.35 mol/l sodium bicarbonate solution	5m	8.95					-11.7	26.6	-1.7			3.9
	cement	0.035 mol/l magnesium sulphate solution	5m	12.12	-13.7	65.4					-1.6	-1.0	3.2	18.5
	cement	0.035 mol/l magnesium bicarbonate solution	5m	7.97					-20.2	45.9	-1.9			4.5
	cement	0.35 mol/l sulphate mixture solution	5m	12.05					-2.2	5.0	-14.5	-1.1	3.5	20.6
	cement	0.35 mol/l bicarbonate mixture solution	5m	11.9					-10.4	23.7	-9.0	-1.0	3.2	14.7

Table 36: TGA characterization of CEM III/C pastes and measured pH values

cement	reference w/b	solution	testing age	pH	gypsum	gypsum g/100g	portlandite g/100g	calcite	calcite g/100g	CSH / ettringite	brucite	brucite g/100g	bound water (30 - 455 °C) g/100g
CEM III/C	0.4	0.35 mol/l sodium sulphate solution	1.5y	12.54				-0.9	2.1	-20.8			24.6
	0.4	0.35 mol/l sodium bicarbonate solution	1.5y	11.33				-12.0	27.2	-5.1			7.2
	0.4	0.027 mol/l calcium hydroxide	1.5y	12.08				-1.6	3.7	-16.9			21.6
	0.4	0.35 mol/l potassium sulphate solution	1.5y	12.75				-1.1	2.5	-20.1			25.2
	0.4	0.35 mol/l magnesium sulphate solution	1.5y	8.69	-12.8	61.3				-3.9			22.5
	0.4	0.35 mol/l bicarbonate mixture solution	1.5y	9.05				-17.0	38.7	-4.7	-1.2	3.8	8.4
	0.4	0.035 mol/l bicarbonate mixture solution	1.5y	12.35				-3.6	8.1	-18.6	-1.0	3.1	23.2
CEM III/C	0.7	0.35 mol/l sodium sulphate solution	1.5y	12.62						-18.8			27.1
	0.7	0.35 mol/l sodium bicarbonate solution	1.5y	9.84				-11.3	25.6	-4.3			7.7
	0.7	0.027 mol/l calcium hydroxide	1.5y	12.1				-4.0	9.2	-12.9			21.0
	0.7	0.35 mol/l potassium sulphate solution	1.5y	12.67						-17.7			26.4
	0.7	0.35 mol/l magnesium sulphate solution	1.5y	8.65	-11.9	57.0				-4.3	-1.5		22.7
	0.7	0.35 mol/l bicarbonate mixture solution	1.5y	8.86				-15.4	35.0	-4.2			9.2
	0.7	0.035 mol/l bicarbonate mixture solution	1.5y	12.45				-4.1	9.2	-16.1			23.8

EDS

CEM I

Initial state
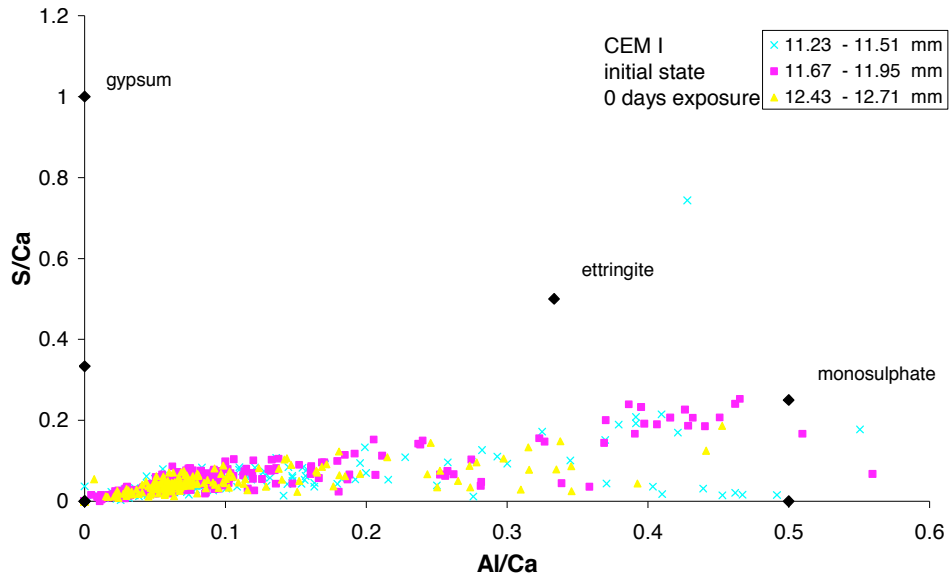
Figure 59: CEM I mortar before sulfate exposure; S/Ca to Al/Ca atomic ratio plot
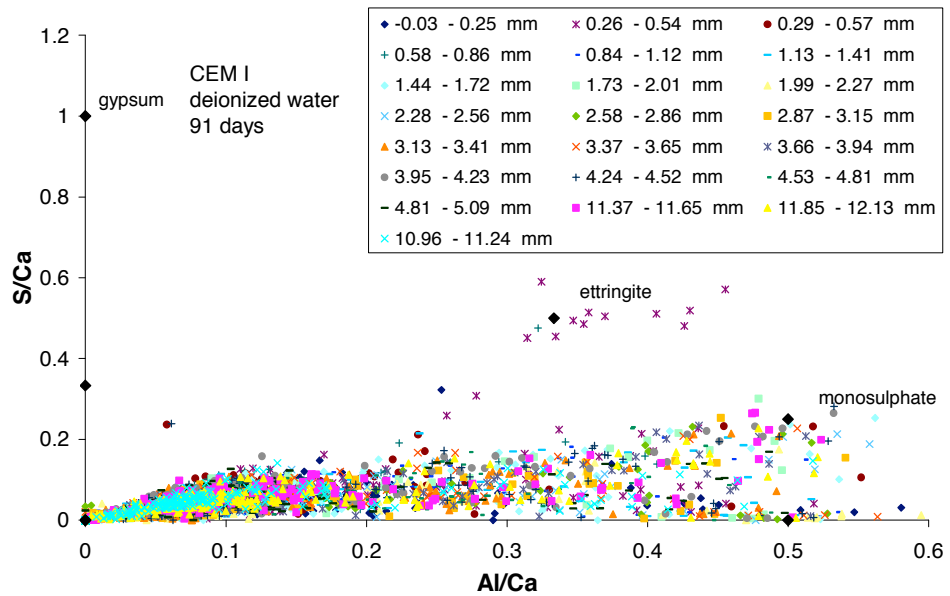
Deionized Water

Figure 60: CEM I mortar after 91 days in deionized water; S/Ca to Al/Ca atomic ratio plot
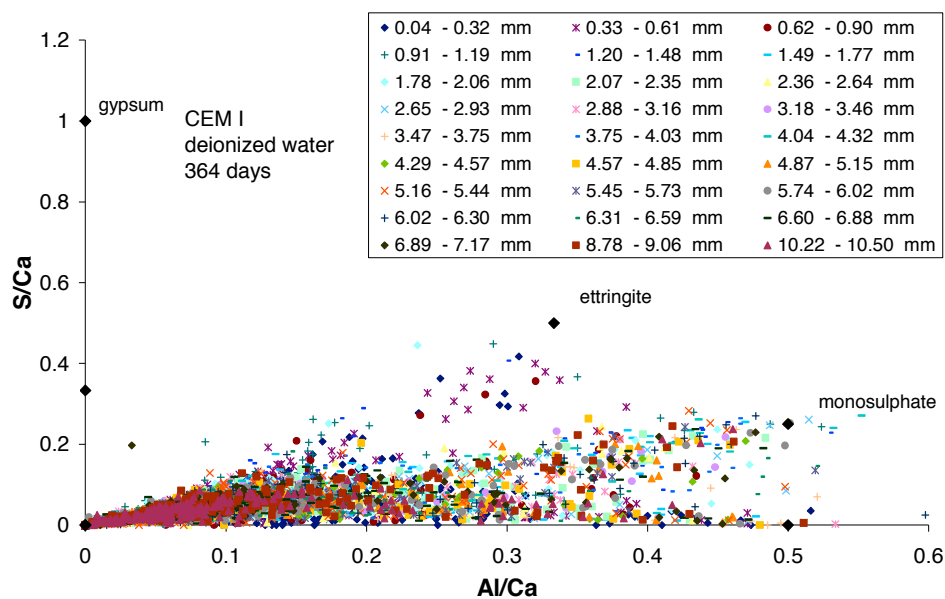
Figure 61: CEM I mortar after 364 days in deionized water; S/Ca to Al/Ca atomic ratio plot

Calcium Hydroxide Solution
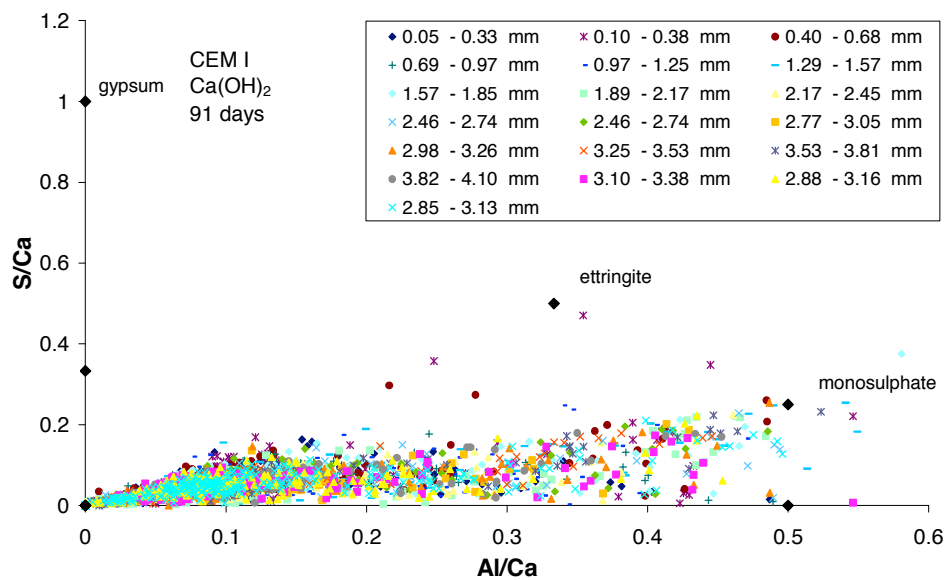
Figure 62: CEM I mortar after 91 days in saturated lime solution at 20°C; S/Ca to Al/Ca atomic ratio plot
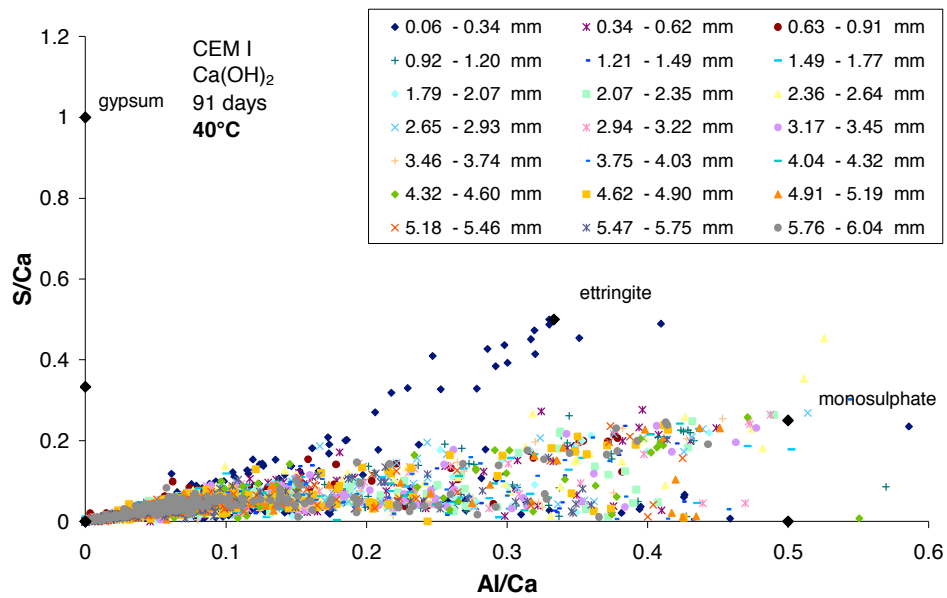
Figure 63: CEM I mortar after 91 days in saturated lime solution at 40°C; S/Ca to Al/Ca atomic ratio plot
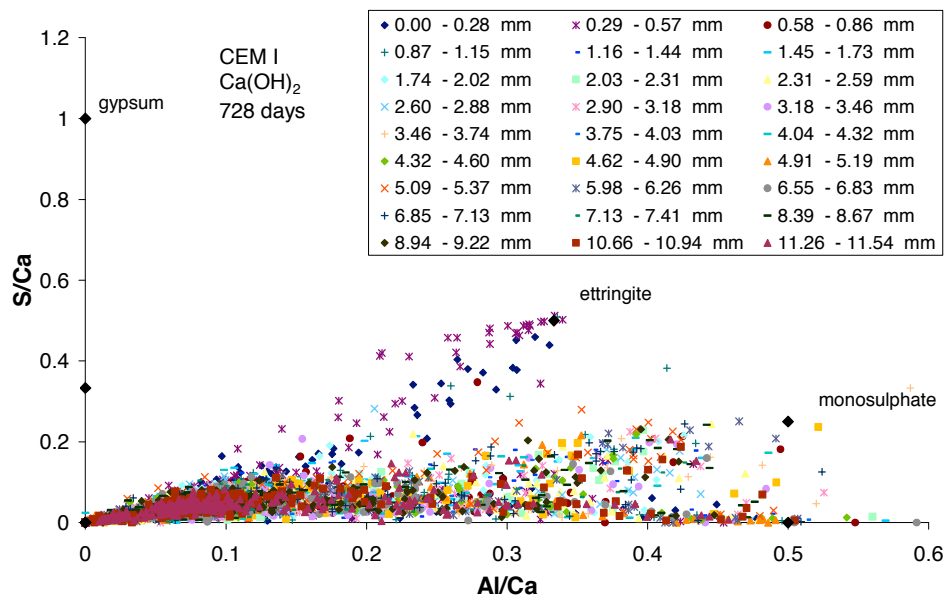
Figure 64: CEM I mortar after 728 days in saturated lime solution at 20°C; S/Ca to Al/Ca atomic ratio plot
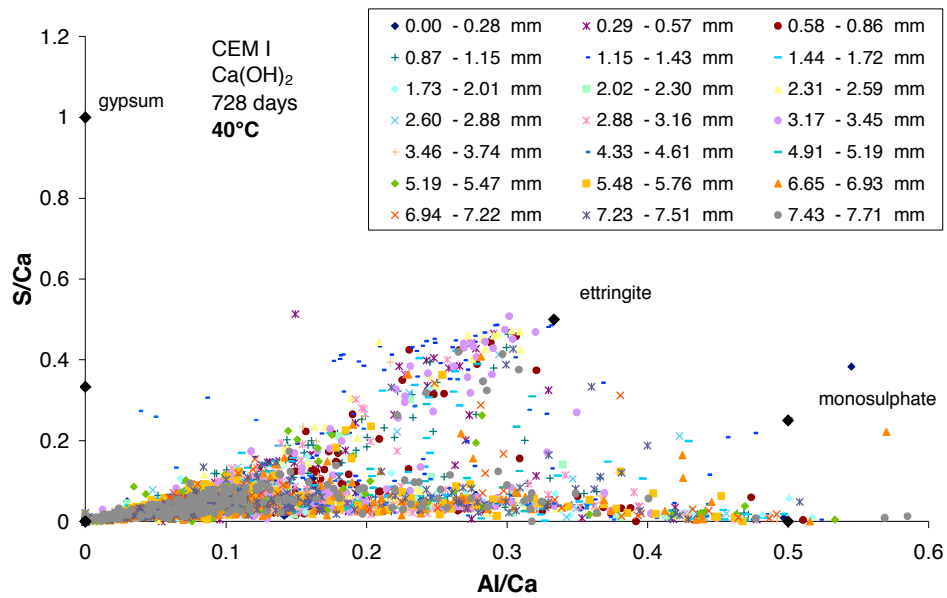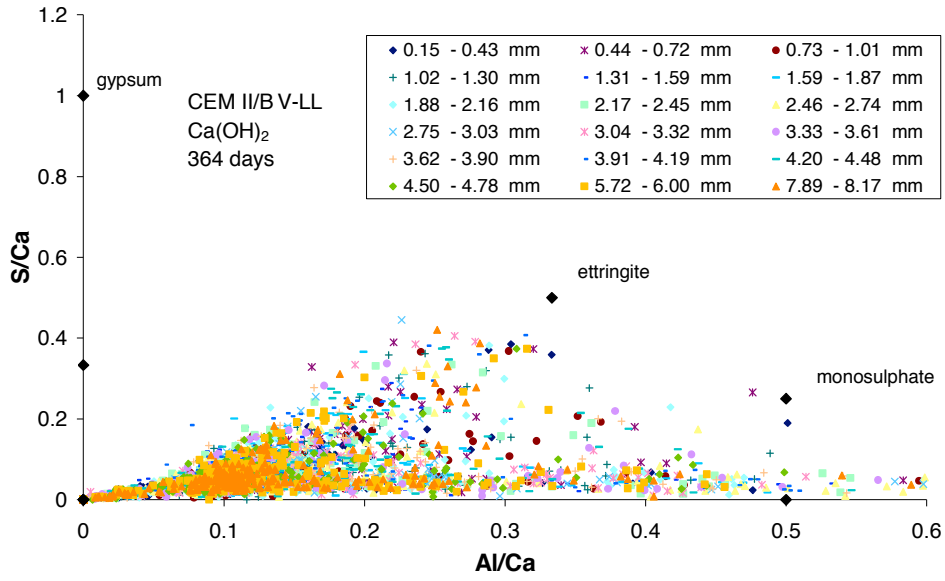
Figure 65: CEM I mortar after 728 days in saturated lime solution at 40°C; S/Ca to Al/Ca atomic ratio plot
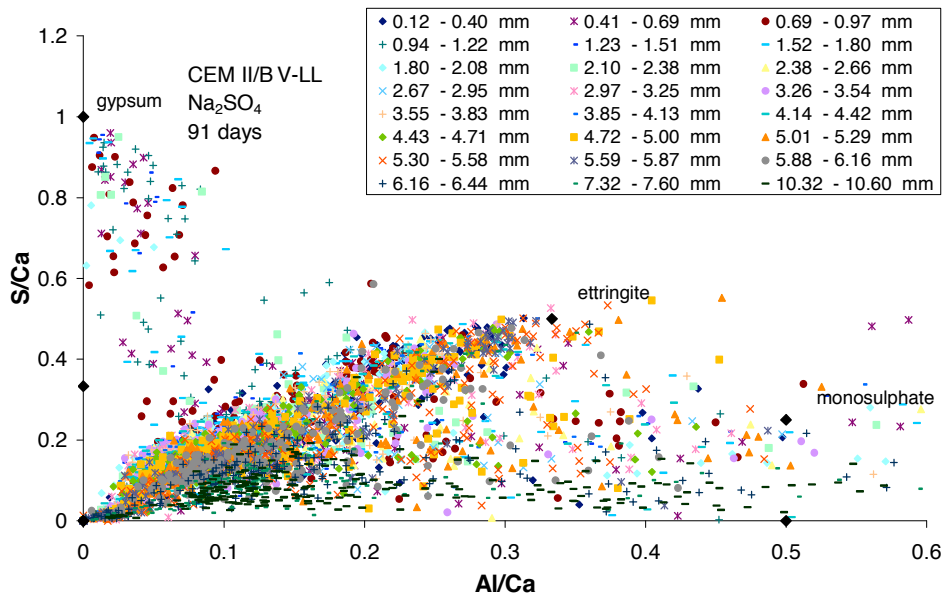
Sodium Sulfate Solution
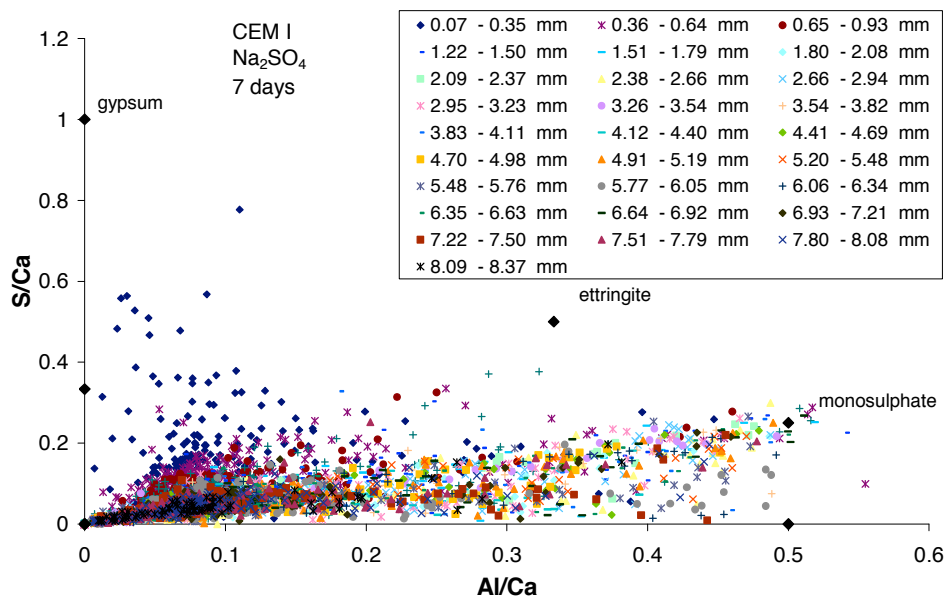
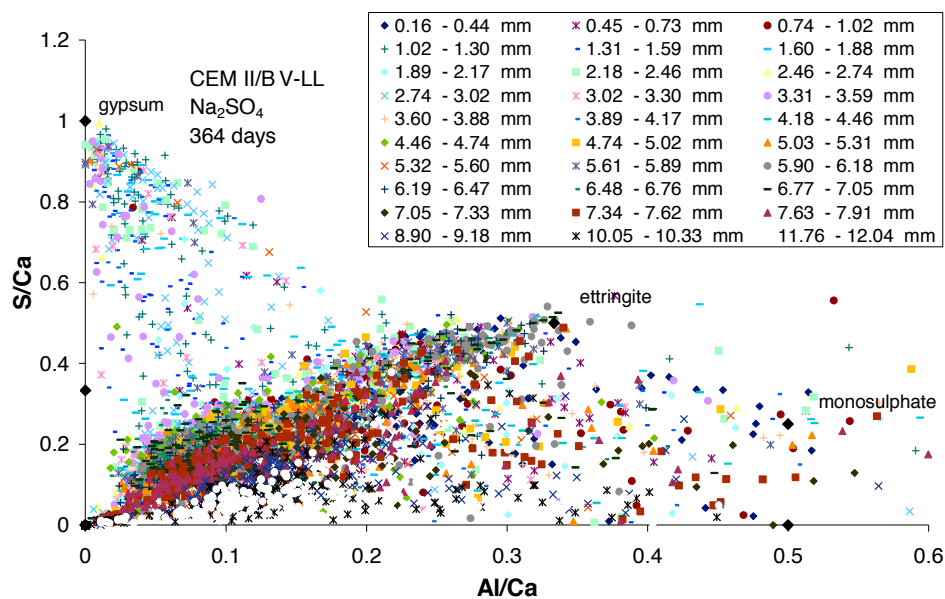**Figure 66**: CEM I mortar after 7 days of sodium sulfate solution exposure at 20°C; S/Ca to Al/Ca atomic ratio plot
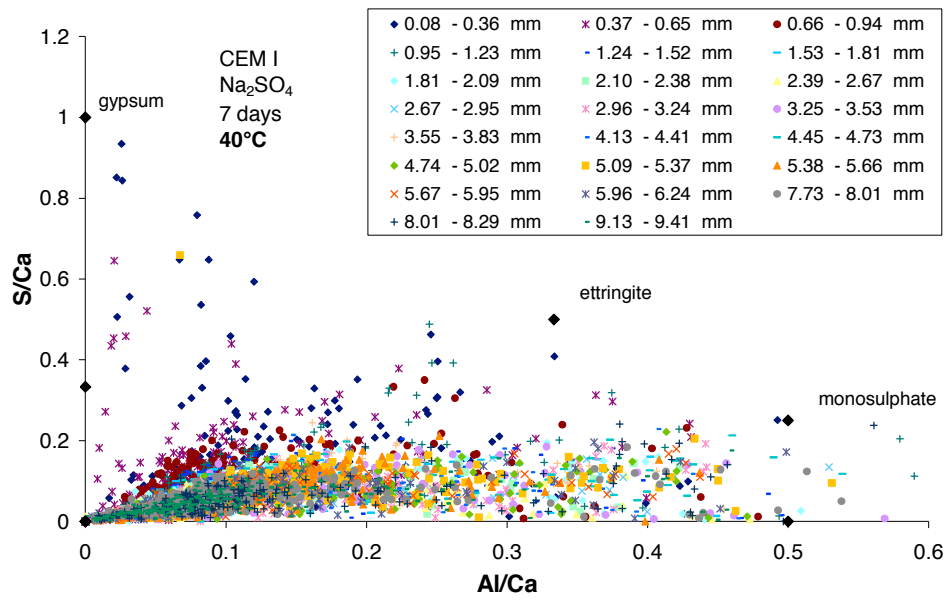
Figure 67: CEM I mortar after 7 days of sodium sulfate solution exposure at <u>40°C</u>; S/Ca to Al/Ca atomic ratio plot
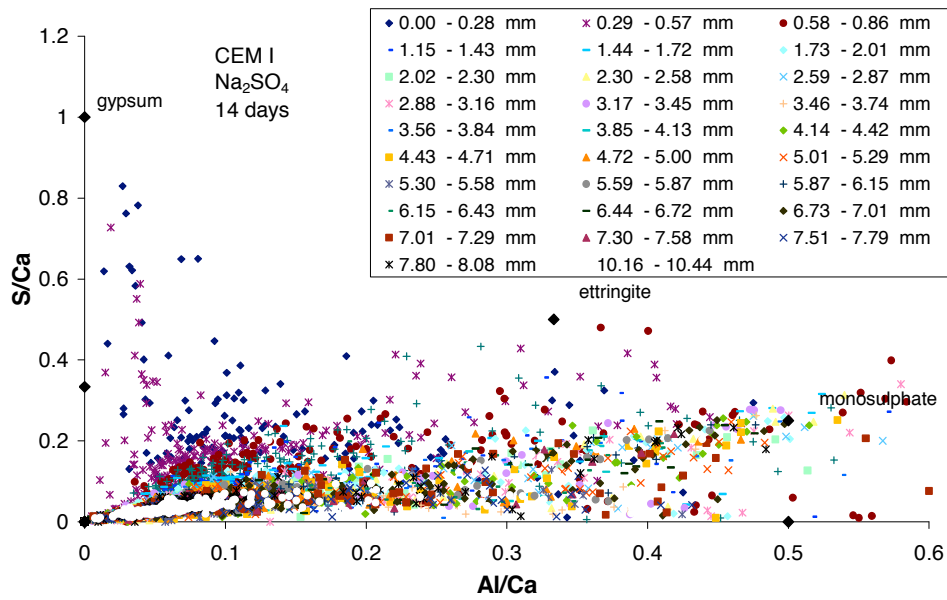
Figure 68: CEM I mortar after 14 days of sodium sulfate solution exposure at 20°C; S/Ca to Al/Ca atomic ratio plot
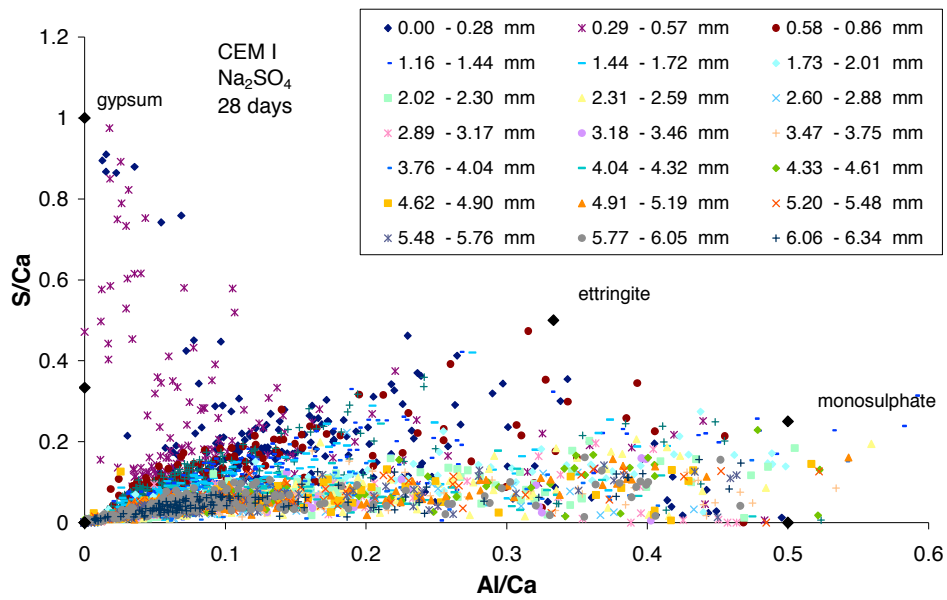
Figure 69: CEM I mortar after 28 days of sodium sulfate solution exposure at 20°C; S/Ca to Al/Ca atomic ratio plot
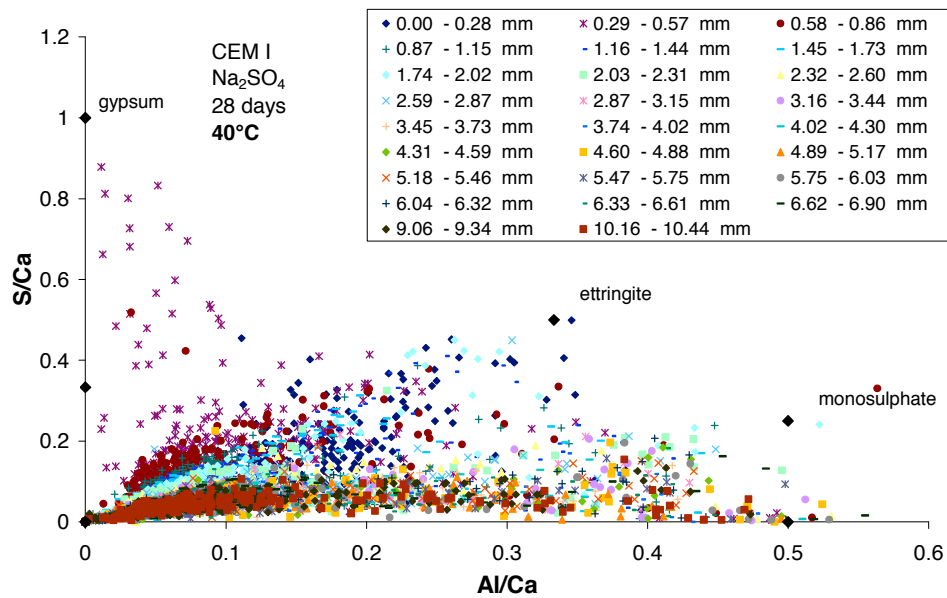
Figure 70: CEM I mortar after 28 days of sodium sulfate solution exposure at 40°C; S/Ca to Al/Ca atomic ratio plot
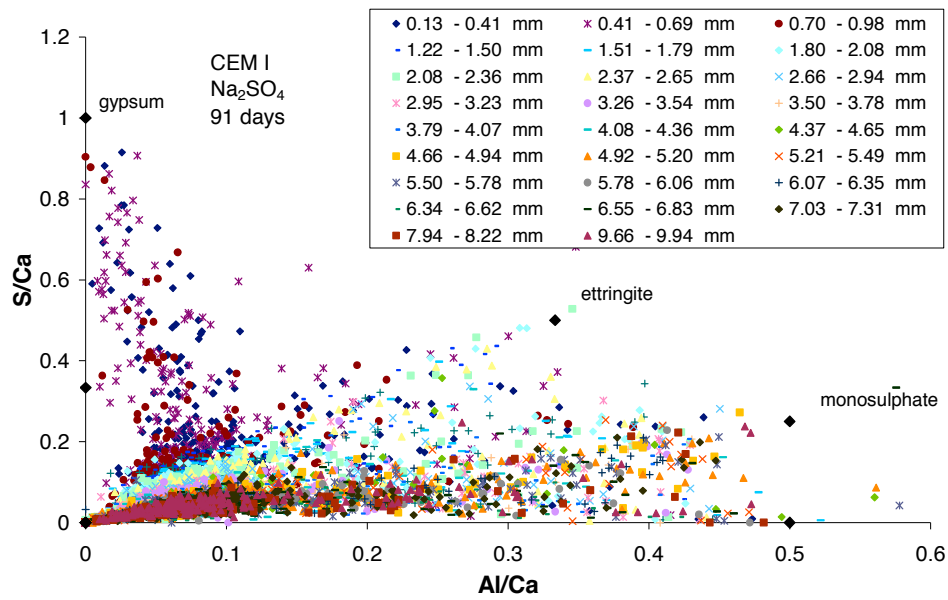
Figure 71: CEM I mortar after 91 days of sodium sulfate solution exposure at 20°C; S/Ca to Al/Ca atomic ratio plot
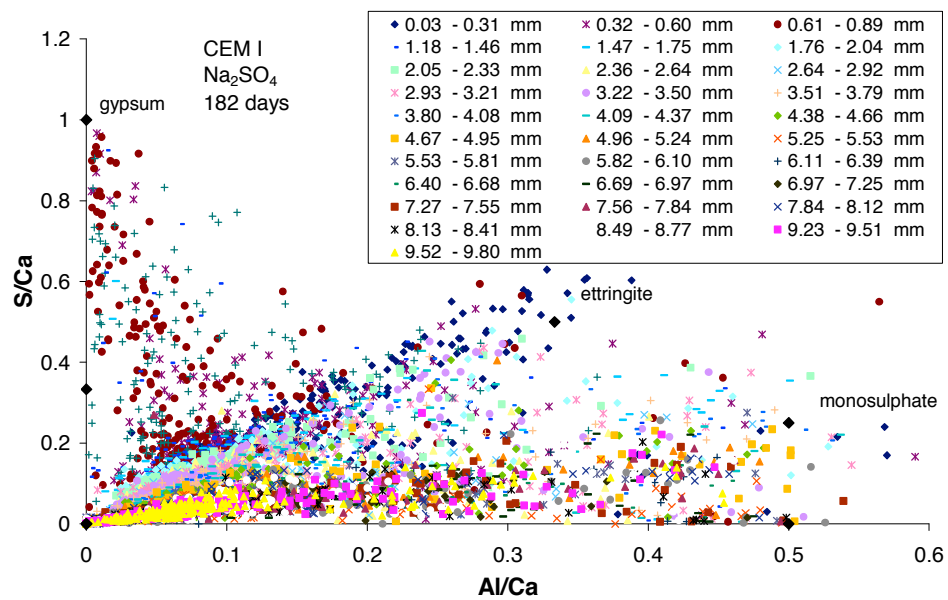
Figure 72: CEM I mortar after 182 days of sodium sulfate solution exposure at 20°C; S/Ca to Al/Ca atomic ratio plot
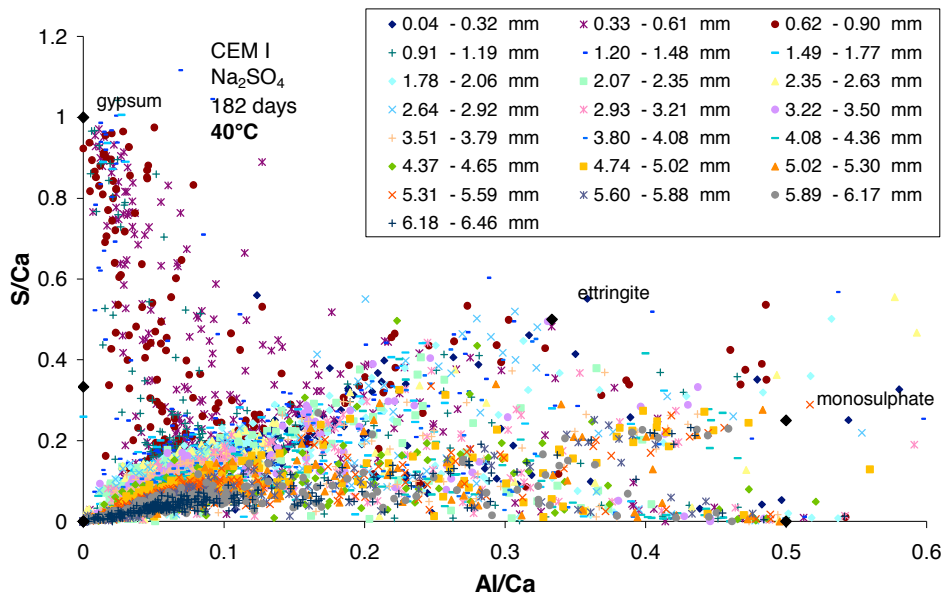
Figure 73: CEM I mortar after 182 days of sodium sulfate solution exposure at <u>40°C</u>; S/Ca to Al/Ca atomic ratio plot
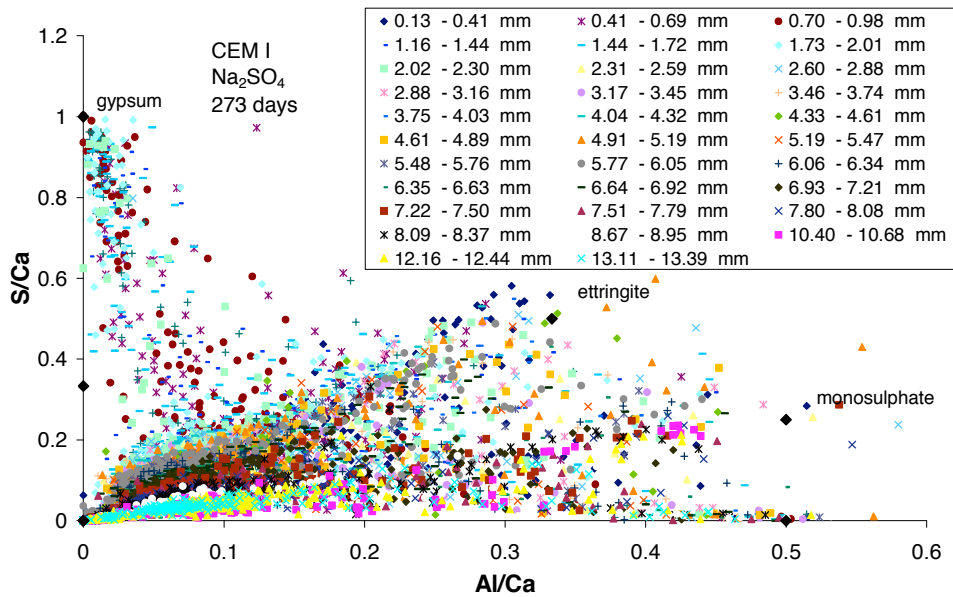
Figure 74: CEM I mortar after 273 days of sodium sulfate solution exposure at 20°C; S/Ca to Al/Ca atomic ratio plot
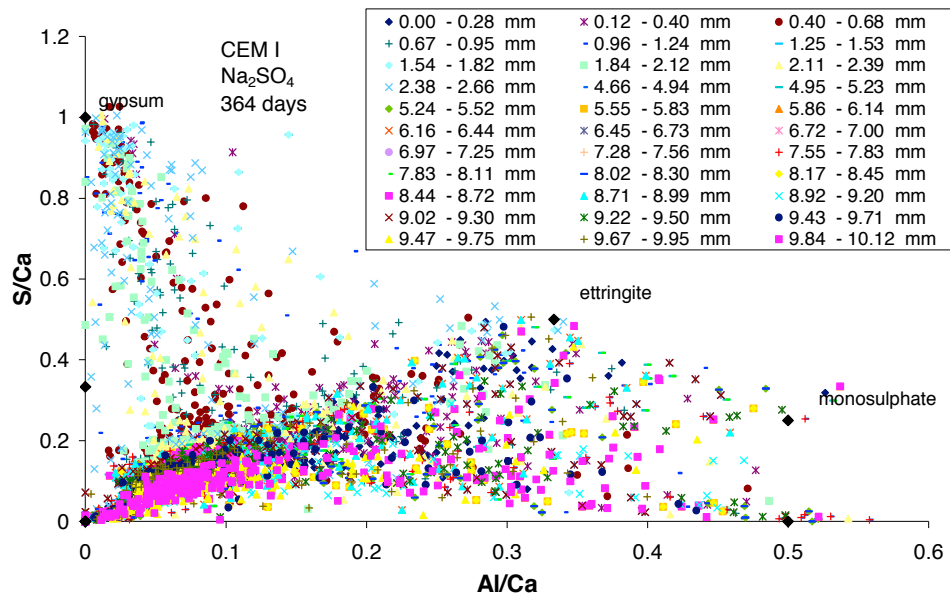
Figure 75: CEM I mortar after 364 days of sodium sulfate solution exposure at 20°C; S/Ca to Al/Ca atomic ratio plot
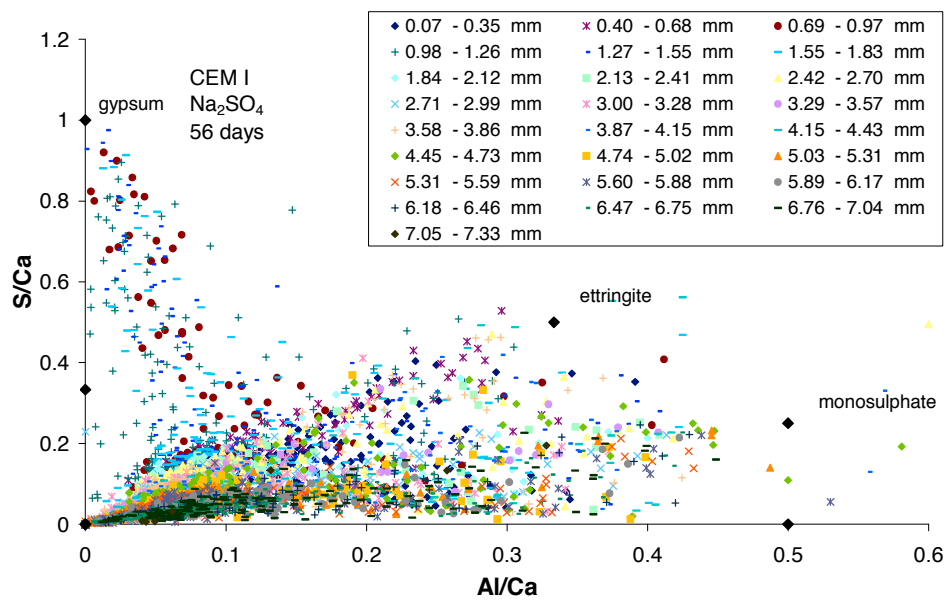
Figure 76: CEM I mortar after 56 days of sodium sulfate solution exposure at 20°C after <u>two years of additional curing</u>; S/Ca to Al/Ca atomic ratio plot
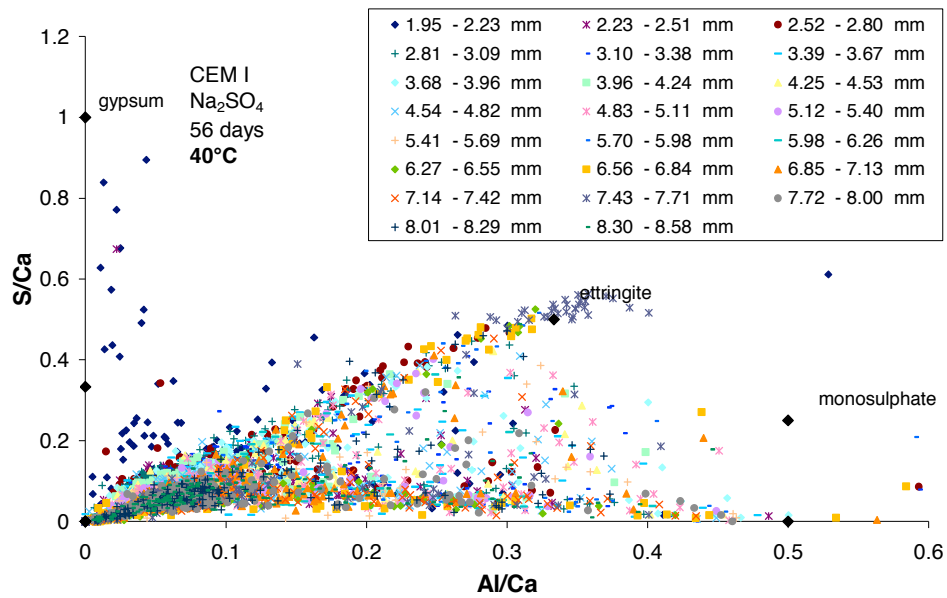
Figure 77: CEM I mortar after 56 days of sodium sulfate solution exposure at <u>40°C</u> after <u>two years of additional curing</u>; S/Ca to Al/Ca atomic ratio plot
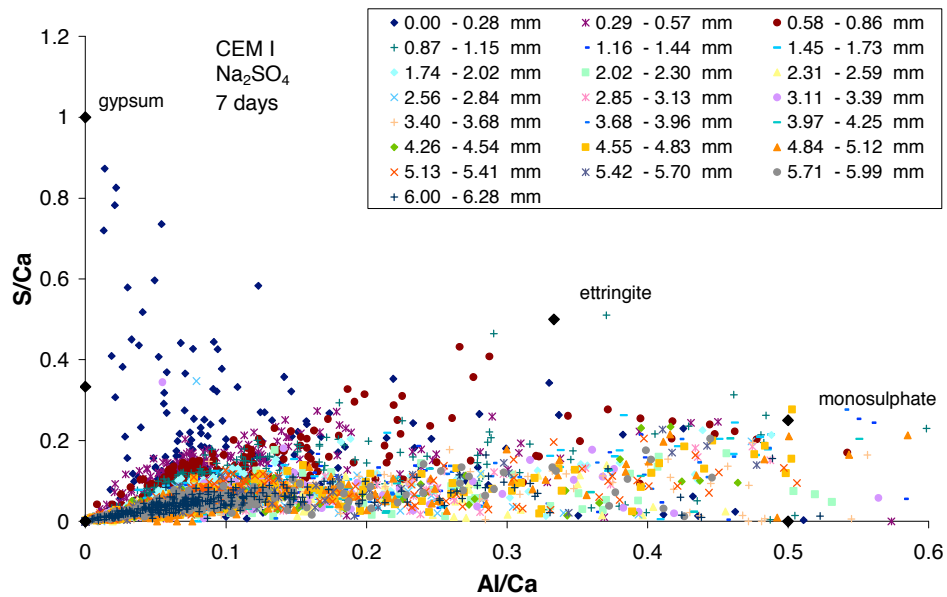
Figure 78: CEM I mortar after 7 days of sodium sulfate solution exposure (1.25 x 1.25 x15 cm³); S/Ca to Al/Ca atomic ratio plot
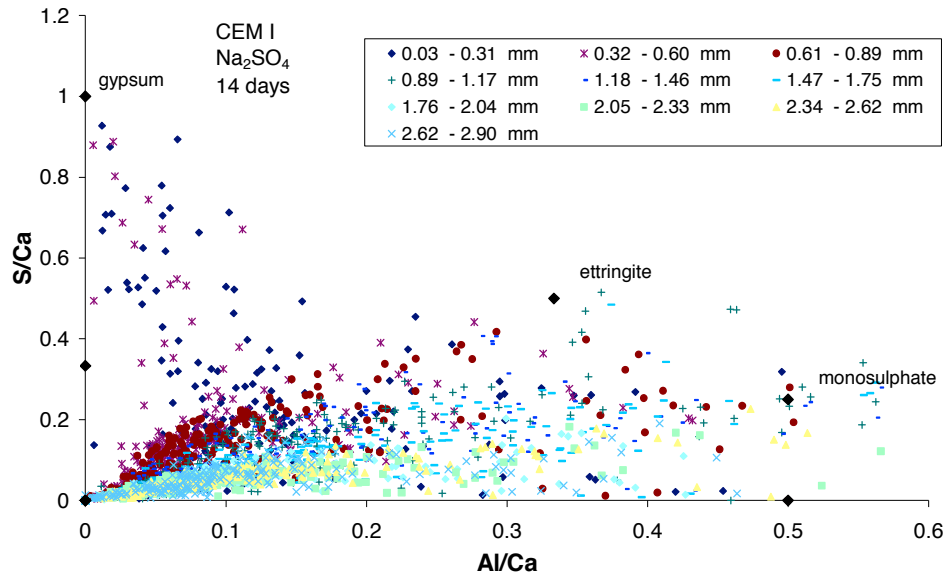
Figure 79: CEM I mortar after 14 days of sodium sulfate solution exposure (1.25 x 1.25 x15 cm³); S/Ca to Al/Ca atomic ratio plot
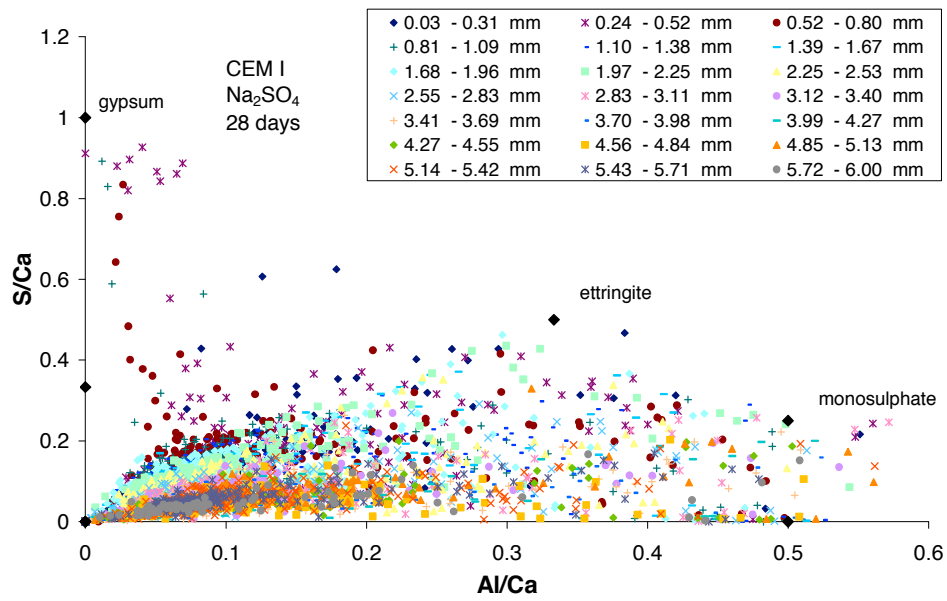
Figure 80: CEM I mortar after 28 days of sodium sulfate solution exposure (1.25 x 1.25 x15 cm³); S/Ca to Al/Ca atomic ratio plot
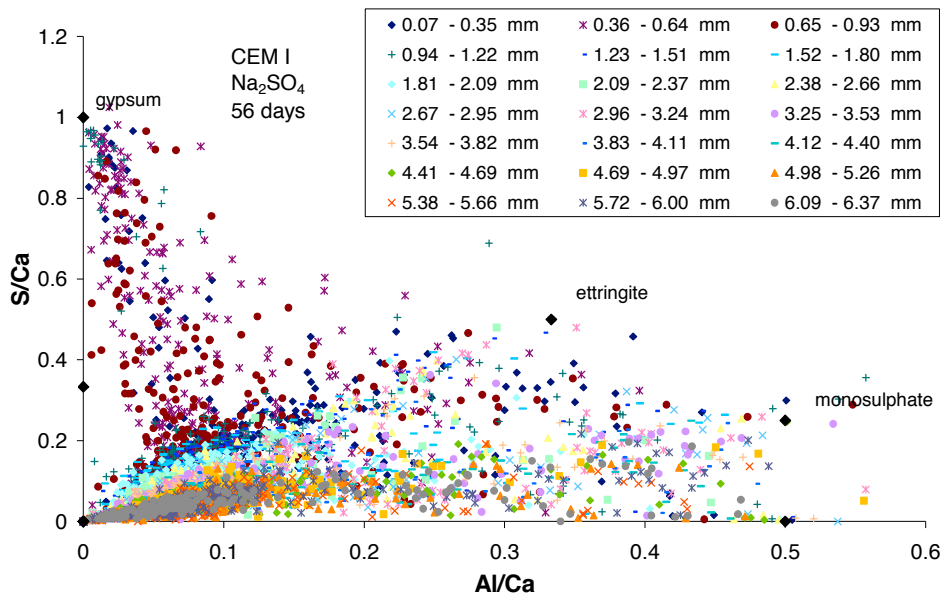
Figure 81: CEM I mortar after 56 days of sodium sulfate solution exposure (1.25 x 1.25 x15 cm^3); S/Ca to Al/Ca atomic ratio plot
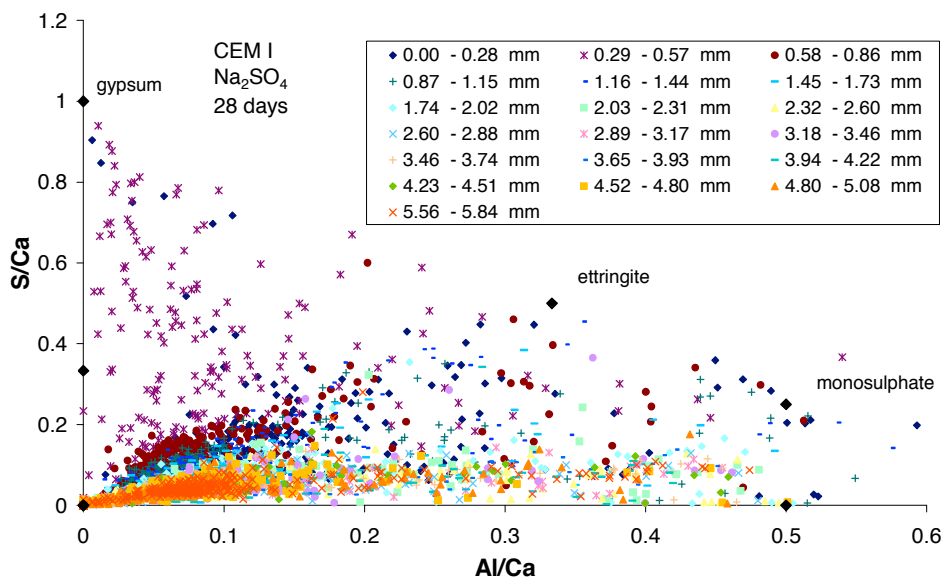
Figure 82: CEM I mortar after 28 days of sodium sulfate solution exposure (5 x 5 x15 cm^3); S/Ca to Al/Ca atomic ratio plot
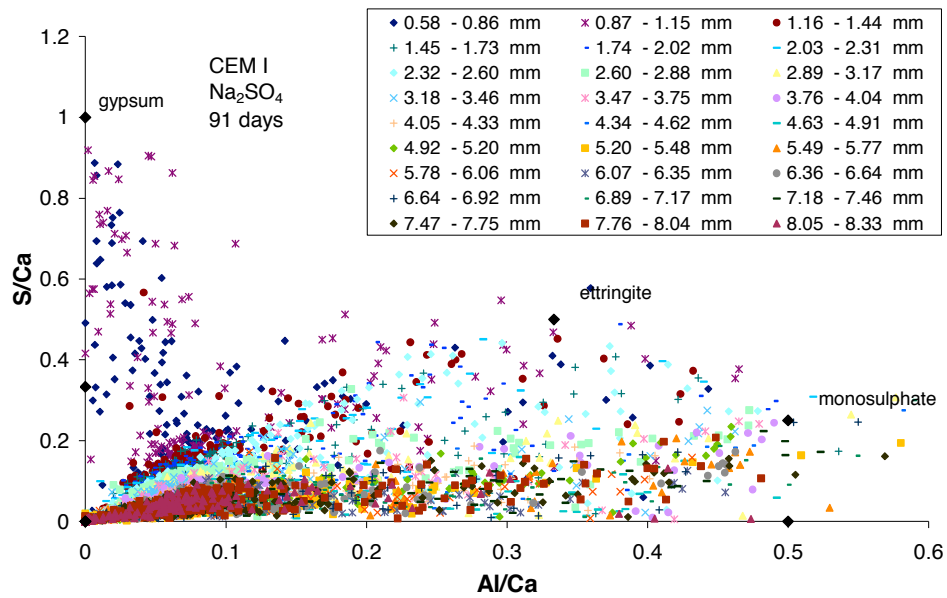
Figure 83: CEM I mortar after 91 days of sodium sulfate solution exposure (5 x 5 x15 cm^3); S/Ca to Al/Ca atomic ratio plot
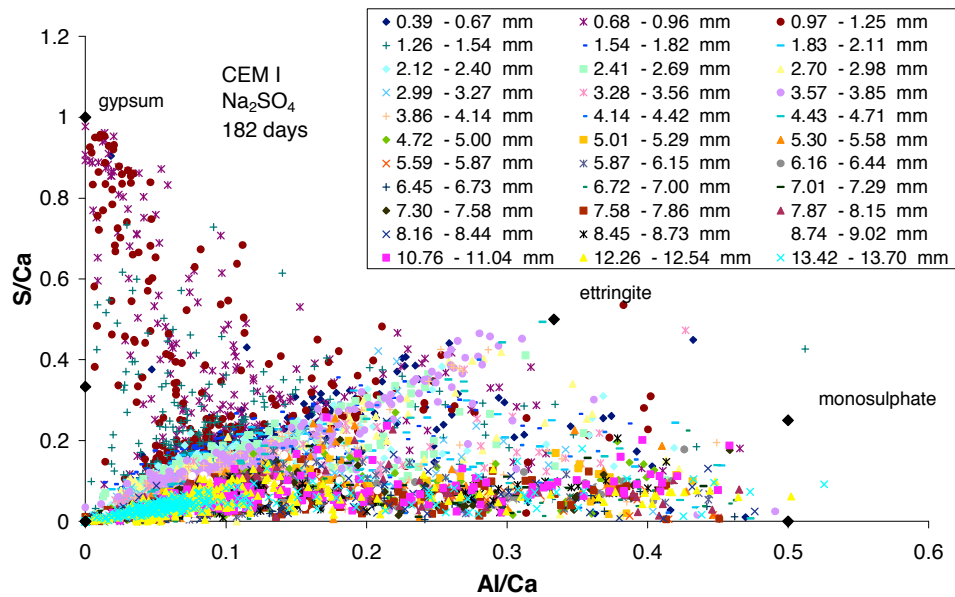
Figure 84: CEM I mortar after 182 days of sodium sulfate solution exposure (5 x 5 x15 cm^3); S/Ca to Al/Ca atomic ratio plot
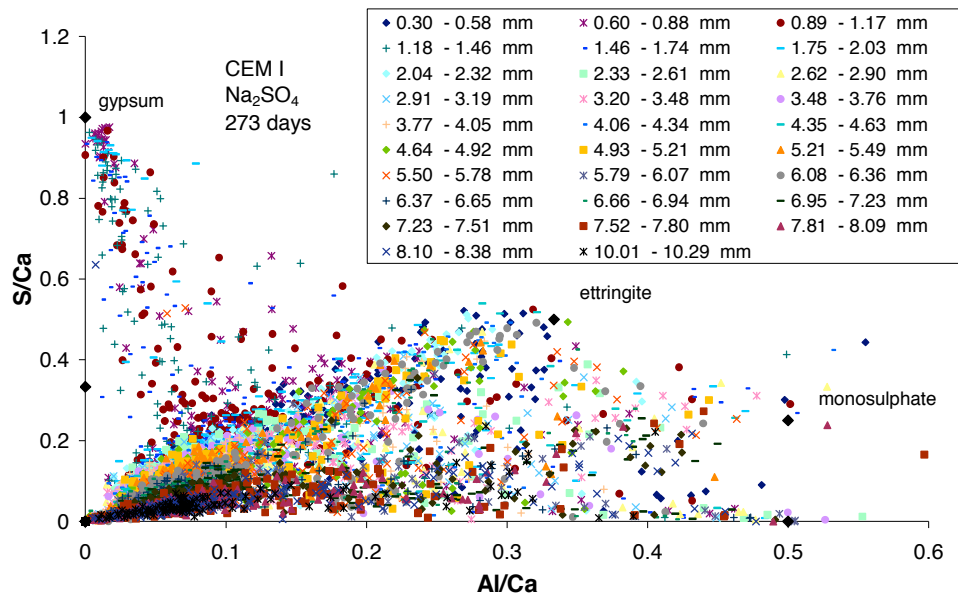
Figure 85: CEM I mortar after 273 days of sodium sulfate solution exposure (5 x 5 x15 cm³); S/Ca to Al/Ca atomic ratio plot

Sodium Bicarbonate Solution
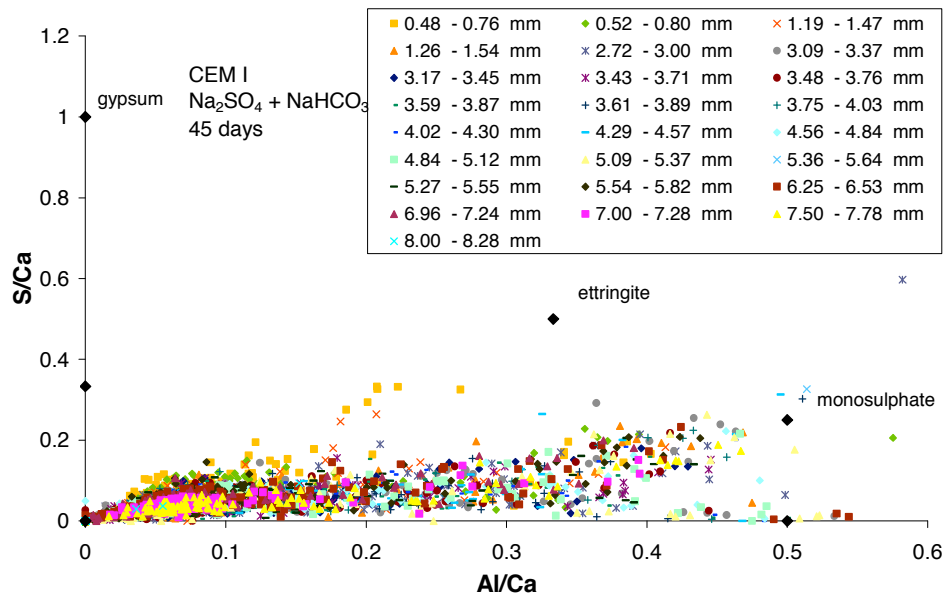
Figure 86: CEM I mortar after 45 days of sodium bicarbonate solution exposure; S/Ca to Al/Ca atomic ratio plot
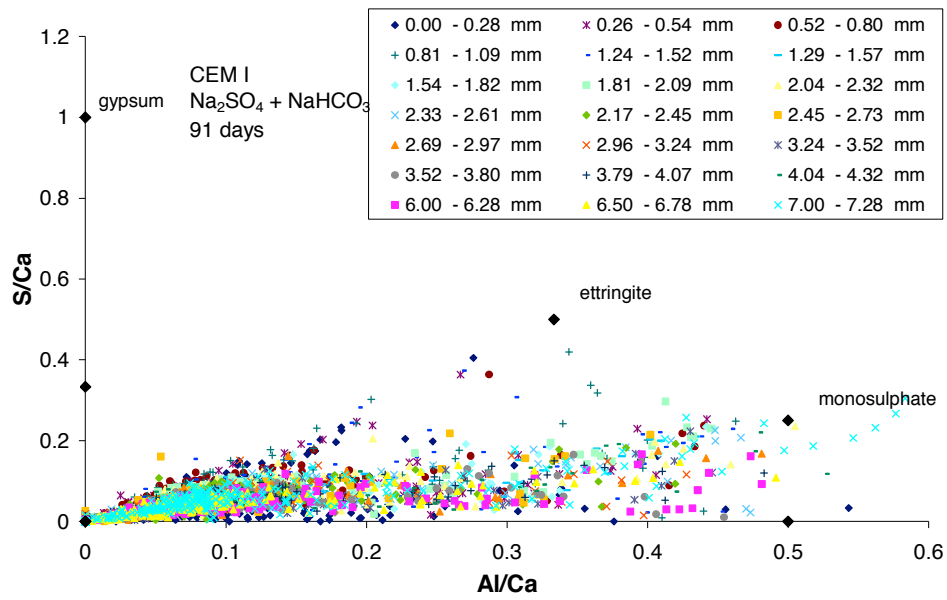
Figure 87: CEM I mortar after 91 days of sodium bicarbonate solution exposure; S/Ca to Al/Ca atomic ratio plot
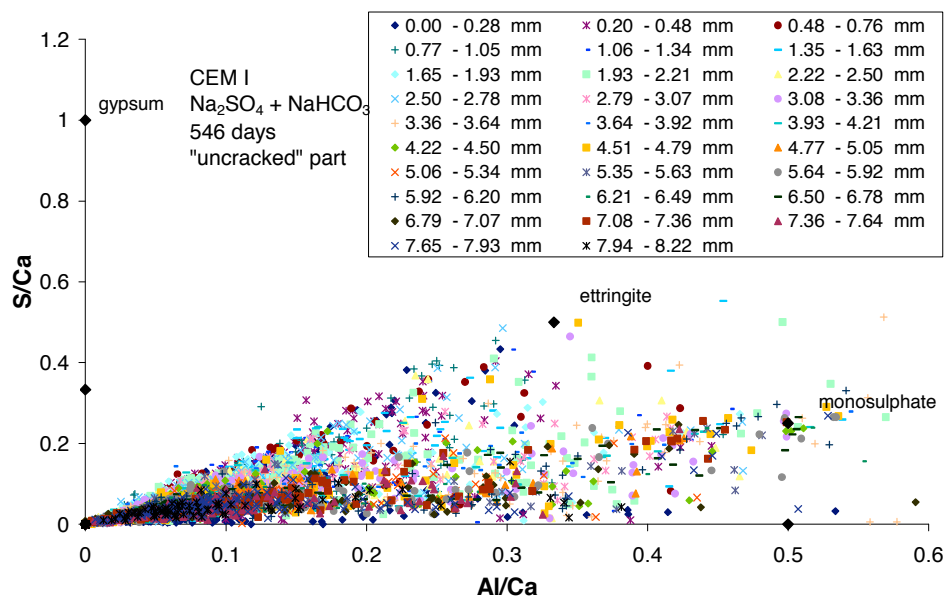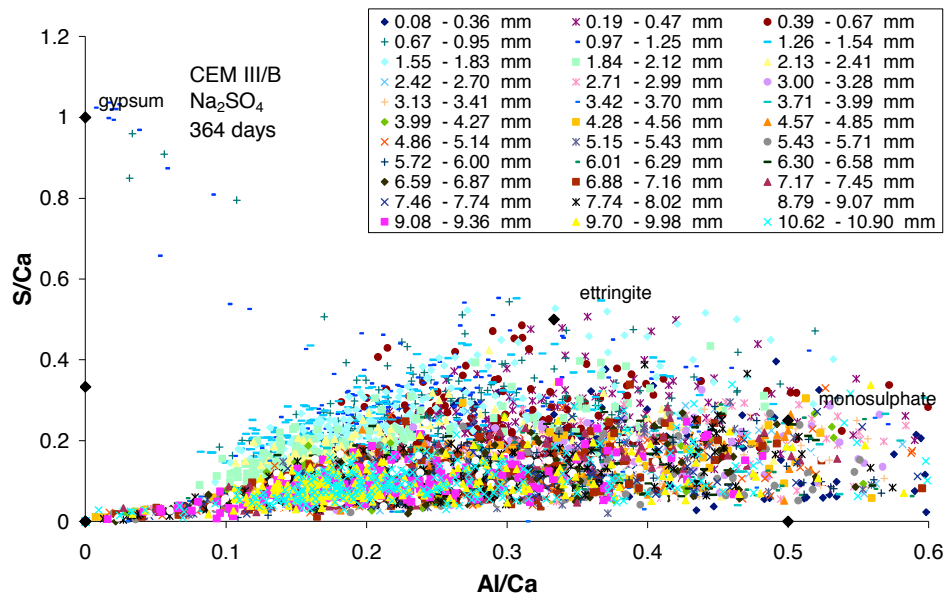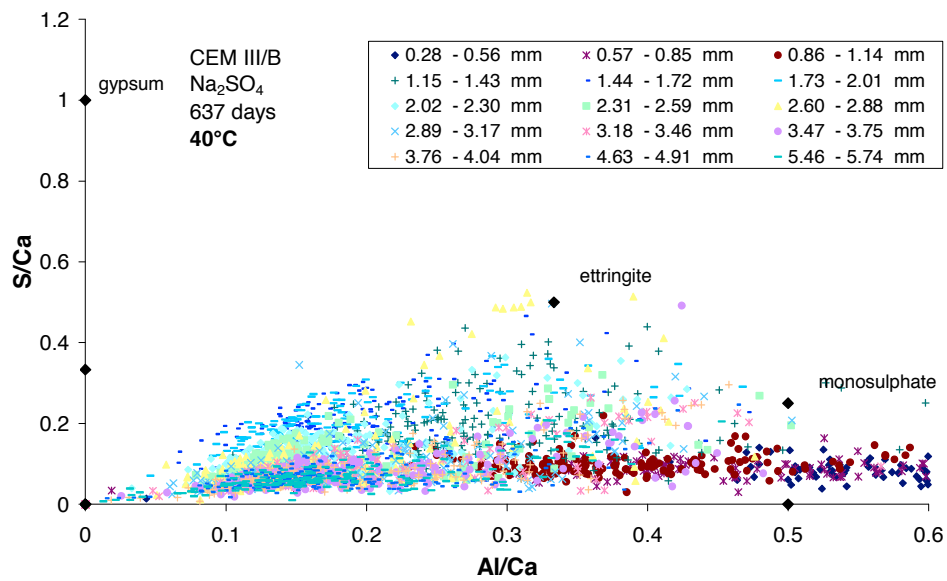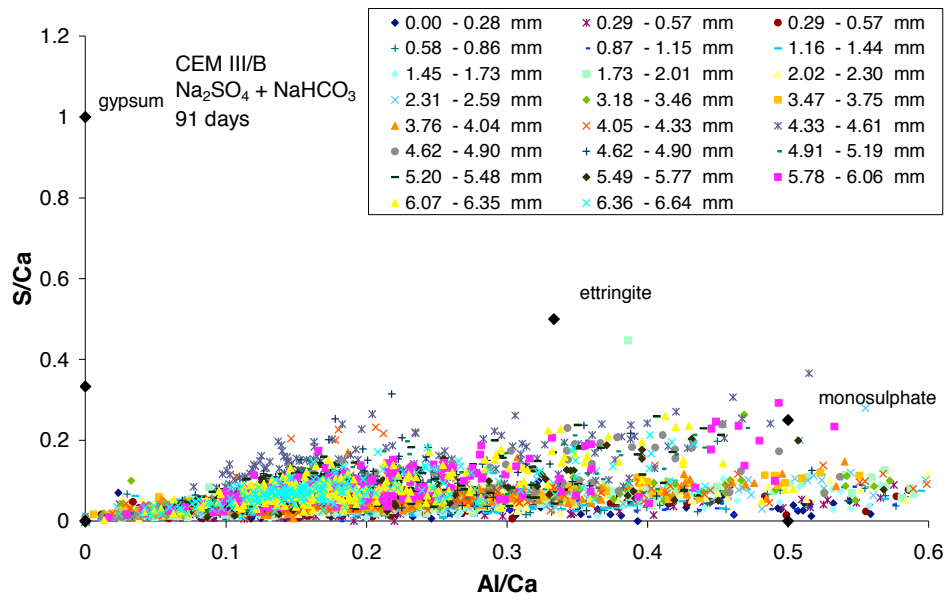

Figure 88: CEM I mortar after 546 days of sodium bicarbonate solution exposure; S/Ca to Al/Ca atomic ratio plot of a not cracked part of a mortar
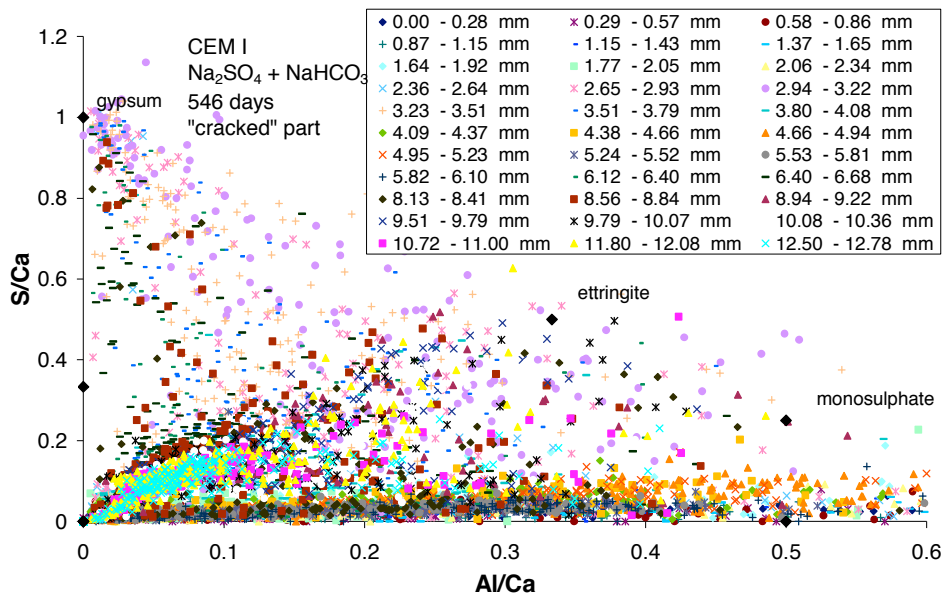
Figure 89: CEM I mortar after 546 days of sodium bicarbonate solution exposure; S/Ca to Al/Ca atomic ratio plot of a <u>cracked</u> part of a mortar

Potassium Sulfate Solution
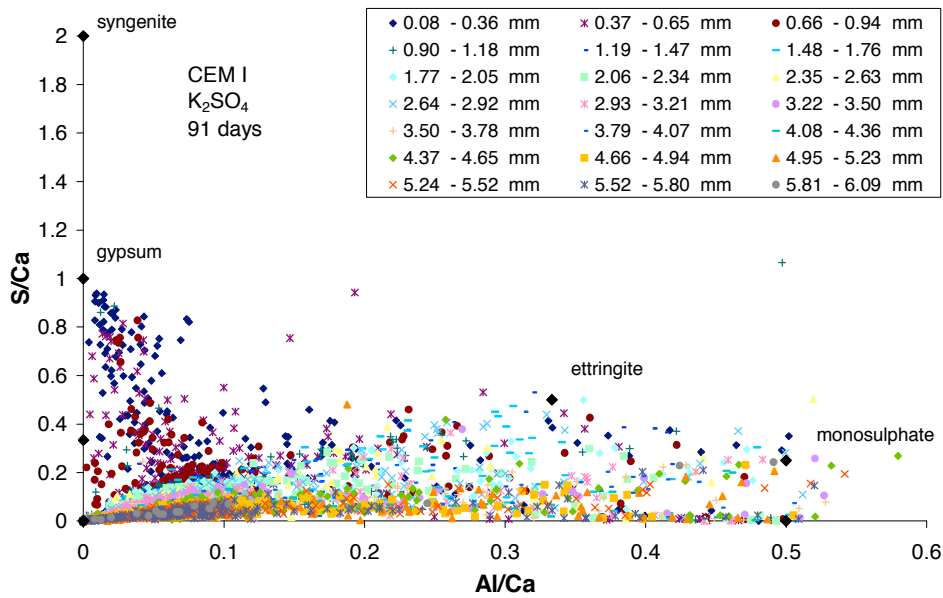
Figure 90: CEM I mortar after 91 days of potassium sulfate solution exposure; S/Ca to Al/Ca atomic ratio plot
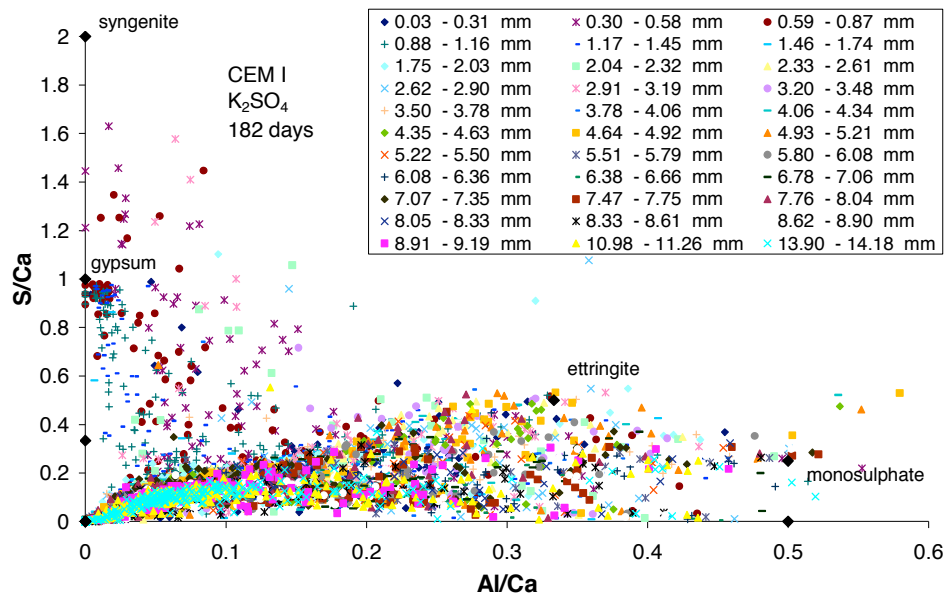
Figure 91: CEM I mortar after 182 days of potassium sulfate solution exposure; S/Ca to Al/Ca atomic ratio plot
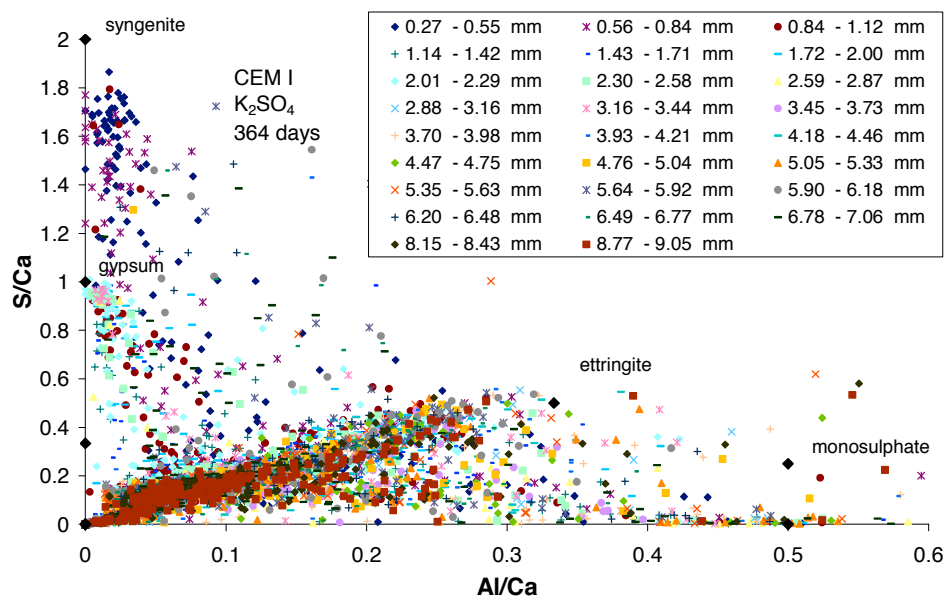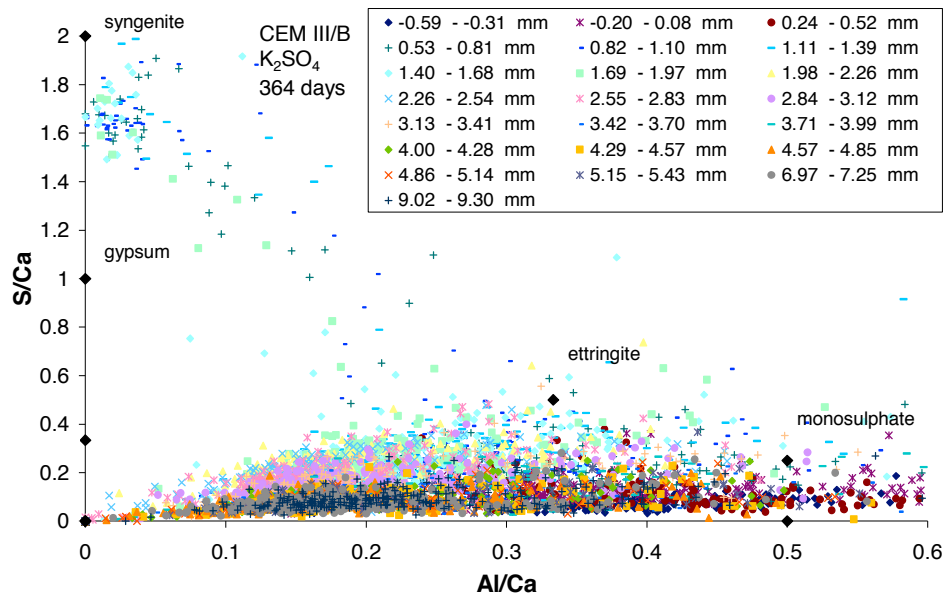

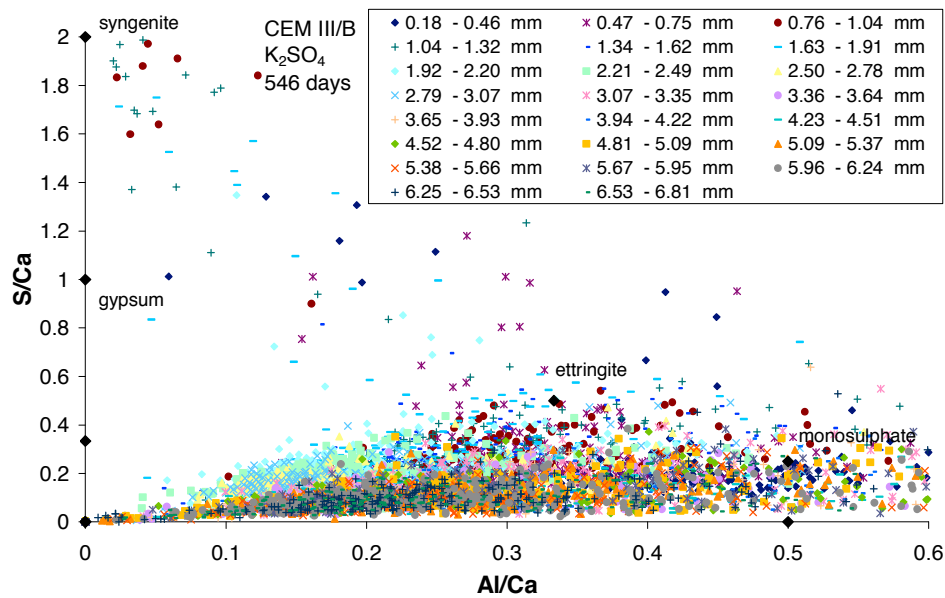**Figure 92**: CEM I mortar after 364 days of potassium sulfate solution exposure; S/Ca to Al/Ca atomic ratio plot

Magnesium Sulfate Solution
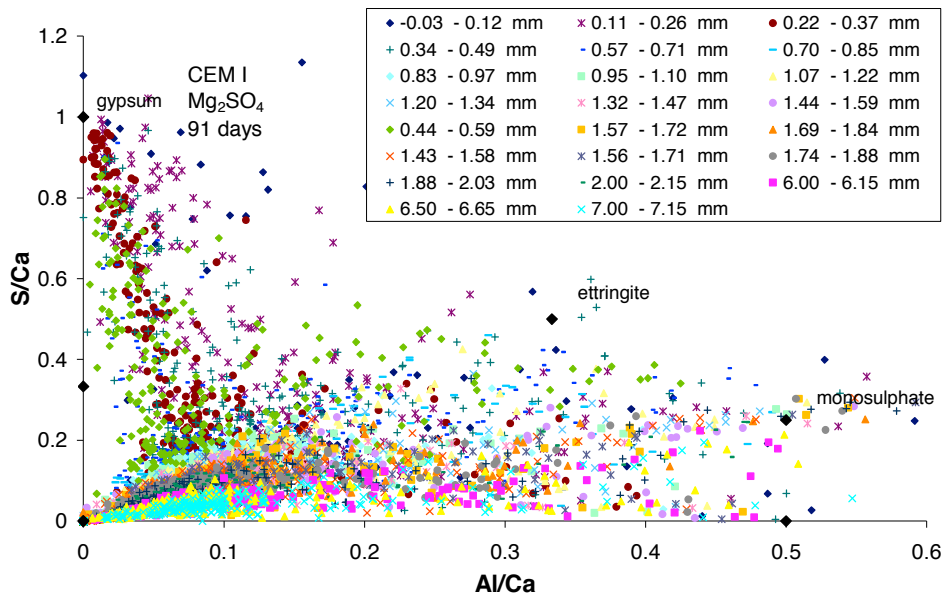
Figure 93: CEM I mortar after 91 days of magnesium sulfate solution exposure (0.35 mol/l); S/Ca to Al/Ca atomic ratio plot
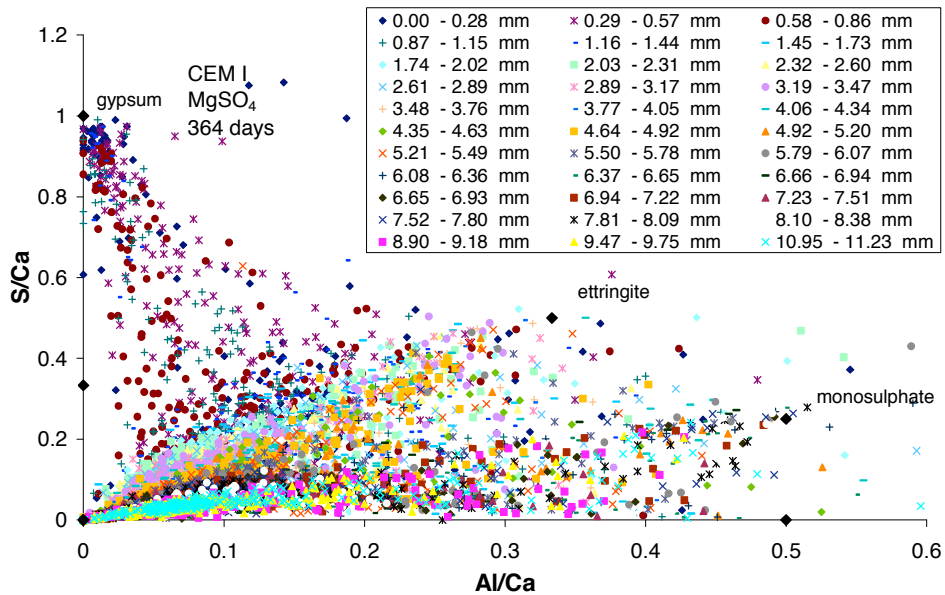
Figure 94: CEM I mortar after 364 days of magnesium sulfate solution exposure (0.35 mol/l); S/Ca to Al/Ca atomic ratio plot
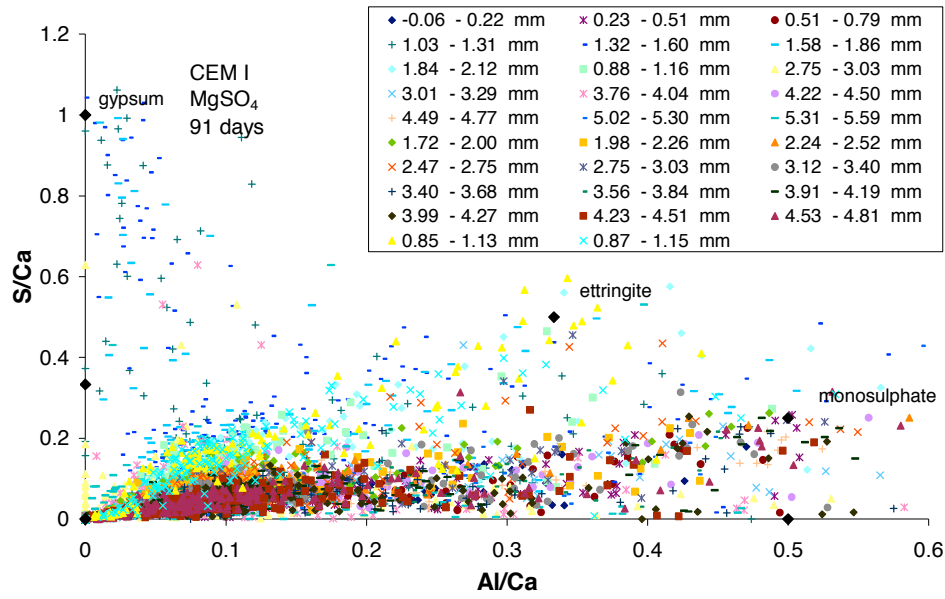
Figure 95: CEM I mortar after 91 days of magnesium sulfate solution exposure (0.035 mol/l); S/Ca to Al/Ca atomic ratio plot
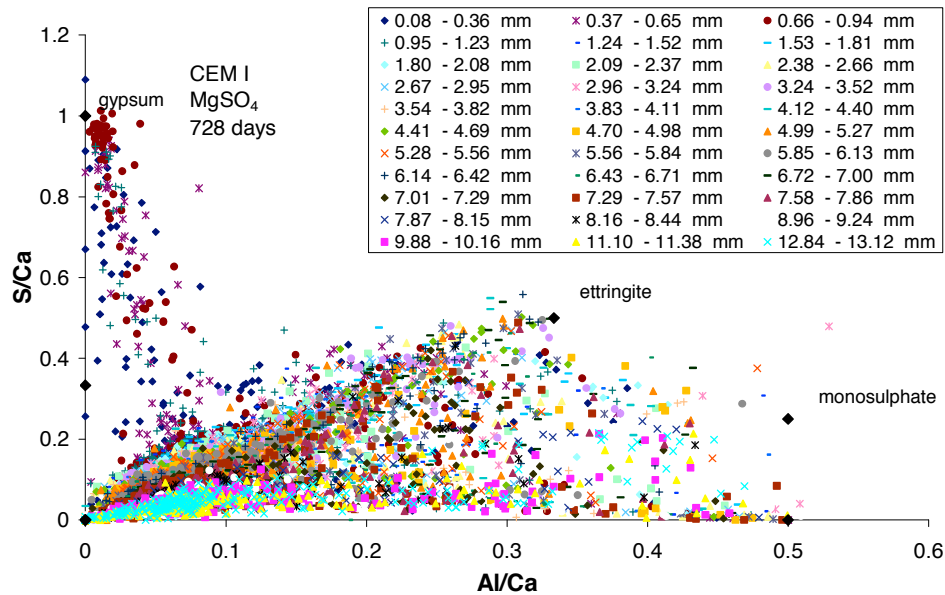
Figure 96: CEM I mortar after 728 days of magnesium sulfate solution exposure (0.035 mol/l); S/Ca to Al/Ca atomic ratio plot
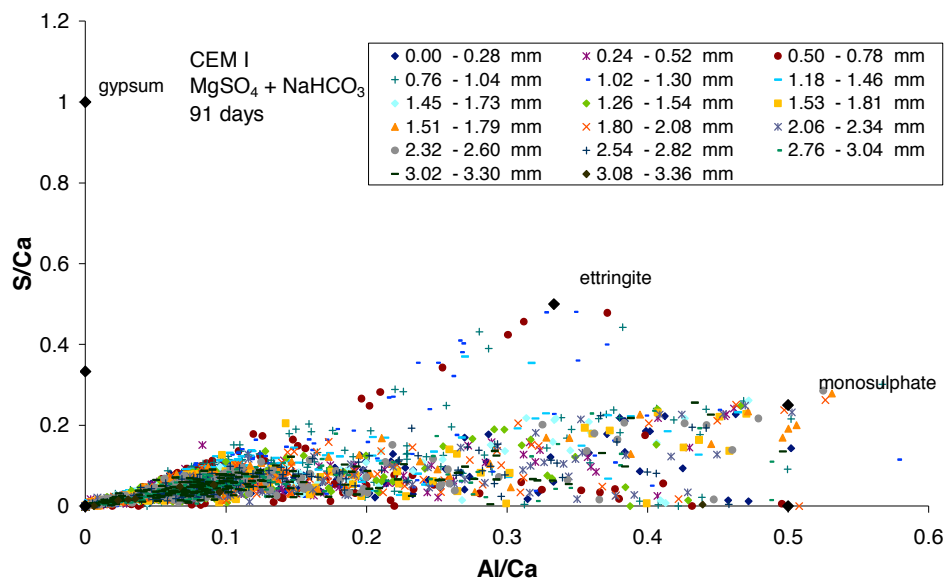
Figure 97: CEM I mortar after 91 days of magnesium bicarbonate solution exposure (0.035 mol/l); S/Ca to Al/Ca atomic ratio plot
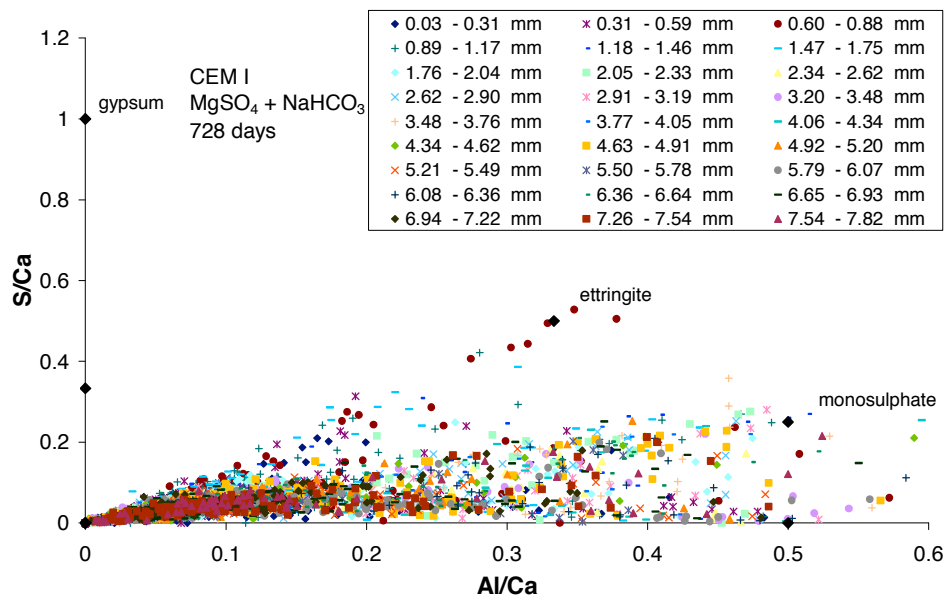
Figure 98: CEM I mortar after 728 days of magnesium bicarbonate solution exposure (0.035 mol/l); S/Ca to Al/Ca atomic ratio plot
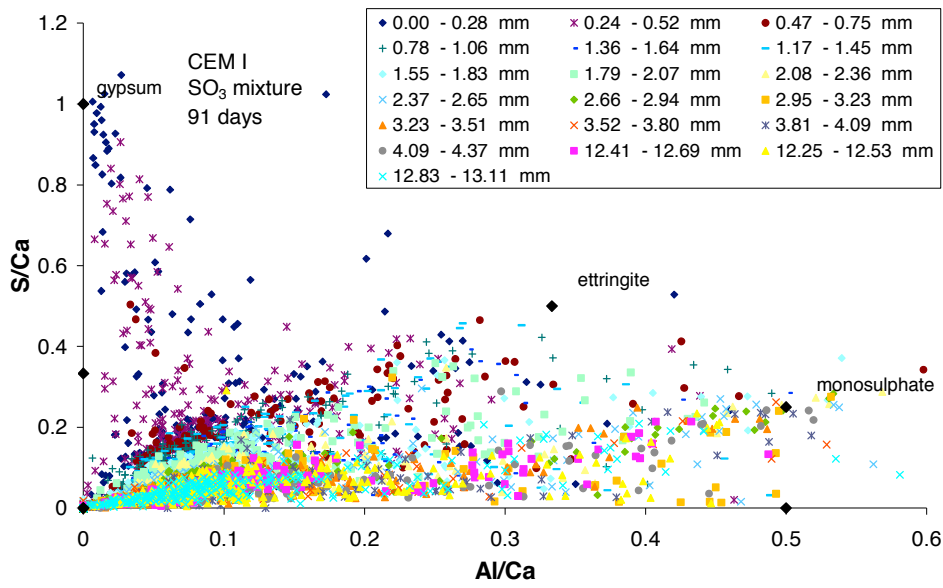
Sulfate mixture

Figure 99: CEM I mortar after 91 days of sulfate mixture solution exposure; S/Ca to Al/Ca atomic ratio plot
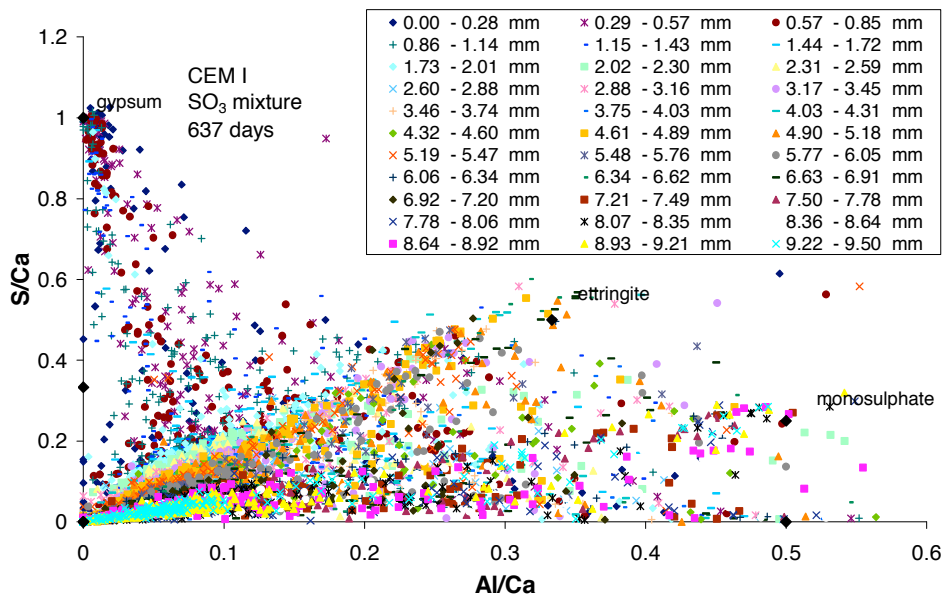
Figure 100: CEM I mortar after 637 days of sulfate mixture solution exposure; S/Ca to Al/Ca atomic ratio plot

Bicarbonate Mixture Solution
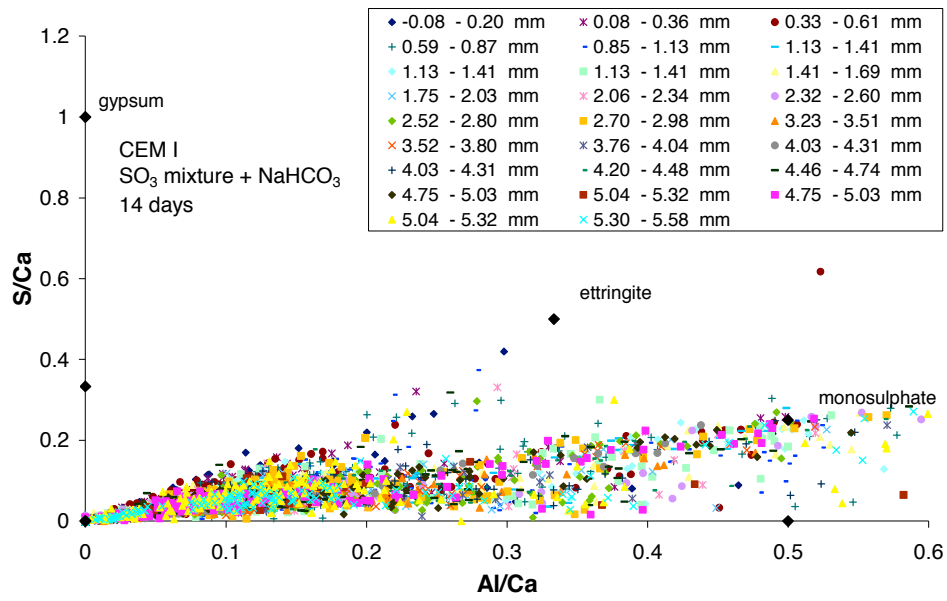
Figure 101: CEM I mortar after 14 days of bicarbonate mixture solution exposure; S/Ca to Al/Ca atomic ratio plot
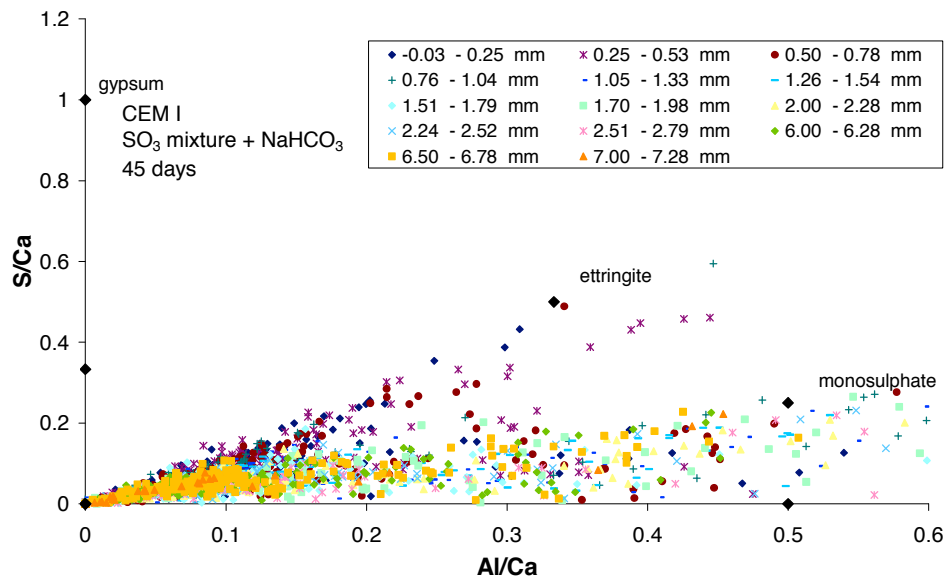
Figure 102: CEM I mortar after 45 days of bicarbonate mixture solution exposure; S/Ca to Al/Ca atomic ratio plot
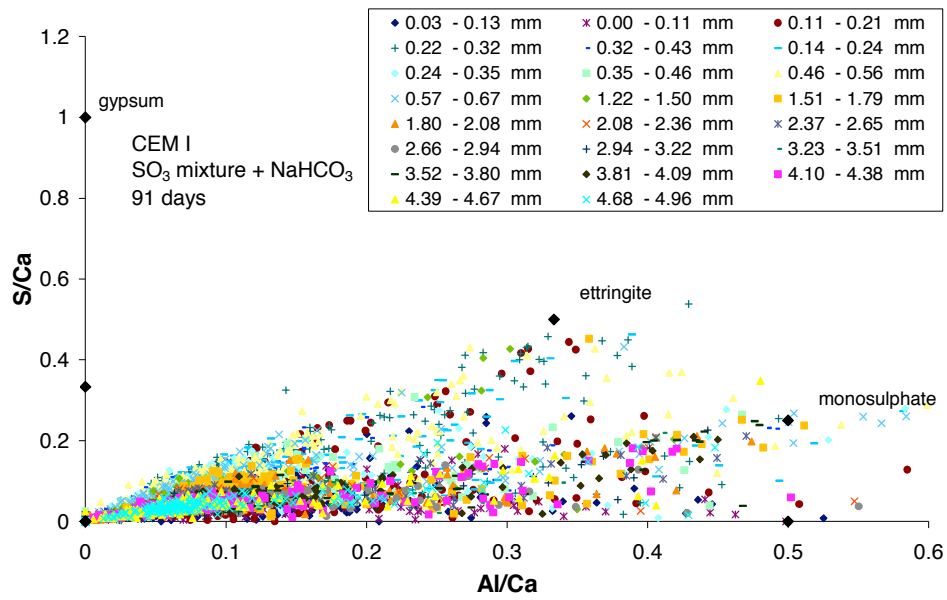
Figure 103: CEM I mortar after 91 days of bicarbonate mixture solution exposure; S/Ca to Al/Ca atomic ratio plot
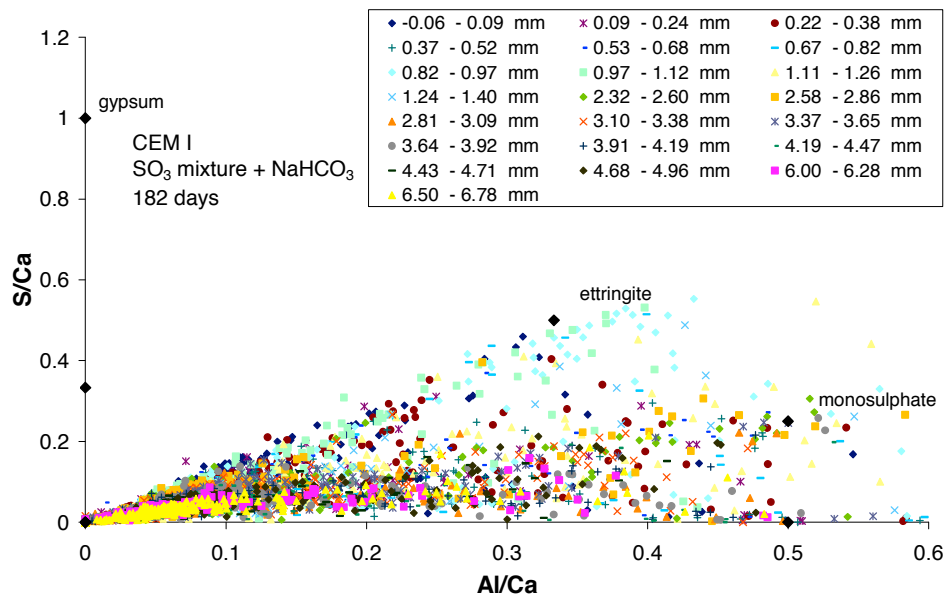
Figure 104: CEM I mortar after 182 days of bicarbonate mixture solution exposure; S/Ca to Al/Ca atomic ratio plot
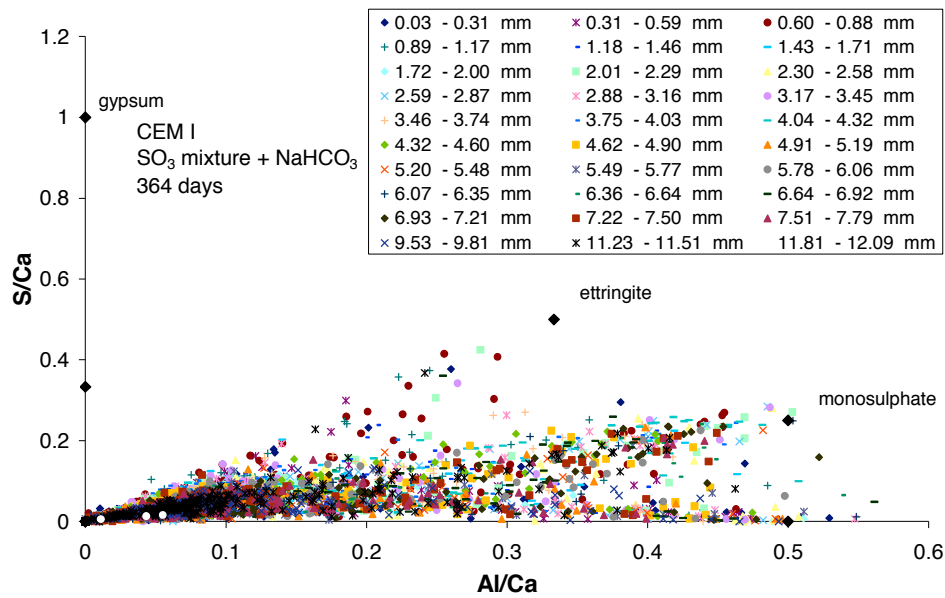
Figure 105: CEM I mortar after 364 days of bicarbonate mixture solution exposure; S/Ca to Al/Ca atomic ratio plot
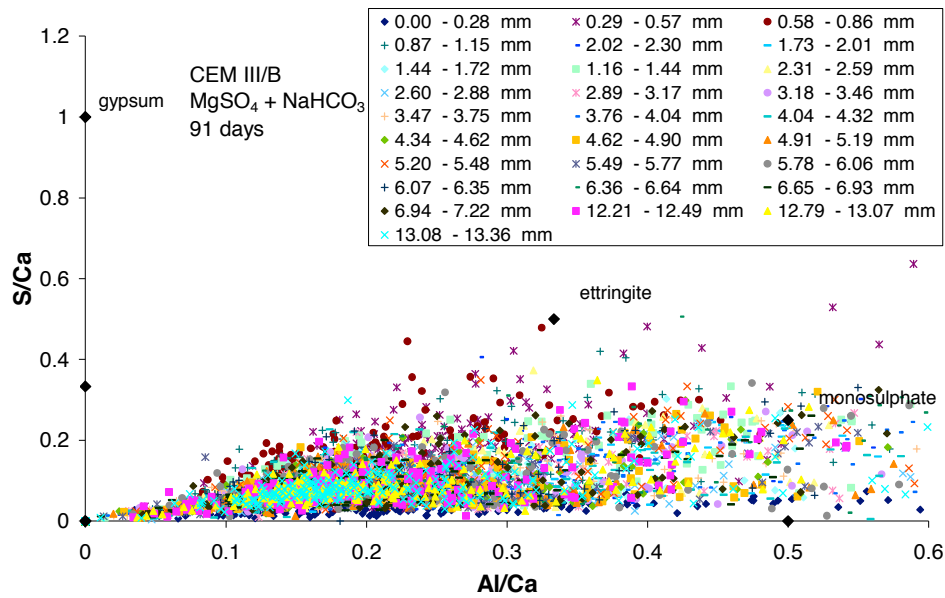
Bicarbonate Mixture Solution *(0.035 mol/l)*
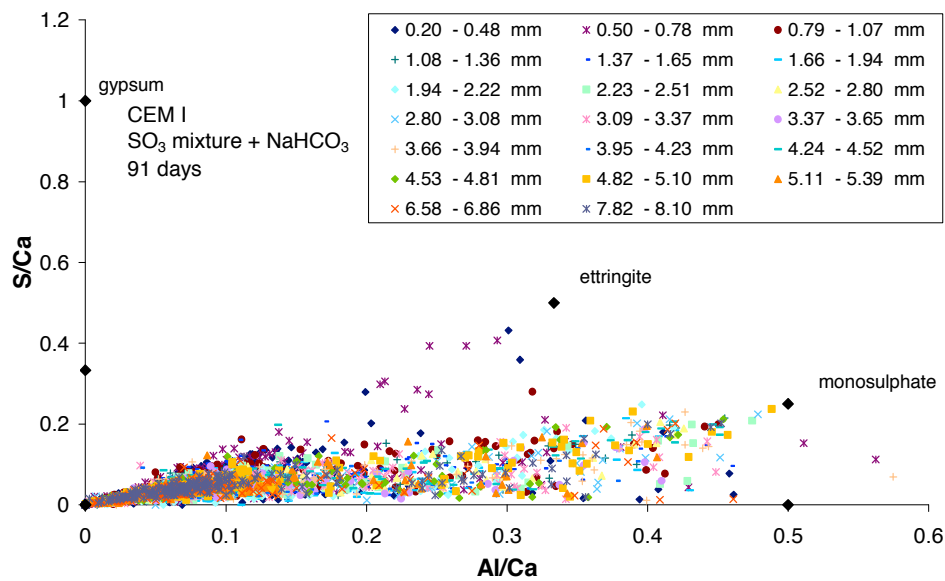
Figure 106: CEM I mortar after 91 days of bicarbonate mixture solution exposure (0.035 mol/l); S/Ca to Al/Ca atomic ratio plot
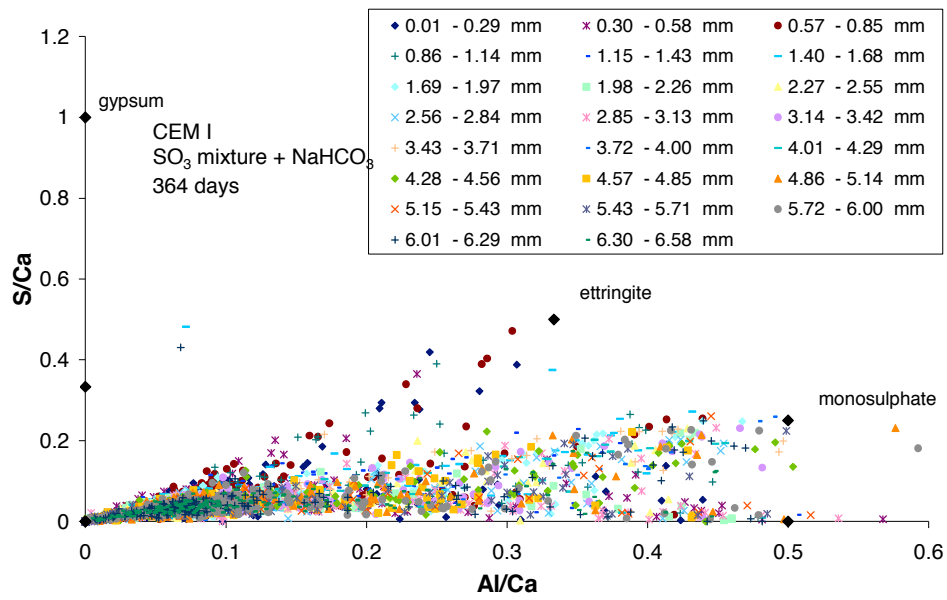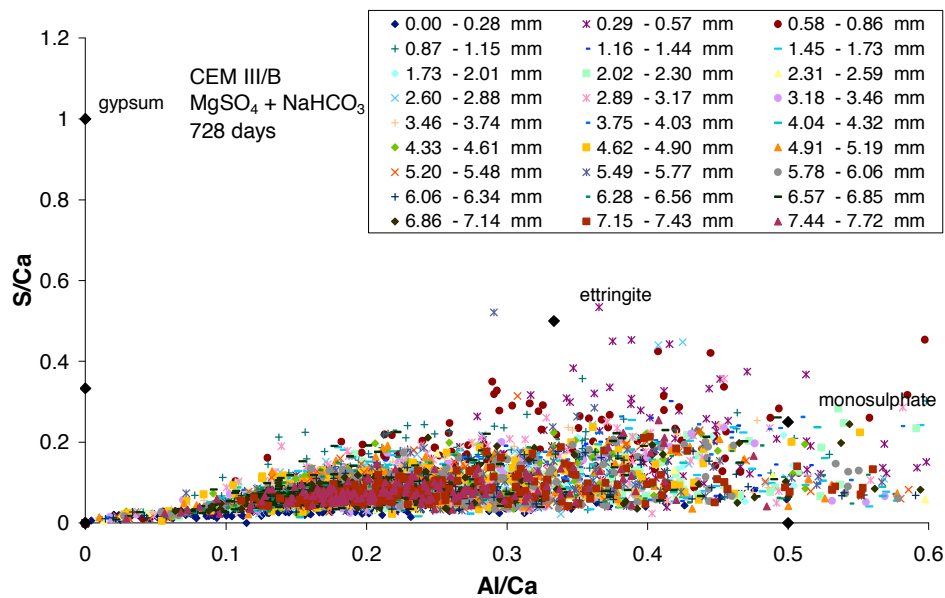
Figure 107: CEM I mortar after 364 days of bicarbonate mixture solution exposure (0.035 mol/l); S/Ca to Al/Ca atomic ratio plot

CEM I + 2% gypsum

Calcium Hydroxide Solution
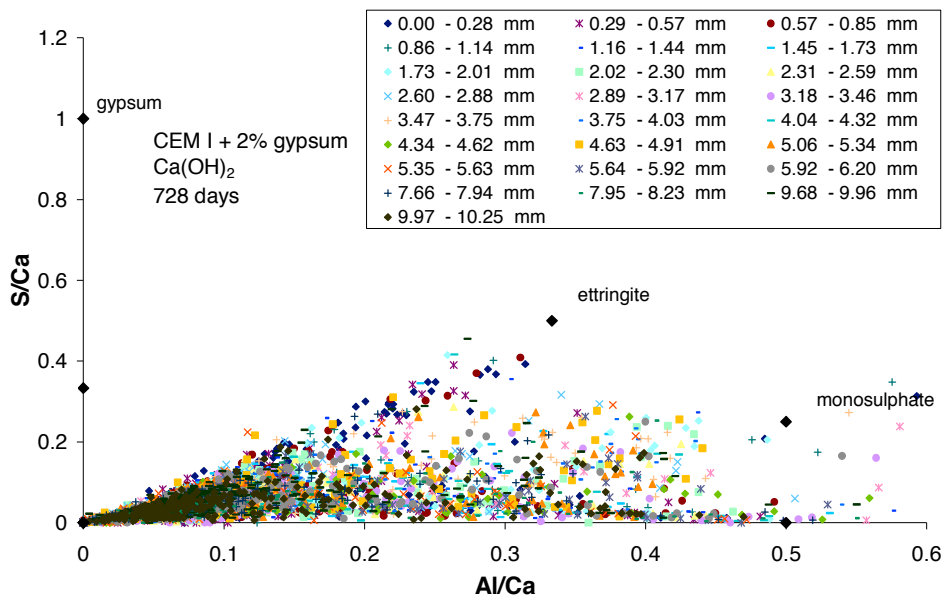
Figure 108: CEM I + 2% gypsum mortar after 728 days in saturated lime solution; S/Ca to Al/Ca atomic ratio plot

Sodium Sulfate Solution
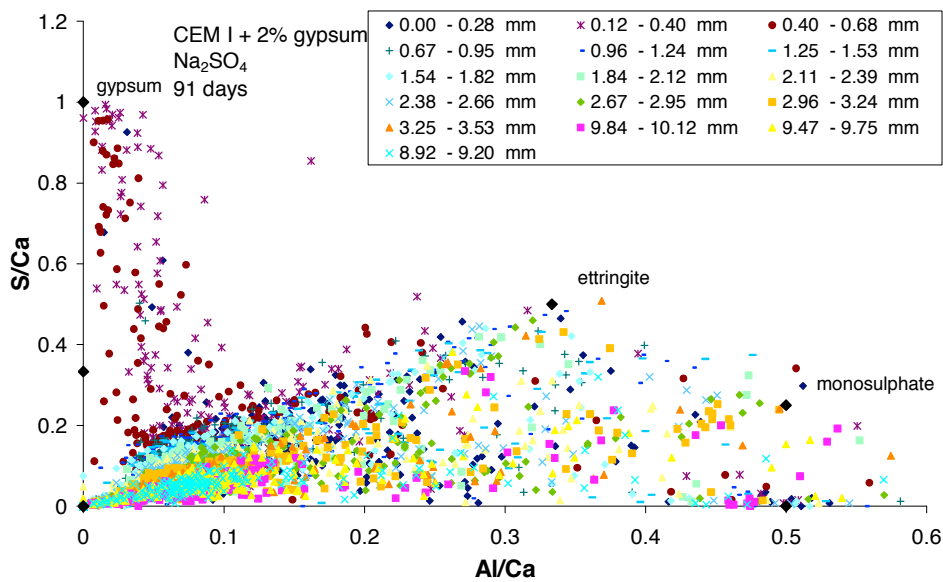
Figure 109: CEM I + 2% gypsum mortar after 91 days of sodium sulfate solution exposure; S/Ca to Al/Ca atomic ratio plot
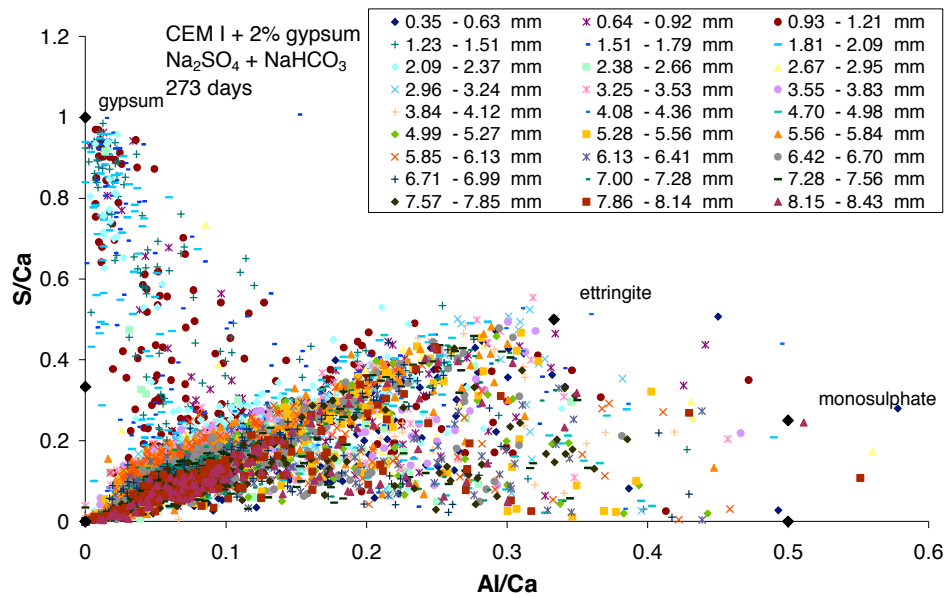
Figure 110: CEM I + 2% gypsum mortar after 273 days of sodium sulfate solution exposure; S/Ca to Al/Ca atomic ratio plot
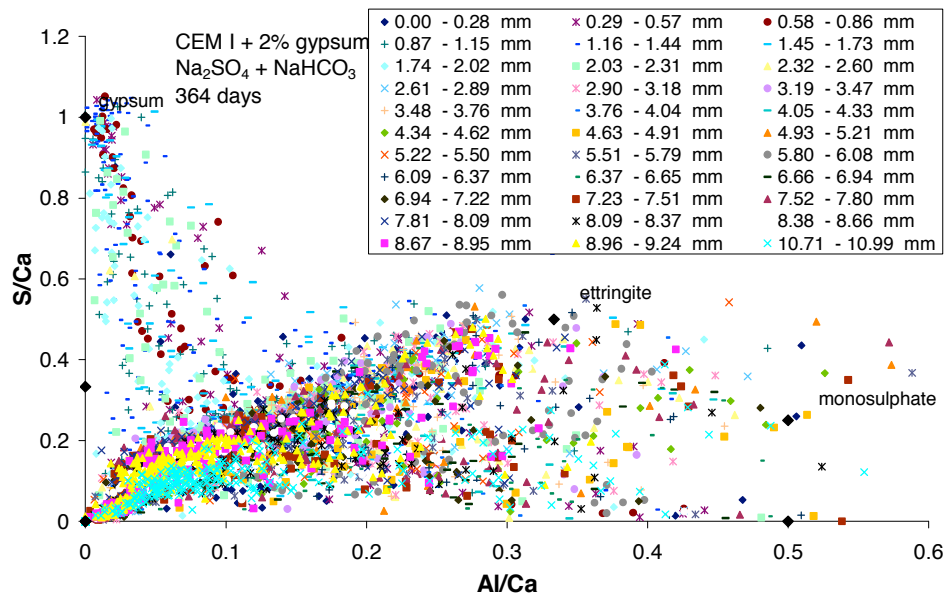
Figure 111: CEM I + 2% gypsum mortar after 273 days of sodium sulfate solution exposure; S/Ca to Al/Ca atomic ratio plot

CEM I + 6% Silica Fume

<u>Calcium Hydroxide Solution</u>
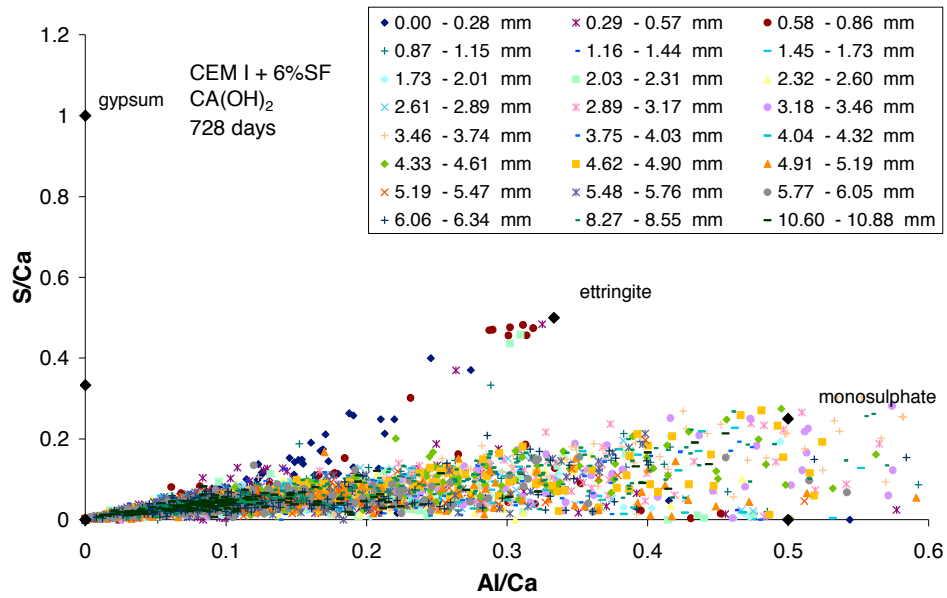
Figure 112: CEM I +6% SF mortar after 728 days in saturated lime solution; S/Ca to Al/Ca atomic ratio plot

<u>Sodium Sulfate Solution</u>
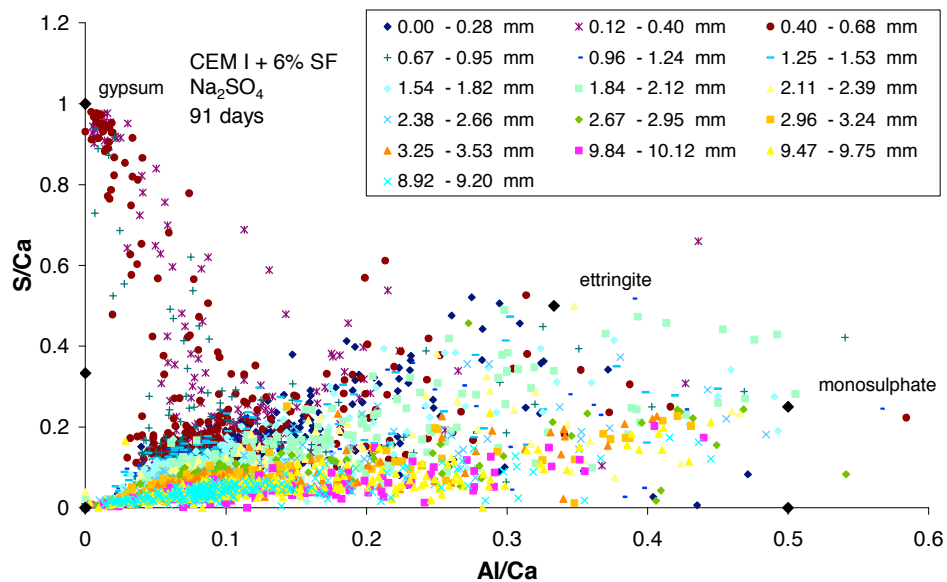
Figure 113: CEM I + 6%SF mortar after 91 days of sodium sulfate solution exposure; S/Ca to Al/Ca atomic ratio plot
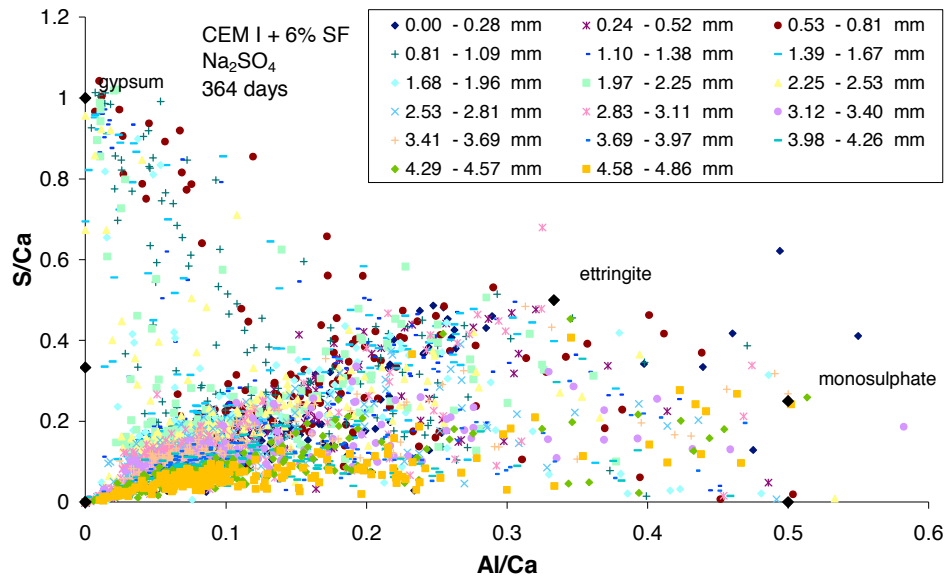
Figure 114: CEM I + 6%SF mortar after 364 days of sodium sulfate solution exposure; S/Ca to Al/Ca atomic ratio plot

Bicarbonate Mixture Solution
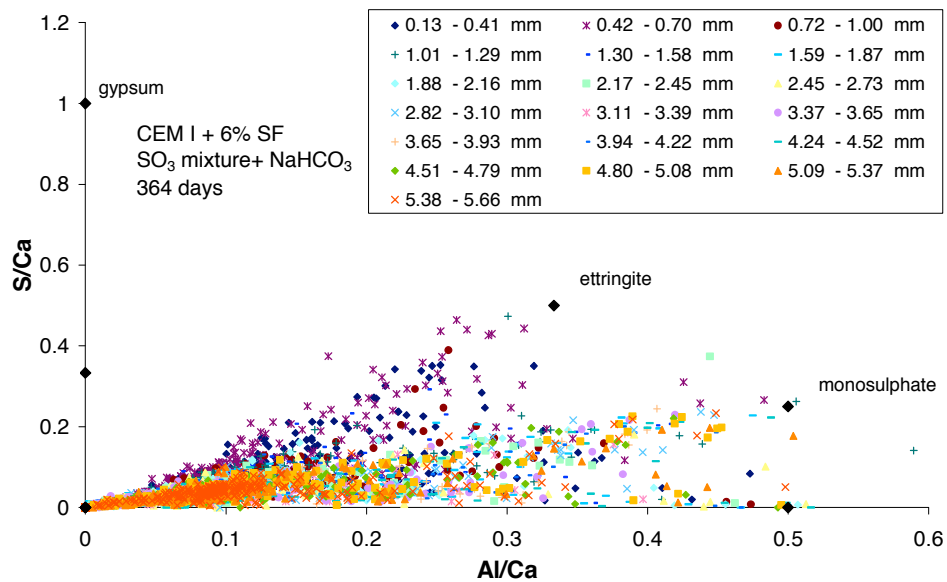
Figure 115: CEM I + 6%SF mortar after 364 days of bicarbonate mixture solution exposure; S/Ca to Al/Ca atomic ratio plot

CEM I + 12% Silica Fume

<u>Initial state</u>
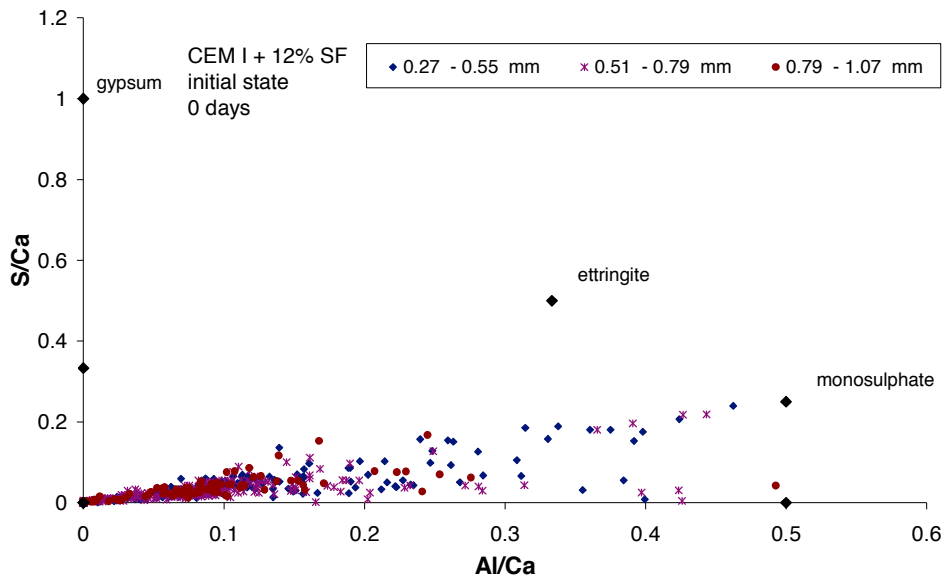
Figure 116: CEM I + 12% SF mortar before sulfate exposure; S/Ca to Al/Ca atomic ratio plot

<u>Calcium Hydroxide Solution</u>
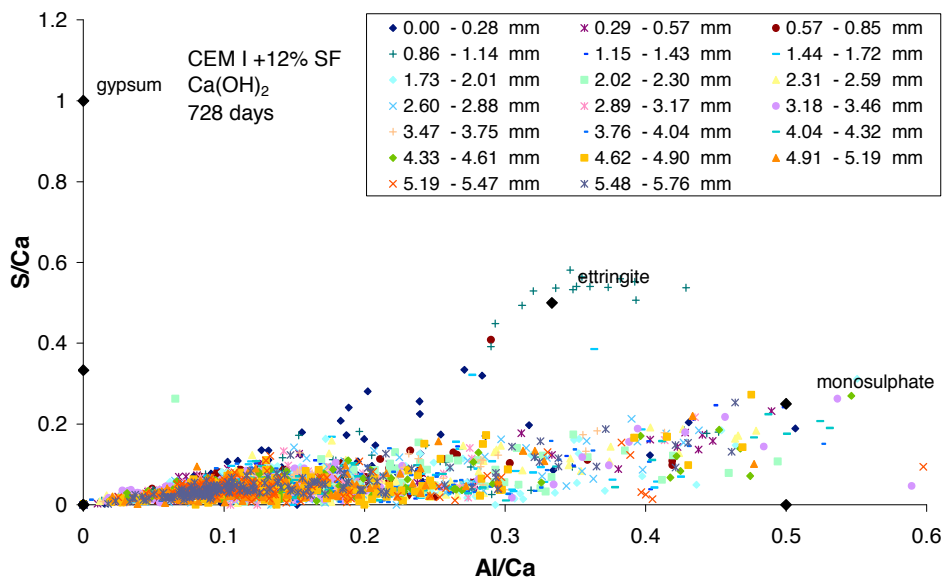
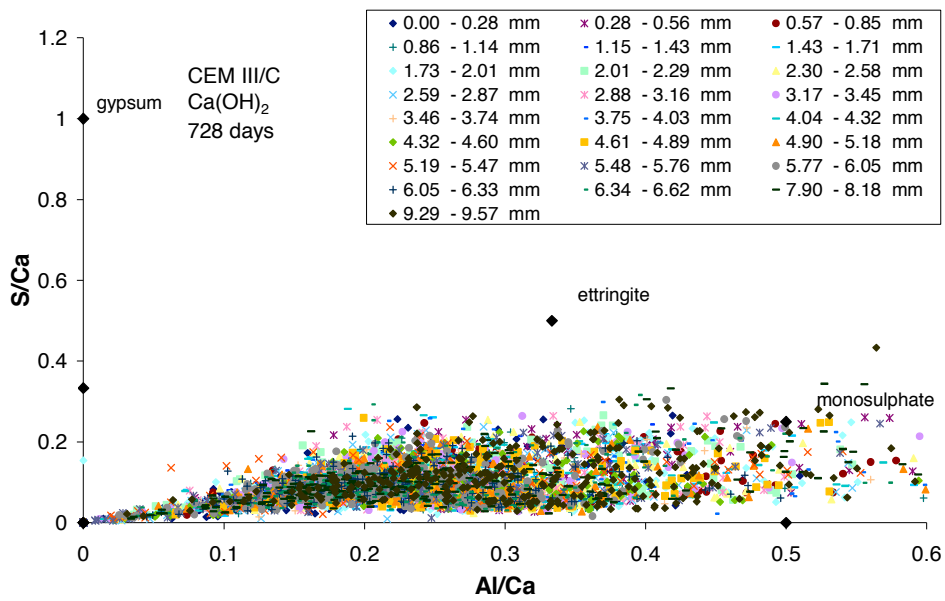**Figure 117**: CEM I +12% SF mortar after 728 days in saturated lime solution; S/Ca to Al/Ca atomic ratio plot
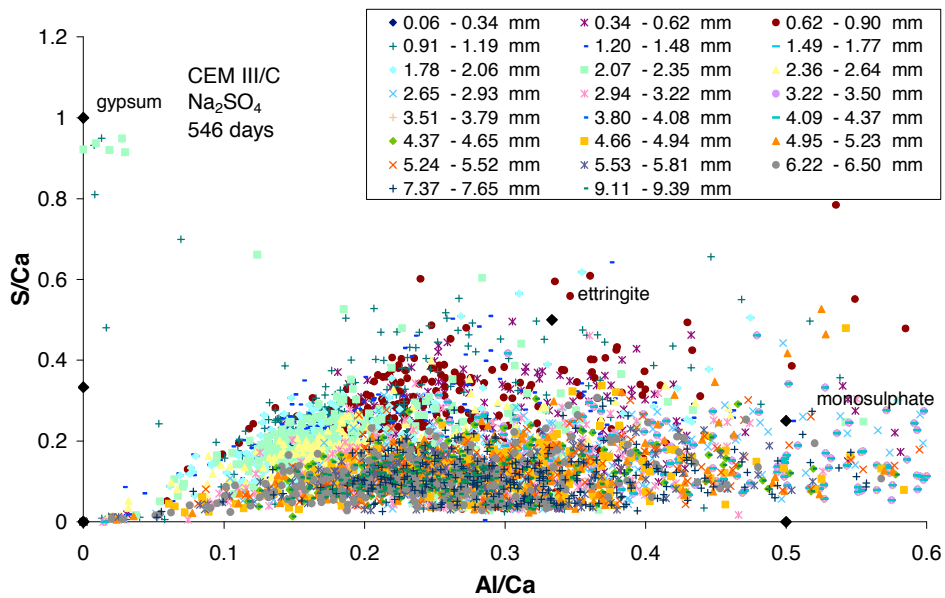
Sodium Sulfate Solution
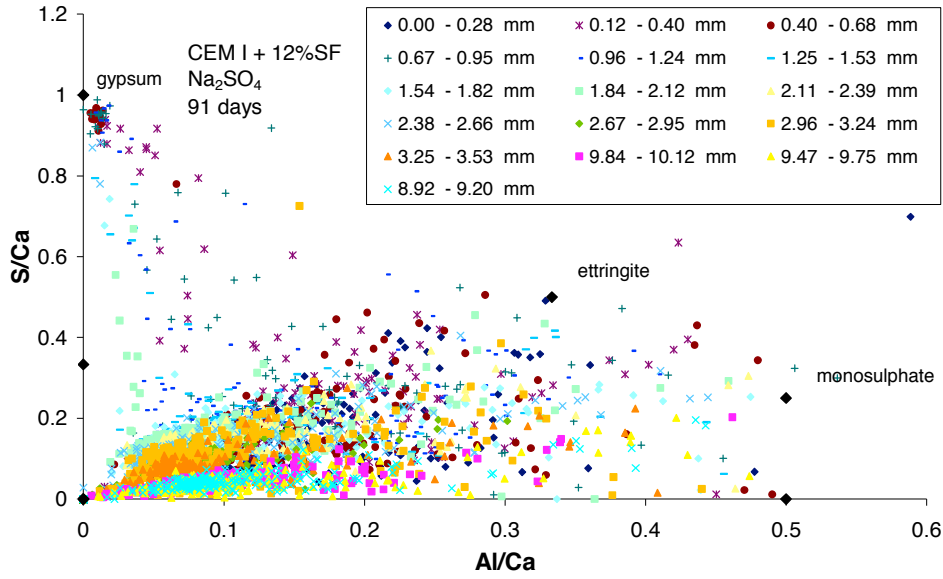
Figure 118: CEM I + 12%SF mortar after 91 days of sodium sulfate solution exposure; S/Ca to Al/Ca atomic ratio plot
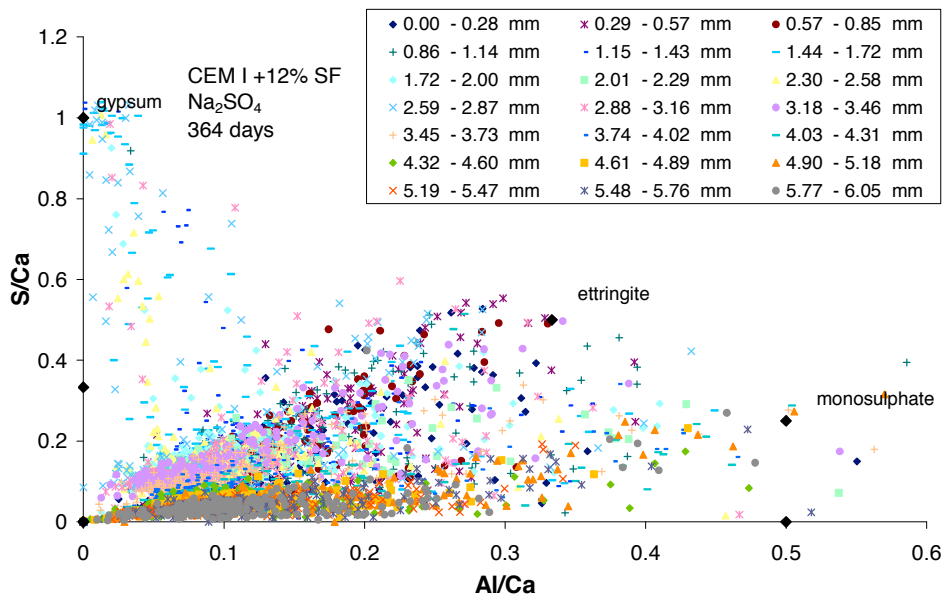
Figure 119: CEM I + 12%SF mortar after 364 days of sodium sulfate solution exposure; S/Ca to Al/Ca atomic ratio plot

Bicarbonate Mixture Solution
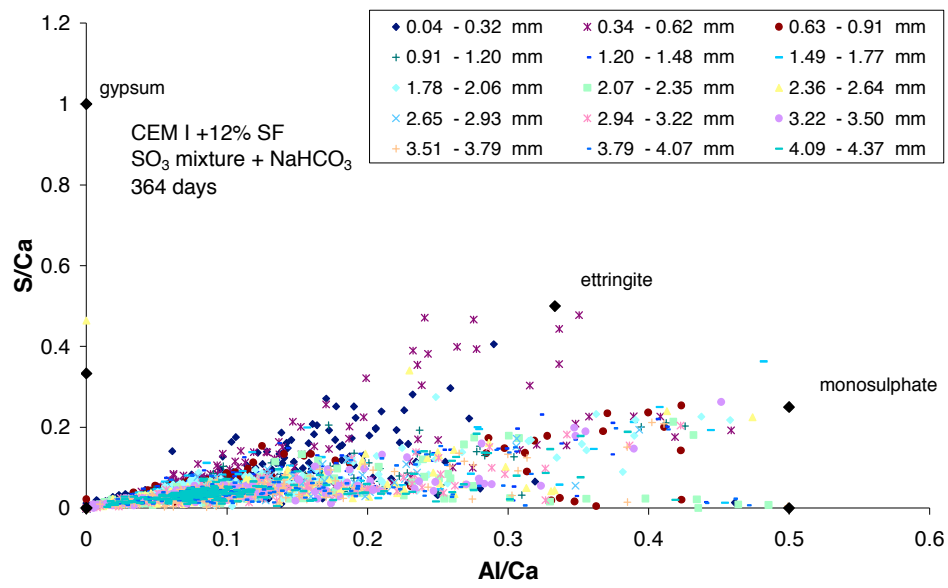
Figure 120: CEM I + 12%SF mortar after 364 days of bicarbonate mixture solution exposure; S/Ca to Al/Ca atomic ratio plot

CEM I HS

Initial state
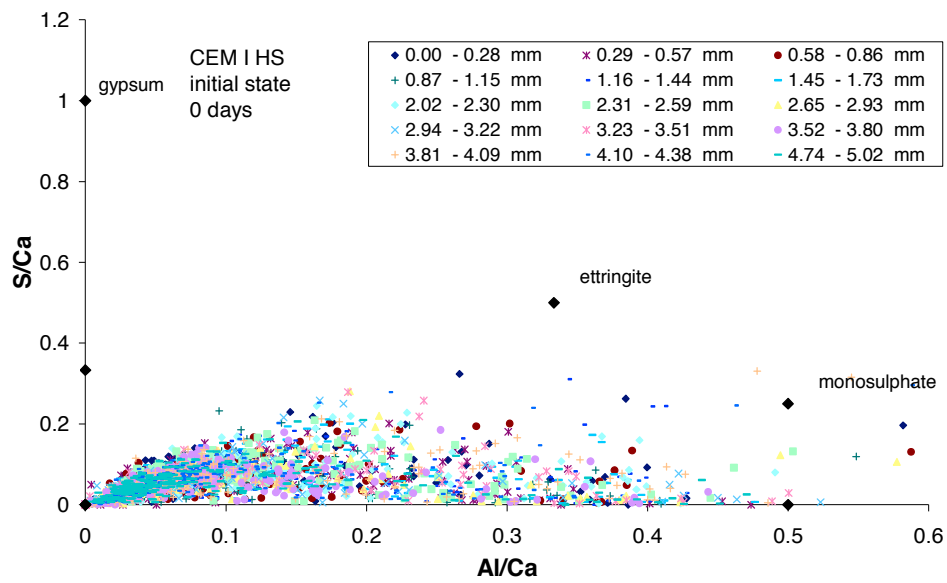
Figure 121: CEM I HS mortar before sulfate exposure; S/Ca to Al/Ca atomic ratio plot

Calcium Hydroxide Solution
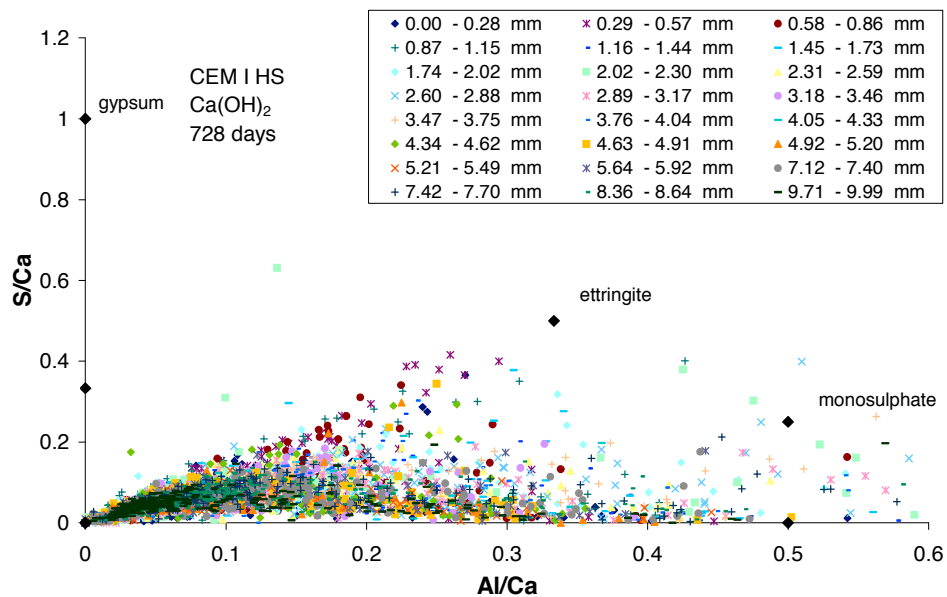
Figure 122: CEM I HS mortar after 728 days in saturated lime solution; S/Ca to Al/Ca atomic ratio plot

Sodium Sulfate Solution
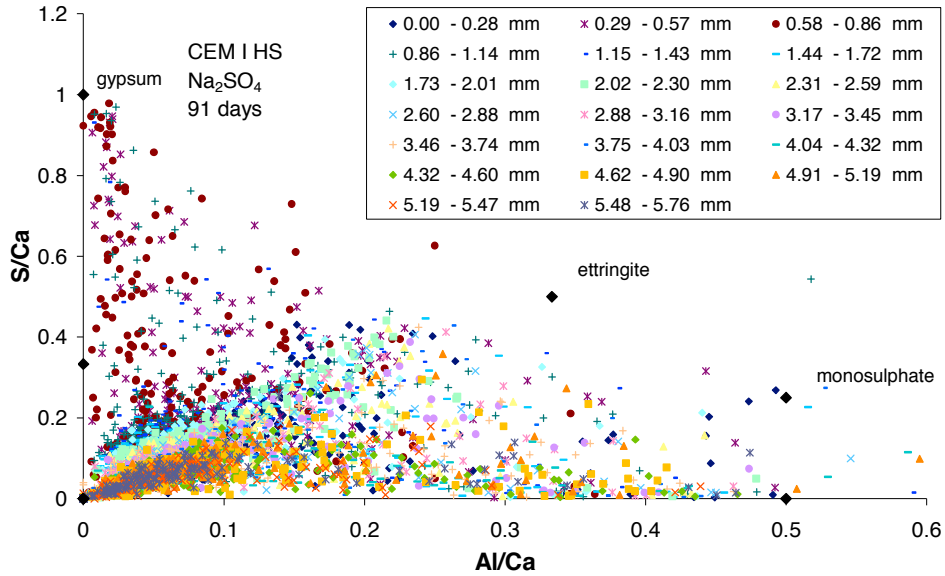
Figure 123: CEM I HS mortar after 91 days of sodium sulfate solution exposure; S/Ca to Al/Ca atomic ratio plot
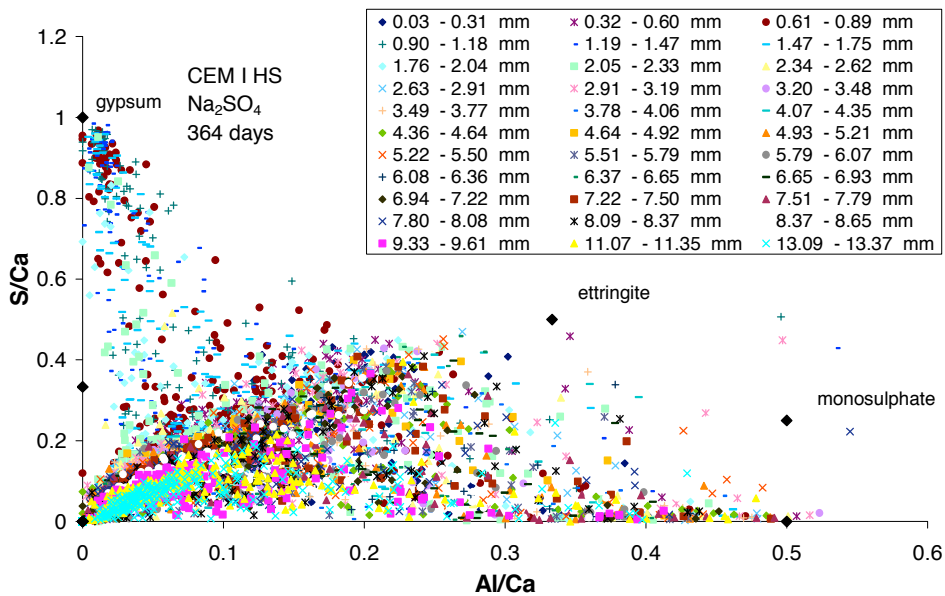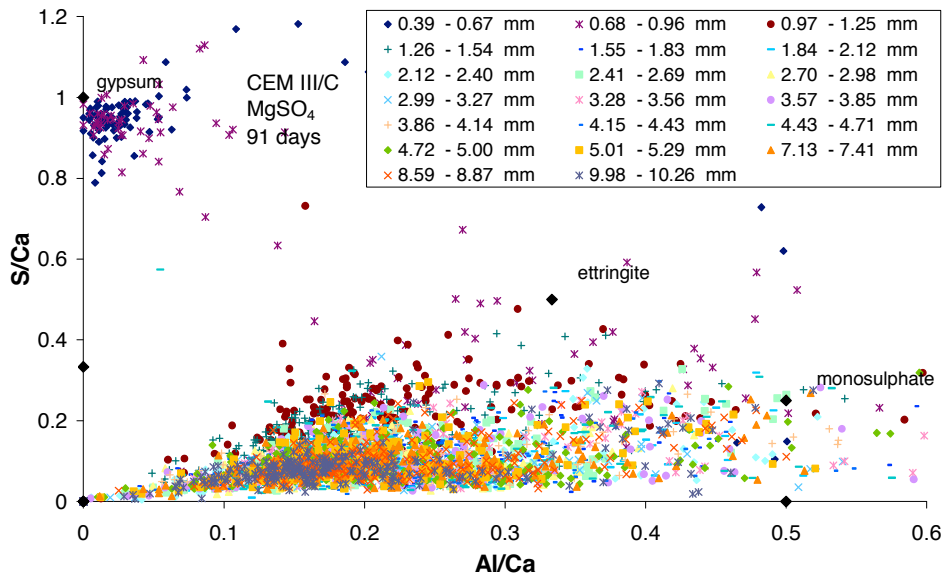

Figure 124: CEM I HS mortar after 364 days of sodium sulfate solution exposure; S/Ca to Al/Ca atomic ratio plot
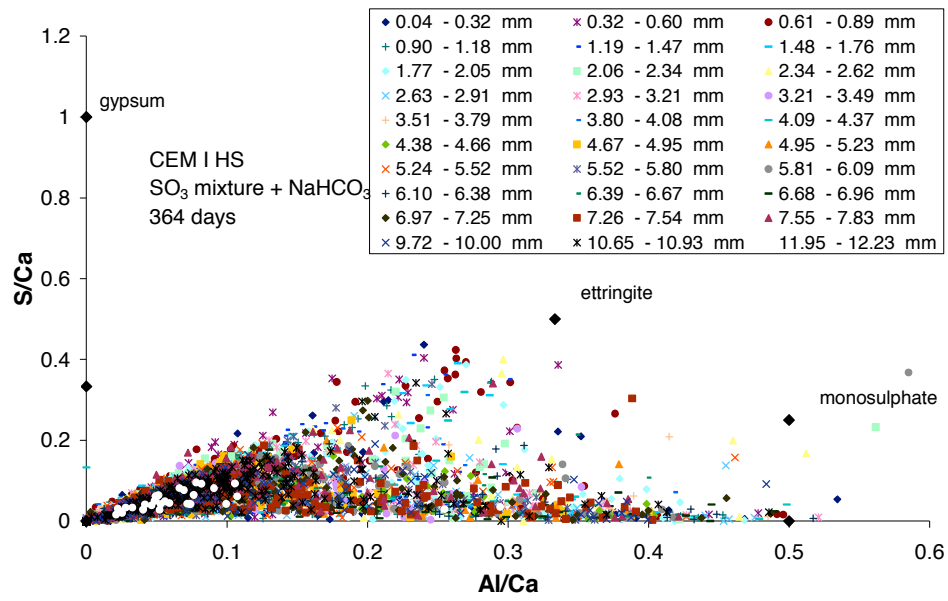
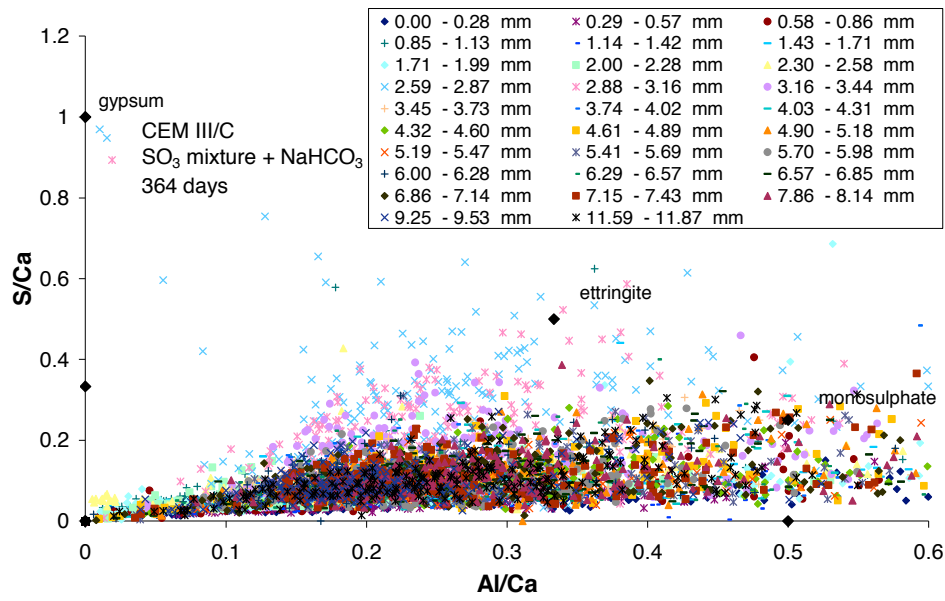**Figure 125**: CEM I HS mortar after 364 days of bicarbonate mixture solution exposure; S/Ca to Al/Ca atomic ratio plot

CEM II/A

Calcium Hydroxide Solution
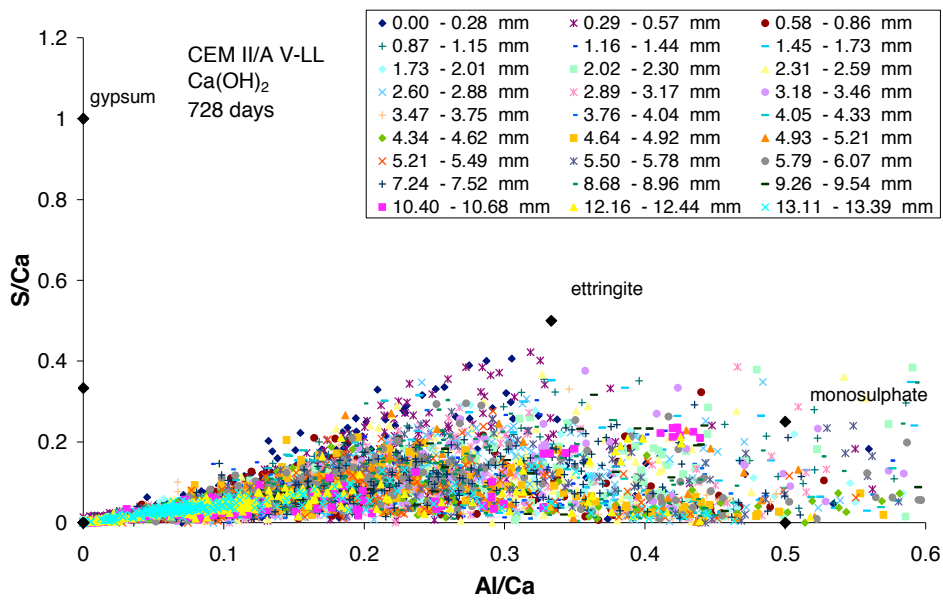
Figure 126: CEM II/A mortar after 728 days in saturated lime solution; S/Ca to Al/Ca atomic ratio plot

Sodium Sulfate Solution
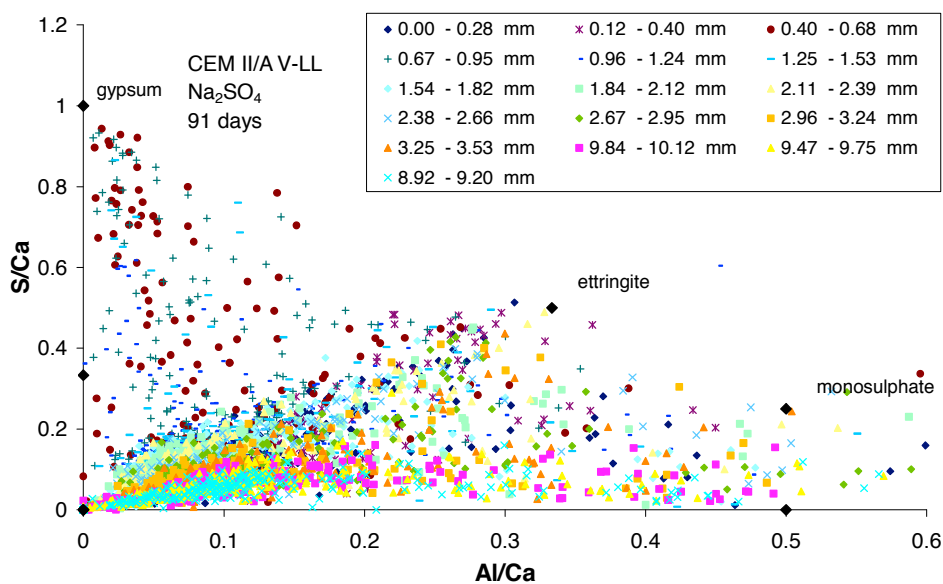
Figure 127: CEM II/A mortar after 91 days of sodium sulfate solution exposure; S/Ca to Al/Ca atomic ratio plot
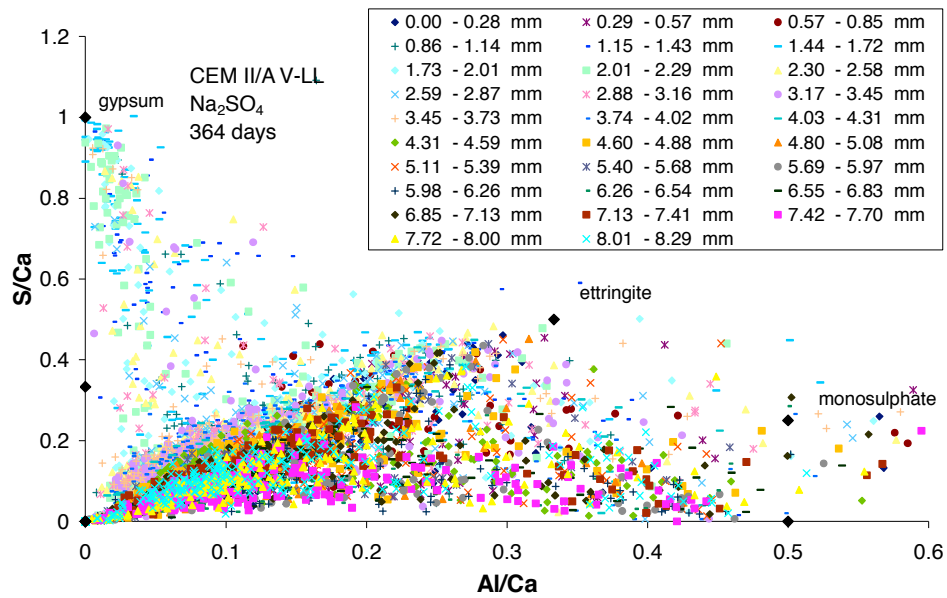
Figure 128: CEM II/A mortar after 364 days of sodium sulfate solution exposure; S/Ca to Al/Ca atomic ratio plot

Bicarbonate Mixture Solution
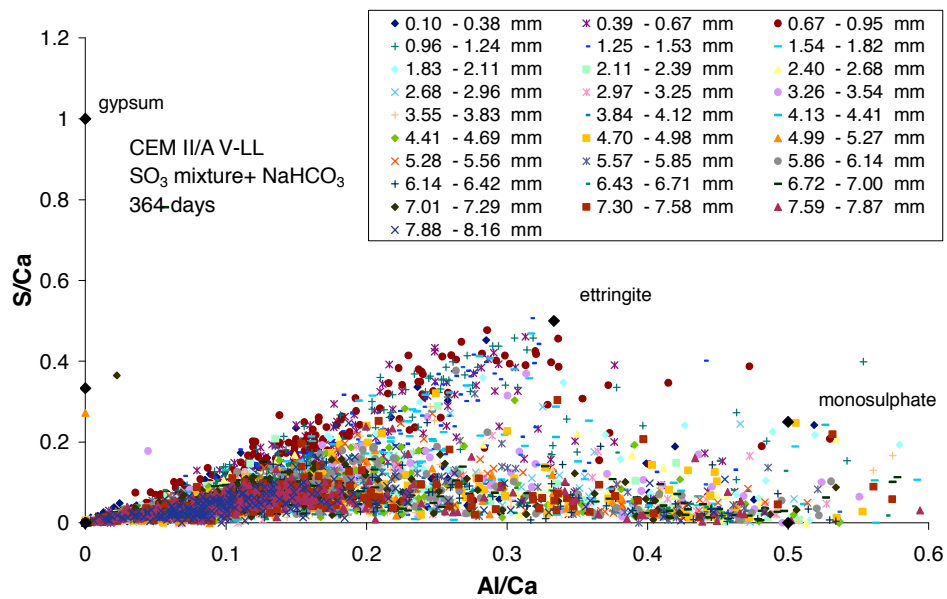
Figure 129: CEM II/A mortar after 364 days of bicarbonate mixture solution exposure; S/Ca to Al/Ca atomic ratio plot
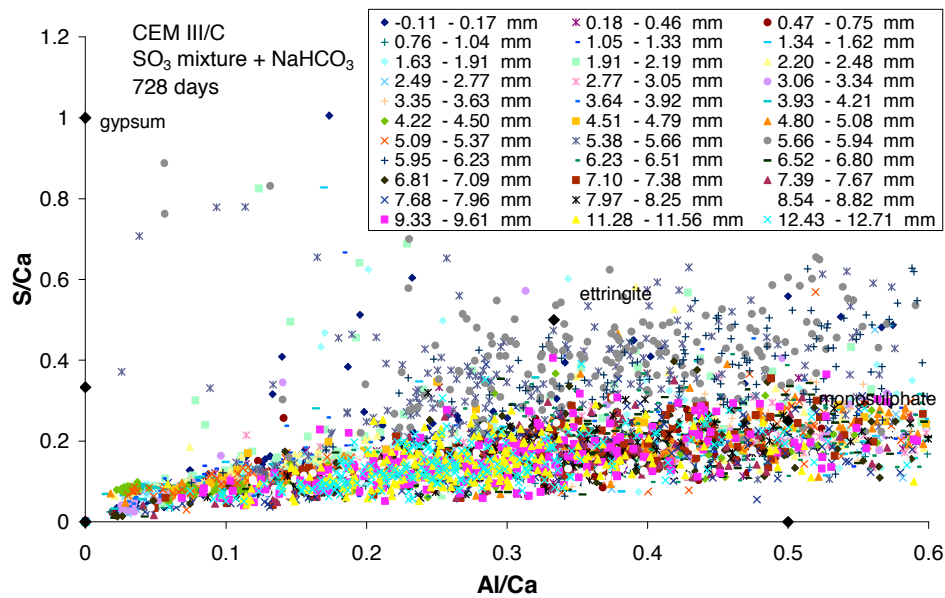
CEM II/B

Calcium Hydroxide Solution

Figure 130: CEM II/B mortar after 364 days in saturated lime solution; S/Ca to Al/Ca atomic ratio plot

Sodium Sulfate Solution

Figure 131: CEM II/B mortar after 91 days of sodium sulfate solution exposure; S/Ca to Al/Ca atomic ratio plot

Figure 132: CEM II/B mortar after 364 days of sodium sulfate solution exposure; S/Ca to Al/Ca atomic ratio plot

Bicarbonate Mixture Solution
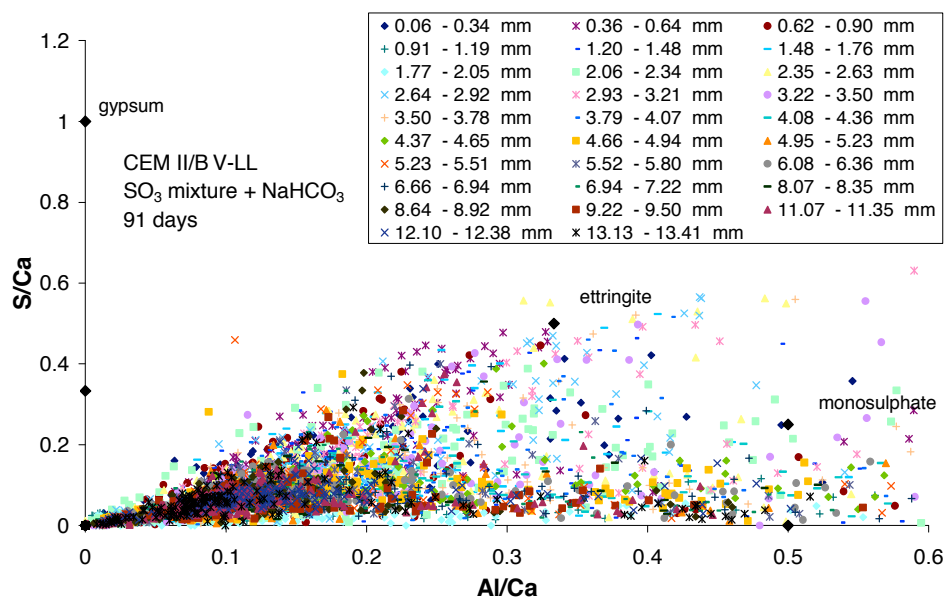
Figure 133: CEM II/B mortar after 91 days of bicarbonate mixture solution exposure; S/Ca to Al/Ca atomic ratio plot
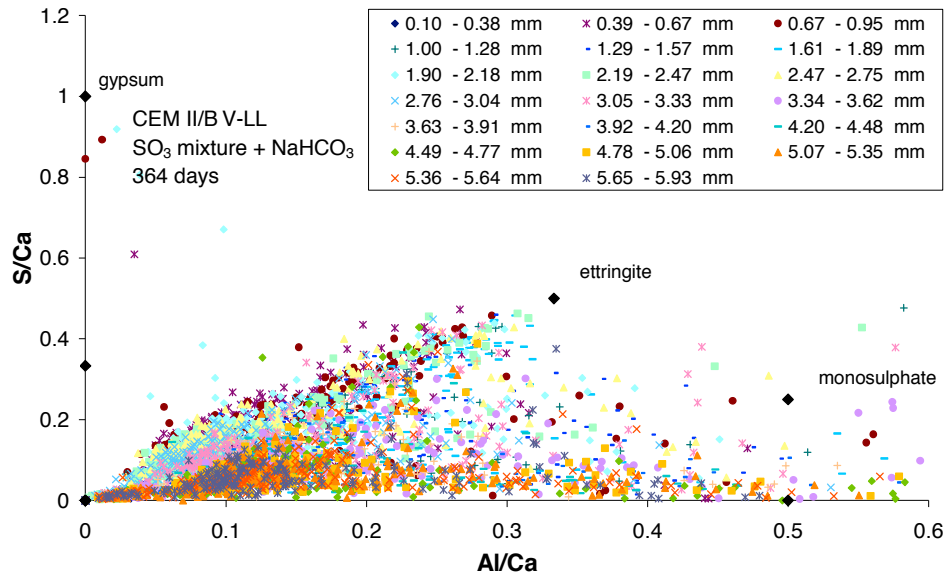
Figure 134: CEM II/B mortar after 364 days of bicarbonate mixture solution exposure; S/Ca to Al/Ca atomic ratio plot

CEM III/B

Initial state
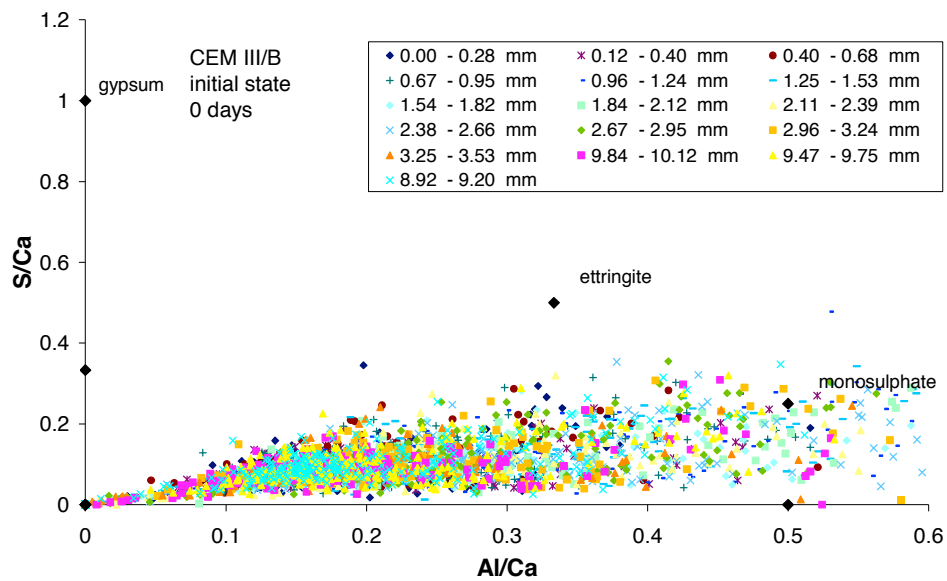
Figure 135: CEM III/B mortar before sulfate exposure; S/Ca to Al/Ca atomic ratio plot
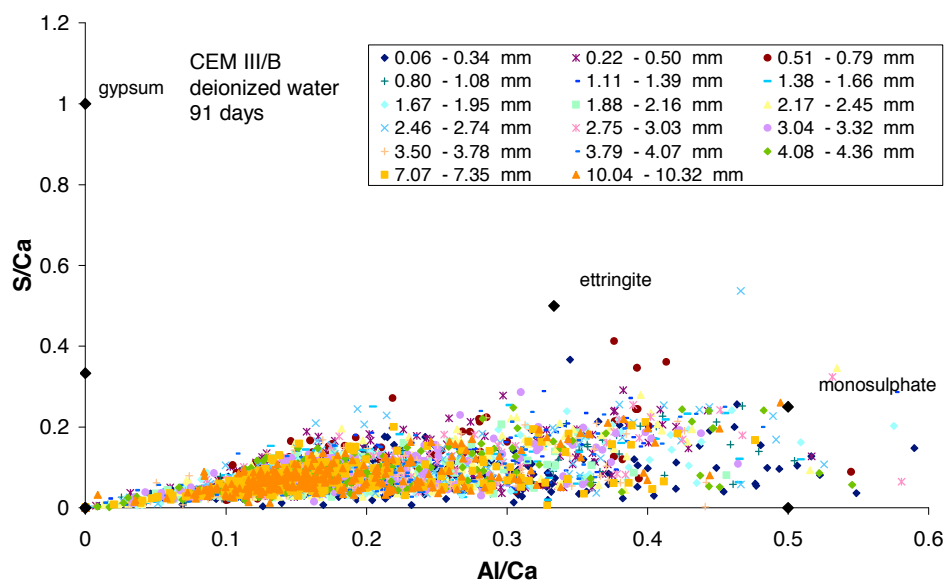
Deionized Water

Figure 136: CEM III/B mortar after 91 days in deionized water; S/Ca to Al/Ca atomic ratio plot
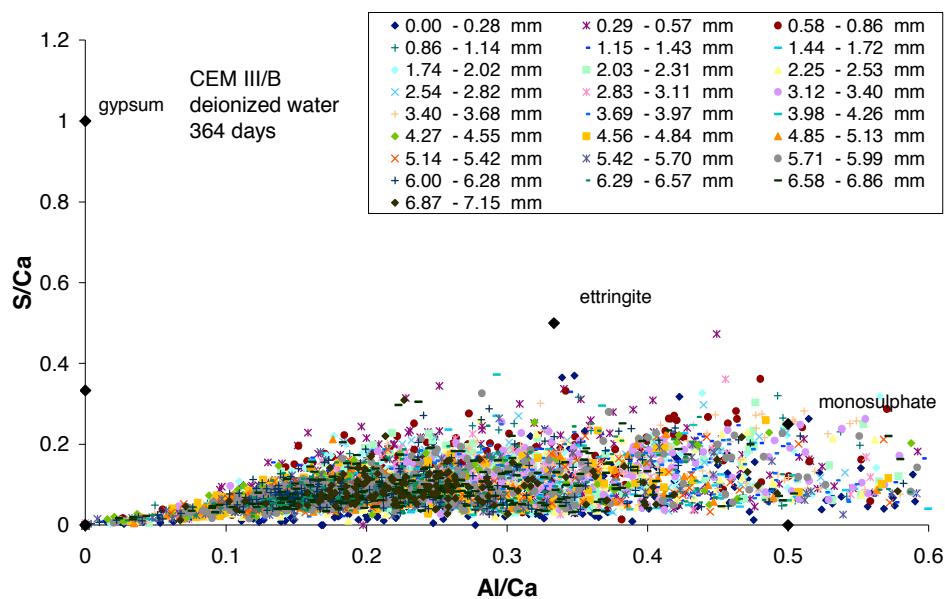
Figure 137: CEM III/B mortar after 364 days in deionized water; S/Ca to Al/Ca atomic ratio plot

Calcium Hydroxide Solution
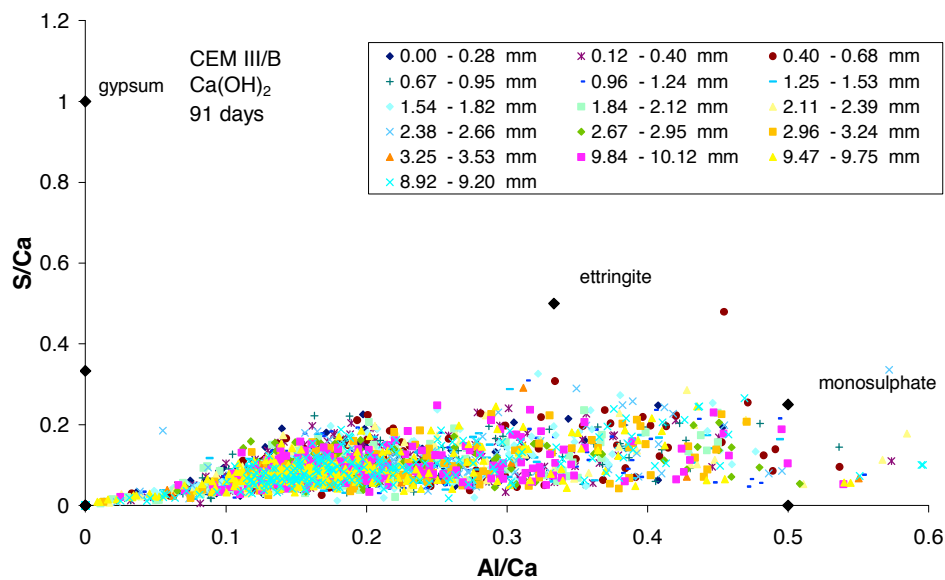
Figure 138: CEM III/B mortar after 91 days in saturated lime solution at 20°C; S/Ca to Al/Ca atomic ratio plot
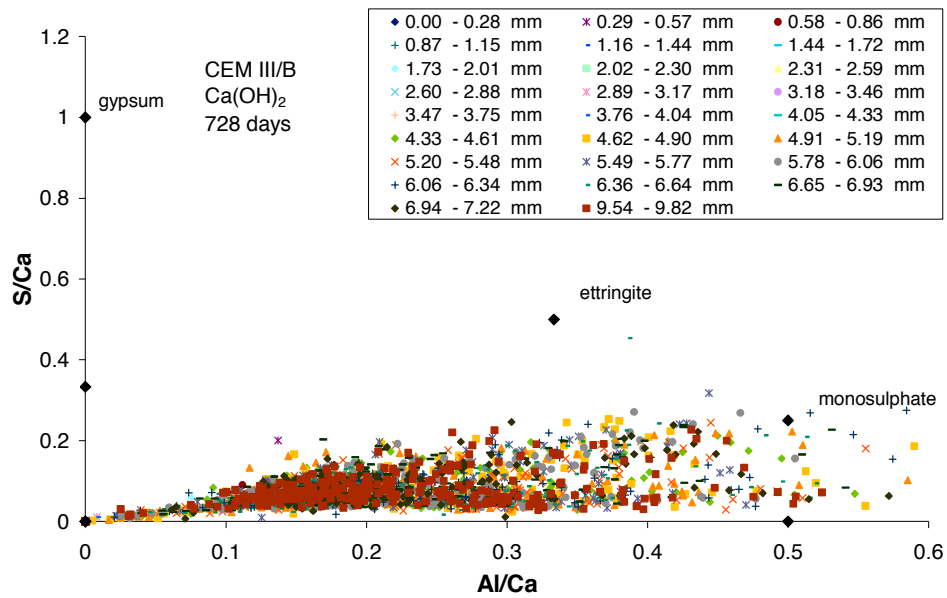
Figure 139: CEM III/B mortar after 728 days in saturated lime solution at 20°C; S/Ca to Al/Ca atomic ratio plot

Sodium Sulfate Solution
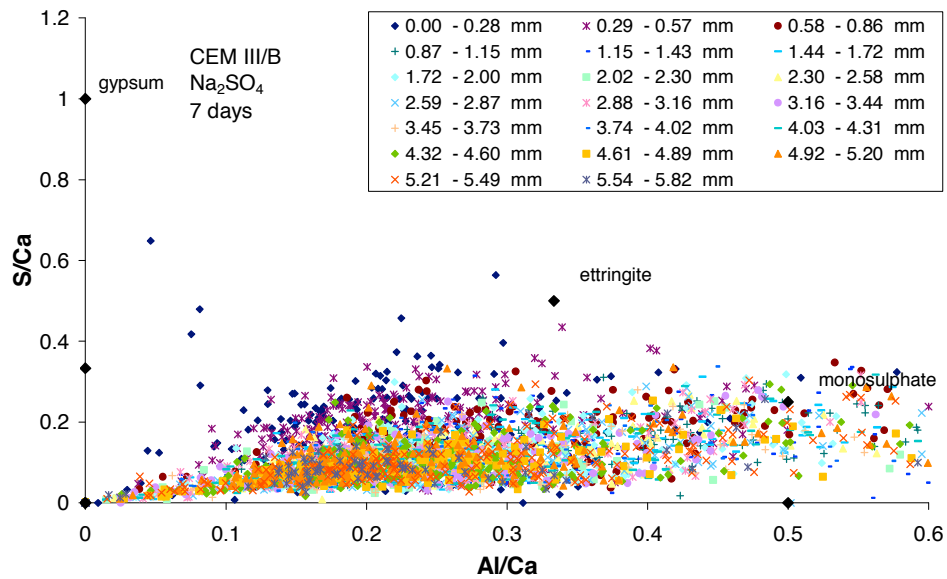
Figure 140: CEM III/B mortar after 7 days of sodium sulfate solution exposure; S/Ca to Al/Ca atomic ratio plot
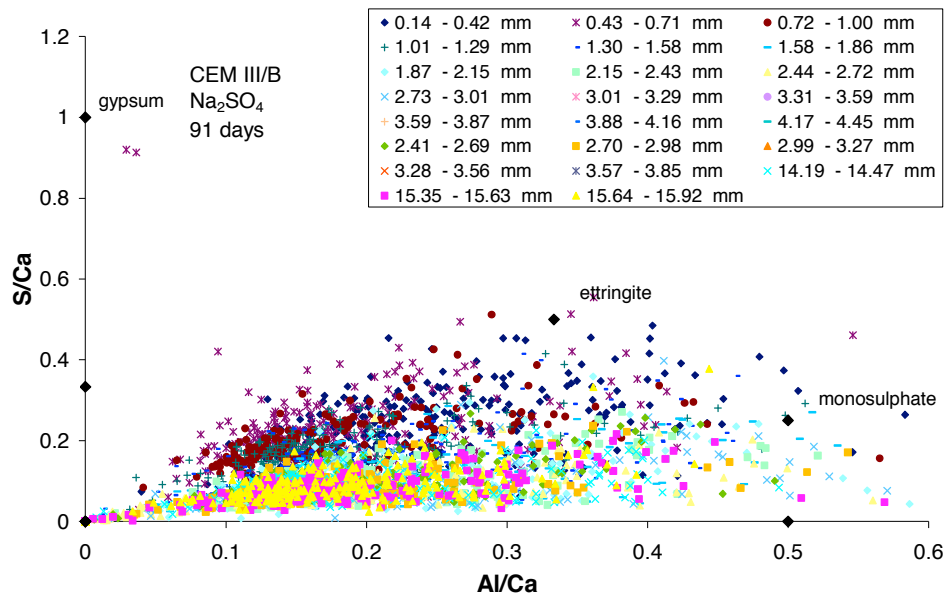
Figure 141: CEM III/B mortar after 91 days of sodium sulfate solution exposure; S/Ca to Al/Ca atomic ratio plot
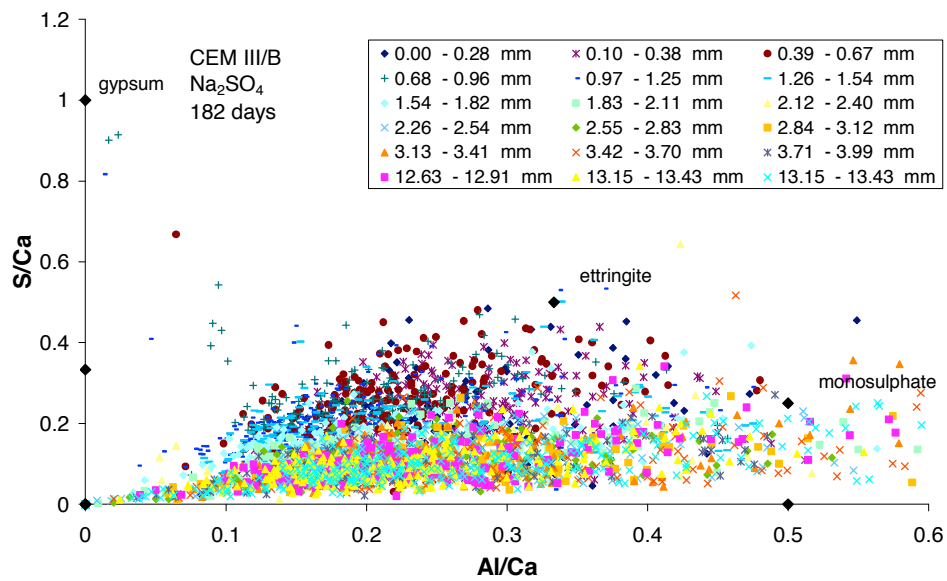
Figure 142: CEM III/B mortar after 182 days of sodium sulfate solution exposure; S/Ca to Al/Ca atomic ratio plot

Figure 143: CEM III/B mortar after 364 days of sodium sulfate solution exposure; S/Ca to Al/Ca atomic ratio plot

Figure 144: CEM III/B mortar after 637 days of sodium sulfate solution exposure <u>at 40°C</u>; S/Ca to Al/Ca atomic ratio plot

Sodium Bicarbonate Solution

Figure 145: CEM III/B mortar after 91 days of sodium bicarbonate solution exposure; S/Ca to Al/Ca atomic ratio plot
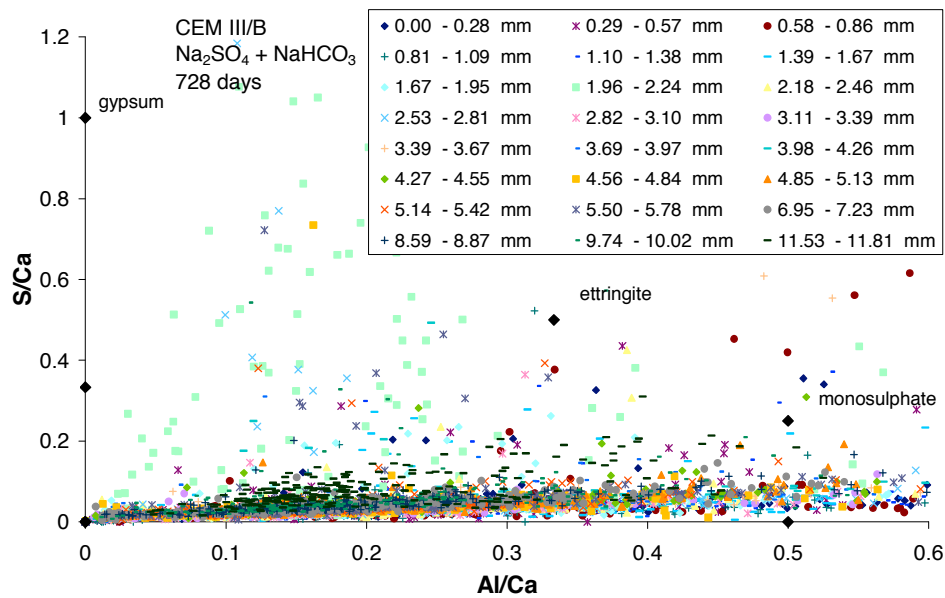
Figure 146: CEM III/B mortar after 728 days of sodium bicarbonate solution exposure; S/Ca to Al/Ca atomic ratio plot

Figure 147: CEM III/B mortar after 364 days of potassium sulfate solution exposure; S/Ca to Al/Ca atomic ratio plot

Figure 148: CEM III/B mortar after 546 days of potassium sulfate solution exposure; S/Ca to Al/Ca atomic ratio plot

Magnesium Sulfate Solution
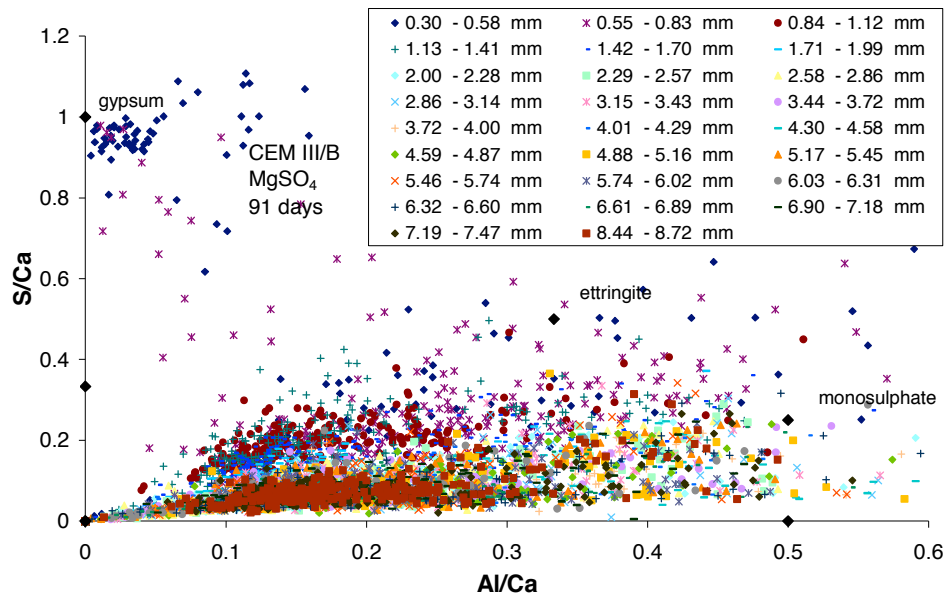
Figure 149: CEM III/B mortar after 91 days of magnesium sulfate solution exposure; S/Ca to Al/Ca atomic ratio plot
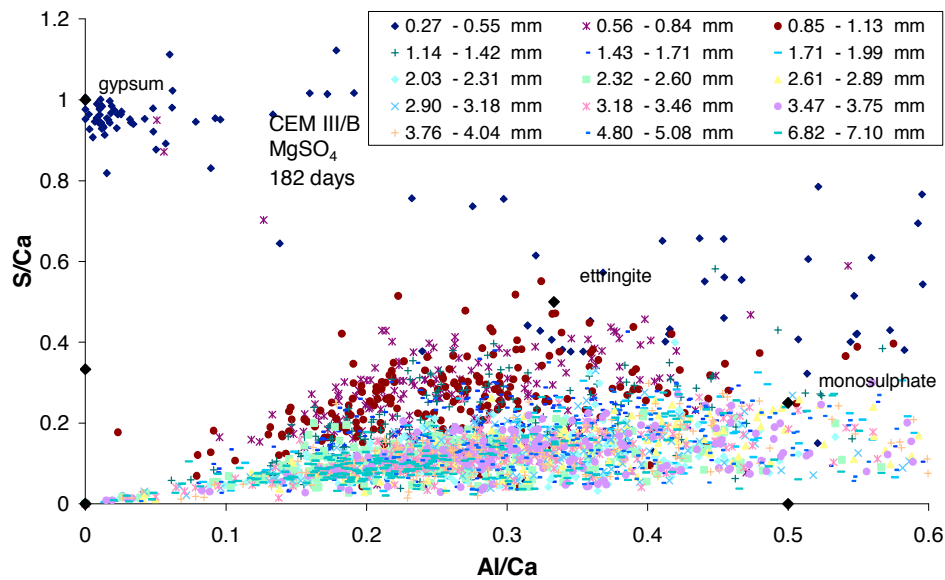
Figure 150: CEM III/B mortar after 182 days of magnesium sulfate solution exposure; S/Ca to Al/Ca atomic ratio plot
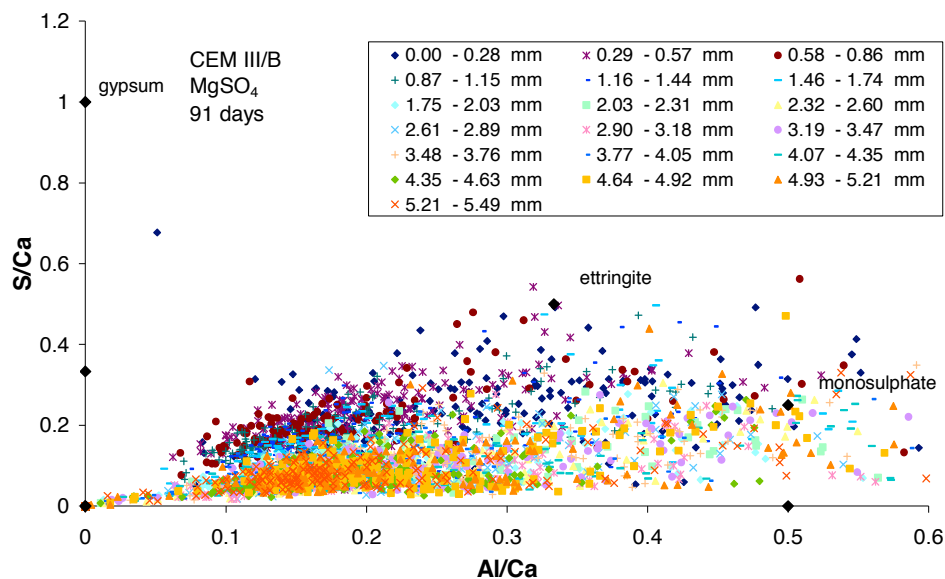
Figure 151: CEM III/B mortar after 91 days of magnesium sulfate solution exposure (0.035 mol/l); S/Ca to Al/Ca atomic ratio plot
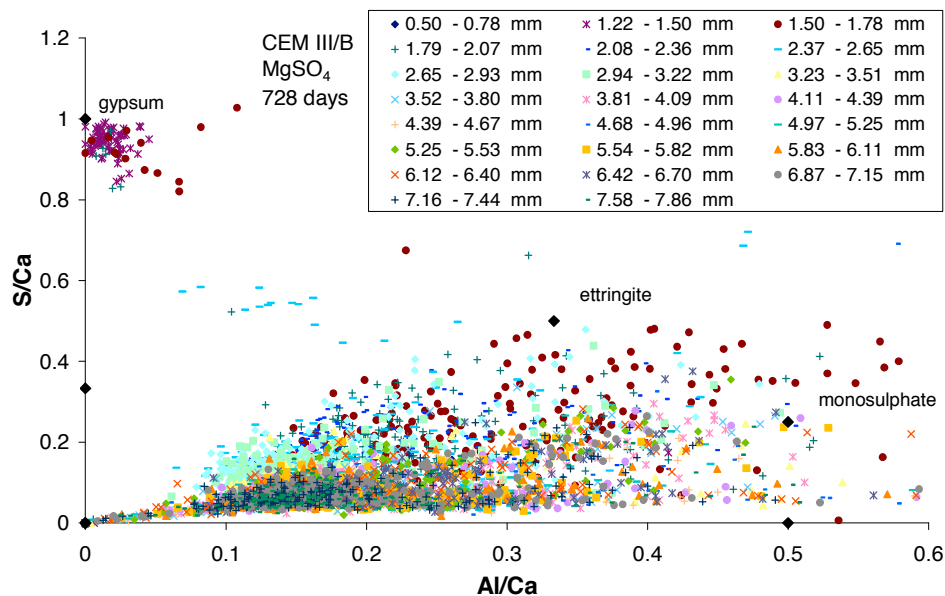
Figure 152: CEM III/B mortar after 728 days of magnesium sulfate solution exposure (0.035 mol/l); S/Ca to Al/Ca atomic ratio plot

Figure 153: CEM III/B mortar after 91 days of magnesium bicarbonate solution exposure (0.035 mol/l); S/Ca to Al/Ca atomic ratio plot

Figure 154: CEM III/B mortar after 728 days of magnesium bicarbonate solution exposure (0.035 mol/l); S/Ca to Al/Ca atomic ratio plot

Sulfate Mixture Solution
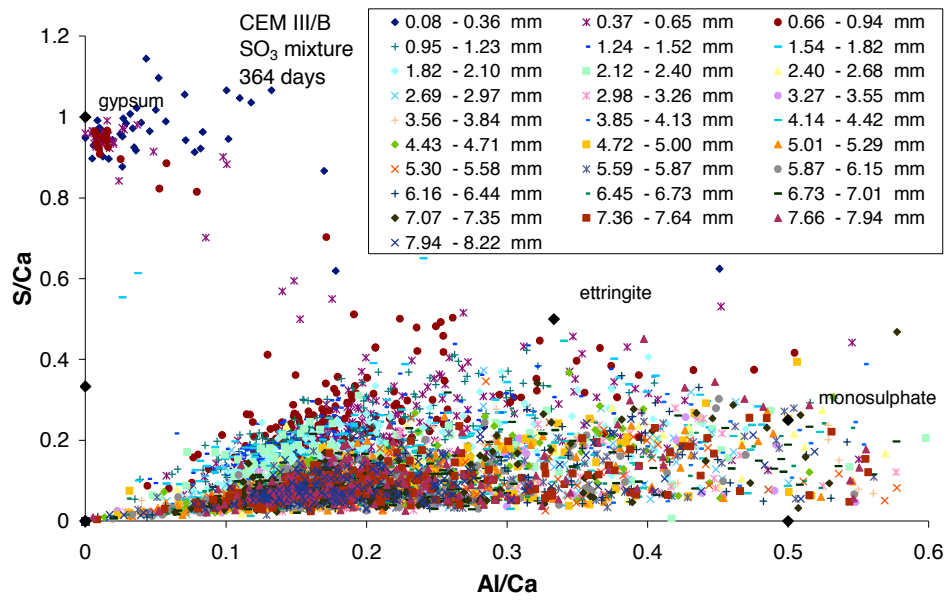
Figure 155: CEM III/B mortar after 364 days of sulfate mixture solution exposure; S/Ca to Al/Ca atomic ratio plot
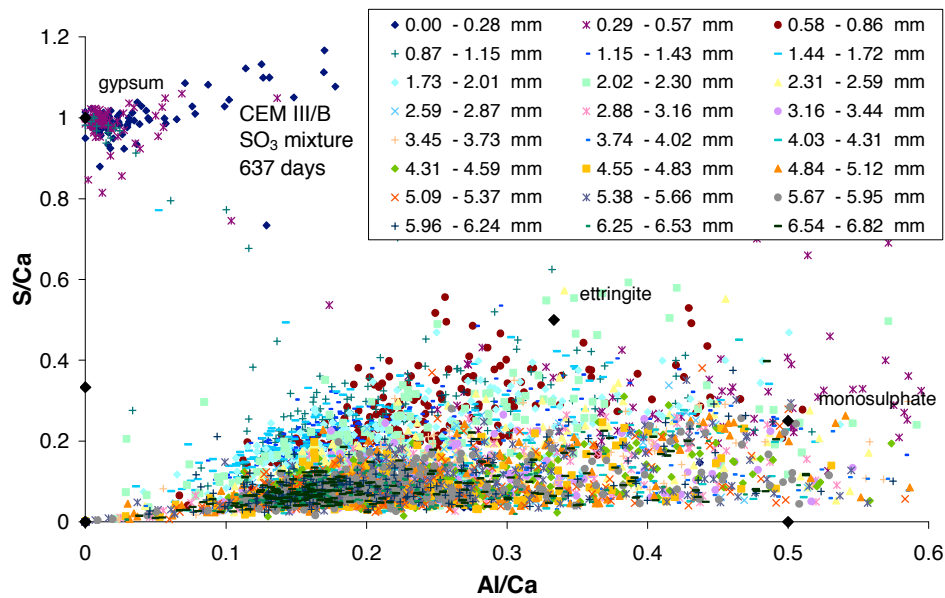
Figure 156: CEM III/B mortar after 637 days of sulfate mixture solution exposure; S/Ca to Al/Ca atomic ratio plot

Bicarbonate Mixture Solution
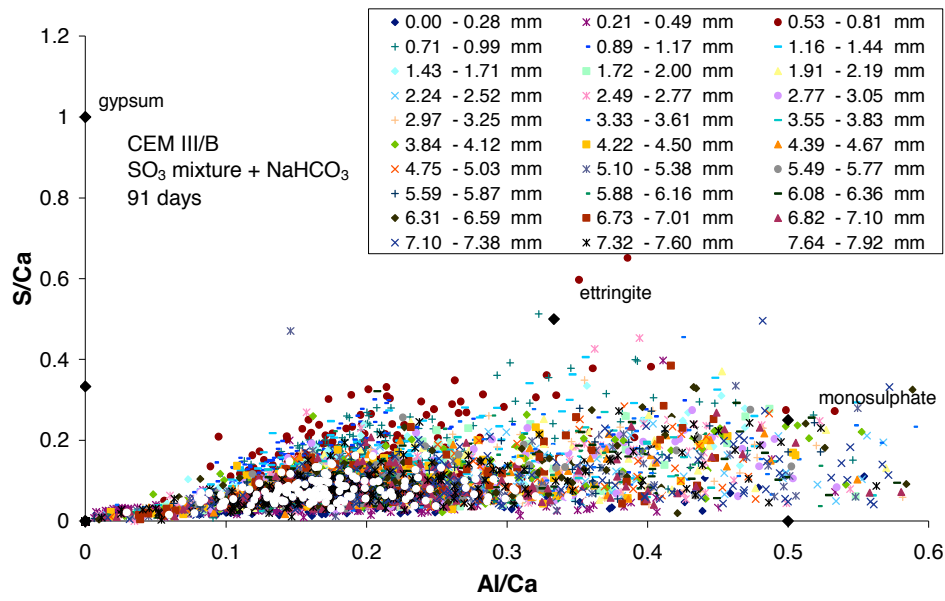
Figure 157: CEM III/B mortar after 91 days of bicarbonate mixture solution exposure; S/Ca to Al/Ca atomic ratio plot
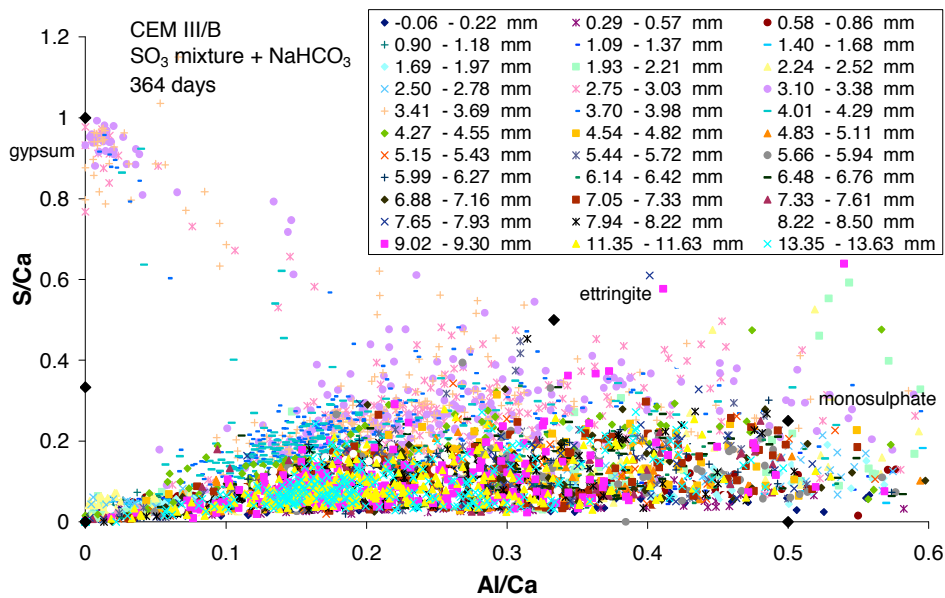
Figure 158: CEM III/B mortar after 364 days of bicarbonate mixture solution exposure; S/Ca to Al/Ca atomic ratio plot
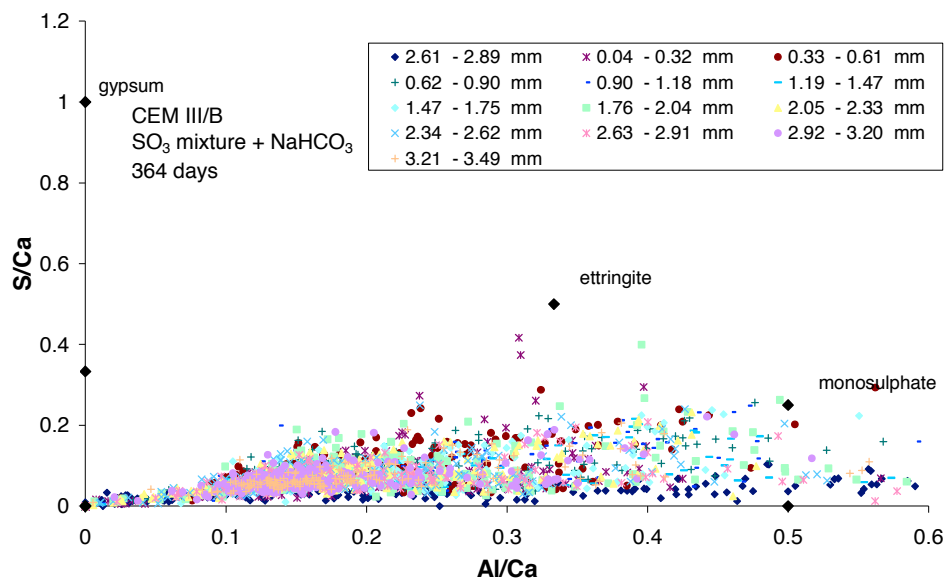
Figure 159: CEM III/B mortar after 364 days of bicarbonate mixture solution exposure (0.035 mol/l); S/Ca to Al/Ca atomic ratio plot

CEM III/C

Calcium Hydroxide Solution

Figure 160: CEM III/C mortar after 728 days in saturated lime solution; S/Ca to Al/Ca atomic ratio plot

Sodium Sulfate Solution

Figure 161 CEM III/C mortar after 546 days of sodium sulfate solution exposure; S/Ca to Al/Ca atomic ratio plot

Potassium Sulfate Solution
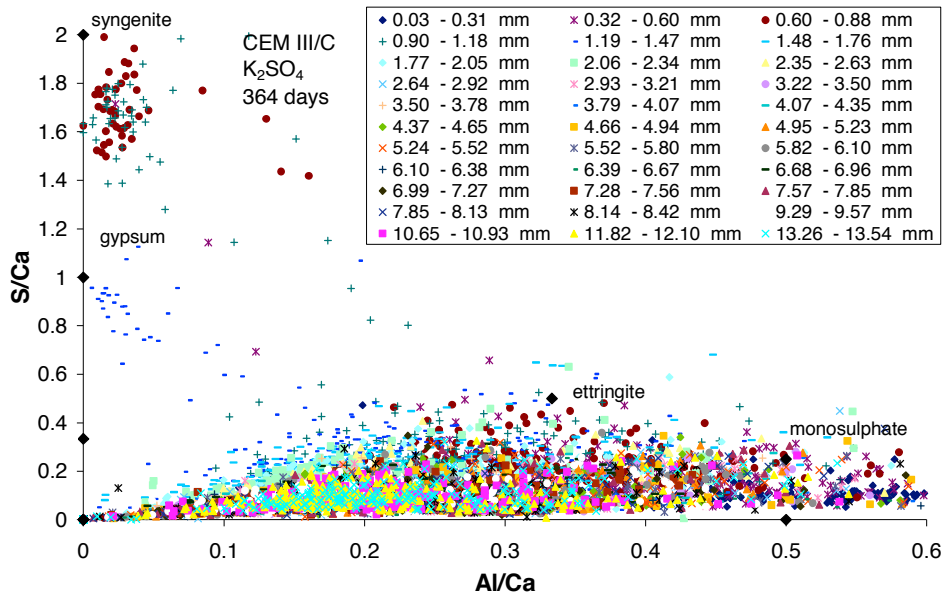
Figure 162 CEM III/C mortar after 364 days of potassium sulfate solution exposure; S/Ca to Al/Ca atomic ratio plot

Magnesium Sulfate Solution

Figure 163 CEM III/C mortar after 91 days of magnesium sulfate solution exposure; S/Ca to Al/Ca atomic ratio plot

Bicarbonate Mixture Solution

Figure 164: CEM III/C mortar after 364 days of bicarbonate mixture solution exposure; S/Ca to Al/Ca atomic ratio plot

Figure 165: CEM III/C mortar after 728 days of bicarbonate mixture solution exposure; S/Ca to Al/Ca atomic ratio plot

Sulfate Binding Characterization by EDS

CEM I

Deionized water
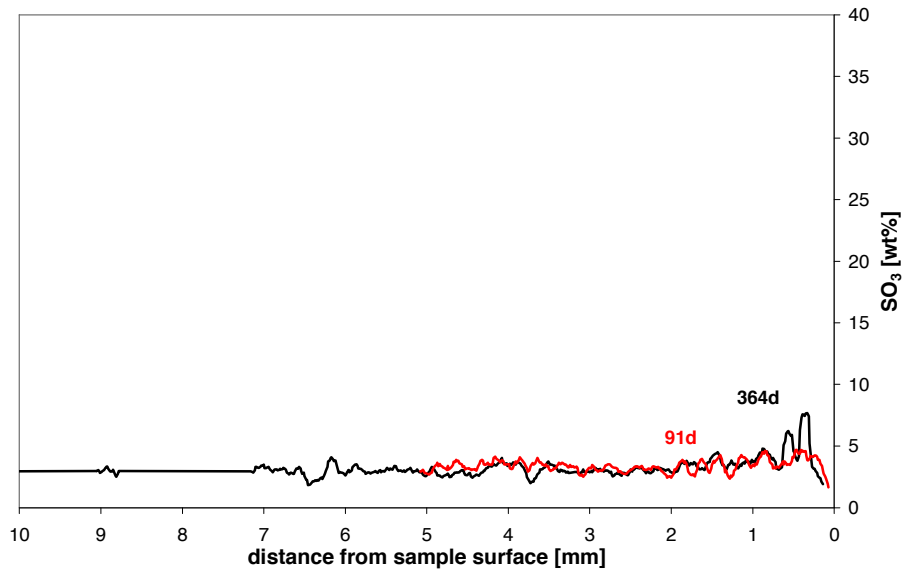
Figure 166: CEM I mortar in deionized water, sulfate profiles (median) for different exposure times

Sodium Sulfate Solution
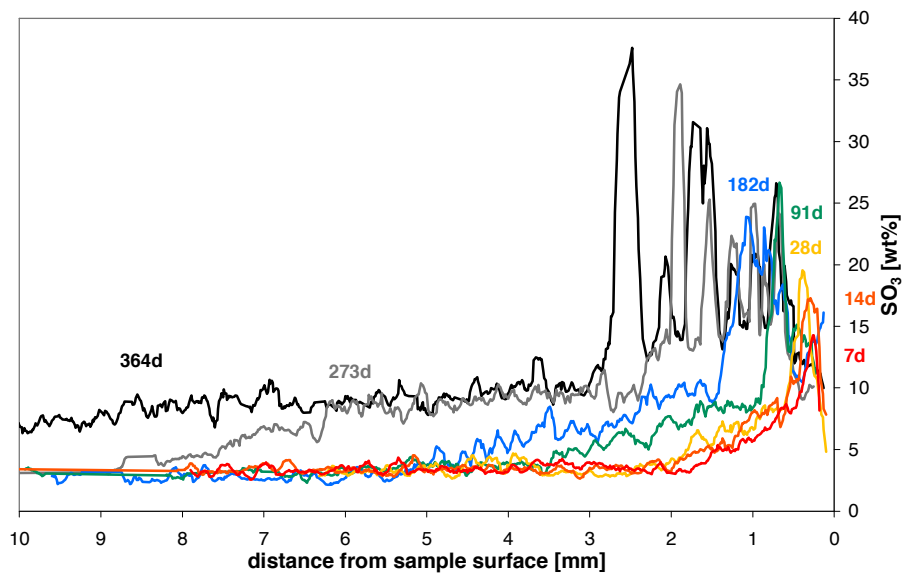
Figure 167: CEM I mortar exposed to sodium sulfate solution, sulfate profiles (median) for different exposure times
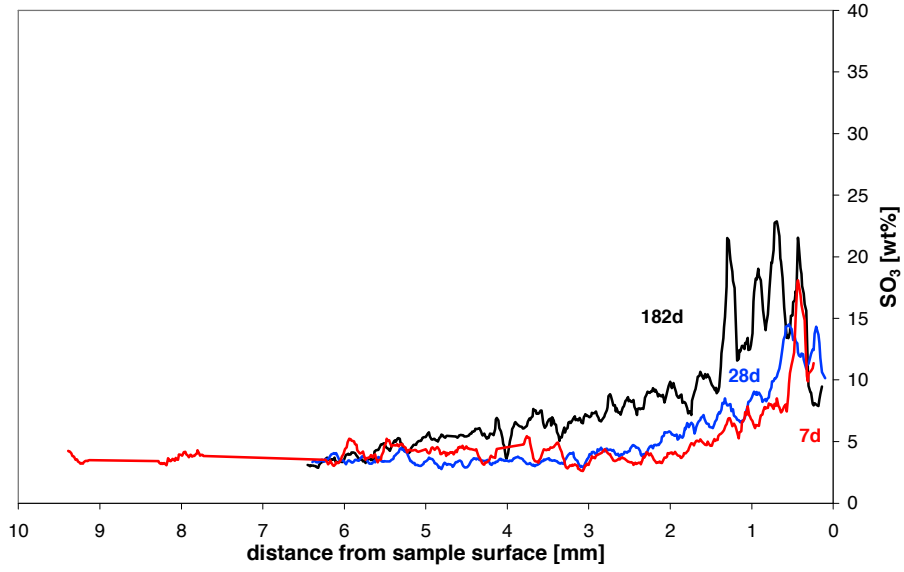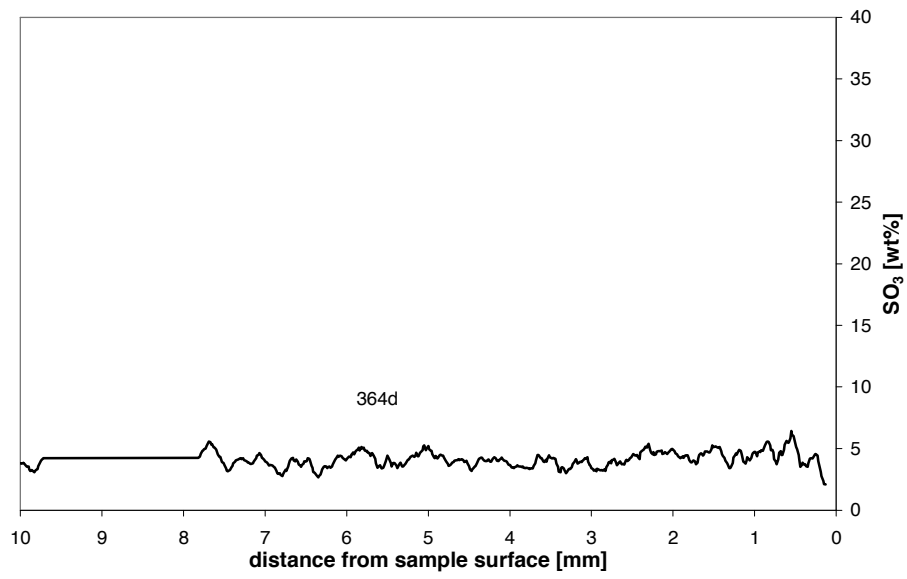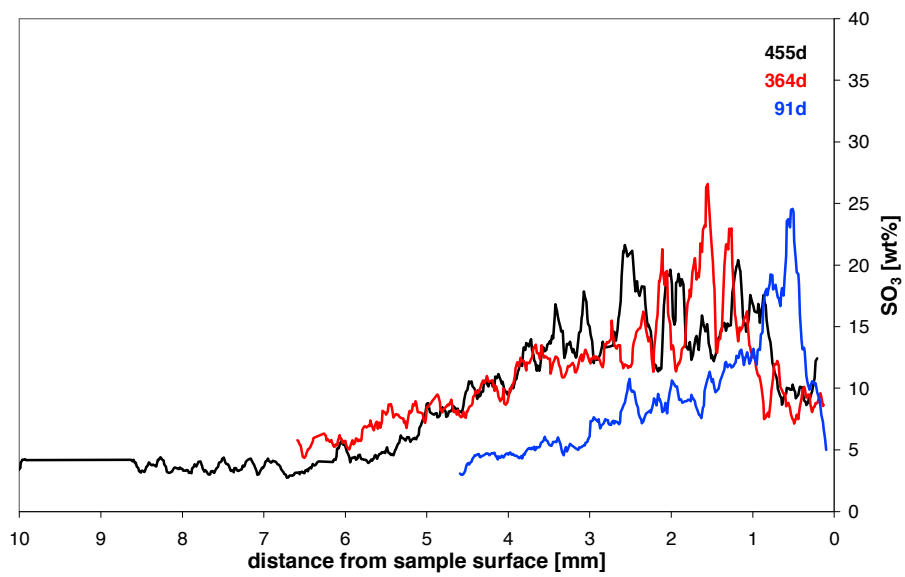
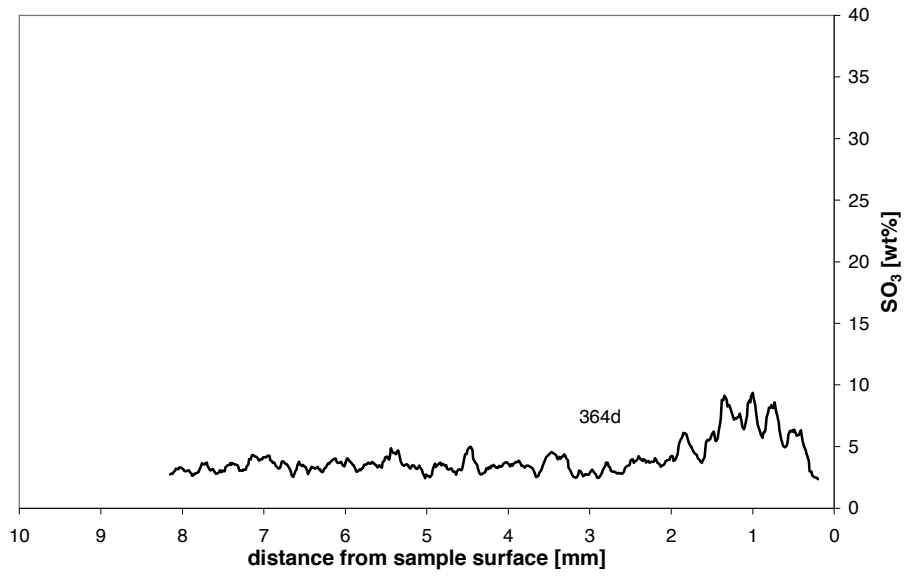**Figure 168**: CEM I mortar exposed to sodium sulfate solution <u>at 40°C</u>, sulfate profiles (median) for different exposure times

size: 1.25 x 1.25 x 15 cm^2
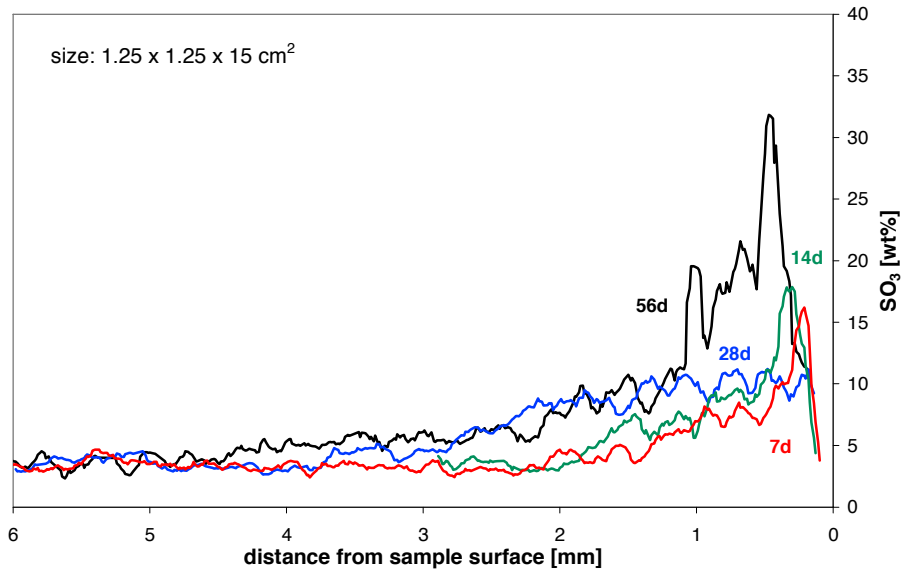
Figure 169: CEM I mortar (1.25 x 1.25 x15 cm^3) exposed to sodium sulfate solution, sulfate profiles (median) for different exposure times
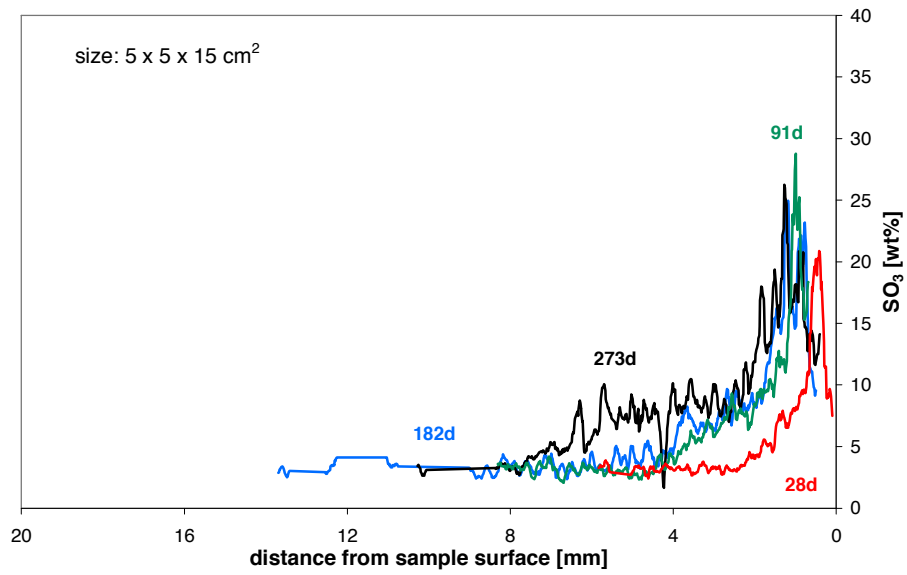
Figure 170: CEM I mortar (5 x 5 x15 cm³) exposed to sodium sulfate solution, sulfate profiles (median) for different exposure times

Sodium Bicarbonate Solution
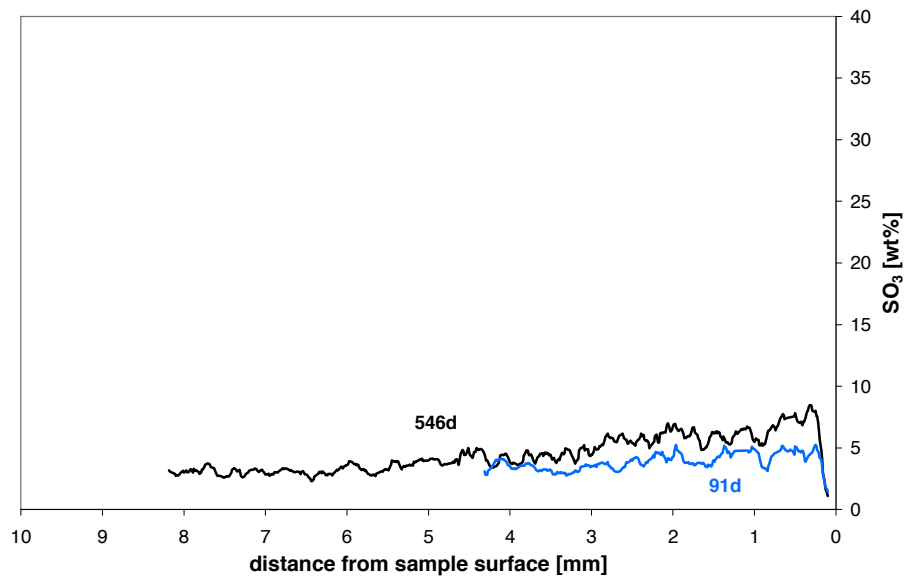
Figure 171: CEM I mortar exposed to sodium bicarbonate solution, sulfate profiles (median) for different exposure times

Potassium Sulfate Solution
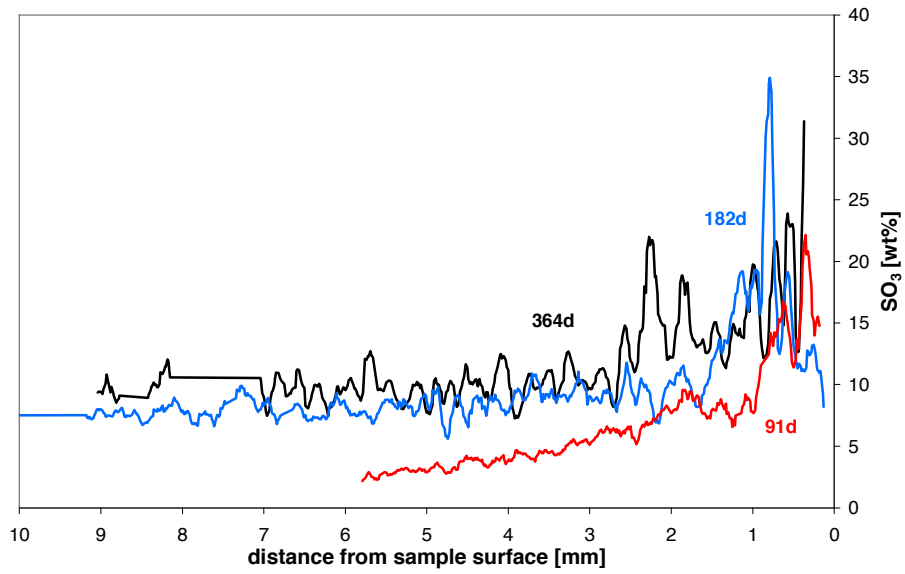
Figure 172: CEM I mortar exposed to potassium sulfate solution, sulfate profiles (median) for different exposure times

Magnesium Sulfate Solution
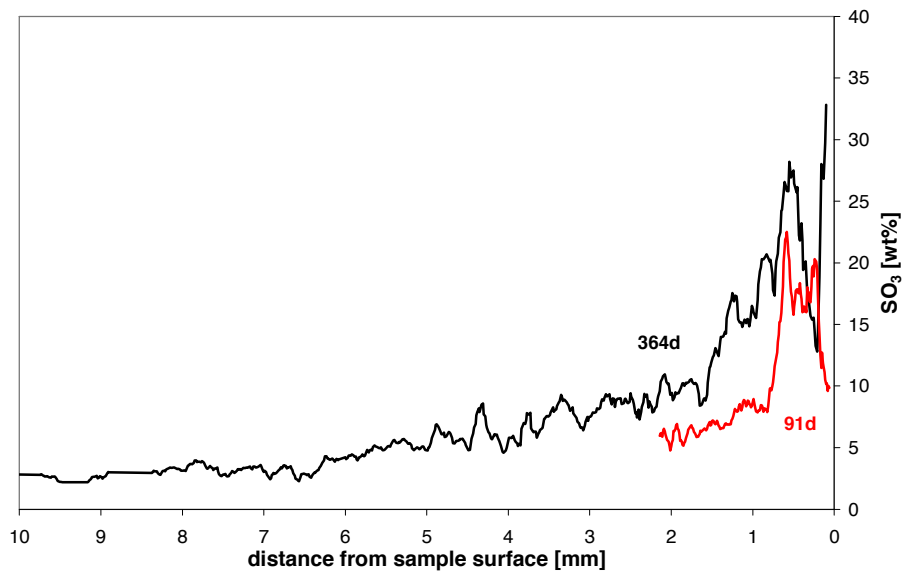
Figure 173: CEM I mortar exposed to magnesium sulfate solution, sulfate profiles (median) for different exposure times
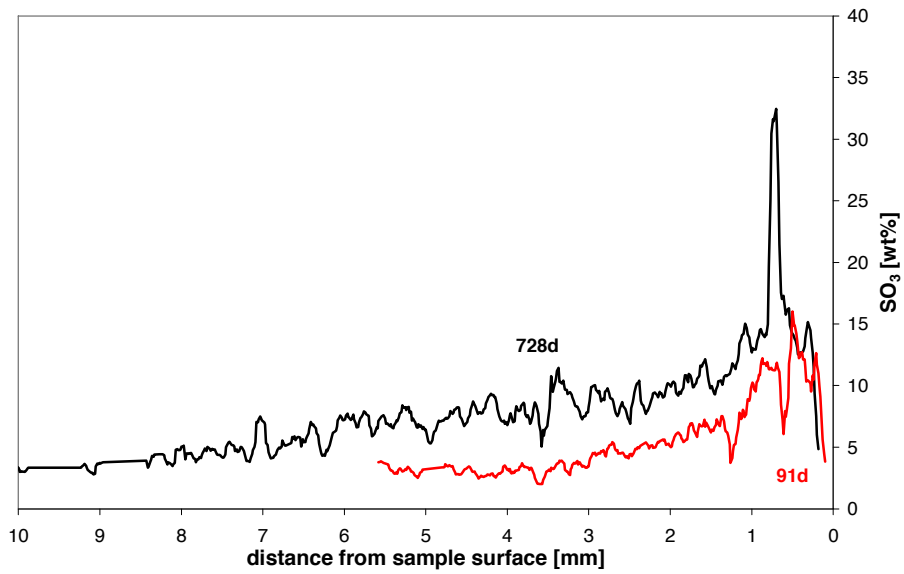
Figure 174: CEM I mortar exposed to magnesium sulfate solution (0.035 mol/l), sulfate profiles (median) for different exposure times

Magnesium Bicarbonate Solution *(0.035 mol/l)*
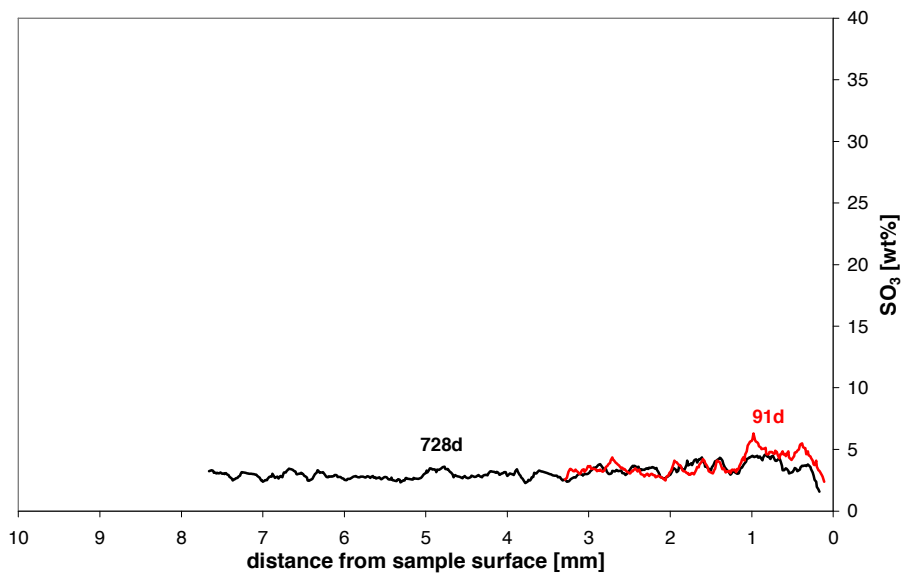
Figure 175: CEM I mortar exposed to magnesium bicarbonate solution (0.035 mol/l), sulfate profiles (median) for different exposure times

Sulfate Mixture Solution
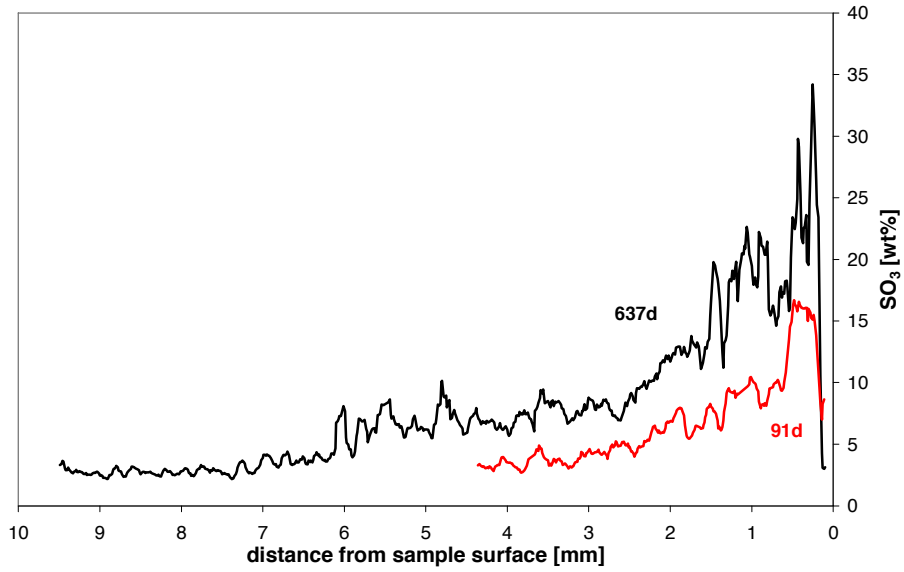
Figure 176 CEM I mortar exposed to sulfate mixture solution, sulfate profiles (median) for different exposure times

Bicarbonate Mixture Solution
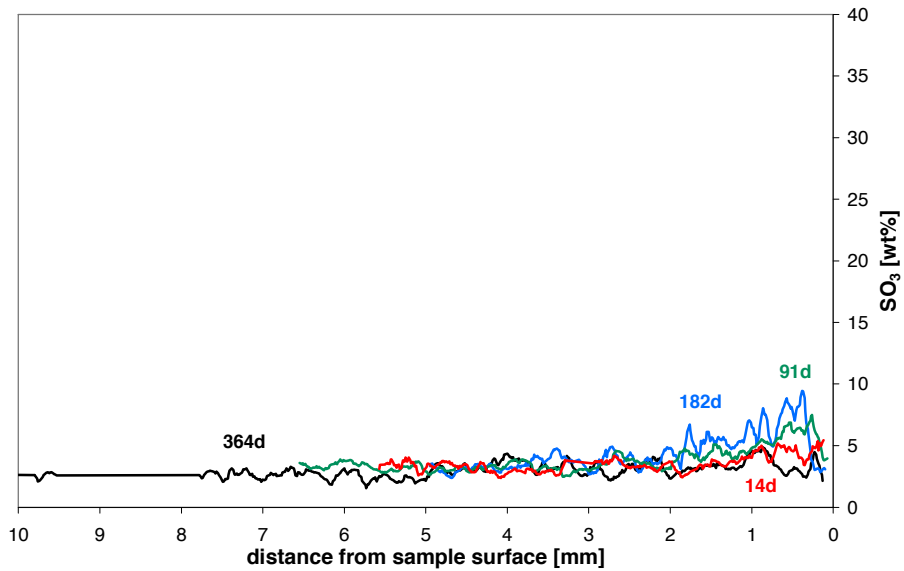
Figure 177: CEM I mortar exposed to bicarbonate mixture solution, sulfate profiles (median) for different exposure times

Bicarbonate Mixture Solution *(0.035 mol/l)*
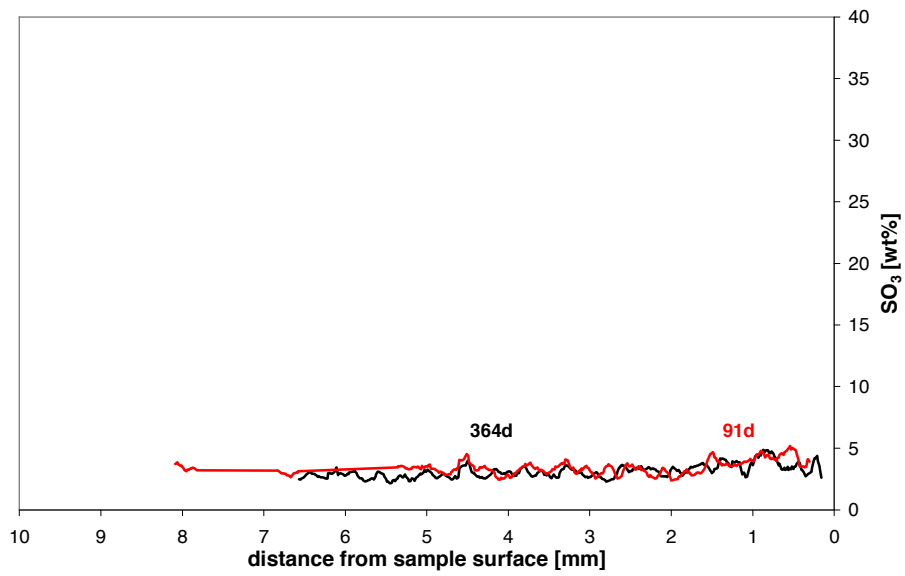
Figure 178: CEM I mortar in bicarbonate mixture solution (0.035 mol/l), sulfate profiles (median) for different exposure times

CEM I + 2% gypsum

Sodium Sulfate Solution
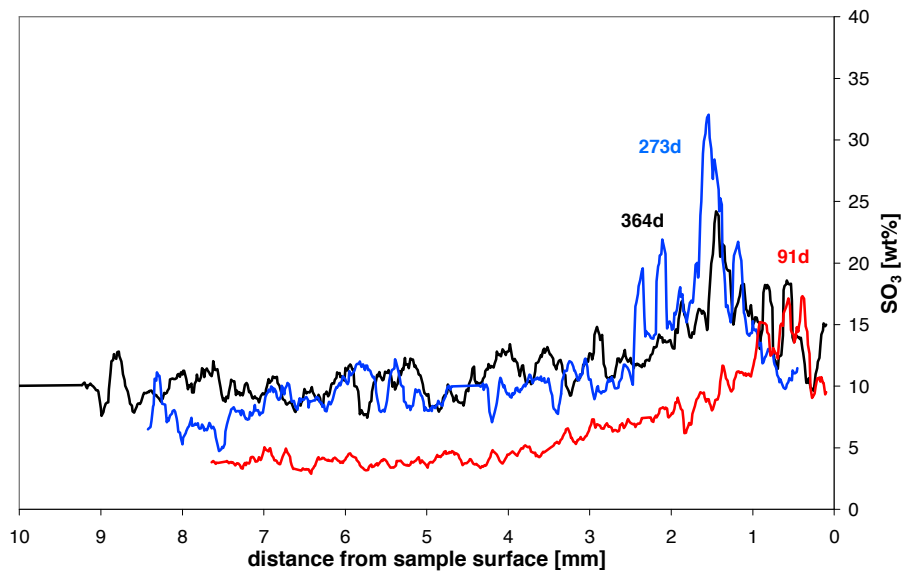
Figure 179: CEM I + 2% gypsum mortar exposed to sodium sulfate solution, sulfate profiles (median) for different exposure times
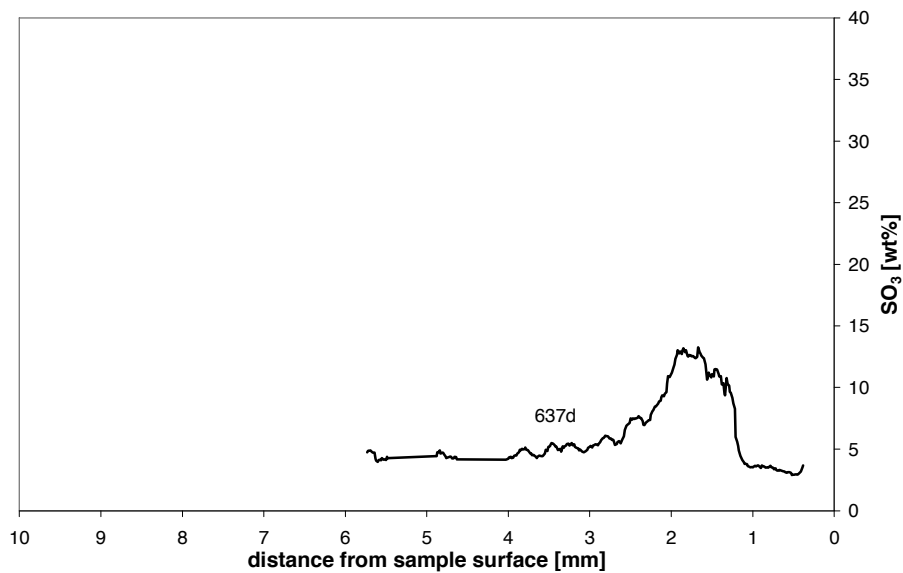
CEM I + 6% Silica Fume

Sodium Sulfate Solution
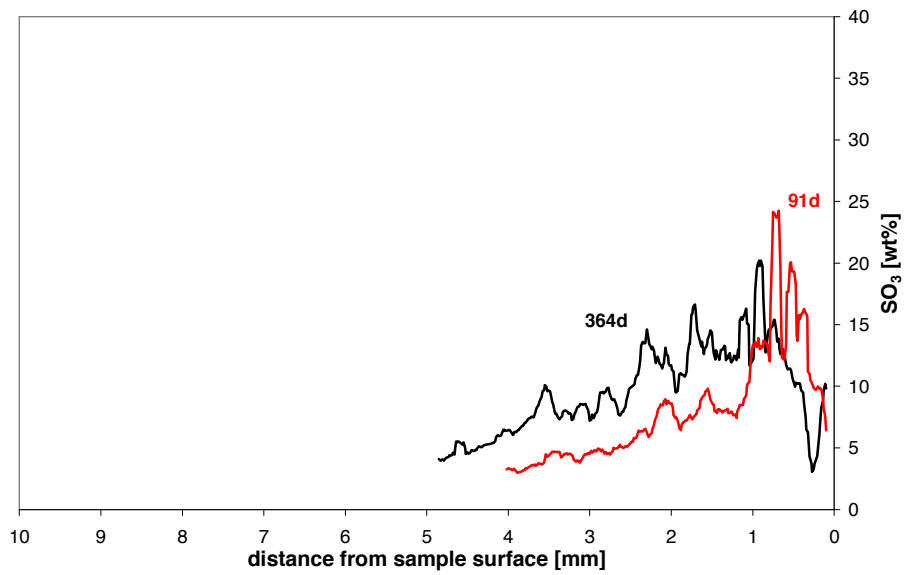
Figure 180: CEM I + 6% SF mortar exposed to sodium sulfate solution, sulfate profiles (median) for different exposure times

Bicarbonate Mixture Solution
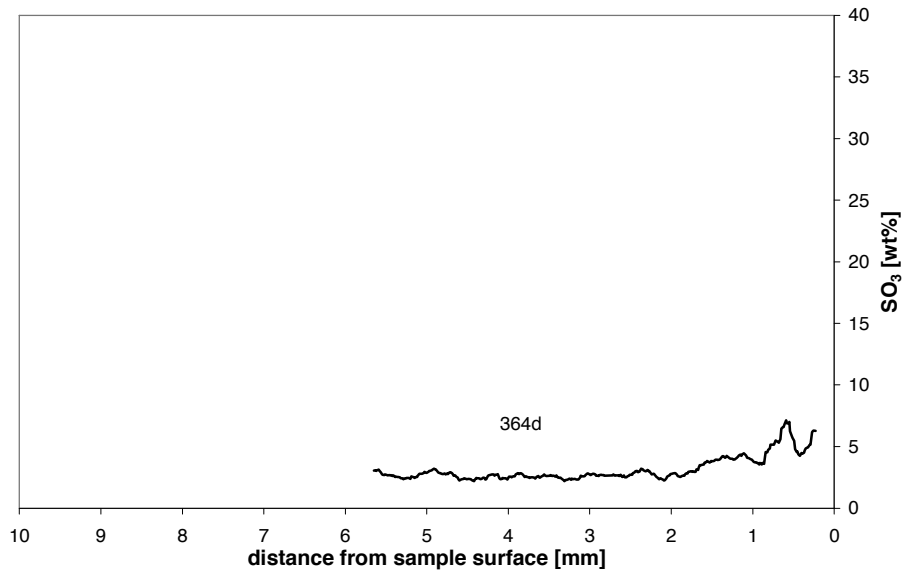
Figure 181: CEM I + 6% SF mortar exposed to bicarbonate mixture solution, sulfate profile (median) after 364 days of exposure

CEM I + 12% Silica Fume

Sodium Sulfate Solution
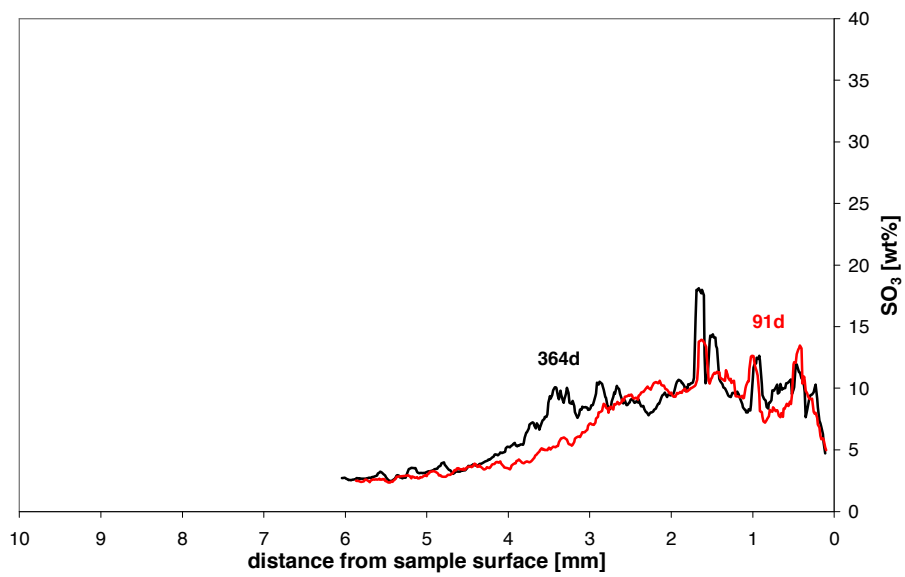
Figure 182: CEM I + 12% SF mortar exposed to sodium sulfate solution, sulfate profiles (median) for different exposure times

Bicarbonate Mixture Solution
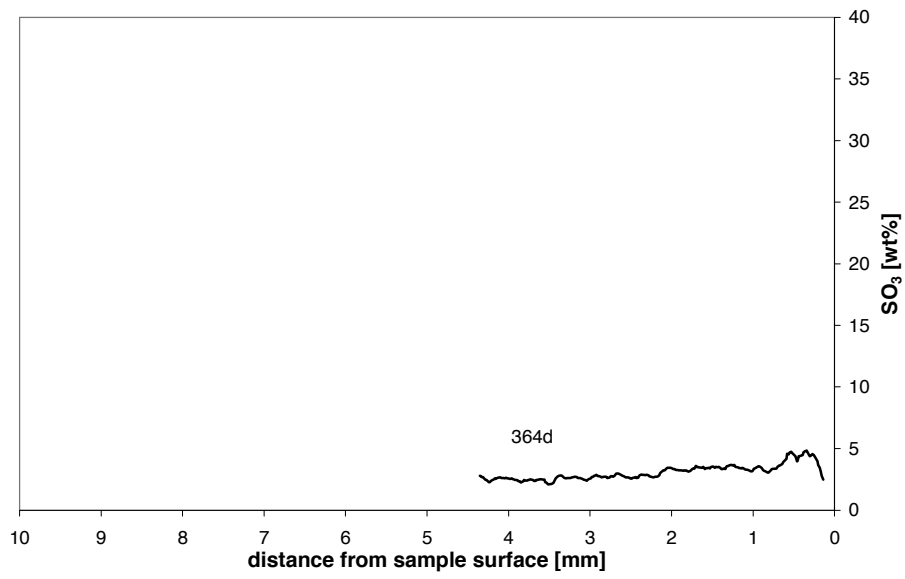
Figure 183: CEM I + 12% SF mortar exposed to bicarbonate mixture solution, sulfate profile (median) after 364 days of exposure

CEM I HS

Sodium Sulfate Solution
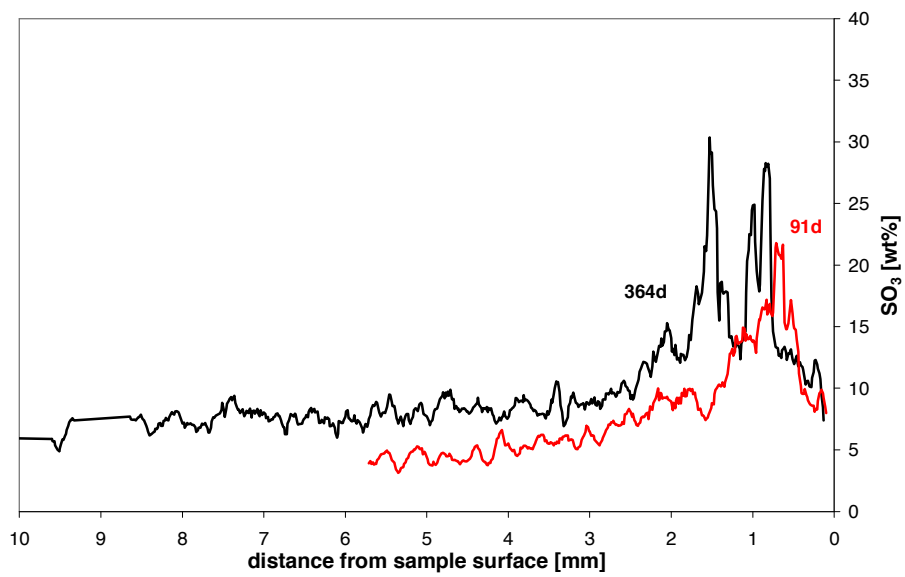
Figure 184: CEM I HS mortar exposed to sodium sulfate solution, sulfate profiles (median) for different exposure times
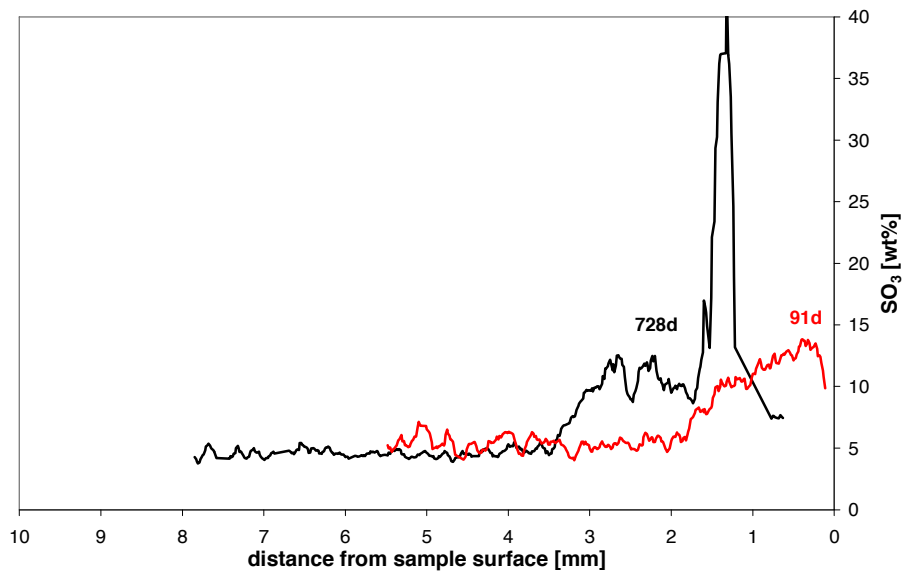
Bicarbonate Mixture Solution

Figure 185: CEM I HS mortar exposed to bicarbonate mixture solution, sulfate profile (median) after 364 days of exposure
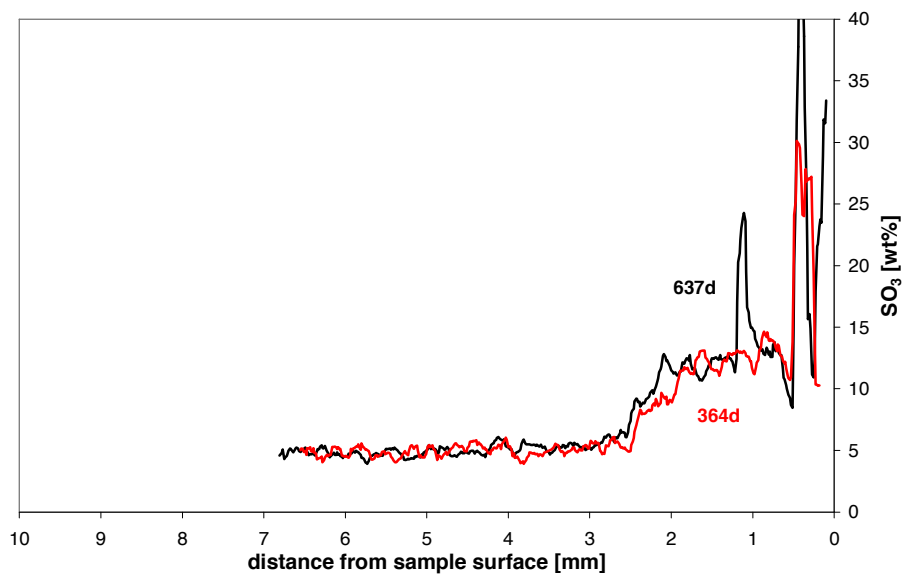
CEM II/A

Sodium Sulfate Solution

Figure 186: CEM II/A mortar exposed to sodium sulfate solution, sulfate profiles (median) for different exposure times

Bicarbonate Mixture Solution

Figure 187: CEM II/A mortar exposed to bicarbonate mixture solution, sulfate profile (median) after 364 days of exposure

CEM II/B

Sodium Sulfate Solution
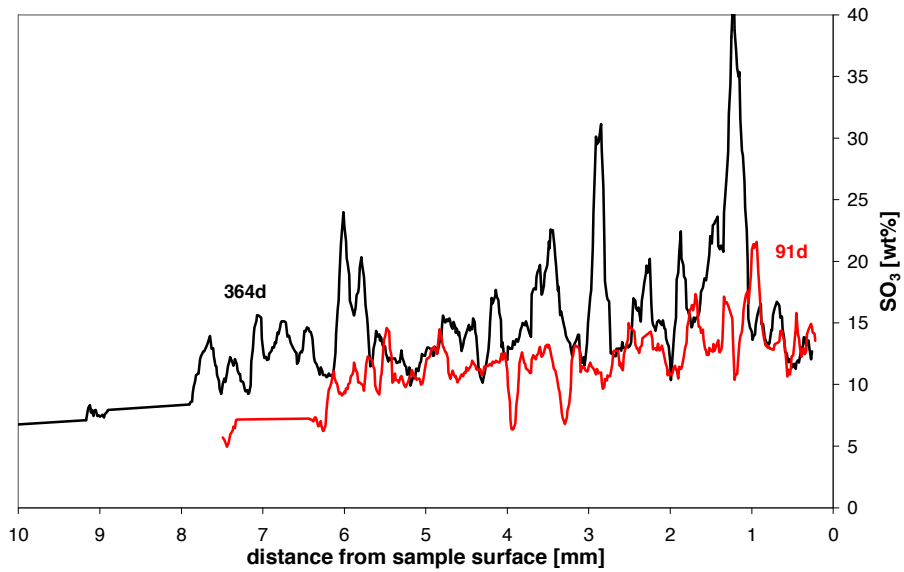
Figure 188: CEM II/B mortar exposed to sodium sulfate solution, sulfate profiles (median) for different exposure times

Bicarbonate Mixture Solution
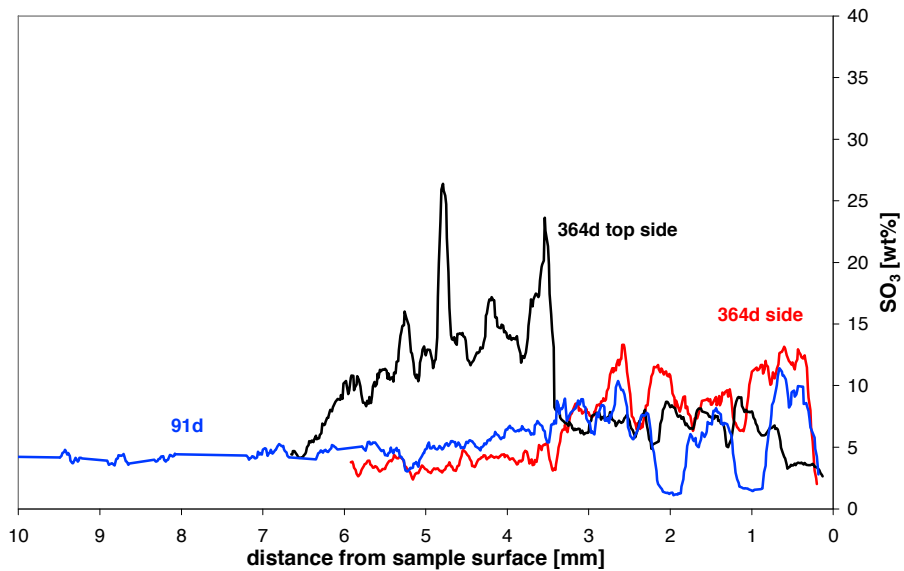
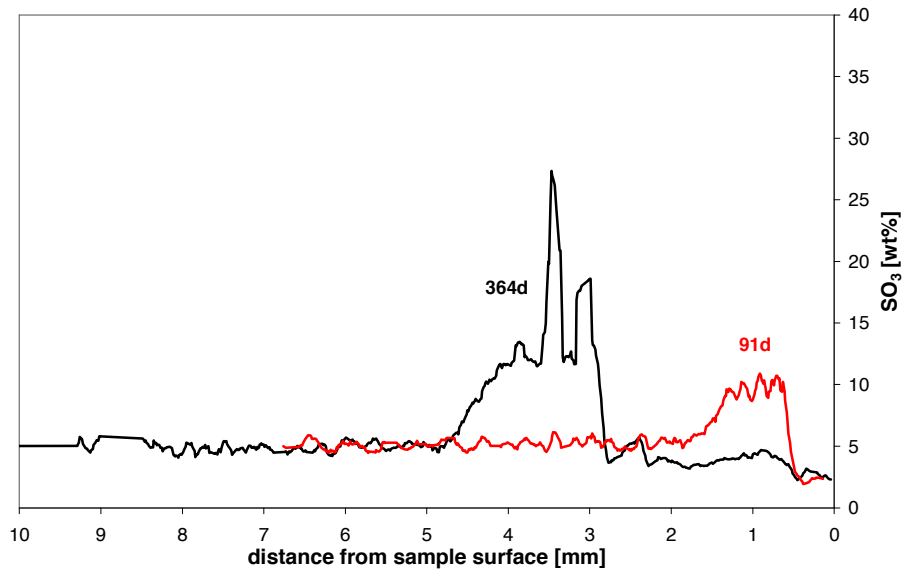**Figure 189**: CEM II/B mortar exposed to bicarbonate mixture solution, sulfate profiles (median) for different exposure times
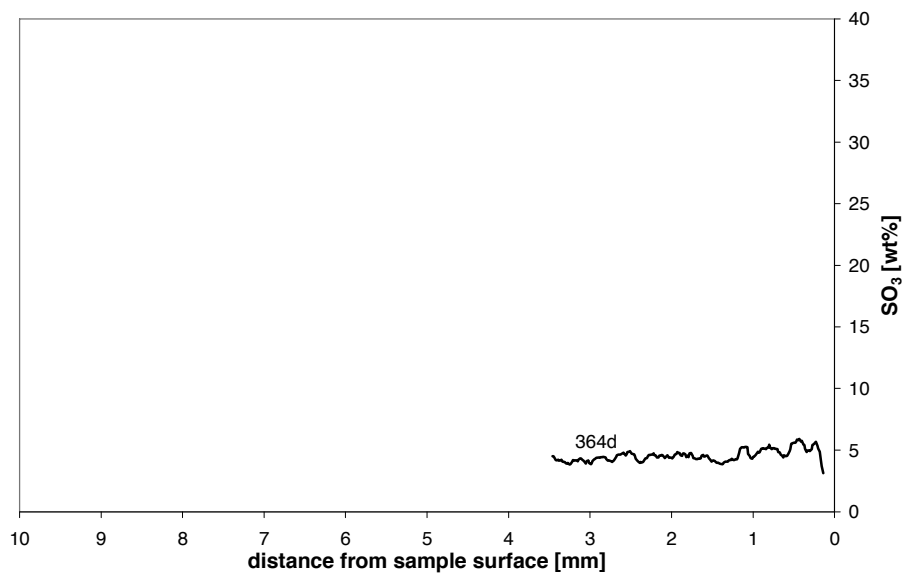
CEM III/B

<u>Initial Condition</u>
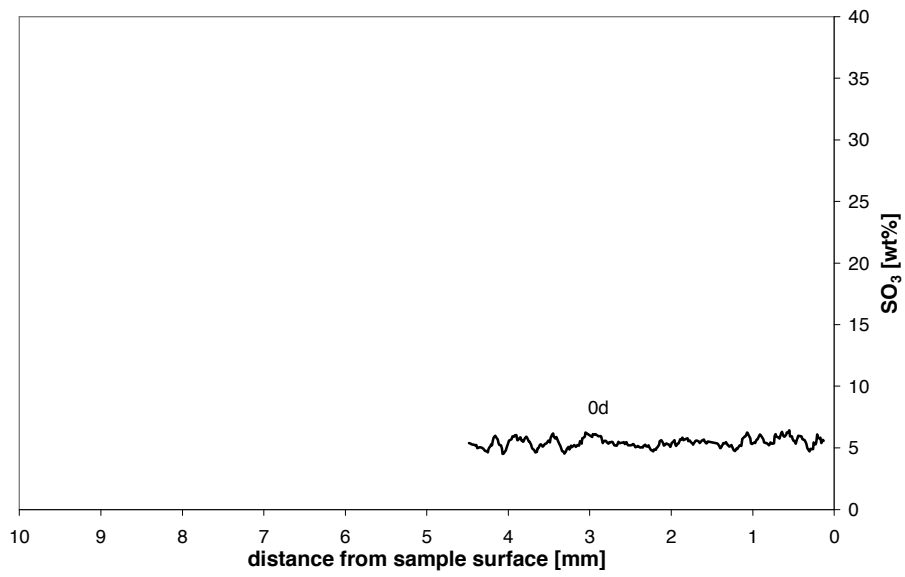
Figure 190: CEM III/B mortar before exposure, sulfate profile (median)

<u>Deionized water</u>
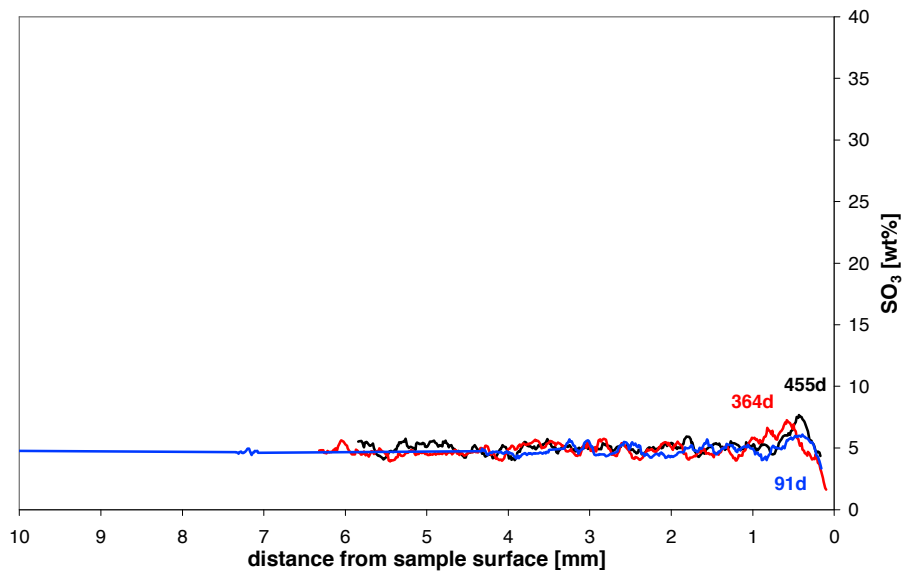
Figure 191: CEM III/B mortar in deionized water, sulfate profiles (median) for different exposure times
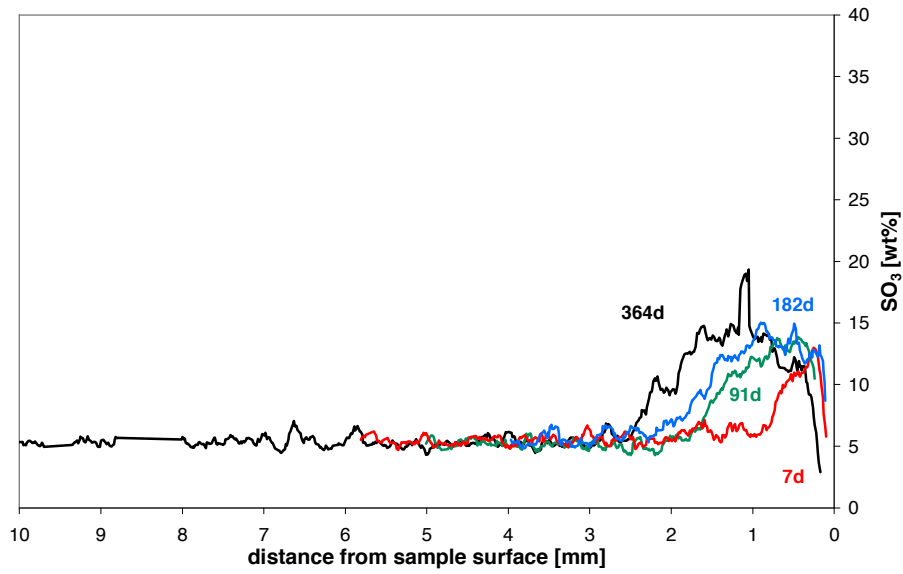
Figure 192: CEM III/B mortar exposed to sodium sulfate solution at 20°C, sulfate profiles (median) for different exposure times

Figure 193: CEM III/B mortar exposed to sodium sulfate solution at 40°C, sulfate profile (median) for 637 days of exposure

Sodium Bicarbonate Solution
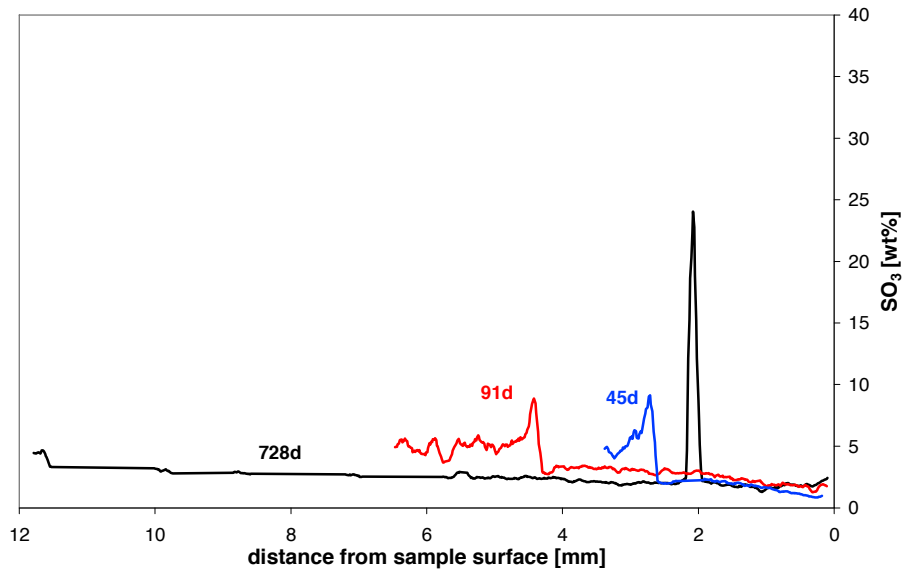
Figure 194: CEM III/B mortar exposed to sodium bicarbonate solution, sulfate profiles (median) for different exposure times

Potassium Sulfate Solution
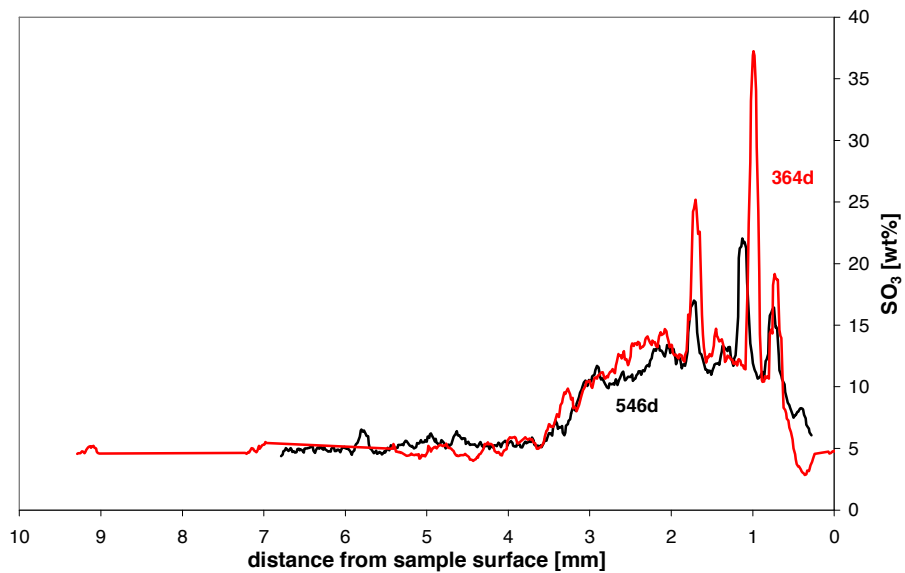
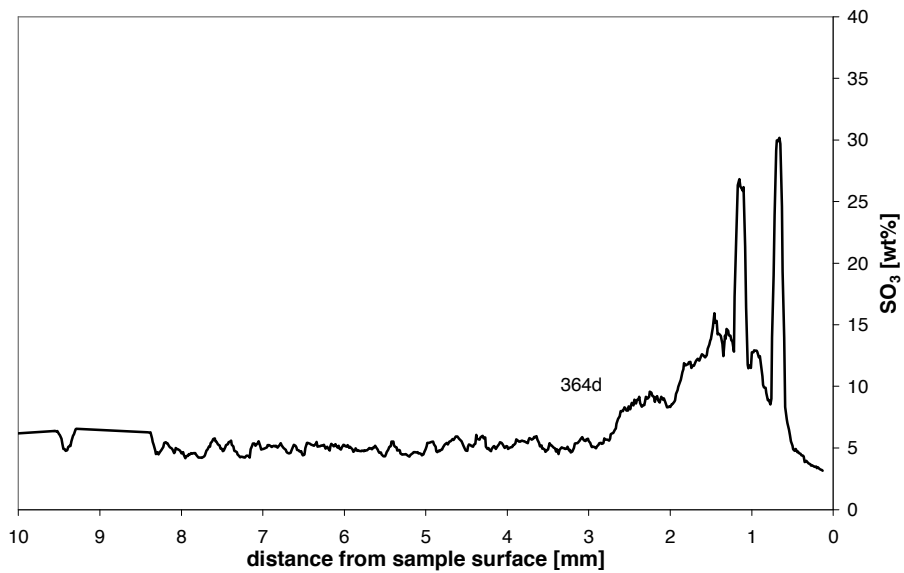**Figure 195**: CEM III/B mortar exposed to potassium sulfate solution, sulfate profiles (median) for different exposure times
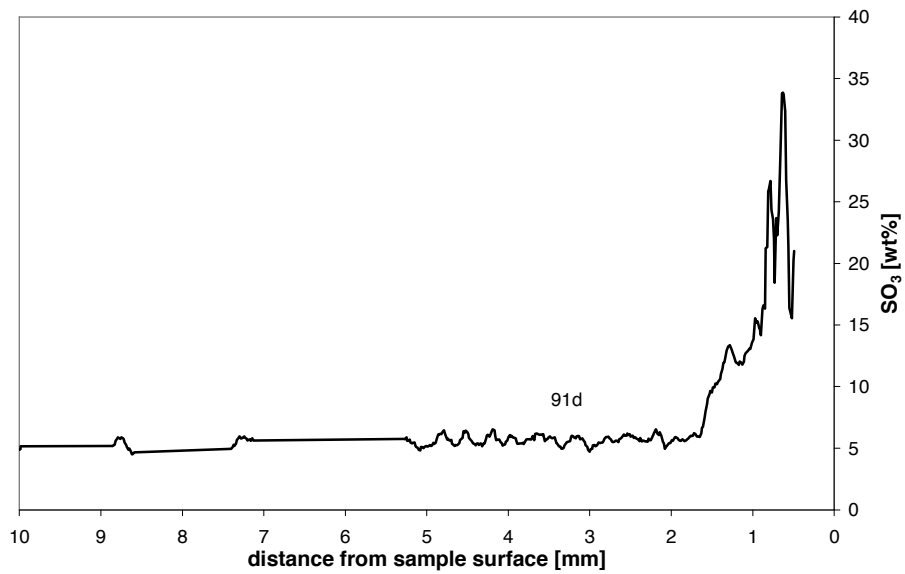
<u>Magnesium Sulfate Solution</u>
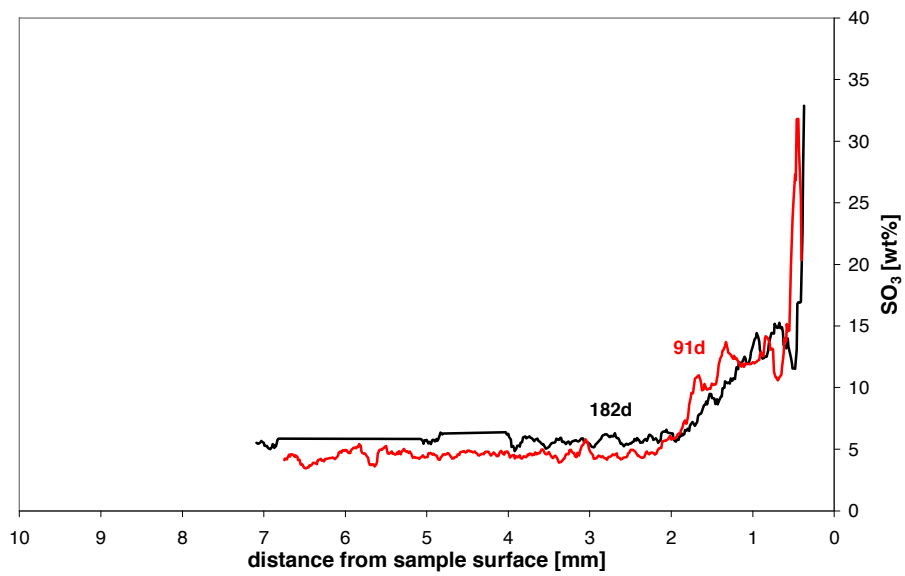
Figure 196: CEM III/B mortar exposed to magnesium sulfate solution, sulfate profiles (median) for different exposure times

Figure 197: CEM III/B mortar exposed to magnesium sulfate solution (0.035 mol/l), sulfate profiles (median) for different exposure times
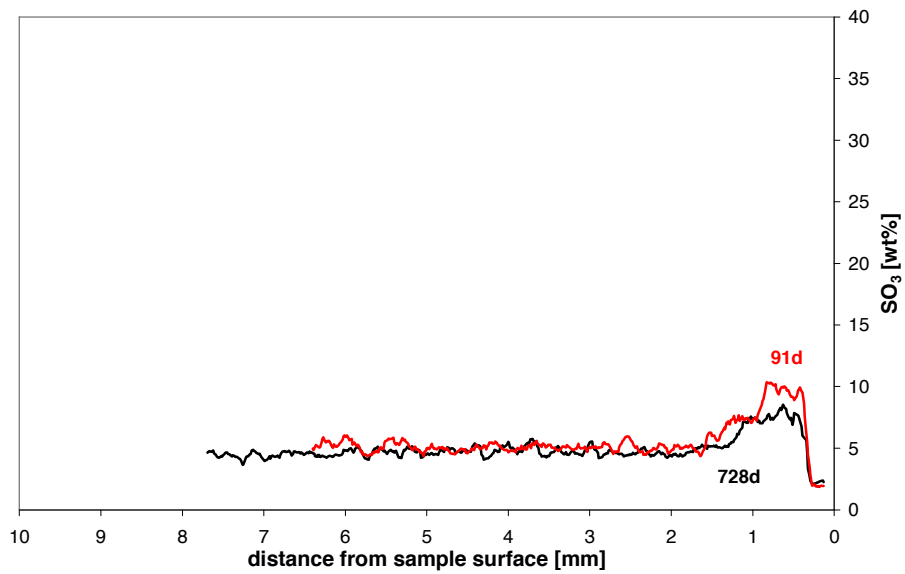
Figure 198: CEM III/B mortar exposed to magnesium bicarbonate solution (0.035 mol/l), sulfate profiles (median) for different exposure times

Sulfate Mixture Solution

Figure 199: CEM III/B mortar in sulfate mixture solution, sulfate profiles (median) for different exposure times

<u>Bicarbonate Mixture Solution</u>

Figure 200: CEM III/B mortar exposed to bicarbonate mixture solution, sulfate profiles (median) for different exposure times

Figure 201: CEM III/B mortar exposed to bicarbonate mixture solution (0.035 mol/l), sulfate profiles (median) for different exposure times

CEM III/C

<u>Sodium Sulfate Solution</u>
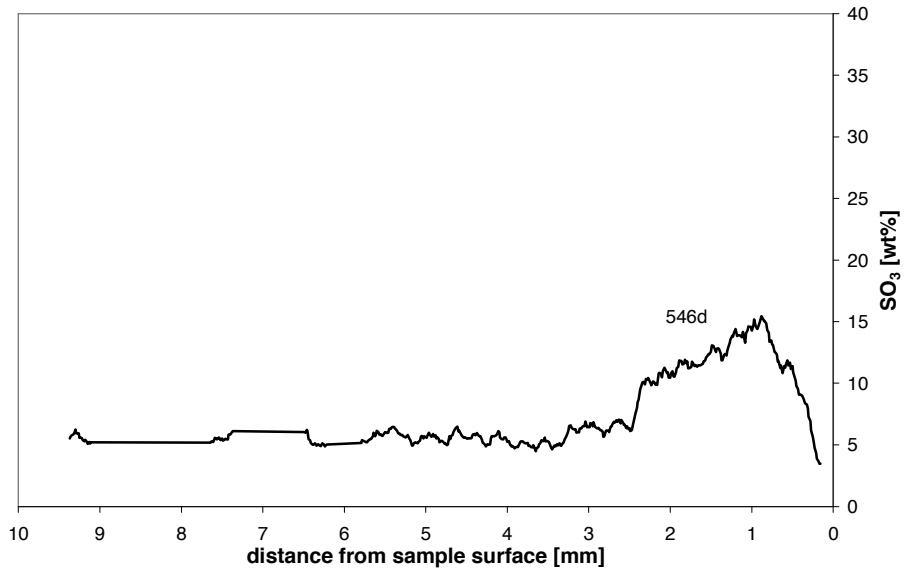
Figure 202: CEM III/C mortar exposed to sodium sulfate solution, sulfate profile (median) for 546 days of exposure

<u>Potassium Sulfate Solution</u>

Figure 203: CEM III/C mortar exposed to potassium sulfatesolution, sulfate profile (median) for 346 days of exposure

Magnesium Sulfate Solution

Figure 204: CEM III/C mortar exposed to magnesium sulfate solution, sulfate profile (median) for 91 days of exposure

Bicarbonate Mixture Solution
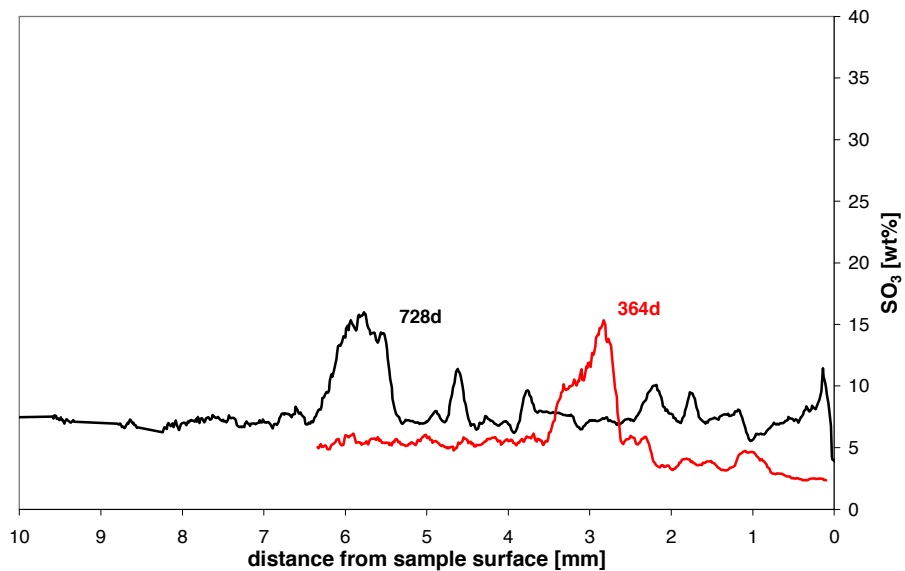
Figure 205: CEM III/C mortar exposed to bicarbonate mixture solution, sulfate profiles (median) for different exposure times

6.9   Mechanical Properties

Table 37: Compressive and flexural strength development for mortars ("w/b" = 0.55)

cement	testing age [d]	compressive strength average	std. dev.	flexural strength average	std. dev.
			[N/mm^2]		
CEM I	1	10.7	0.3	2.8	0.1
	7	28.0	0.1	5.3	0.5
	28	40.6	1.7	6.6	0.7
	730	59.4	---	8.4	---
CEM I + 2% gypsum	7	25.2	0.8	4.6	0.1
	28	35.0	0.6	6.1	0.3
	730	53.4	---	8.5	---
CEM I + 6% SF	7	30.1	0.2	6.0	0.2
	28	48.0	0.9	7.1	0.5
	730	64.0	---	8.1	---
CEM I + 12% SF	7	29.2	0.1	5.7	0.3
	28	52.4	0.9	7.4	0.9
	730	67.5	---	8.2	---
CEM I HS	1	7.8	0.4	2.2	0.2
	7	30.8	0.6	6.2	0.2
	28	41.9	0.4	7.2	0.4
	730	64.1	---	9.1	---
CEM II/A V-LL	1	6.3	0.0	1.9	0.1
	7	25.8	0.4	5.0	0.1
	28	33.0	0.5	6.1	0.3
	730	55.6	---	9.9	---
CEM III/B	1	3.5	0.1	1.1	0.0
	7	21.1	0.4	4.7	0.4
	28	40.3	0.3	7.4	0.1
	730	75.6	---	10.7	---
CEM III/C	7	19.8	0.5	4.6	0.1
	28	36.0	0.6	7.2	0.0
	730	65.1	---	9.9	---

6.10 Length Changes
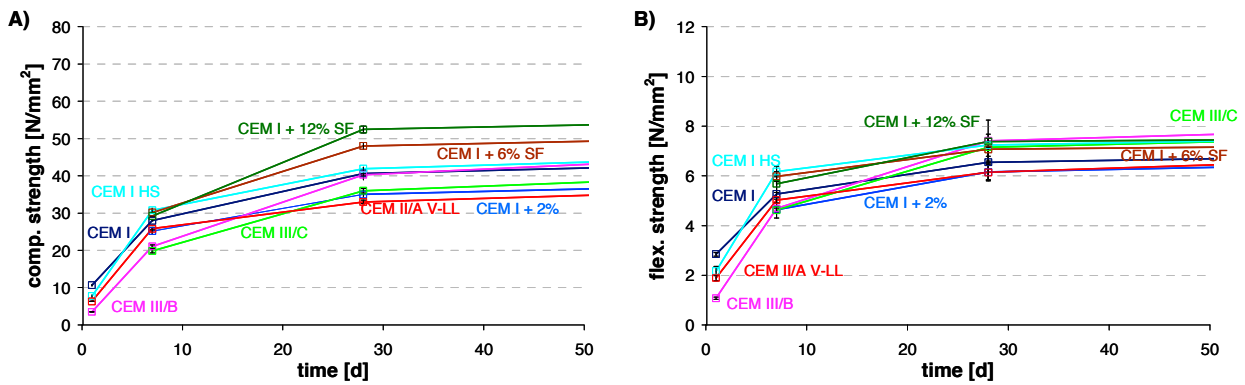
Figure 206: A) compressive strength and B) flexural strength development of the tested mortars
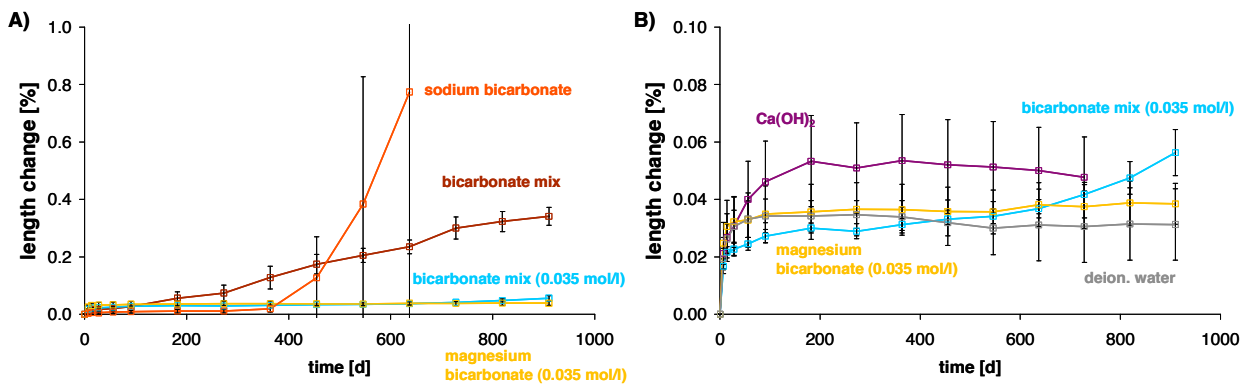
Figure 207: Length changes of CEM I mortar bars exposed to A) sulfate solutions with sodium bicarbonate and B) reference solutions
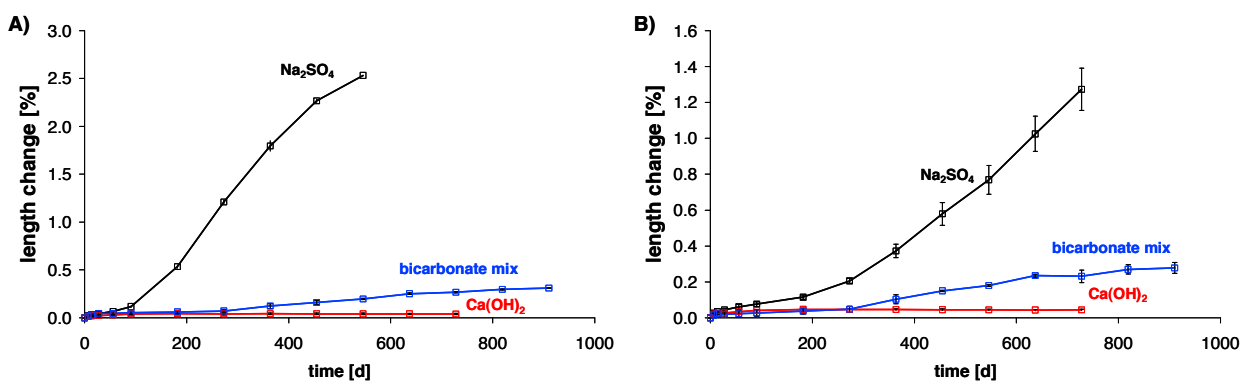

Figure 208: Length changes with time for all solutions tested with the A) CEM I +2% gypsum and B) CEM I HS mortar bars
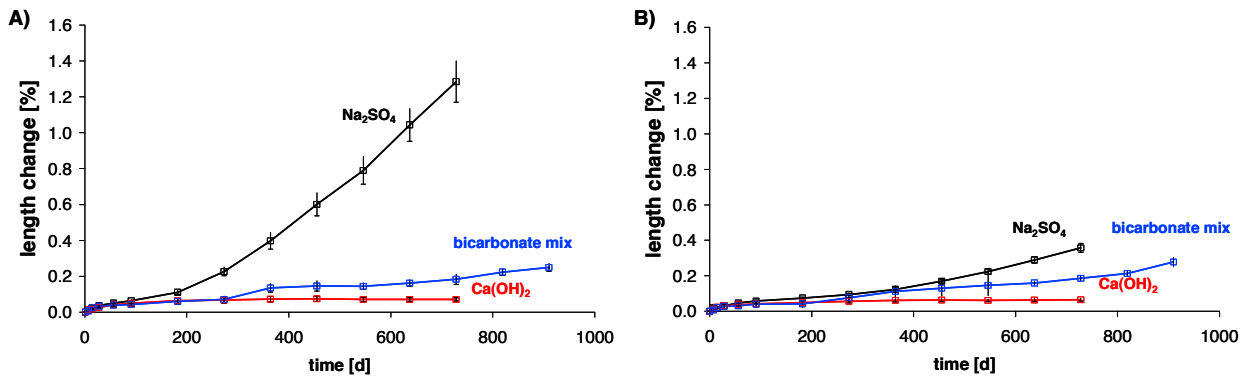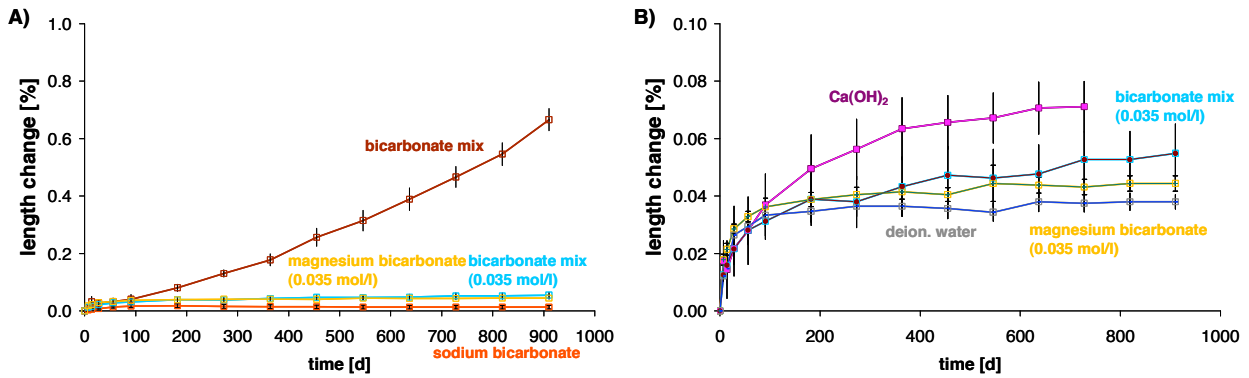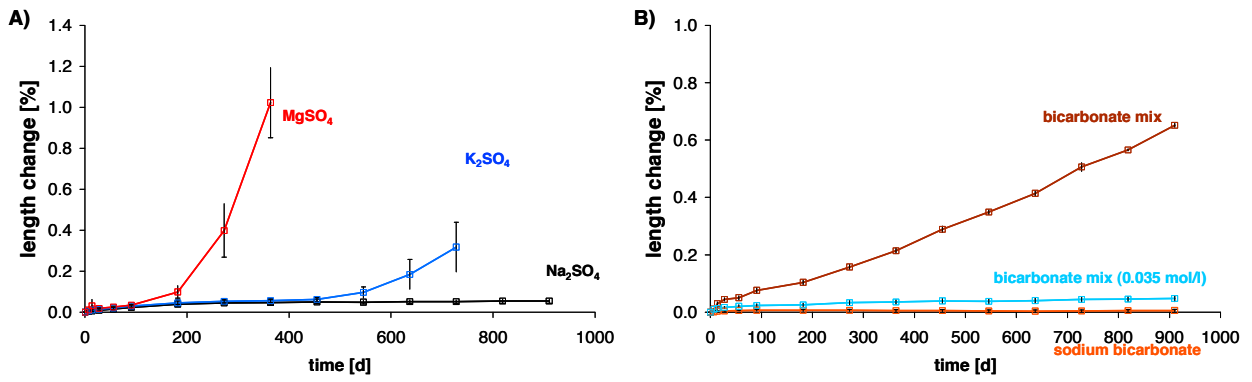
Figure 209: Length changes with time for all solutions tested with the A) CEM I +6% SF and B) CEM I +12% SF mortar bars
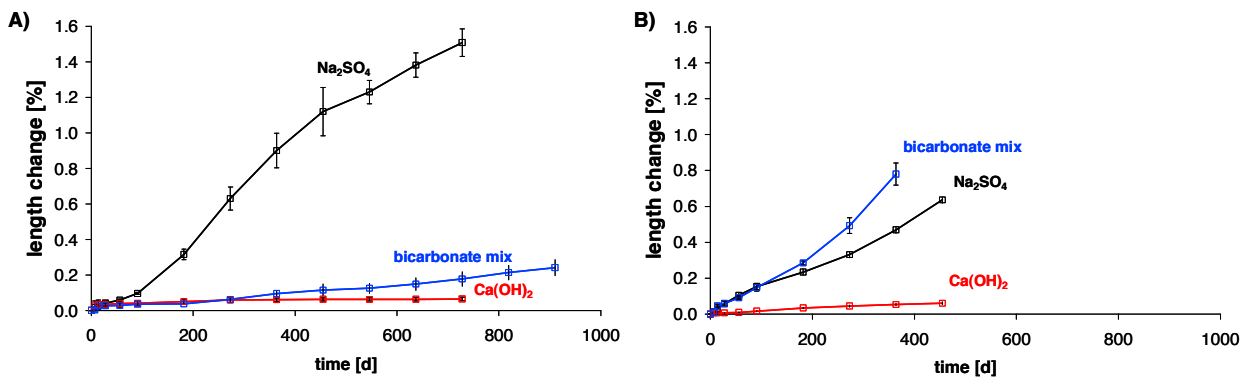
Figure 210: Length changes with time for all solutions tested with the A) CEM II/A and B) CEM II/B mortar bars

Figure 211: Length changes of CEM III/B mortar bars exposed to A) sulfate solutions with sodium bicarbonate and B) reference solutions

Figure 212: Length changes of CEM III/C mortar bars exposed to A) sulfate solutions and B) sulfate solutions with sodium bicarbonate
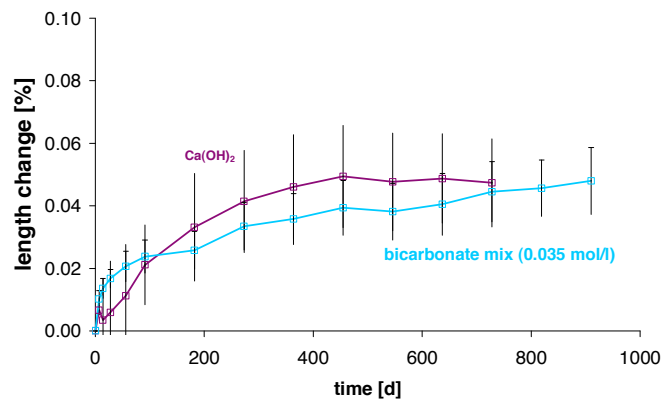
Figure 213: Length changes of CEM III/C mortar bars exposed to saturated lime solution and bicarbonate mixture (0.035 mol/l)
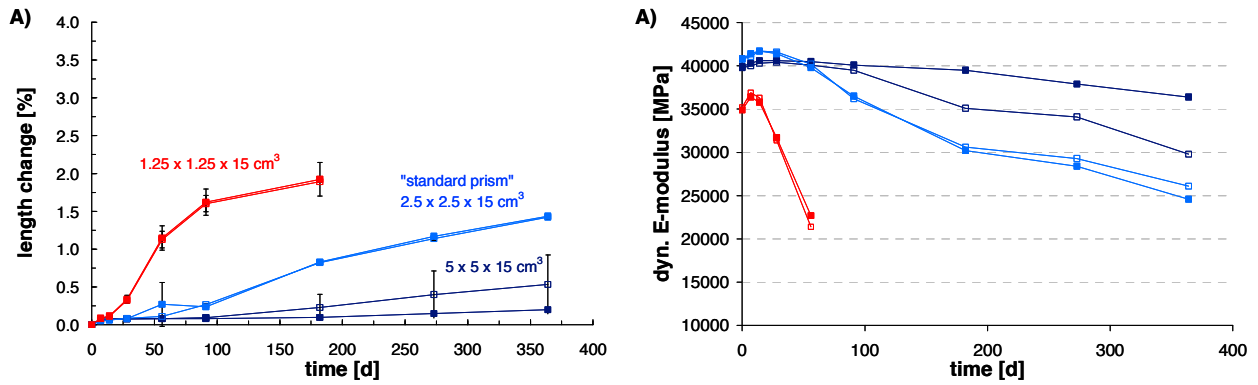
Size Effects:
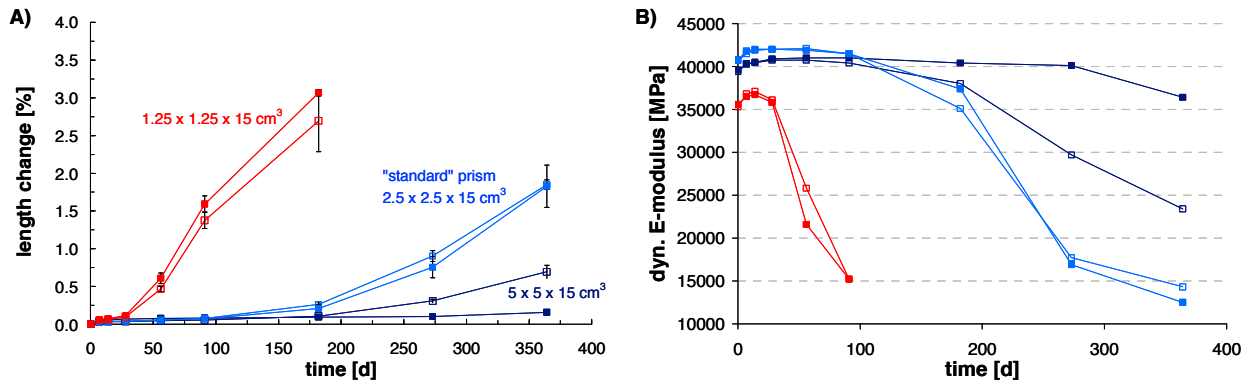
Figure 214: Development of the A) length changes and B) dynamic E-modulus for CEM I mortar prisms of different sample sizes exposed to sodium sulfate solution at 20°C; full squares represent mortars with sealed ends
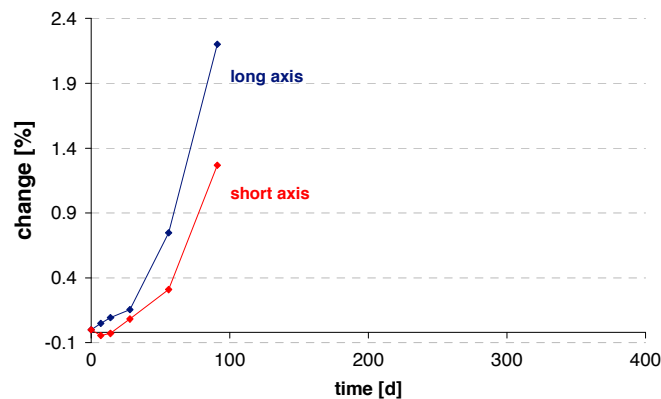

Figure 215: Development of the A) length changes and B) dynamic E-modulus for CEM I mortar prisms of different sample sizes exposed to sodium sulfate solution at 40°C; full squares represent mortars with sealed ends

Figure 216: Comparison of length changes in the long and short axes (average of both) of CEM I mortar prisms for in sodium sulfate solution (specimen size: 1.25 x 1.25 x 15 cm³)
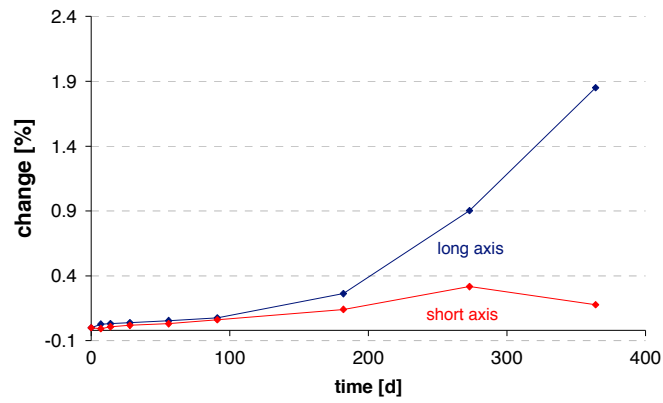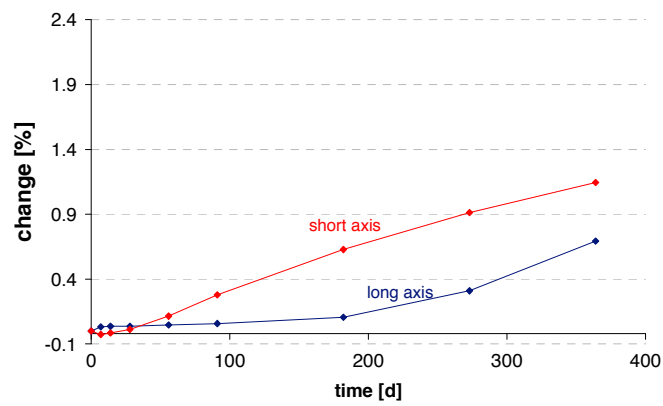
Figure 217: Comparison of length changes in the long and short axes (average of both) of CEM I mortar prisms for in sodium sulfate solution (<u>specimen size</u>: 2.5 x 2.5 x 15 cm^3)

Figure 218: Comparison of length changes in the long and short axes (average of both) of CEM I mortar prisms for in sodium sulfate solution (<u>specimen size</u>: 5 x 5 x 15 cm^3)

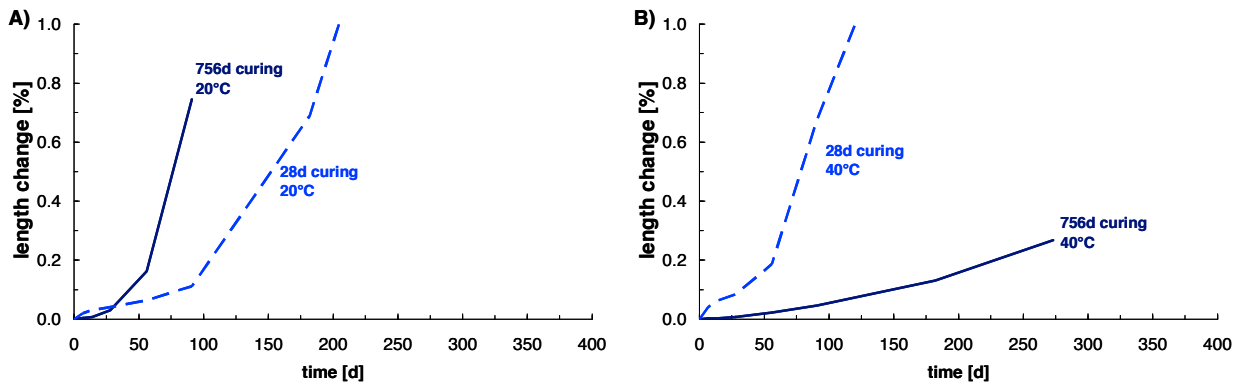**Effect of Additional Curing on Length Changes**

Figure 219: Length changes with time for the CEM I mortar bars in sodium sulfate solution with and without extensive curing at A) 20°C and B) 40°C
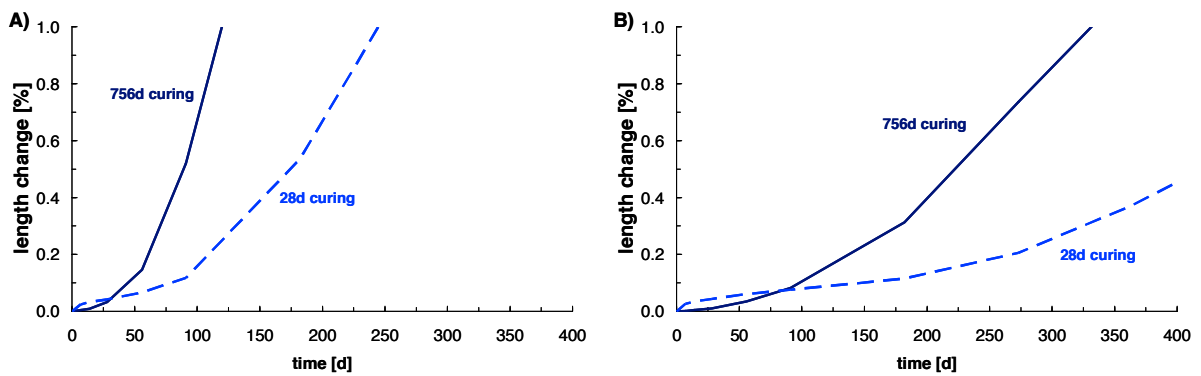

Figure 220: Length changes with time for the A) CEM I +2% gypsum and B) CEM I HS mortar bars in sodium sulfate solution with and without extensive curing
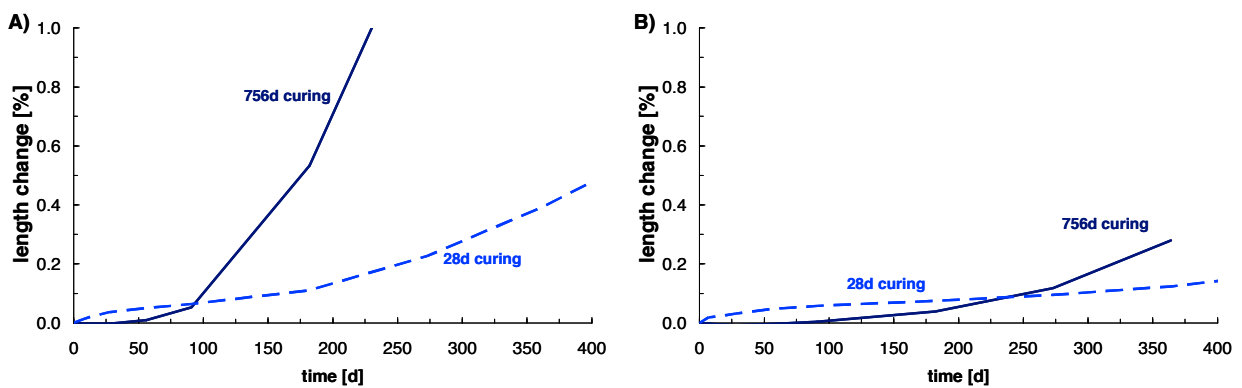

Figure 221: Length changes with time for the mortar bars in sodium sulfate solution with and without extensive curing made from A) CEM I +6% SF and B) CEM I +12% SF
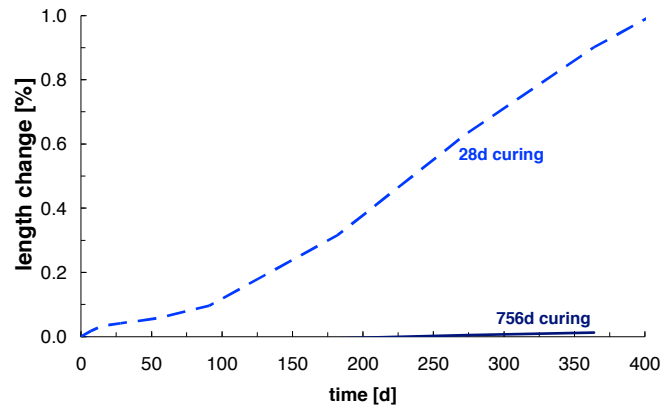
Figure 222: length changes with time for the CEM II/A in sodium sulfate solution with and without extensive curing

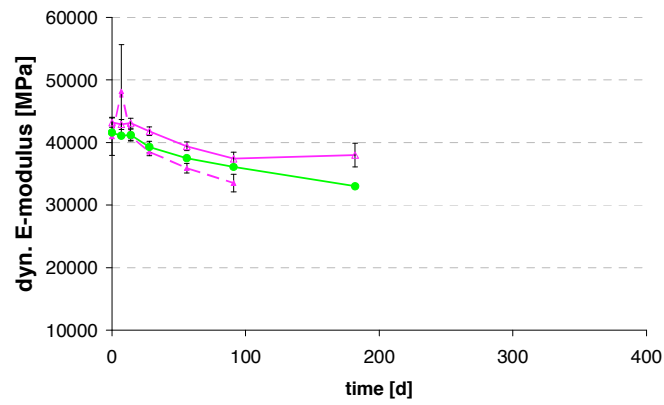## Effect of Additional Curing on Dynamic E-Modulus

Figure 223: development of the dynamic E-modulus for CEM III prisms in magnesium sulfate solution at 20°C and 40°C after two years of extra curing in lime water
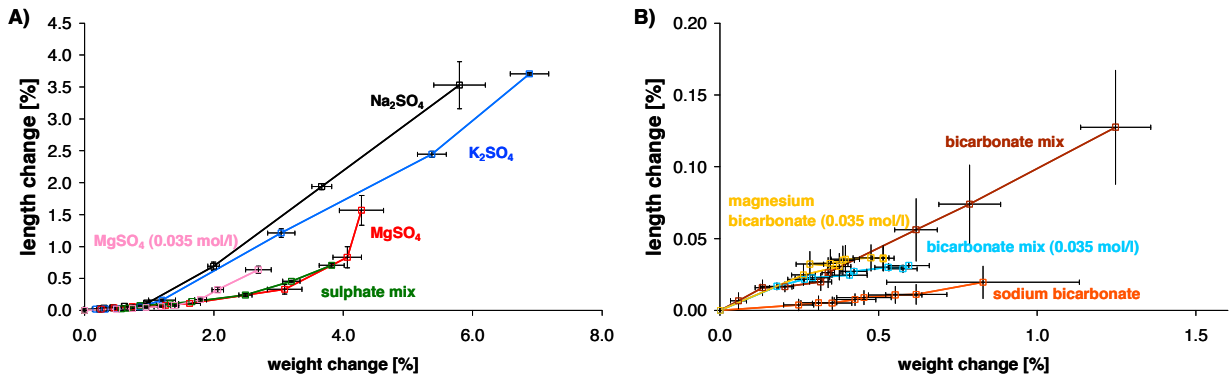
6.11 Length and Mass Changes

Figure 224: Relation of length and weight changes for selected sulfate solutions up to one year, for A) solutions without and B) solutions with sodium bicarbonate, CEM I
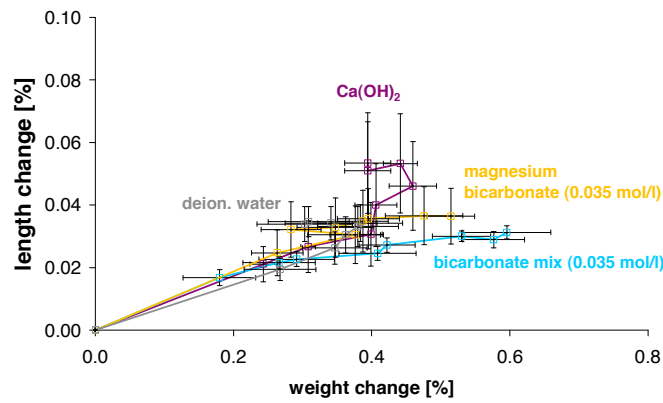

Figure 225: Relation of length and weight changes for reference solutions and low expansion systems up to one year, CEM I
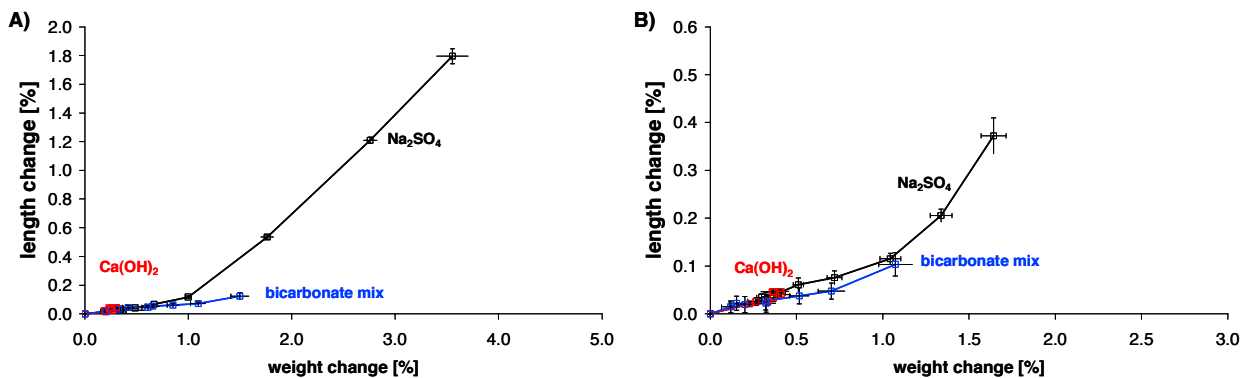
Figure 226: Relation of length and weight changes for all tested solutions <u>up to one year</u>; for A) CEM I + 2% gypsum and B) CEM I HS mortar bars
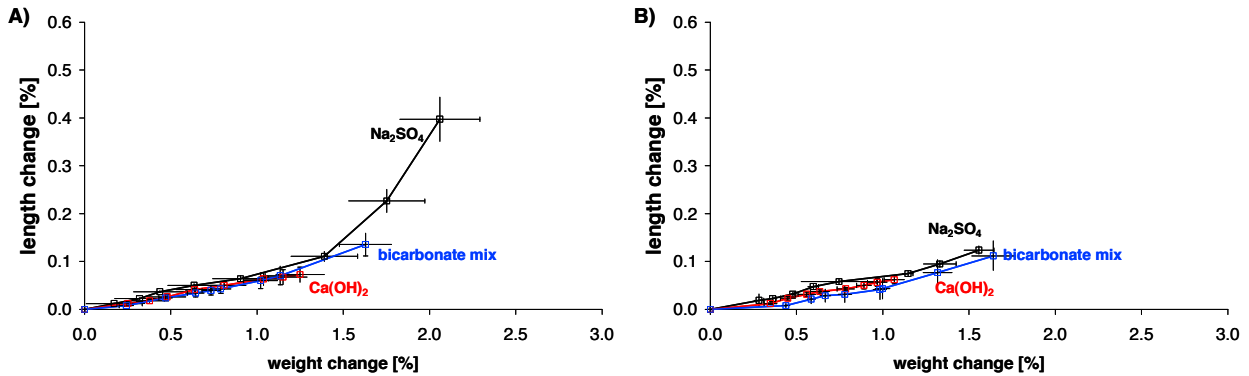

Figure 227: Relation of length and weight changes for all tested solutions <u>up to one year</u> for A) CEM I + 6% SF and B) CEM I + 12% SF mortar bars
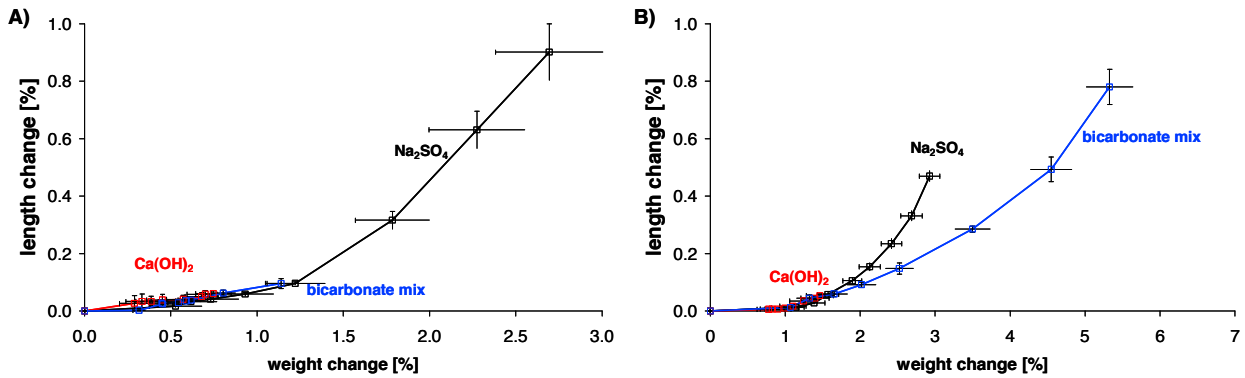

Figure 228: Relation of length and weight changes for all tested solutions <u>up to one year</u> for A) CEM II/A and B) CEM II/B mortar bars

Figure 229: Relation of length and weight changes for selected sulfate solutions <u>up to one year</u>, for A) solutions without and B) solutions with sodium bicarbonate, CEM III/B

Figure 230: Relation of length and weight changes for reference solutions and low expansion systems up to one year, CEM III/B
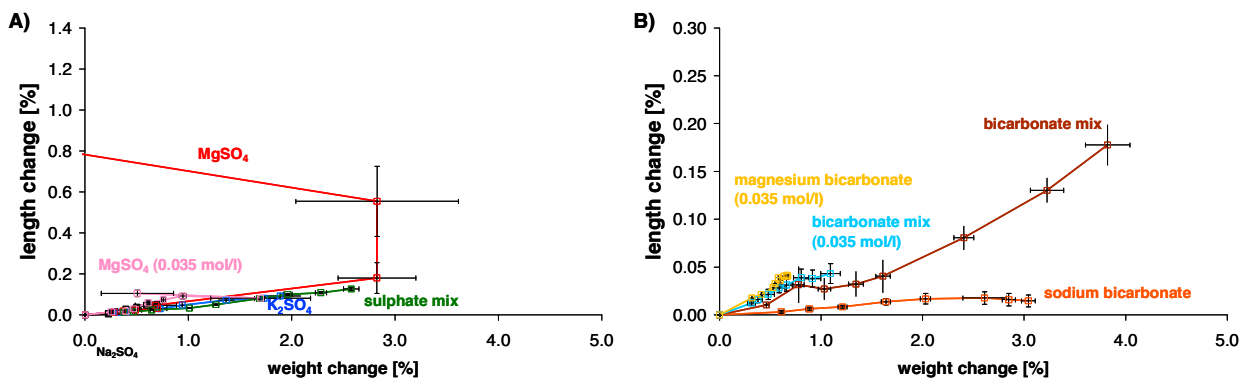

Figure 231: Relation of length and weight changes for selected sulfate solutions up to one year, for A) solutions without and B) solutions with sodium bicarbonate, CEM III/C
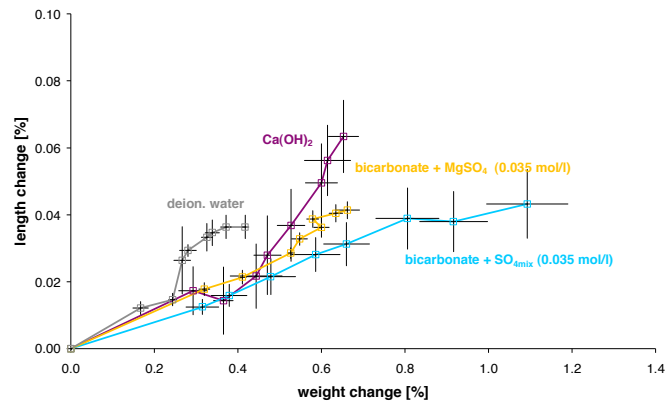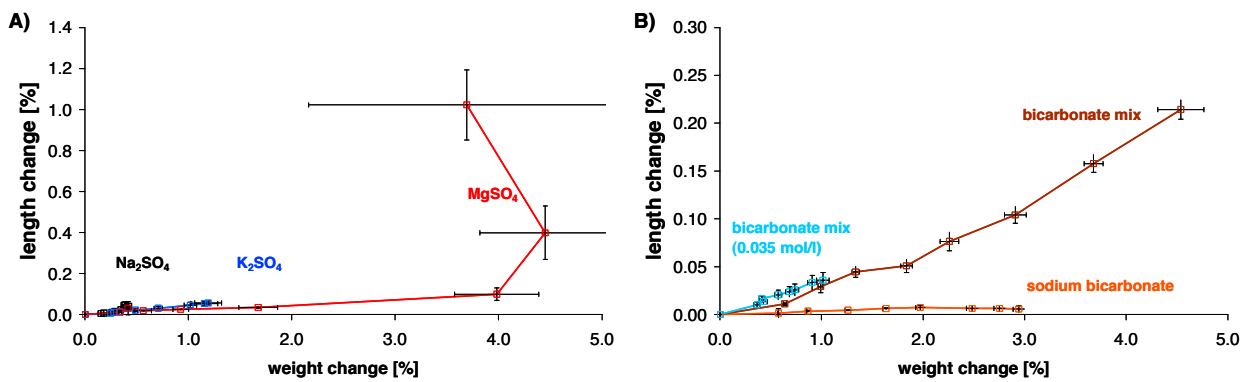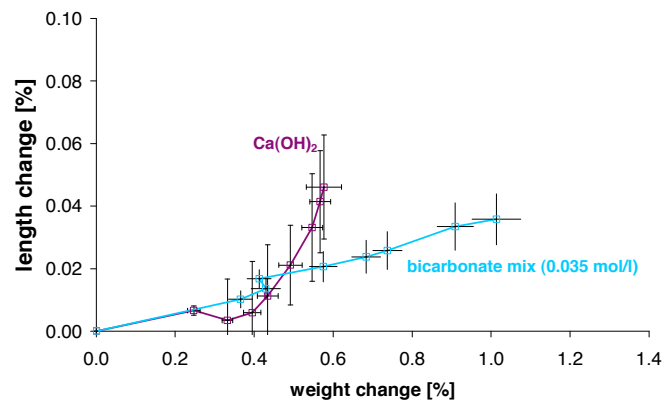

Figure 232: Relation of length and weight changes for saturated lime solution and bicarbonate mixture solution (0.035 mol/l) up to one year, CEM III/C

Curriculum Vitae

Wolfgang	**Kunther**

Birthday	15. October 1974
Born in	Hamburg, Germany
Nationality	German
University degrees	Civil engineering diploma, Aachen University, Germany
	MSc in concrete technology, Reykjavik University, Iceland

Academic Education

May 2008 – today	External PhD student at EPF Lausanne, Switzerland
Sept.2006 – May 2007	MSc in Concrete Technology, Reykjavik University, Iceland
	Masters Thesis: "The Efficiency of Selected Dispersing Agents on Rheological Properties of Mortars"
	Award for "outstanding scientific contributions"
Apr. 2005 – Apr. 2007	Post graduate courses in law, micro- and macroeconomics, and accounting at Fernuniversität Hagen
Nov. 2003 – May 2004	Diploma work about sedimentation behaviour of kaolinite under influence of organic polymers
Sept. 1997 – May 2004	Diploma in civil engineering, RWTH Aachen University
Aug. 1981 – July 1994	Schooldays

Practical Work

May. 2008 – Jan 2012	PhD student at Empa, Dübendorf, Switzerland
June 2006 – April 2008	Research engineer at the Innovation Center Iceland (former Icelandic Building Research Institute) for rheology and microstructural investigations, Reykjavik, Iceland
Feb. 2005 – April 2006	Internship construction management for a shopping mall in Hamburg, F.C. Trapp Baugesellschaft, Wesel
Dec. 2000 – Nov. 2003	Student job at the Institute of Hydraulic Engineering and Water Resources Management, Aachen University
April 1997 – Aug. 1997	Internships on road construction and building construction sites with different contractors, Hamburg
Aug. 1994 – Jan. 1997	Apprenticeship as draughtsman, Dorsch Consult Ingenieurgesellschaft mbH, Hamburg

Submitted Papers

W. Kunther, B. Lothenbach, K. Scrivener: *On the relevance of volume increase for the length changes of mortar bars in sulfate solutions*, submitted to Cement and Concrete Research, July 2012

W. Kunther, B. Lothenbach, K. Scrivener: *Influence of bicarbonate ions on the deterioration of mortar bars in sulfate solutions*, submitted to Cement and Concrete Research, June 2012

W. Kunther, B. Lothenbach, K. Scrivener: *Deterioration of mortar bars immersed in magnesium containing sulfate solutions*, submitted to Materials and Structures, July 2012

Scientific Presentations

W. Kunther, B. Lothenbach, M. Ben Haha, K. Scrivener: *Thermodynamic modelling of compositional variations of an ordinary Portland cement and their effect on the phase changes under sulfate attack,* short oral communication and poster, International Congress on the Chemistry of Cement, Madrid, Spain, 3-8 July, 2011

W. Kunther, B. Lothenbach, K. Scrivener: *Thermodynamic modelling of cements in different sulfate environments*, in: Symposium on Concrete Modelling (CONMOD 2010), Lausanne, Switzerland, June 22-25, 2010

W. Kunther, B. Lothenbach, K. Scrivener: *Influence of different sulfate environments on the properties of ordinary Portland cement*, MC-RTN Final Conference, Villars-sur Ollon, Switzerland, September 1-3, 2009

Ó. H. Wallevik, S. Kubens, W. Kunther: *Microstructural investigations on alite*, in: Scandem 2007, Proceedings of the 58th Annual Meeting of the Nordic Microscopy Society, Espoo, Finland, June 18-20, 2007

Scientific Poster

W. Kunther, B. Lothenbach, K. Scrivener: *Experimental determination of oxide profiles in a cementitious matrix with EDS*, in: Transport in Porous Materials, PSI, Villingen, Switzerland, August 19, 2010

W. Kunther, B. Lothenbach, K. Scrivener: *Influence of different sulfate environments on the properties of ordinary Portland cement*, in: 17. Int. Baustofftagung (IBAUSIL), Weimar, Germany, September 23-26, 2009

W. Kunther, B. Lothenbach, K. Scrivener: *Influence of carbonate in sulfate environments*, in: Concrete in aggressive aqueous environments - Performance, Testing, and Modelling, Toulouse, France, June 3-5, 2009